ARENBERG DOCTORAL SCHOOL
Faculty of Engineering Technology

EINDHOVEN DOCTORAL SCHOOL
Faculty of Industrial Engineering &
Innovation Sciences

Development of a new road lighting concept

Rik Marco Spieringhs

Supervisors:
Prof. dr. Peter Hanselaer
Prof. dr. Ingrid Heynderickx
Prof. dr. Kevin A. G. Smet

Joint dissertation presented in partial fulfilment of the requirements for the degree of Doctor of Engineering Technology (PhD) KU Leuven and Doctor of Philosophy (PhD) TU Eindhoven

6th May 2024

Development of a new road lighting concept

Rik Marco SPIERINGHS

Preliminary Defence KU Leuven
Examination committee:
Prof. dr. Hilde Breesch, chair
Prof. dr. Peter Hanselaer, supervisor
Prof. dr. Ingrid Heynderickx, supervisor
Prof. dr. Kevin A. G. Smet, supervisor
Prof. dr. Philip Dutre
MSc. Bruno Depre
Prof. dr. Antal Haans
(Eindhoven University of Technology)
dr. Maurice Donners
(Eindhoven University of Technology)
Prof. dr. George Zissis
(Universite Toulouse III - Paul Sabatier)
BSc. Willem Zandvliet
(Rijkswaterstaat)

Dissertation presented in partial fulfilment of the requirements for the degree of Doctor of Engineering Technology (PhD) KU Leuven

6th May 2024

Development of a new road lighting concept

PROEFSCHRIFT

ter verkrijgen van de graad van doctor aan de Technische Universiteit Eindhoven, op gezag van rector magnificus prof.dr.ir. S.K. Lenaerts, voor een commissie aangewezen door het College voor Promoties, in het openbaar te verdedigen op 6 mei 2024 om 16:00 uur

door

Rik Marco Spieringhs

geboren te De Bilt

Dit proefschrift is goedgekeurd door de promotoren en de samenstelling van de promotiecommissie voor de publieke verdediging TU Eindhoven is als volgt:

Voorzitter:	Prof. dr. ir. Geert-Jan van Houtum
Promotoren:	Prof. dr. Ingrid Heynderickx
	Prof. dr. Peter Hanselaer (KU Leuven)
Co-promotor:	Prof. dr. Kevin A.G. Smet (KU Leuven)
leden:	Prof. dr. Philip Dutre (KU Leuven)
	Prof. dr. Antal Haans
	dr. Maurice Donners
	Prof. dr. George Zissis (Universite Toulouse III - Paul Sabatier)

Het onderzoek dat in dit proefschrift wordt beschreven is uitgevoerd in overeenstemming met de TU/e Gedragscode Wetenschapsbeoefening.

Uitgegeven in eigen beheer, Rik Marco Spieringhs

ISBN 978-90-386-6017-2

Preface

Embarking on a PhD journey is similar to running a Marathon, navigating uncharted territory that appears to stretch endlessly before you. Beginning this expedition at the end of 2019, a period followed by unprecedented challenges, proved to be an additional stumbling block. It's like running a marathon while confined within the walls of one's home, a feat that requires incredible resilience, adaptability, and most importantly emotional support. Living abroad, in a time where simply crossing the border to friends and family seemed a forbidden measure, puts even the simplest of minds in a dark place. It's like starting the marathon on a sunny day, to be followed by thunderstorms and heavy headwinds. Though even in the darkest of places lighting always provides a solution. A tunnel to be ever-lit by friends, family, and ever-supporting colleagues. I am grateful for all the people I have had the chance to run with, stumble with, and share my experiences. It is for these people that I am the person today and am able to finally light up this tunnel, a task that seemed impossible at the time.

A marathon is never the same; I've run both the Ghent and Eindhoven marathons, metaphorically and physically, and even though being just across the border they couldn't have been more different. Though I am grateful for the opportunity to participate in both marathons, each presented its own set of challenges. Fortunately, I had two extremely illuminating promoters Prof. Ingrid Heynderickx and Prof. Peter Hanselaer that helped me across, and without them, this journey would not have been the same. Thank you to both my Promoters, co-promoters, and assessors for their valuable discussions and feedback.

One might assume that two marathons would be plenty, yet another marathon in Utrecht followed suit. Although metaphorically and not physically, maybe a marathon to run in my future endeavors, this leg of the journey was sponsored by Rijkswaterstaat. A government agency and department tasked with illuminating people's lives, both figuratively and physically. A person's life tends to be forgotten, however, lighting plays a pivotal role in people's well-being and most importantly safety. Therefore, this project held significant importance for me, not only on a personal level but also as a societal responsibility. Willem Zandvliet, who comprehended this responsibility deeply, ensured the integration of innovative lighting solutions. He understood the importance of people's perceptions of their surroundings in road lighting better than anyone else, and he was a valuable contributor to the research described in this manuscript. Additionally, I would like to express my sincere gratitude to Bram van den Heuvel and the members of the lighting society for their significant involvement, which was integral to this journey.

A marathon would not be the same without support on the sidelines. For my support in Ghent, standing there through thick and thin, believing in me, and being there for me during my lowest moments. A heartfelt thank you to all 2.5 members, both official and unofficial (Hang, Nick, Gareth, Jonas, Stijn, Jeroen, Nathan, Chingwei, Tommaso, Kong, and Jojo), for an unforgettable journey. Your willingness to listen when I needed it and your presence have truly brightened my life. Especially helpful for I started running in the dark. For my support in Eindhoven, I extend my gratitude for providing me with a desk and a place to stay. To me, HTI became a sanctuary of warmth and understanding, where I could share my stories and enjoy coffee with supportive colleagues.

Standing on the shoulder of giants, this section is an allude to my parents, siblings, friends, and extended family, echoing the African proverb 'If you want to go fast, go alone. If you want to go far, go together'. To my mom whose stature may be small in physical form but towers metaphorically. Thank you for standing by my side through hardship, through trials and triumphs, through all times, and throughout my whole life. It is by the presence of people who truly believe in you that you can achieve the most. To my dad who has always been there for me all across the globe, thank you for lending a careful ear and offering invaluable guidance. To my younger sister and brother, your constant encouragement means the world. To my circle of friends (Rens, Jeroen, Mart, Lucas, Michel, Bjorn, Patrick, Joris, Armand, 'de buurt', and countless others) I am deeply grateful for your unwavering support.

Lastly, who always stands faithfully waiting at the finish line, my wife Saskia. Truly the brightest luminaire in my life, someone who has been there from the beginning to the end, a constant companion throughout an endless journey. Thank you for always believing in me. Your love and support are the guiding light that always has and always will illuminate my path beyond.

Rik Spieringhs,
May 2024
Heesch

Abstract

Road lighting aims to improve the driving conditions for motorized traffic when driving during the night. Road lighting improves visual performance, visual guidance, driver's alertness, and visual comfort. In this way, it is an important factor to improve the safety of drivers, pedestrians, and cyclists. However, the activation of artificial road lighting contributes to the overall electrical energy consumption. With policies to reduce energy consumption, the primary challenge in the design of road lighting is to reduce energy consumption while still maintaining traffic safety. One way to reduce energy consumption is to dim or switch off the road lighting, however, this deteriorates traffic safety. Another way to reduce energy consumption is to create more efficient light sources while maintaining the standard light level requirements. A third and less explored option in road lighting (of highways) is the use of smarter illumination concepts which optimize visibility and contrasts at lower light levels. One of such concepts is called 'Probeam'.

In the Probeam concept, luminaires direct most of their luminous flux forwards, in the direction of view of the driver. One of its objectives is to illuminate retroreflective road markings at distances beyond the reach of car headlights creating an optimal guide for motorized traffic. To optimize 'Probeam' in terms of the balance between energy consumption and traffic safety and to define the level of illumination that should be applied in practice, it is essential to understand the contrast perception between road markings and the background road surface. As such, the optical characteristics of the outdoor road scene, i.e., the light intensity distribution of the light source and the reflection characteristics of road marking and road surface materials, are crucial in determining the optimal level of illumination which fulfills the contrast and visibility requirements.

Sufficient contrast between the road surface and road markings is critical for a safe and comfortable driving experience. This calls for a comprehensive and well-established contrast (threshold) model. In this study, participants were presented with a rendering of a highway, including road marking arrows of various sizes and luminance, and were asked to indicate the direction of the arrow. The luminance of the road surface, acting as a background for the markings, was varied too. Due to the very low luminance values and the very small differences in luminance, measurement accuracy and calibration issues required special attention. The results indicated good agreement with Adrian's basic visibility model, the model commonly used in road lighting, in terms of luminance contrast, background luminance, and size. More recently, new image-based contrast metrics that also predict supra-threshold contrast visibility have been proposed, but the corresponding visibility thresholds are not yet known. Therefore, contrast thresholds were defined for several image-based contrast models. Unfortunately, it seemed to be impossible to state one unique threshold contrast value independent of object angular size and road luminance for these image-based contrast models.

Contrast perception is strongly dependent on the age of the observer. In a second experiment, the contrast thresholds of elderly were determined and compared with the results of the younger participant group. In addition, the impact of glare on the contrast thresholds was examined and compared to Adrian's prediction. The results indicate an interaction effect between arrow angular size, road surface luminance, and glare. On average, the luminance difference thresholds were always higher in the presence of a glare source than without a glare source. As expected, this difference was largest at the lowest road surface luminance. In addition, comparing the results with results measured with young participants we observed an effect of age, indicating that, not surprisingly, luminance difference thresholds for older participants are higher than for younger participants. Adrian's model provided a moderate to poor fit to the experimental thresholds.

To predict the luminance level of the road surface and the road markings, it is crucial to accurately characterize the reflective properties of these materials when simulations of different road lighting concepts are to be performed. Most reflectance data for road lighting materials are unfortunately limited to only those few directions concerning the illumination and viewing direction applicable for standard symmetric road lighting concepts. In this study, the number of directions was extended, and it was investigated whether the retroreflective properties of common road marking materials can be captured with existing BDRF models. BRDF measurements of several road marking samples were performed in a large near field goniometer (LNFG) which was slightly adapted towards these non-standard measurements. The BRDF measurements for many different viewing angles and incident angles were made by rotating both the sample holder (changing the incident angle) and the luminance camera (changing the viewing angle). We explored to what extent existing BRDF models fit the data. Since the data exhibit a peaked (retro)reflective cosine lob-like behavior, at first the classic Phong model was investigated. This model was adapted resulting in a modified Phong (called RetroPhong) model. The model was benchmarked to other BRDF models adapted for retroreflection. From these other models, the ABC-Retro model comes closest to the performance of the RetroPhong model, however, still results in a slightly worse fit. However, the RetroPhong model contains six fitting parameters, whereas, the ABC-Retro model contains eight fitting parameters. Other BRDF models contain less fitting parameters but also result in a considerably worse fit. In general, it can be concluded that the RetroPhong model fits the measurements better than the other models.

With a well-established contrast (threshold) model and a model for the retroreflective characteristics of road markings, a typical light intensity distribution for a probeam luminaire following current road lighting standards can be calculated. In these calculations, we compared 'Probeam' with more traditional, symmetric road lighting concepts when implemented on a (Dutch) highway. Calculations reveal that probeam lighting improves the average visibility of objects and road markings over symmetrical lighting, however, comes with a 14% increase in luminous flux in case the current road lighting standards are followed. However, by designing the probeam luminaire to match symmetrical lighting's average visibility of vertical objects, energy consumption is reduced by 52%. Halving the probeam luminaire's mounting height leads to an impressive 82% energy reduction. In this approach however, the current road luminance requirement as given in the standards is not fulfilled anymore. The standard requirements originate from the generally accepted "silhouette principle" in which an object or person beyond the reach of car headlights should become visible in negative contrast to the background. Using Probeam represents a paradigm shift in which positive contrast is targeted, moving beyond the traditional silhouette principle.

The proof of concept was practically validated with field measurements at the KU Leuven Gent campus and the "Test Centrum of Dienst Wegverkeer (RDW)" in Lelystad. The field measurements indicated that Probeam could perform well but does produce an annoying reflection/glare in the side mirror of the car. This issue was further investigated with simulations and resulted in a different illumination zone targeted by the probeam luminaire. A corresponding optimized LID of the probeam luminaire has been proposed.

The valorization plan describes a collaboration with the luminaire manufacturer Innolumis and with government institutions (e.g. Rijkswaterstaat and Agentschap Wegen en Verkeer) to manufacture and design customized lenses following the Probeam concept. This plan included a detailed business model canvas and a freedom to operate analysis.

In conclusion, Probeam offers a number of advantages over the use of classical symmetric lighting of highways: it avoids disability glare (which is in particular important for older drivers), it increases the vertical illuminance and contrast, and uses the retroreflective properties of road markings to guide the drivers beyond the reach of car headlamps. Probeam can lead to a reduction in energy consumption while maintaining traffic safety, however, the current road lighting standards cannot be strictly adhered to. Indeed, the introduction of Probeam requires a paradigm shift within the road lighting community towards the acceptance of positive contrast based illumination concepts.

Beknopte samenvatting

Wegverlichting is bedoeld om de rijomstandigheden voor gemotoriseerd verkeer te verbeteren wanneer natuurlijk licht onvoldoende aanwezig is. Wegverlichting verbetert de visuele prestaties, visuele geleiding, alertheid van de bestuurder en visueel comfort. Op deze manier is het een belangrijke factor om de veiligheid van bestuurders, voetgangers en fietsers te verbeteren. De activering van kunstmatige wegverlichting draagt echter bij tot het totale elektrische energieverbruik. Binnen een algemeen beleid dat een reductie van energieverbruik nastreeft, is de belangrijkste uitdaging bij het ontwerp van wegverlichting om het elektriciteitsverbruik te verminderen en toch de verkeersveiligheid te behouden. Eén manier om het verbruik te verminderen is de wegverlichting te dimmen of uit te schakelen, maar dit gaat ten koste van de verkeersveiligheid. Een andere manier bestaat er in efficiëntere lichtbronnen te gebruiken met behoud van het standaard vereiste lichtniveau. Een derde en minder onderzochte optie in wegverlichting (van snelwegen) is het gebruik van slimmere verlichtingsconcepten die de zichtbaarheid en contrasten optimaliseren bij lagere lichtniveaus. Een van deze concepten is 'Probeam'.

In het Probeam concept richten armaturen het grootste deel van hun lichtstroom in de kijkrichting van de bestuurder. Eén van de doelstellingen is om op die manier retroreflecterende wegmarkeringen te verlichten op afstanden buiten het bereik van de koplampen van auto's, en zo een optimale geleiding voor gemotoriseerd verkeer te creëren. Om Probeam te optimaliseren wat betreft de balans tussen energieverbruik en verkeersveiligheid, en om het verlichtingsniveau te bepalen dat in de praktijk moet worden toegepast, is het essentieel om inzicht te krijgen in de contrastperceptie tussen wegmarkeringen en het wegdek. De optische kenmerken van de wegomgeving, d.w.z. de lichtintensiteitsverdeling van de lichtbron en de reflectiekarakteristieken van wegmarkeringen en wegdekmaterialen, zijn dus van cruciaal belang bij het bepalen van het optimale verlichtingsniveau dat voldoet aan de vereisten voor contrast en zichtbaarheid.

Voldoende contrast tussen het wegdek en de wegmarkeringen is cruciaal voor een veilige en comfortabele rijervaring. Hiervoor is een uitgebreid en goed onderbouwd

contrast(drempel)model nodig. In een specifiek daartoe opgezet experiment kregen deelnemers een rendering van een snelweg te zien, met pijlen van wegmarkeringen van verschillende grootte en luminantie, en werd hen gevraagd de richting van de pijl aan te geven. De luminantie van het wegdek, als achtergrond voor de markeringen, werd ook gevarieerd. Vanwege de zeer lage luminantiewaarden en de zeer kleine verschillen in luminantie, moest aan de meetnauwkeurigheid en kalibratie speciale aandacht worden besteed. De resultaten gaven een goede overeenkomst aan met het zichtbaarheidsmodel van Adrian, het model dat vaak wordt gebruikt bij wegverlichting, en dit in termen van luminantiecontrast, achtergrondluminantie en pijlgrootte. Meer recentelijk zijn er nieuwe (meestal "image based") contrastmetrieken voorgesteld die ook de zichtbaarheid boven de drempelwaarde voor contrast voorspellen, maar de bijbehorende zichtbaarheidsdrempels zijn nog niet bekend. Daarom werden de contrastdrempels voor deze contrastmodellen experimenteel bepaald. Helaas bleek het onmogelijk om voor deze contrastmodellen één unieke contrastdrempelwaarde te bepalen die onafhankelijk is van de hoekgrootte van het object en de luminantie van de weg.

Contrastwaarneming is sterk afhankelijk van de leeftijd van de waarnemer. In een tweede experiment werden de contrastdrempels van ouderen bepaald en vergeleken met de resultaten van de jongere deelnemersgroep. Daarnaast werd de invloed van verblinding op de contrastdrempels onderzocht en vergeleken met de voorspelling van het model van Adrian. De resultaten wijzen op een interactie-effect tussen de hoekgrootte van de pijl, de luminantie van het wegdek en verblinding. Gemiddeld waren de drempels voor luminantieverschillen altijd hoger in aanwezigheid van een verblindingsbron dan zonder een verblindingsbron. Zoals verwacht was dit verschil het grootst bij de laagste luminantie van het wegdek. Als we de resultaten bovendien vergelijken met resultaten gemeten met jonge deelnemers, zien we een effect van leeftijd, wat aangeeft dat, niet verrassend, drempelwaarden voor luminantieverschillen bij oudere deelnemers hoger zijn dan bij jongere deelnemers. Het model van Adrian voorspelde slechts matig tot slecht de experimentele drempelwaardes.

Om het luminantieniveau van het wegdek en de wegmarkeringen te voorspellen, is het van belang om de reflecterende eigenschappen van deze materialen nauwkeurig te karakteriseren wanneer simulaties van wegverlichtingsconcepten moeten worden uitgevoerd. De meeste reflectiegegevens voor wegverlichtingsmaterialen zijn helaas beperkt tot die hoeken met betrekking tot de verlichtings- en kijkrichting die van toepassing zijn voor standaard symmetrische wegverlichtingsconcepten. In deze studie werd het aantal hoeken uitgebreid en werd onderzocht of de retroreflecterende eigenschappen van gewone wegmarkeringsmaterialen kunnen worden vastgelegd met bestaande BDRF-modellen. BRDF-metingen van verschillende wegmarkeringsmaterialen werden uitgevoerd in een 'large near field goniometer' (LNFG) die enigszins werd aangepast voor deze niet-standaard metingen. De BRDF-metingen voor verschillende kijkhoeken en invalshoeken werden uitgevoerd door zowel de houder (waardoor de invalshoek veranderde) als de luminantiecamera (waardoor de kijkhoek veranderde) te draaien. We onderzochten in hoeverre bestaande BRDF-modellen passen bij de gegevens. Aangezien de gegevens een gepiekt (retro)reflectief gedrag vertonen, werd eerst het klassieke Phong-model onderzocht. Dit model werd aangepast tot een “RetroPhong” model. Het model werd vergeleken met andere BRDF-modellen die ook rekening houden met retroreflectie. Van deze andere modellen komt het ABC-Retro model het dichtst in de buurt van de prestaties van het RetroPhong model. Het RetroPhong-model bevat echter zes parameters, terwijl het ABC-Retro-model acht parameters bevat. Andere BRDF-modellen bevatten minder parameters maar resulteren ook in een aanzienlijk slechtere fit. In het algemeen kan geconcludeerd worden dat het RetroPhong model het best presteert m.b.t. de beschrijving van het reflectiegedrag van de onderzochte materialen.

Met een beproefd contrast(drempel)model en een model voor de retroreflecterende eigenschappen van wegmarkeringen kan een typische lichtintensiteitsverdeling voor een probeam-armatuur worden berekend. In deze berekeningen hebben we Probeam vergeleken met de meer traditionele, symmetrische wegverlichtingsconcepten wat betreft een implementatie op een (Nederlandse) snelweg. Uit de berekeningen blijkt dat probeam-verlichting de gemiddelde zichtbaarheid van objecten en wegmarkeringen verbetert ten opzichte van symmetrische verlichting, maar dat dit gepaard gaat met een toename van de lichtstroom van 14% als de huidige normen voor wegverlichting worden gevolgd. Door het ontwerp van de probeam-armatuur echter af te stemmen op de gemiddelde bereikte zichtbaarheid van verticale objecten bij symmetrische verlichting, daalt het energieverbruik met 52%. Halvering van de hoogte van de probeam-armatuur leidt tot een indrukwekkende energiebesparing van 82%. Bij deze aanpak wordt echter niet meer voldaan aan de huidige normvereisten voor wegverlichting. De normvereisten komen voort uit het algemeen aanvaarde "silhouetprincipe"waarbij een object of persoon buiten het bereik van de koplampen van auto’s zichtbaar moet worden in negatief contrast met de achtergrond. Het gebruik van Probeam vertegenwoordigt een paradigmaverschuiving waarbij positief contrast wordt nagestreefd, en gaat verder dan het traditionele silhouetprincipe.

Het proof of concept werd praktisch gevalideerd met veldmetingen op de campus van KU Leuven-Gent en het “Testcentrum van Dienst Wegverkeer (RDW)” in Lelystad. De veldmetingen gaven aan dat Probeam goed kon presteren, maar wel een hinderlijke reflectie/verblinding in de zijspiegel van de auto produceert. Dit probleem werd verder onderzocht met simulaties en resulteerde in een andere zone die door de probeam-armatuur wordt uitgelicht. Een overeenkomstige geoptimaliseerde LID van de probeam-armatuur werd voorgesteld.

Het valorisatieplan beschrijft een samenwerking met de armaturenfabrikant Innolumis en met overheidsinstellingen (bijv. Rijkswaterstaat en Agentschap Wegen en Verkeer) voor de productie en het ontwerp van op maat gemaakte lenzen volgens het Probeam-concept. Dit plan omvat een gedetailleerd “business model canvas” en een “freedom to operate” analyse.

Concluderend biedt probeam verlichting een aantal voordelen ten opzichte van het gebruik van klassieke symmetrische verlichting van snelwegen: het voorkomt verblinding (wat vooral belangrijk is voor oudere bestuurders), het verhoogt de verticale verlichtingssterkte en het contrast en maakt gebruik van de retroreflecterende eigenschappen van wegmarkeringen om bestuurders buiten het bereik van de koplampen van auto’s beter te leiden. Probeam kan leiden tot een vermindering van het energieverbruik met behoud van de verkeersveiligheid, maar de huidige normen voor wegverlichting kunnen niet strikt worden nageleefd. De introductie van Probeam vereist dus de acceptatie van op positieve contrasten gebaseerde verlichtingsconcepten en een aanpassing van de standaarden.

Contents

List of Figures

List of Tables

Chapter 1

Introduction

1.1 Road Lighting, Electrical Energy Consumption, and Safety

An experienced driver knows that driving a vehicle in the dark or on a poorly lit road is significantly more dangerous than driving the same vehicle during daytime or on a well lit road. Indeed, the task of driving at night, under mesopic or scotopic vision, becomes much more demanding and complex than under photopic vision [1]. Visibility of the environment, the road and all objects on the road deteriorates at lower light levels [2, 3], because of the related reduced human visual acuity and contrast sensitivity. In addition, according to Fors & Lundkvist [4], drivers are unaware of their poor night vision while driving. As a consequence, there are as many accidents at night as during the day, although only 25% of all traffic occurs at night [5]. For these reasons, researchers advocate for road lighting during nighttime (van Bommel, 2014; Fors & Lundkvist, 2009; Jory, 2001; etc. [2, 3, 6]) in order to improve visual performance, visual guidance, driver alertness, and visual comfort. Proper road lighting has been shown to improve the safety of drivers and to decrease the number of accidents at night time (Fors & Lundkvist, 2009; Wanvik, 2009; Elvik, 1995; etc. [4, 7, 8]). It is estimated that road lighting reduces the number of road accidents by at least 17% [8]. If, for example, 15% of the total road lighting would be turned off, this would increase the number of road accidents by at least 3% (i.e., 17% x 15%), resulting for the Netherlands in an estimate of about 700 more accidents [9].

However, the activation of artificial road lighting also contributes to the overall electrical energy consumption. From this point of view, there is a strong urge to dim or even turn off road lighting. Belgium, the Netherlands and other European countries have signed the European climate law to achieve net zero greenhouse gas emissions by 2050. One way of reaching this ambition is to strongly reduce energy consumption from road lighting. In line with this, the Netherlands set a goal of reducing road lighting energy consumption by 50% in 2030 as compared to 2013 [10].

Combining both goals mentioned above implies that the primary challenge in the design of road lighting is to reduce energy consumption while still maintaining traffic safety. Apart from dimming or switching off road lighting, energy consumption can be reduced by using more efficient light sources. Since 2013, the Netherlands replaced old low- and high-pressure sodium lighting with LED lighting, resulting in a reduction of energy consumption for road lighting by about 5% [11].

A third and less explored option to reduce the energy consumption of road lighting (of highways) is the use of smarter illumination concepts that optimize object visibility and contrast thanks to a dedicated light intensity distribution (LID) of the luminaires. As recently shown in tunnel and pedestrian lighting, new luminaries with dedicated LIDs are designed to increase the vertical illuminance, as such illuminating an object on the road rather than the dark road surface. In addition, these LIDs can also be optimized towards the reflection characteristics of road markings, ultimately leading to an improved guidance of drivers. When the retroreflectivity of the road markings is optimized for the lighting geometry of the road lighting instead of the car headlamps, this new road lighting concept can – at least theoretically – result in larger contrasts for the same luminous flux. The latter would not only lead to improved visibility of road markings for drivers, but also for image-based advanced driver-assistance systems (ADAS).

This thesis explores the advantages and implementation of a new road lighting concept, based on a LID, in which most of the light intensity is emitted in the driving direction, i.e. the so-called Probeam concept. Three important aspects of this road lighting concept are further introduced in this chapter. First, in order to know how to optimize the LID for the Probeam concept, it is key to understand perceived contrast of road markings on a road surface. The state-of-the-art literature on contract perception and models is given in chapter 1.2. Second, the actual shape of the optimized LID will also depend on the reflectivity of the materials used for the road surface and road marking. State-of-the-art knowledge on how to characterize and measure this (retro)reflectivity is described in chapter 1.3.. Finally, the Probeam concept needs to be designed such that it fulfills a number of essential light characteristics. Subsequently, we need to compare the final design with alternative existing lighting concepts. The related relevant literature is discussed in chapter 1.3.

1.2 Contrast and Contrast Threshold

1.2.1 Contrast

Contrast is a relevant aspect determining visibility of objects under different types of road lighting. However, there exist multiple definitions of contrast, and these definitions are used differently depending on the domain or task. In the CIE international lighting vocabulary, for example, 'perceived contrast' can be specified as brightness contrast, successive contrast, color contrast, etc. In road lighting we typically use achromatic contrast (i.e., luminance contrast), where widely accepted definitions include contrast ratio, Webers contrast, and Michelson contrast.

The contrast ratio is simply defined as the ratio between the luminance of two adjacent surfaces L_1 and L_2:

$$C_{\text{ratio}} = \frac{L_1}{L_2} \tag{1.1}$$

This definition, however, neglects the luminance difference between the two surfaces. For an object (L_o) on a large uniform background (L_b), the perceived contrast also depends on the luminance difference between object and background. Webers contrast includes this dependency by dividing the luminance difference by the background luminance:

$$C_{\text{Weber}} = \frac{L_o - L_b}{L_b} \tag{1.2}$$

For a periodic pattern of both dark (L_{min}) and bright (L_{max}) features where the background is unclear (i.e., no uniform large background), Michelson contrast is used:

$$C_{\text{Michelson}} = \frac{L_{\text{max}} - L_{\text{min}}}{L_{\text{max}} + L_{\text{min}}} \tag{1.3}$$

Since the evaluation of road lighting mostly involves the visibility of objects on a largely uniform road, typically contrast ratios or Webers contrasts are used.

In addition to these overall contrast definitions, also local contrast measures, based on properties of the human visual system, were introduced during the second half of the 20th century (Rodieck and Stone, 1965; Rodieck, 1965; De Monasterio, 1978; Shapley and Perry, 1986; Enroth-Cugell and Robson, 1966; etc. [12–16]. The discovery of receptive fields [13–16]) at multiple stages in the visual system (namely at the photoreceptors, the retinal ganglion cells, the lateral geniculate nucleus (LGN) and at the visual cortex cells) enabled the description of more local visual contrast. Hubel and Wiesel, in 1962 [17], formulated the idea of a hierarchical process in which receptive fields at one level in the visual process were determined by signals from cells at the lower levels. With this idea, simple receptive fields at a lower level could be combined into highly complex receptive fields. This idea was later refuted, however, did put forward a new field of research. A later finding within this field of research was the presence of a difference in activation in retinal ganglion and V1 cells between the center and the surrounding area [12, 16]. This finding resulted in the exploration of early contrast models based on so-called ON- and OFF-center receptive fields. Groups of photoreceptors (cones and/or rods) coupled to a specific bipolar cell emit a reduced (inhibitory) or increased (excitatory) signal to the ganglion cell. This results in an ON-center receptive field or an OFF-center receptive field. For an ON-center receptive field, i.e., exposure to the center and no exposure to the surrounding area results in increased ganglion cell activity. For an OFF-center receptive field, there is little to no activity of the ganglion cell. The receptive field is typically approximated by taking the difference between a center and surround gaussian where the spread (standard deviation) of the surround gaussian is larger than that of the center.

In 2000, Tadmor and Tolhurst [18] investigated the usefulness of the difference of a gaussian (DoG) receptive field model for predicting contrasts in scenes as experienced by the retinal ganglion cells and the neurons in the lateral geniculate nucleus (LGN). The final overall contrast of the image is determined by taking the average of all local contrast values determined for each pixel using the above functions. The model of Tadmor and Tolhurst is limited to local components of contrast, whereas later models focused on including also the global components; however, still the Tadmor and Tolhurst model remains one of the more often used image based contrast models.

Another contrast model that was introduced a few years later than the Tadmor and Tolhurst contrast model was the RAMMG model [19]. The RAMMG model was proposed by Rizzi et al. and is an abbreviation of the authors family names [19]. The RAMMG model is an efficient model to determine the perceived contrast of a complex image presented on a display while including both global and local components of contrast; however, it is limited through its simplification of determining the local contrast by taking the average difference in lightness between the pixel and its eight surrounding other pixels.

In 2011, Joulan et al. [20] proposed a framework to compute the visibility of objects in a luminance image of a road scene based on edge detection. The framework exists of two algorithms, one that takes into account the visual adaptation and a second one that uses a set of spatial filters (DoG) based on coefficients computed from Barten's contrast sensitivity function (CSF). Interestingly this so-called SDoG model combines both the DoG and CSF for computing both edge localization and edge visibility. The model includes both local and global components of contrast. Although the local components of contrast are described in much detail, the global adaptation is modelled as a relative simple gain factor.

In 2012, Simone et al. [21] introduced the weighted-level framework (WLF) that includes the DoG model, the pyramidal subsampling with prefiltering, and weights in the recombination of the pyramid layers. Similar to Rizzi et al., the WLF is based on a multilevel analysis using pyramidal subsampling, but it uses an antialiasing filter in addition. For each level of the subsampled RGB image, the local contrast of each pixel is calculated using the Tadmor and Tolhurst DoG model. This then results in a local contrast map for each level, from which the averaged contrast is determined. Subsequently, an overall contrast measure is calculated for the R, G and B channel separately by a weighted recombination of the average contrast of each level. Finally, a global contrast measure $C^{WLF(RSC)}$ is determined by the weighted sum of the overall contrast measures over the three channels.

The model by Simone et al. was validated by an experiment where observers were presented with images of various characteristics and had to rate the contrast from 1 to 100, where 1 was the lowest and 100 the maximum. To this dataset, the weighted-level framework showed the best fit compared to the other contrast models (i.e., RAMMG and Tadmore and Tolhurst model). The model by Simone et al. seems promising in determining the perceived contrast of images with various complexity and characteristics, however, does not quantify the minimum required contrast for an object to be visible (i.e., contrast thresholds).

1.2.2 Contrast threshold

In 1946, Blackwell [22] was one of the first introducing research on the contrast threshold of the human eye. He performed a psychophysical experiment where participants had to assess visibility of a uniform stimulus. During this experiment the visual angle and the brightness of the stimuli were changed, as well as the room adaptation brightness. Blackwell indicated that for a decrease in the visual angle, and for a drop in adaptation brightness, the contrast threshold increased. Another important observation was that at high brightness and with sufficiently large stimuli, the contrast threshold became constant as a function of adaptation brightness. This relation reflects the Weber-Fechner law of perception.

Later in 1989, Adrian [23] used the data obtained by Blackwell [22] and combined them with the contrast threshold data from other studies [24–28] to determine a general model for the visibility of targets. His model, however, was determined for an average observer of 23 years old. Meanwhile, it is known (by Mortenson-Blackwell and Blackwell [29], and Weale [30]) that the ocular transmittance decreases with age. The CIE [31] also reports several other visual changes that come with age: reduced accommodation, increased interocular light scatter, reduced spatial contrast sensitivity, reduced retinal illuminance, and slower dark adaptation. To account for the changes in the visual system over age, Adrian introduced an age factor.

Apart from the age factor, Adrian's model uses the luminous flux function and luminance function combined with the exposure time and target size to construct a general formula for calculating the luminance difference threshold, needed to see a uniform object in a uniform background. Then this threshold can be used to determine the visibility level (VL) of a target by calculating the ratio between the luminance difference between target and background and the corresponding predicted luminance difference threshold from Adrian's model.

Adrian's model has been used in a road lighting context for predicting the visibility of objects on an illuminated road. In this context it showed good performance, however so far only for relatively simple scenes with uniform targets in size and luminance [20]. On real roads, however, the background luminance is not constant, and already a simple road arrow is not uniform in shape (i.e., not circular or squared) and luminance. Detecting the direction of a road arrow is also more than just a visibility task, since it asks for discriminating a left-arrow from a right-arrow. Since understanding the minimum luminance difference between the road surface and road marking to distinguish the direction of an arrow is essential for safe driving, the first research question is "How well do current contrast models predict the contrast threshold for the discrimination of a road marking surrounded by the road surface?".

1.3 Surface Reflection

1.3.1 Introduction

Visibility of an object on a road is determined by the amount of light reflected from that object in the direction of the driver in relation to the amount of light reflected from the road surface. When objects and surfaces would be perfect Lambertian reflectors, the direction of the incident light would not matter, as the reflection would be the same for all directions. However, most materials relevant for road lighting are non-Lambertian, and thus the angle of the incident light and the angle of observation are crucial for determining the amount of reflected light.

Asphalt concrete (i.e., gap, open, and dense graded asphalt [32, 33]) is certainly non-lambertian. At grazing angles of incident light, these road surfaces exhibit specular reflection into the opposite direction, caused by small surface facets (microfacets).

Road markings (positioned horizontally) and road signs (positioned vertically) are known to exhibit retroreflection, where most light is reflected in the direction of the incident light [34–37]. Retroreflectors in general are therefore also non-lambertian reflectors [38, 39].

To characterize the reflection properties of such non-lambertian materials, the concept of a Bidirectional Reflectance Distribution Function (BRDF) is introduced. A BRDF provides the reflectance of a material as a function of the angle of incidence and the viewing angle. It is determined as the ratio of the differential luminance (dLr in cd/m^2) as observed from a given viewing angle (θ_r, ϕ_r) to the differential illuminance (dE in lux) at the surface of the material caused by the illumination from an incident direction (θ_i, ϕ_i). Mathematically, this can be written down as follows:

$$f_r(\theta_i, \phi_i, \theta_r, \phi_r) = \frac{dL_r(\theta_r, \phi_r)}{dE(\theta_i, \phi_i)} \tag{1.4}$$

With f_r the BRDF expressed in sr^{-1} (i.e., inverse steradians). Determining a complete BRDF requires many measurements for different angles of incidence and viewing angles and represents a huge amount of data. For this reason, other more simple quantities to describe the reflection properties have been used.

1.3.2 Road Surface Reflection

The CIE Technical Committee 4-25 "Road Surface and Road Marking Reflection Characteristics" of Division 4 "Transportation and exterior application " introduced the CIE 144 document in 2001. The document reports reflectance of road surfaces determined for a reference point on the road surface (p) and for different angles of incidence and observation. Relevant angles are: the angle of observation relative to the horizontal road surface (α), the angle of the incident light relative to the downward vertical of the light source (γ), the angle between the vertical plane of observation and the vertical plane of incidence (β), and the angle between the path axis and the vertical plane of observation (δ), see Fig. 1.1.

In determining the reflectance of a road surface, the CIE 144 [32] describes the use of R-tables. The coefficient given in these tables is the luminance reduction coefficient (R) defined as:

$$R = q(\gamma, \beta) \cos^3(\gamma) \tag{1.5}$$

and is expressed in mcd/m^2/lux; q is the luminance coefficient that can be calculated by dividing the luminance (L) of point p (in cd/m^2) by the horizontal illuminance (E) at point p (in lux):

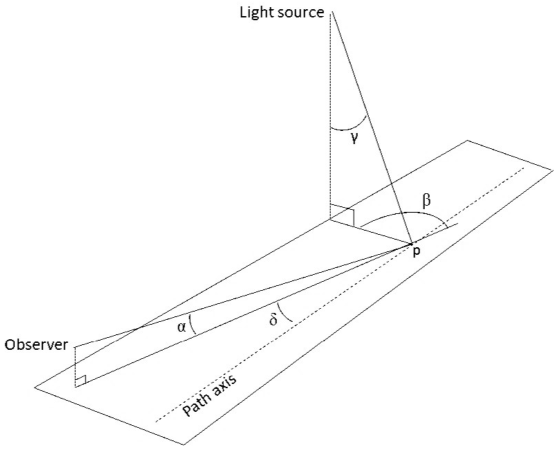

Figure 1.1: The recommended geometrical system for measuring the reflectance of road surfaces as defined by the CIE.

$$q = \frac{L}{E} \tag{1.6}$$

With the luminance reduction coefficient (R) of the road surface known, its luminance can be calculated from the height (H) and the luminous intensity (I) of the light source illuminating the road at p:

$$L = \frac{R \cdot I}{H^2} \tag{1.7}$$

In road surface reflection standards, the angle of observation (α) is fixed at 1°, consistent with an observer's height of 1.5 m at a distance from the reference point p of 85.9 m. The angle β can vary between 0 and 180°, and γ between 0 and 85°. Based on research of De Boer, Onate and Oostrijck (1952) [40], the CIE determines a computational grid starting at 60 m and ending at 160 m from the observer for a maximum width of 21.8 m.

The luminance reduction coefficient (R) in the R-table is used to calculate two other variables specified in the CIE 144 document: the average luminance coefficient Q_0 and the specular factor S_1. The Q_0 variable is calculated as the average value of the luminance coefficient (q) over a solid angle Ω_1:

$$Q_0 = \frac{1}{\Omega_1} \int_{\Omega_1} q(\gamma, \beta)\, d\Omega = \frac{1}{\Omega_1} \int_{\Omega_1} \frac{R}{\cos^3(\gamma)}\, d\Omega \tag{1.8}$$

with Ω_1 being the solid angle measured from the road surface at point p for all incident light of an uniform lambertian hemisphere light source.

The specular factor S_1 is calculated from the ratio of two values in the R table:

$$S_1 = \frac{R(\beta = 0, \gamma = 63)}{R(\beta = 0, \gamma = 0)} \tag{1.9}$$

It is the ratio between the luminance reduction coefficient for a steep incident angle ($\gamma = 63$) over perpendicular incidence ($\gamma = 0$) viewed in the opposing direction to the incidence (i.e., specular reflection, $\beta = 0$). Using the specular factor S_1 and the average luminance coefficient Q_0, a road surface is classified into four R-classes (R1, R2, R3 and R4) specified in the CIE 144 document and shown in Table 1.1. When the actual reflectance of a road surface is not known, road lighting calculations use the standard S_1 and Q_0-values of a given class based on the average of a large number of road surfaces measured in that class.

Table 1.1: Road R classification (R1, R2, R3, and R4) according to CIE 144.

R Class	Diffuse/Specular	Specular limitations	Standard S_1	Standard Q_0
R1	Diffuse	$S_1 < 0.42$	0.25	0.10
R2	Slightly specular	$0.42 \leq S_1 < 0.85$	0.58	0.07
R3	Fairly specular	$0.85 \leq S_1 < 1.35$	1.11	0.07
R4	Very specular	$1.35 \leq S_1$	1.55	0.08

1.3.3 Road Marking Retroreflection

The recommended geometrical system for measuring retroreflection of road markings is defined by three axes, namely the retroreflector, observation and illumination axes. As defined in document CIE 54.2 2001, the retroreflector axis for (horizontal) road markings is defined as the normal to the retroreflector in a reference point, which is often chosen as the center of the reflecting surface.

In this system, shown in Fig. 1.2, the axis of illumination is the axis from the retroreflector reference point to the light source reference point. As standardized in measuring road markings, the light source is located at an angle of incidence β_c of 1.24° from the retroreflector surface, whereas the observer is positioned at an angle v_c of 2.29° from the retroreflector surface. These standardized angles (β_c, v_c) are based on the average driver's eye height of 1.2 m and a headlight height of 0.65 m for a distance between the car and the road marking of 30 m. The illuminance axis and the observation axis are often considered in the same plane. The angle between the observation axis and the light source axis α_o is thus 2.29° - 1.24° = 1.05°.

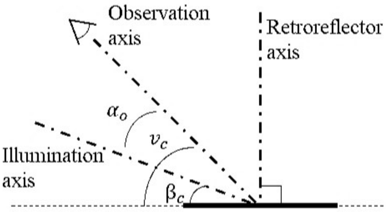

Figure 1.2: The recommended geometrical system for measuring retroreflection of road markings as defined by the CIE.

Road markings can be classified into two different types: a Type 2 road marking is intended to improve retroreflection in wet road conditions, whereas this is not necessarily the case for a Type 1 road marking. Standards for road markings, including daytime and nighttime visibility, make use of two coefficients: the coefficient of retroreflected luminance R_L for night visibility and the luminance coefficient Q_d for daytime visibility. The coefficient of retroreflected luminance R_L is defined as:

$$R_L = 1000\left(L \cdot \cos(\beta_c)\right)/E \tag{1.10}$$

where the illuminance E can be provided by either street lights or headlights of a car; R_L is expressed in units of mcd/m^2/lx. The luminance coefficient Q_d is defined as:

$$Q_d = 1000\frac{L}{E} \tag{1.11}$$

and is a measure of the light reflectance of a road surface or road marking illuminated by diffuse sky light; it is also expressed in units of mcd/m^2/lx.

The NEN-EN 1436 standard provides required values for R_L and Q_d for both types of road markings for night and daytime vision, and specifically for dry and wet roads in the case of Type 2 road markings. The limitation of the CIE 54.2 2001 document and the NEN-EN 1436 standardization is that the requirements are determined only for a very specific angle of incidence (1.24°) and viewing angle (2.29°), while the actual relevant angles depend strongly on the position of the car, streetlight and driver to the road marking. Especially for streetlights, the angle of incidence is usually much larger than 1.24°. For these other relevant angles, BRDF values need to be measured in order to determine the visibility of a road marking under a given type of illumination. To determine the luminance of the road markings from illumination by Probeam or other lighting concepts, the second research question states “What are the reflective characteristics of road marking materials under non-conventional incident angles inherent to Probeam and how to model these characteristics?".

1.4 Road Lighting Concepts

1.4.1 Conventional Approach

The current most important road lighting quality parameters for motorized traffic defined by the CIE publication on lighting of roads for motorized traffic (CIE 115 [41]) and mentioned in the European standards EN13201 [42] are:

- Lighting level (Lav)
- Uniformity (U0 and Ul)
- Lighting of the Surrounds (SR)
- Glare restriction (TI)

1.4.1.1 Lighting Level (Lav)

The lighting level (L_{av}) is the average luminance of the road surface for the region beyond the surface illuminated by the headlights of the car (i.e., from 60 to 160 m). The average road surface luminance is important for the silhouette principle, in which objects appear in negative contrast against the luminous background being the road surface.

1.4.1.2 Uniformity (U0 and Ul)

Two uniformity parameters are specified to avoid luminance patterns on the road surface, namely U_0 and U_l. U_0 refers to the overall uniformity of the road surface luminance, and is determined by dividing the minimum luminance of the road surface by the average luminance of the road surface Lmin/Lav [42]. U_l refers to the lengthwise uniformity, calculated by dividing the minimum road surface luminance along the lengthwise line that is parallel to the road axis with the average road surface luminance along that same line [42].

1.4.1.3 Lighting of the Surrounds (SR)

The surrounds are defined as the regions next to the road at both the left and right side. Lighting the surrounds is important for visibility of objects near the road, for visual guidance and for a gradual transition between the road and its surround. The relative light level of the surround is calculated by dividing the average of the horizontal illuminance of both strips bordering the road (outwards) by the average illuminance of the road surface for strips at the left and right part of the road itself (inwards), resulting in [2]:

$$SR = \frac{E_{\text{surround}(right+left)}}{E_{\text{road}(right+left)}} \tag{1.12}$$

In some cases, the edge-illuminance ratio (EIR) is calculated for each side separately:

$$EIR_{\text{right}} = \frac{E_{\text{surround(right)}}}{E_{\text{road(right)}}} \tag{1.13}$$

$$EIR_{\text{left}} = \frac{E_{\text{surround(left)}}}{E_{\text{road(left)}}} \tag{1.14}$$

This edge-illuminance ratios provide a more detailed estimation of the overall lighting of the surrounds, and are used as a standard in European road lighting [42].

1.4.1.4 Glare Restriction (TI)

Two kinds of glare can be distinguished, namely disability and discomfort glare. Disability glare is the impairment of the visibility of objects without necessarily causing discomfort [43], whereas discomfort glare causes discomfort without necessarily impairing the visibility of objects [43]. In road lighting recommendations and standards for motorized traffic, only disability glare is considered. It is characterized by the threshold increment TI [42], being:

$$TI = 65\frac{L_v}{L_{av}^{0.8}} \tag{1.15}$$

with L_v the veiling luminance and L_{av} the average road surface luminance. This formula is valid within a background luminance range from 0.05 to 5 cd/m^2. The equivalent veiling luminance is the luminance in object space which produces a retinal illuminance in an ideal eye equal to the illuminance generated by the scattering in the non-ideal eye. Its value can be calculated by summing up the contributions of each luminaire in the field of view, starting with the first luminaire that is at or under a viewing angle of 20° and limiting it to glare sources within a distance of 500 m. This results in:

$$L_v = \sum_{i=1}^{n} L_{v,i} \tag{1.16}$$

where $L_{v,i}$ is the equivalent veiling luminance from glare source i. Depending on the glare source angle θ_i, i.e. the angle between the viewing direction towards source i and the horizontal (in degrees), the equivalent veiling luminance is calculated as:

$$L_{v,i} = 9.86\left[1 + \left(\frac{A}{66.4}\right)^4\right]\frac{E_{gl,i}}{\theta_i^2} \quad (1.5 < \theta_i < 60) \tag{1.17}$$

$$L_{v,i} = \left(\frac{10}{\theta_i^3} + \frac{5}{\theta_i^2}\right)\left[1 + \left(\frac{A}{62.5}\right)^4\right]E_{gl,i} \quad (0.5 < \theta_i < 1.5) \tag{1.18}$$

where $E_{gl,i}$ is the illuminance measured at the eye of source i, and A is the age (in years) of the observer.

1.4.2 Road Lighting Classes for Motorized Traffic

In the EN 13201 [42], road lighting requirements are specified depending on the ambient lighting, quality of visual guidance, traffic characteristics and the geometry of the environment. The requirements are categorized into six lighting classes (M1-M6) each with values for each quality parameter as indicated in Table 1.2.

Table 1.2: The minimum required values (except for the TI where the maximum value is given) of each road lighting quality parameter for each lighting class.

	Lav	U0	Ul	TI	EIR
M1	2.00	0.40	0.70	10	0.35
M2	1.50	0.40	0.70	10	0.35
M3	1.00	0.40	0.60	15	0.30
M4	0.75	0.40	0.60	15	0.30
M5	0.50	0.35	0.40	15	0.30
M6	0.30	0.35	0.40	20	0.30

1.4.3 Alternative Road Lighting Concepts

The rational of conventional road lighting is to illuminate the road surface such that objects appear in negative contrast to the driver, referring to the so-called Silhouette Principle [2]. Using this principle, road lighting is designed such that the silhouette of any object or person is clearly visible, especially at distances beyond the reach of car headlights (i.e., 60 m; [42]). Important for creating this negative contrast is the light level and light uniformity of the road surface. When the light level is too low, the contrast will be too low and the object will not be visible. When the uniformity is too low, dark patches on the road with bad visibility of the object may occur.

Before the introduction of LED lighting, there was no good way of designing specific LIDs, and therefore the emitted light followed mostly a symmetrical pattern. In this pattern the emitted light intensities were equally aimed forwards and backwards and some overlap exists in the areas illuminated by two neighboring luminaires. A disadvantage of the symmetrical illumination is that the contrast of an object depends on the position of that object on the road surface: the object may appear in positive contrast when illuminated from the front or in negative contrast when illuminated from the back. Furthermore, the luminous intensity of the luminaire in the direction of the driver can induce glare.

Having an asymmetrical light distribution may be advantageous in some circumstances. One type of application of an asymmetrical light distribution is called Counterbeam, where most of the luminous flux is directed toward the driver's viewing direction, as shown in Fig. 1.3. This obviously creates a lot of glare. Alternatively, with Probeam most of the light flux is directed in the driver's viewing direction (see also Fig. 1.3), as such avoiding direct glare. This type of lighting is currently being investigated for tunnel lighting and pedestrian lighting [44–47].

Probeam has some clear advantages for tunnel lighting. In 2007, Lee and Lee [48] published results of an analysis of four simulations of lighting conditions, including both probeam and symmetrical luminaires, used near the end of a tunnel. They showed that the luminance of the rear end of cars as well as of the road surface was lower in probeam illumination than in symmetrical illumination. Another study by Sato and Hagio in 2014 [44] discussed object visibility in a tunnel in which the symmetrical (sodium lamp) lighting was replaced with probeam (LED) lighting [44]. According to this study, the uniformity of the road surface improved from 0.4 with the sodium symmetrical lighting to 0.8 with the LED probeam lighting. In addition, they found improved visibility with the LED probeam lighting. Hirakawa, Karasawa and Yoshida [47] reported similar results in 2014, based on luminance images of different, relatively dark objects in a tunnel in Japan illuminated with either symmetrical lighting or probeam lighting, both with car headlamps on and off. The luminance images indicated that with and without headlights, objects and people were more visible

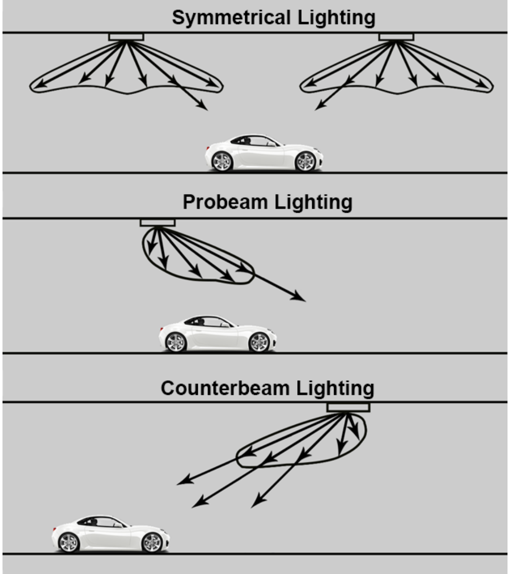

Figure 1.3: Three types of lighting distributions for tunnel lighting. Top: symmetrical lighting, middle: probeam lighting, and bottom: counterbeam lighting.

under the probeam lighting than under symmetrical lighting. Later in 2018, Renzler et al. [45] created a road tunnel model, in which they tested the visibility of the tunnel for different brightness, luminaire distances and light intensity distributions. The results of this study showed increased scattering in the car windshield for the symmetrical and counterbeam lighting. probeam lighting induced less glare and showed higher visibility of road markings than counterbeam and symmetrical lighting. Road surface uniformity reached the highest levels when using probeam lighting, however generating the lowest average road surface luminance.

In addition to tunnel lighting, probeam lighting was also investigated for pedestrian crosswalks, where lighting is paramount to help individuals cross the street safely at night. In Poland, Tomczuk [49] investigated the use of probeam lighting at a pedestrian crossing, on which eight objects with a reflectance value of $\rho = 0.2$ were placed at equally spaced positions along the crosswalk. Using luminance images of both sides of the crosswalk at about 60 m away from the objects, Tomczuk calculated the contrast of each object with the road surface background and concluded that the averaged contrast was fairly good (i.e., 1.80 for one direction and 2.38 for the other) given the relatively dark objects on the crosswalk.

As these studies indicate promising results for the use of Probeam in tunnels and at pedestrian crossings, it is worthwhile considering the concept of probeam lighting for highways as well. Probeam lighting may contribute to improved visibility of objects and road markings, and as such may lead to the possibility of reducing the overall light flux, and hence the energy consumption, while maintaining traffic safety. Generalizing the findings with Probeam from tunnel and pedestrian lighting to highways is not straightforward though, since – compared to tunnels and pedestrian crossings – the illumination of highways is different in that it uses higher light poles, larger distances between the poles, larger road widths, and different road lighting standards. Thus another emerging research question can be formulated as "Can we reduce energy consumption while maintaining traffic safety using the Probeam road lighting concept?".

1.5 Overview

The Probeam concept makes use of a new generation of road lighting sources (LEDs) and road marking materials, and it employs improved light control to direct the majority of the light flux in the driver's forward viewing direction (i.e., the direction of traffic). In tunnel and pedestrian illumination, Probeam has recently demonstrated promising results in terms of object visibility, but its application in highway illumination is yet to be investigated. Car headlights help guide the driver due to the retroreflective properties of road markings, but only for the first 60 meters. At greater distances, road lighting should take over. First and foremost, we need to determine the contrast threshold between a road marking and the surrounding road surface for this type of illumination (with specific incident and viewing angles) for both younger and older drivers. Secondly, we must understand the reflection properties of road markings and road surfaces within the very specific geometry of illumination inherent to the Probeam concept. With this knowledge, we can develop guidelines for an effective probeam light intensity distribution, and answer the main research question: can we reduce energy consumption while maintaining traffic safety using the Probeam road lighting concept?

Chapter 2 and Chapter 3 focus on modeling the contrast visibility threshold for human observers. In chapter 2, the applicability of Adrian's contrast threshold model is evaluated for measured thresholds of the direction detectability of a road marking arrow, of which we varied the angular size and the surrounding road surface luminance. Various image based contrast models are applied and it was investigated which model could yield a unique contrast threshold value for detecting the direction of the arrow, irrespective of the luminance of the road and the size of the arrow. Chapter 3 continues to evaluate Adrian's model for predicting the direction detectability of a road marking arrow, but now for elderly participants, and in the presence of a glare source. To predict these results, different equations for determining the veiling luminance as well as for predicting the effect of age are explored.

Chapter 4 focuses on the full characterization of the reflection characteristics of a road surface and different road marking materials. BRDF measurements of road marking samples are performed for many different incident and viewing angles relevant for highway lighting using a non-conventional setup. The experimental data are fitted to a new optimized BRDF model, and this new model is benchmarked against existing (retro)reflective BRDF models.

Chapter 5 formulates and investigates the concept of Probeam as an alternative lighting concept. Using simulations and renderings, a Probeam proof of concept is developed and compared to symmetrical lighting for a standard highway scenario. The resulting LIDs and visibilities of objects and road markings are computed using Adrian's model and the new road marking BRDF model, and are further discussed. The simulation results are compared to the experimental data. A strong glare contribution perceived in the side mirror of the car led to the optimization of the illumination zone and the adaptation of the original Probeam concept.

Chapter 6 explains how to valorize the research of this PhD thesis. It presents an exploitation plan for the new asymmetric probeam lighting for illuminating highways from the point of view of Innolumis, a Dutch company active in the assembly and sales of luminaires.

Finally, Chapter 7 provides the general conclusions of this manuscript and discusses potential future work and opportunities for improvements of the Probeam road lighting concept.

Chapter 2

Road marking contrast threshold revisited

Abstract: Sufficient contrast between road surface and road markings is key for a safe and comfortable driving experience. This calls for a comprehensive and well established contrast (threshold) model, which ideally results in a single contrast threshold value independent of object angular size or road luminance. The contrast threshold model introduced by Adrian is still commonly used in road lighting. More recently, new contrast metrics that also predict supra-threshold contrast visibility have been proposed, but the corresponding visibility thresholds are not yet known. In the present study, participants are presented a rendering of a highway, including road marking arrows of various size and luminance and were asked to indicate the direction of the arrow. The luminance of the road surface, acting as background for the markings, was varied too. Due to the very low luminance values and the very small differences in luminance, measurement accuracy and calibration issues require special attention. The results show good agreement with Adrian's visibility model ($R^2 = 0.75$) in terms of luminance contrast, background luminance and size. In addition, we used our experimental data to define contrast thresholds for several other existing image based contrast models. Unfortunately, it seems to be impossible to state one unique threshold contrast value independent of object angular size and road luminance.

Spieringhs, R. M., Smet, K., Heynderickx, I., & Hanselaer, P. (2022). Road marking contrast threshold revisited. *Leukos*, 18(4), 493-512. https://doi.org/10.1080/15502724.2021.1993893

What follows is the complete and unedited content of this paper.

2.1 Introduction

Reducing energy consumption while maintaining traffic safety is a main challenge in the design of road lighting. Traffic safety requires a sufficiently high perceived luminance contrast between the road surface and road markings. This luminance contrast is the result of illumination by car headlamps and road lighting in relation to the reflection characteristics of the road surface and the road markings. As LEDs are small-sized light sources, they offer new opportunities in (even asymmetric) beam control using dedicated lenses. In addition, by mainly creating light where it is needed, LEDs offer the opportunity to apply dimming, which contributes to a reduction of energy consumption. An advanced way of reducing energy in road lighting, while maintaining good visibility of objects or signs, is the road lighting concept called 'Probeam' [44, 46]. In this concept, luminaires direct most of their luminous flux forwards, in the direction of view of the driver. One of its objectives is to illuminate retroreflective road marking arrows at distances beyond the reach of car headlights creating an optimal guide for motorized traffic. To optimize 'Probeam' in terms of the balance between energy consumption and traffic safety and to define the level of illumination that should be applied in practice, it is essential to understand contrast perception between road markings and the background road surface. The current study aims to evaluate to what extent the Adrian model [23], known to be accurate in predicting the visibility of targets in uniform backgrounds, can also be used to determine contrast thresholds for the discrimination of the direction of road marking arrows of different size presented on road surfaces, for a set of luminance values attributed to both surfaces. The visual task of determining the direction of a road marking arrow is more complex than just detecting the object itself, and therefore we expect this increase in complexity of the visual task to result in higher contrast thresholds. More importantly, more recent contrast models, such as a difference of gaussian receptive field model and a pyramidal multilevel model, are explored and the corresponding threshold values have been determined. These models only require a luminance image as input and need no specific information on object angular size, background luminance, or luminance of the target, which would make them more easily applicable in realistic complex scenes. Ideally, each model yields a constant contrast threshold value for detecting the arrow direction, irrespective of the luminance of road and arrow and the size of the arrow.

2.1.1 State of the art

One of the most prevalent and relevant models within road lighting for determining the visibility of an object is Adrian's contrast threshold model [50]. This model is based on predicting the luminance difference threshold needed to see an object and follows both Ricco's and Weber's law [23]. This contrast threshold model was extended to road markings by a study of the European commission DG Transport committee described in the COST 331 report [51].

The relative visual performance (RVP) model, in which the ratio of visual performance (VP) over an optimal VP value is calculated, was introduced by Rea and Ouellette in 1991 [52]. The RVP model predicts visual performance rather than only the visibility threshold, and has been applied in commercial and industrial environments [52]. Although mainly established for indoor lighting, this model has also been used in outdoor lighting [50]. However, since our study focuses on finding visibility thresholds and not on supra-threshold visibility performance, the RVP model is not included in our evaluation.

Besides the visual performance and visibility models used for road lighting, there has been an extensive amount of research done on predicting contrast perception in digital images. Image-based contrast models can be useful in overcoming the limitations and complications of Adrian's contrast model and Rea's RVP model, such as applications in which heterogeneous backgrounds and targets are involved. Additionally, the image-based contrast models could result in a more applicable visibility metric where the only necessary input is the luminance image. From the many existing contrast models, we here use the most relevant and applicable ones [21]. They are generally based on two distinguishable concepts of the human visual system: the difference of Gaussians (DoG) and the retinal-like subsampling of contrast [18, 21, 53]. The first feature was adopted and modified by Tadmor and Tolhurst in 2000 [18], who investigated the usefulness of a DoG-based receptive field model for predicting the perception of contrast in natural scenes, as experienced by the retinal ganglion cells and the neurons in the lateral geniculate nucleus (LGN). Later Joulan et al. [20] extended the DoG model by including a multi-scale spatial filter based on parameters determined by the contrast sensitivity function (CSF). The second feature was adopted by Rizzi et al. in 2004 [53] to determine a contrast measure in digital images. In 2012, Simone et al. [21] extended and combined these two features into a weighted level framework model. All these contrast models have in common that no attempt has been made to define threshold values for a discrimination task.

To be able to further optimize new road lighting concepts, the visibility and contrast models mentioned above are evaluated to predict the direction detectability of a road marking arrow. With this application in mind, all models are only evaluated for positive contrasts, in which the arrow is brighter than the road surface background.

2.2 Adrian's contrast threshold model (1989)

In 1946, Blackwell [22] measured the detectability threshold of a dark spot on a white screen. He indicated that for a decrease in the visual angle and an increase in adaptation brightness, the contrast threshold needed to detect the dark spot increased. Another important observation was that at high brightness and with sufficiently large stimuli, the contrast threshold became linear as a function of adaptation luminance. This relation reflects the Weber-Fechner law of perception.

Later in 1989, Adrian [23] used the data obtained by Blackwell (1946) [22] and combined them with the contrast threshold data from other studies [24–28] to determine a model for the visibility of targets, as shown in Eq. 2.1:

$$\Delta L_{\text{threshold}} = k \left(\frac{\sqrt{\phi}}{\alpha} + \sqrt{L} \right)^2 \cdot \mathrm{PF} \cdot \mathrm{EF} \cdot \mathrm{AF} \tag{2.1}$$

where $\Delta L_{\text{threshold}}$ refers to the difference in luminance between target and background at threshold visibility, Φ to the luminous flux function, α to the size of the object in arc minutes, L to the luminance function (i.e., a function related to the background luminance), and k is a constant that is dependent on the experimental conditions. Finally, EF, AF, and PF are factors accounting for exposure time, age, and contrast polarity, respectively. Adrian's visibility model basically follows a geometric summation based on the Weber-Fechner law (contribution of the luminance function) and Ricco's law (contribution of the luminous flux function) suggested by Berek [54]. For a detailed explanation of these functions and factors, we refer to Adrian [24].

Since the current study concerns positive contrasts, exposure times of 2 seconds and a relatively young group of participants (i.e., students), the contrast polarity, exposure time and age factor are all very close or equal to 1, and as such only a part of Adrian's model is investigated.

2.3 Image processing contrast models

2.3.1 Tadmor and Tolhurst (2000)

In 2000, Tadmor and Tolhurst [18] investigated the usefulness of the difference of Gaussian (DoG) receptive field model for predicting the perception of contrast in natural scenes experienced by the retinal ganglion cells and the neurons in the lateral geniculate nucleus (LGN). They assumed that the spatial sensitivity of the center of the receptive field is characterized by a bivariate circular-symmetric Gaussian with a peak amplitude of 1 and a radius r_c. The spatial sensitivity of the surround receptive field is characterized by a second bivariate circular-symmetric Gaussian with a larger radius r_s and a scaled amplitude.

The output of the center receptive field with the midpoint at pixel coordinates x, y is calculated as:

$$R_c(x,y) = \sum_{i=x-3r_c}^{x+3r_c} \sum_{j=y-3r_c}^{y+3r_c} G(i-x, j-y, r_c)L(i,j) \tag{2.2}$$

where $L(i, j)$ indicates the luminance at the pixel location i, j, and $G(i - x, j - y, r_c)$ represents a bivariate Gaussian centered at x, y and with radius r_c.

The output of the surround receptive field with the midpoint at pixel coordinates x, y is calculated similarly to the center receptive field by:

$$R_s(x,y) = \sum_{i=x-3r_s}^{x+3r_s} \sum_{j=y-3r_s}^{y+3r_s} 0.85\left(\frac{r_c}{r_s}\right)^2 G(i-x, j-y, r_s)L(i,j) \tag{2.3}$$

The traditional DoG model defines the response of the retinal ganglion cells and the neurons in the LGN as a subtraction of the surround receptive field output from that of the center receptive field:

$$\mathrm{DoG}(x,y) = R_c(x,y) - R_s(x,y) \tag{2.4}$$

Tadmor and Tolhurst [18] suggested some modifications to the traditional DoG model based on the dependency of the gain of the LGN and retinal ganglion cells on the local mean luminance due to the process of light adaptation. The traditional DoG model assumes that the response of a neuron depends solely on the local luminance difference and, therefore, must be normalized by the local mean luminance to account for the process of light adaptation.

This modification of the DoG model by Tadmor and Tolhurst resulted in three hypothetical measures of contrast. The first measure is a normalization based on center adaptation only (C_c):

$$C_c(x,y) = \frac{R_c(x,y) - R_s(x,y)}{R_c(x,y)} \tag{2.5}$$

The second measure is a normalization based on surround adaptation only (C_s):

$$C_s(x,y) = \frac{R_c(x,y) - R_s(x,y)}{R_s(x,y)} \tag{2.6}$$

The third measure is a normalization based on an adaptation at both the center and surround receptive field (C_{cs}):

$$C_{cs}(x,y) = \frac{R_c(x,y) - R_s(x,y)}{R_c(x,y) + R_s(x,y)} \tag{2.7}$$

These measures of contrast result in local contrast values for each pixel p.

2.3.2 Rizzi, Algeri, Medeghini and Marini (2004)

Another contrast model that was introduced a few years later than the Tadmor and Tolhurst contrast model is the RAMMG model [53]. It refers to the abbreviation of the authors' family names. The RAMMG is based on a multilevel analysis using pyramidal under-sampling of a CIELAB lightness image. For each pixel in the lightness image for each of the pyramid layers, a local neighboring contrast value $|P_{p,l} - P_{j,p,l}|$ is calculated. A global contrast estimate (C^{RAMM}) is then provided by taking the average of all the local contrasts over all the different levels, as shown in Eq. 2.8:

$$C^{\text{RAMM}} = \frac{1}{N_L} \sum_{l=1}^{N_L} \left(\frac{1}{N_{p,L}} \sum_{p=1}^{N_{p,L}} \left(\sum_{j=1}^{8} |P_{p,l} - P_{j,p,l}|/8 \right) \right) \tag{2.8}$$

The number of levels N_L is determined by the pyramidal under-sampling and depends on the resolution of the original image. $N_{p,L}$ marks the number of pixels for a specific pyramid layer, and j signifies the eight neighboring pixels of a pixel in the layer.

2.3.3 Joulan, Hautiere, and Brémond (2011)

In 2011, Joulan et al. [20] proposed a framework to compute the visibility of objects in a luminance image of a road scene based on edge detection [20]. The framework consists of two algorithms, one that takes into account the visual adaptation and a second one that uses a set of DoG spatial filters based on coefficients computed from Barten's contrast sensitivity function (CSF) [55].

The first algorithm applies a gain factor $(1/L_a)$ to the input luminance image I_0 where the gain factor is set to the inverse of the adaptation luminance (L_a), defined as the averaged luminance of I_0:

$$I_1 = I_0 \cdot \frac{1}{L_a} \tag{2.9}$$

The second algorithm applies a weighted sum of DoG (SDoG) to the image I_1 for a set of filters k:

$$SDoG(I_1) = \sum_k \omega_k \left\lfloor G_{\sigma_k^+} - G_{\sigma_k^-} \right\rfloor (I_1) \tag{2.10}$$

where ω_k is the weight of the DoG for filter k, G_{σ_k} is the normalized Gaussian with the standard deviation σ_k^+ for the center and σ_k^- for the surround for filter k. The standard deviation for the center is computed from Barten's CSF, and the standard deviation for the surround is given by $\sigma_k^- = \lambda\sigma_k^+$ with $\lambda = 3$. We refer to Joulan et al. (2011) [20] for more details.

2.3.4 Simone, Pederson, and Hardeberg (2012)

In 2012, Simone et al. [21] introduced the weighted-level framework (WLF) that includes the Difference of Gaussian (DoG) model, the pyramidal subsampling with prefiltering, and weights in the recombination of the pyramid layers [21]. Similar to Rizzi et al. [53], the WLF is based on a multilevel analysis using pyramidal subsampling, but it uses an antialiasing filter in addition. For each level of the subsampled RGB image, the local contrast of each pixel is calculated using the Tadmor and Tolhurst DoG model. This results in a local contrast map for each level l, from which the averaged contrast $\bar{c}$ is determined. Subsequently, an overall contrast measure C is calculated for the R, G, and B channels separately by a weighted recombination of the average contrast of each level, where the weights τ are the variance in local contrast values, and N_l is the total number of levels. Finally, a global contrast measure $C^{(WLF(RSC))}$ is determined by the weighted sum of the overall contrast measure over the three channels, where the weights ω are the variance in overall contrast values:

$$C^{(WLF(RSC))} = \omega_R C_R^{RSC} + \omega_G C_G^{RSC} + \omega_B C_B^{RSC} \tag{2.11}$$

where

$$C_R^{RSC} = \frac{1}{N_l} \sum_{l=1}^{N_l} \tau_{R,l} \bar{c}_{R,l} \tag{2.12}$$

$$C_G^{RSC} = \frac{1}{N_l} \sum_{l=1}^{N_l} \tau_{G,l} \bar{c}_{G,l} \tag{2.13}$$

$$C_B^{RSC} = \frac{1}{N_l} \sum_{l=1}^{N_l} \tau_{B,l} \bar{c}_{B,l} \tag{2.14}$$

2.4 Method

The current study evaluates to what extent existing visibility models can be generalized towards predicting the direction detectability of road marking arrows. Since the existing experimental studies on the visibility of road markings did not focus on the detection of the direction of road marking arrows, a subjective experiment was performed.

2.4.1 Scenes

For this study, test scenes of a highway were rendered in the physical-based-renderer (PBR) Mitsuba [56], and a 3D model of the scene was created in Blender [57]. The scene was created in different layers by using single Mitsuba renderings of the sky, grass, lamp poles, railing, the road surface, the striped middle road markings, the long left road marking, the long right road marking, and the road arrow, as illustrated in Figs. 2.1 and 2.2. Since these elements are displayed at a relatively large angle from the target in the visual field, it is not expected that the addition of these objects will affect our findings.

After artificially altering the digital counts of each layer, the layers were united into a single image, which was then presented to the participants on a calibrated display.

The camera used in Blender to capture the scene and to render in Mitsuba is set at 1.5 m above the road surface and at 1.3 m from the middle striped road marking, aiming 1 degree below the horizontal, simulating the position and viewing direction of a typical (car) driver on a highway [58]. The focal length and sensor size of the camera are 16.7 mm and 22.3 mm, respectively. These camera settings are used to simulate the human eye [59, 60].

The road of 7 m wide is split into two lanes of each 3.5 m wide, representing typical dimensions of a Dutch highway [61]. The left and right road markings are 15 cm wide. The middle road markings are 10 cm wide, 3 m long, and have a spacing of 9 m [51]. These dimensions correspond to the guidelines for road markings by the Directorate-General for Public Works and Water Management Rijkswaterstaat (1991) [62]. Road markings are always shown in positive contrast to the road surface.

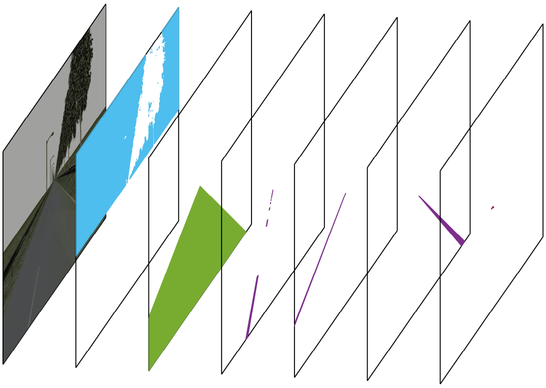

Figure 2.1: Example of the separated layers in side view: sky in blue, the road in green, road markings in purple, and the road marking arrow in red.

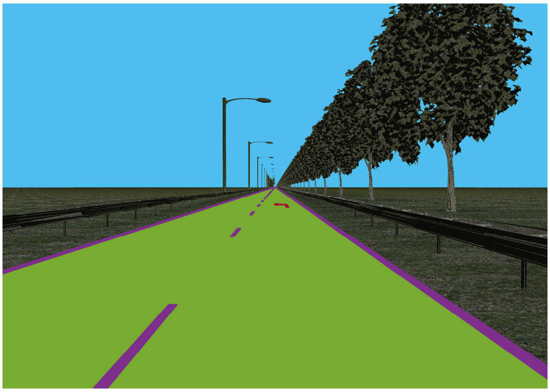

Figure 2.2: Example of the separated layers presented in Fig. 2.1, but now in front view.

Lamp poles with a height of 18 m are positioned on the left side of the road at 90 m intervals. Trees are placed on the right side of the road at 25 m intervals. To each side of the road, railings and grass planes are added as shown in Fig. 2.3. The trees, railings, grass plane, and lamp posts add complexity to the scene and make the environment more realistic.

2.4.2 Experimental conditions

For this study, three road luminance values (i.e., 0.25, 0.66, and 0.99 cd/m^2) were selected, representative of typical values found under bad, average, and good road

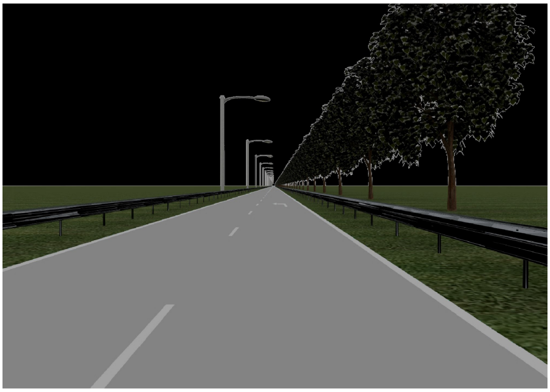

Figure 2.3: A representative highway scene rendered by Mitsuba.

lighting conditions [58]. For each road luminance value, we determined the required contrast to detect the correct pointing direction of an arrow varying in angular extent (deduced from its distance to a driver position) and luminance. The road arrows were 7.5 m in length and at most 1.05 m in width [62]. The corresponding angular size was calculated in arc minutes based on the plane angle subtended by the length of the road marking in front of the eye (see Fig. 2.4) at four observer distances (i.e., 40, 60, 80, and 100 m).

Figure 2.4: Image of a road marking arrow with an indication of its length.

To determine a good range of luminance values for the arrows, we started with a pilot experiment that followed the exact same protocol as the main experiment (further described below), but with random luminance values for the arrows instead of controlled values. This pilot experiment was executed with 3 observers, and based on its results, we selected five arrow luminance values for each road luminance and each angular size of the arrow. These values are expected to cover a visibility range from non-perceptual (50%) to a 100% correct evaluation. Table 2.1 shows these luminance values, calculated in the CIE 1931 2° color space, because of the small angular extent of our stimuli.

Table 2.1: Five luminance values of the arrow (in cd/m^2) for each combination of road surface luminance (in cd/m^2) and angular length of the arrow (in arcmin).

Arrow size (')	L_{road} (cd/m^2)	L_{arrow} (cd/m^2)				
20.3	0.25	0.25	0.27	0.29	0.31	0.33
9.5	0.25	0.25	0.27	0.29	0.31	0.33
5.5	0.25	0.27	0.29	0.31	0.33	0.35
3.6	0.25	0.29	0.31	0.33	0.35	0.38
20.3	0.66	0.66	0.70	0.74	0.78	0.82
9.5	0.66	0.66	0.70	0.74	0.78	0.82
5.5	0.66	0.66	0.70	0.74	0.78	0.82
3.6	0.66	0.74	0.78	0.82	0.86	0.90
20.3	0.99	0.99	1.04	1.09	1.14	1.19
9.5	0.99	0.99	1.04	1.09	1.14	1.19
5.5	0.99	1.03	1.09	1.14	1.19	1.24
3.6	0.99	1.09	1.14	1.19	1.24	1.29

2.4.3 Experimental setup

The experimental setup consisted of a calibrated 65-inch Samsung QE65Q90 display, a keyboard, and a chinrest, as shown in Fig. 2.5. The display had a resolution of 3840 x 2160 (4k) pixels and a refresh rate of 120 Hz. The display's absolute full-brightness value was substantially lowered to enable sufficiently high resolution in luminance at the low luminance levels required in the experiment. As a consequence, its maximum luminance (i.e., R=G=B=256) was 33.19 cd/m^2. The display was positioned perpendicularly to the observer's eyes with its center aligned at the height of the observer's eyes and at a distance of 108 cm. As such, the display covered a vertical and horizontal field of view (FOV) of 42° and 68°, respectively. The experiment took place in a dark room, and participants were seated on a chair with their chin placed on the chinrest. Fixing the eye height and the visual field was needed to match the camera characteristics used to capture the rendered scene in Blender, and hence ensured that distances on the screen matched the physical reality represented in the scene.

2.4.4 Calibration and measurements

Calibration and characterization of the display were of utmost importance, as we wanted to display small luminance values and luminance differences. To this end, spectral radiance measurements were performed with an air-cooled Ocean Optics QE65 Pro spectrometer equipped with a Bentham TEL301 fiber-coupled telescope with a variable aperture. The integration time of the spectrometer could range from 8

Figure 2.5: Picture of the experimental setup, showing the display, chinrest, and keyboard.

ms up to 15 minutes. Its signal-to-noise ratio was 1000:1 at full signal. The telescope was positioned at a distance of 1.5 m from the display at eye height. Before measuring the stimuli, a dark current measurement was carried out. To convert the spectrometer responses to spectral radiance, two Bentham SRS8 Halogen spectral radiance standards were used. For measuring the low luminance values of our experiment, an aperture size of 3.5 mm was required, but this resulted in saturation when targeting the radiance standard. A second radiance standard, equipped with a neutral density filter with optical density 0.9, was calibrated with respect to the primary radiance standard using a smaller aperture (i.e., 1.17 mm).

To bridge the dynamic range between the calibration standard and our low-luminance stimuli, linearity of the detector response with integration time was crucial. This was checked by measuring the response of a 150 x 150 pixels stimulus located at the middle of the display, driven with an 8-bits signal of R=G=B=150. The size of this stimulus was slightly larger than the field of view of the spectrometer. The position of the stimulus was identical to the position of the road marking arrows during our experiment. The stimulus was measured at 16 integration times, varying between 0.027 and 58 seconds. The dark current response was also measured and subtracted. The dark-corrected spectrometer response for each peak wavelength as a function of integration time confirms the spectrometer's linearity with integration time.

Finally, we checked the stability of the display over time. To this end, a 150 x 150 pixel square with an 8-bits signal of R=G=B=150 was measured 29 times over the course of several days. The first 21 measurements were taken within the first 1.5 hours and resulted in a mean luminance of 1.55 cd/m^2 and a standard deviation of 0.002 cd/m^2. Three measurements were taken the day after and, even without recalibration, yielded a mean luminance of 1.55 cd/m^2 and a standard deviation of 0.002 cd/m^2. Four other measurements were taken five days later resulting in a mean luminance of 1.54 cd/m^2 and a standard deviation of 0.0007 cd/m^2. These results show the high stability of the display and the accuracy of the measuring process.

The whole calibration and measurement procedure resulted in an accurate look-up table relating RGB-values to actual luminance values.

2.4.5 Design and Procedure

In the experiment, participants had to judge the direction (i.e., left or right) of a road marking arrow on a road surface using the method of constant stimuli [63]. We used a full-factorial semi-between subject design with the luminance of the road surface (i.e., 3 levels: 0.25, 0.66, and 0.99 cd/m^2), the luminance of the road marking arrow (i.e., 5 levels depending on the road surface luminance), and the arrow's angular size (i.e., 4 levels: 20.3, 9.5, 5.5, and 3.6 arcmin) as independent semi-between subject variables and the luminance difference thresholds (as defined below) as the dependent variable. In total, each participant had to judge 1 road surface luminance value, 5 luminance values of the road arrow, 4 angular sizes of the arrow, and 2 directions (arrow pointing left or right), with each condition repeated ten times, which resulted in 400 stimuli (i.e., 5x4x2x10). Participants were split into three groups, one for each value of the road surface luminance.

Before starting the experiment, participants who were not familiar with its procedure received an introduction, in which possible unclarities were resolved and a few trials were performed. After these trials, the participants were requested to adapt to a grey image (subtending 3840 x 2160 pixels at R=G=B=119, which corresponded to 0.31 cd/m^2) for two minutes in a dark room such that the impact of previous adaptation to any reference was minimized. After this adaptation period, the experiment started with a full grey image shown for 3 seconds. Afterwards, we displayed one of our stimuli for 2 seconds, followed by again the full grey adaptation image for 3 seconds. Participants were instructed to indicate whether the arrow on the road was pointing to the left or right, by pressing the corresponding arrow key on the keyboard. Responses could only be given while the stimulus was on the display screen, so a maximum of 2 seconds response time was used. If a participant correctly identified the direction of an arrow, a response of 1 was recorded, and when a participant incorrectly identified the direction of an arrow, a response of 0 was recorded. When participants did not observe any arrow, they could abstain from responding. When a participant did not give a response within the time of exposure (i.e., 2 s), a value of 0.5 was recorded (i.e., assuming to be the average response of having to guess between two equal options). All stimuli were presented in random order. The experiment took about 45 minutes to finish.

2.4.6 Participants

Participants were recruited among the members of the authors' lab and interested students. In total, 18 participants conducted the experiment, i.e., 6 per road luminance condition. Of these 18 participants, 6 were female and 12 were male. The participants were aged from 18 to 35 years old, with an average age of 26.9 years (SD = 3.1).

2.5 Results

2.5.1 Analysis of the experiment

Each scene has been evaluated 10 times by each observer. In the analysis, the proportion of correct responses for each participant, at each road surface luminance and angular size of the arrow (i.e., 3x4=12 combinations) were plotted against the difference in luminance of the road marking arrow with the road surface. A psychometric curve was fitted through these plots per participant, road surface luminance, and angular size of the arrow. Based on a two alternative forced choice task, the luminance difference threshold was defined as the 0.75 proportion correct.

Initially, we considered the Wichmann and Hill method (2001a) [64] for fitting the psychometric curves, using the Monte Carlo simulation of bootstrap. However, previous research indicated that the confidence intervals obtained by bootstrapping may be too small [65–67] in case of small data sets. Therefore, considering the small data set of our study as well, more credible intervals were determined with Bayesian statistics [64, 68]. In this approach, the intervals were calculated based on a standard prior, cumulative Gaussian distribution, and a fixed lower asymptote at 0.5 with the psignifit (v.4) software that used the formulae provided by Schütt, Harmeling, Macke, and Wichmann (2016) [68]. Fig. 2.6 shows as an example the psychometric function of participant 1 for a road surface luminance of 0.25 cd/m^2 and an angular size of the arrow of 9.5 arcmin.

For all participants and all 12 combinations of road surface luminance and angular size of the arrow, the psychometric curve was successfully fitted (with an average

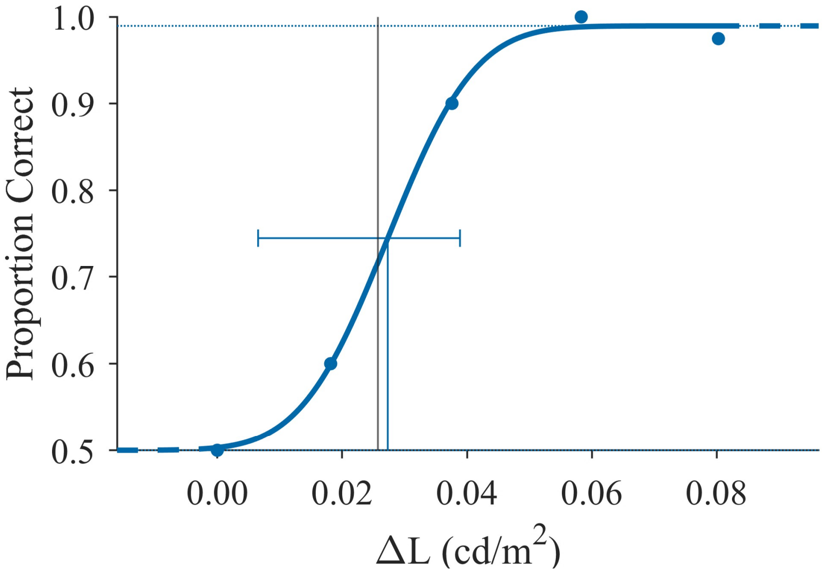

Figure 2.6: The psychometric curve (solid blue line) for participant 1 measured for a road surface luminance of 0.25 cd/m^2 and an arrow's angular size of 9.5 min as a function of the luminance difference between arrow and road surface. The threshold is determined from the 0.75 proportion correct, and the corresponding confidence interval is indicated by the horizontal blue line. The corresponding threshold estimated by Adrian (including age) is indicated with the vertical black line.

R^2 of 0.91 and R^2 values ranging between 0.25 and 1.00), except for participant 10 at a road surface luminance of 0.25 cd/m^2 and an arrow angular size of 3.6 arcmin, in which condition the data was overly dispersed (R^2 of -0.88). Nevertheless, even for this participant, a best threshold estimate was provided by the psignifit (v.4) software. We also investigated 'pooling' the data over the six participants and then fit a normal cumulative distribution to the combined dataset, however, found the results to be similar.

For determining the inter-observer variability, the standard residual sum of squares (STRESS) was calculated as provided by Garcia, Huertas, Melgosa, and Cui [69], for each road surface luminance separately (i.e., 6 observers), as shown in Eqs. 2.15 and 2.16:

$$\text{STRESS} = \frac{1}{6}\sum_{i=1}^{6}\left(\frac{\sum_{j=1}^{4}(E_{i,j}-\bar{V}_j)^2}{\sum_{j=1}^{4}(\bar{V}_j)^2}\right)^{\frac{1}{2}} \tag{2.15}$$

with

$$f = \frac{\sum_{j=1}^{4}(E_{i,j})^2}{\sum_{j=1}^{4}E_{i,j}\bar{V}_j} \tag{2.16}$$

where $E_{i,j}$ indicates the luminance difference threshold of observer i for the angular size of the road arrow j, and $\bar{V}_j$ indicates the luminance difference threshold averaged over all (six) observers for the angular size of the road arrow j. The resulting STRESS values were converted to percentages by multiplying them by 100. The STRESS percentages for the 0.25, 0.66, and 0.99 cd/m^2 road surface luminance were 11%, 10%, and 5%, respectively. As suggested in the multidimensional scaling literature, these STRESS percentages would be considered around fair (10%) to good (5%) [69, 70].

Fig. 2.7 shows the luminance difference thresholds obtained from the psychometric fits. It clearly shows that the luminance difference threshold decreases with increasing arrow size and decreasing road luminance (or background luminance).

To confirm the statistical significance of the decrease in luminance difference threshold with increased angular size of the arrow and decreased background luminance, we performed a mixed repeated-measures factorial ANOVA with the road surface luminance and arrow angular size as independent factors (including also their interaction) and with the measured luminance difference threshold as the dependent factor. The arrow angular size was taken as a within-subject independent variable, while the road surface luminance was included as a between-subject factor. Prior to further analysis, the assumptions of homogeneity of variance and sphericity were checked. For the within-subject variable, the sphericity hypothesis according to Mauchly's test across the four angular sizes of the arrow was rejected ($p < 0.05$); therefore, a Greenhouse-Geisser correction was used. The Levene's test of equality of error variances was rejected only for the arrow angular size of 20.3 arcmin ($p = 0.026$). Since this implies that the variance was similar for all other angular sizes and road surface luminance values, a mixed repeated-measures factorial ANOVA was used.

This analysis revealed a statistically significant main effect for the angular size of the arrow ($F_{18.1,1.2} = 123.96$; $p < .001$; $\eta^2 = .89$) and for the road surface luminance ($F_{15,2} = 17.24$; $p < .001$; $\eta^2 = .70$). Furthermore, it revealed a significant interaction between arrow angular size and road surface luminance ($F_{18.1,2.4} = 3.98$; $p < .05$; $\eta^2 = .35$). These effects are not surprising, as similar findings were reported before in Cao [71] and Mayeur et al. [72].

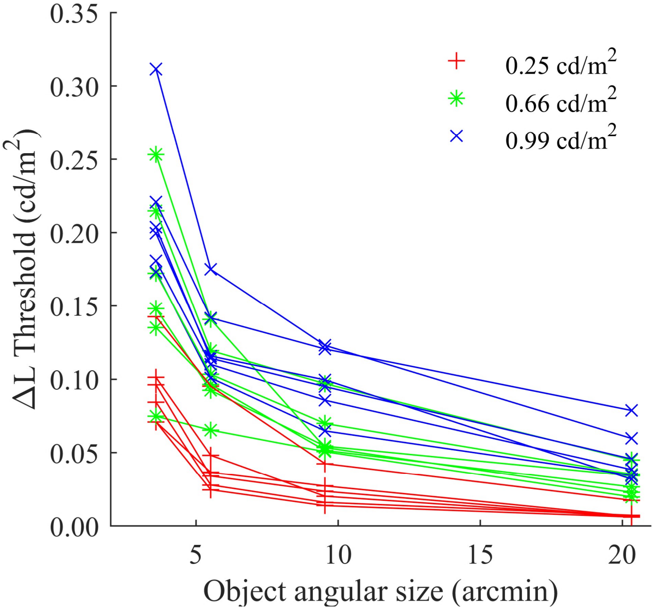

Figure 2.7: The luminance difference threshold for each of the 6 observers plotted against the arrow size (i.e., 20.3, 9.5, 5.5, 3.6 arcmin) for each road surface luminance (i.e., 0.25, 0.66, and 0.99 cd/m^2).

2.5.2 Applicability of the Adrian model

To compare our experimentally measured luminance difference threshold values with the values predicted by the visibility model of Adrian [23], we calculated their mean value over all observers (and the respective 95% confidence interval) per road surface luminance and arrow angular size. The resulting mean luminance difference thresholds as a function of road surface luminance for the different values of the angular size of the arrow, and as a function of angular size of the arrow for the different values of the road surface luminance were fitted with Adrian's model using Eq. 2.1. The resulting fits are shown in Fig. 2.8 and Fig. 2.9, respectively. In both figures, the solid lines indicate the predicted visibility by Adrian's model, while the experimental data are shown by the crosses and their 95% confidence interval.

Fig. 2.10 presents the overall correspondence between our experimental data and Adrian's model in a scatter plot. The solid black line indicates perfect correspondence for a visibility level equal to 1 following the standard Adrian's model for detection thresholds. Two goodness-of-fit values are determined: one with the model parameter k (see Eq. 2.1) taken as 2.6 (i.e., the recommended value for a forced-choice method

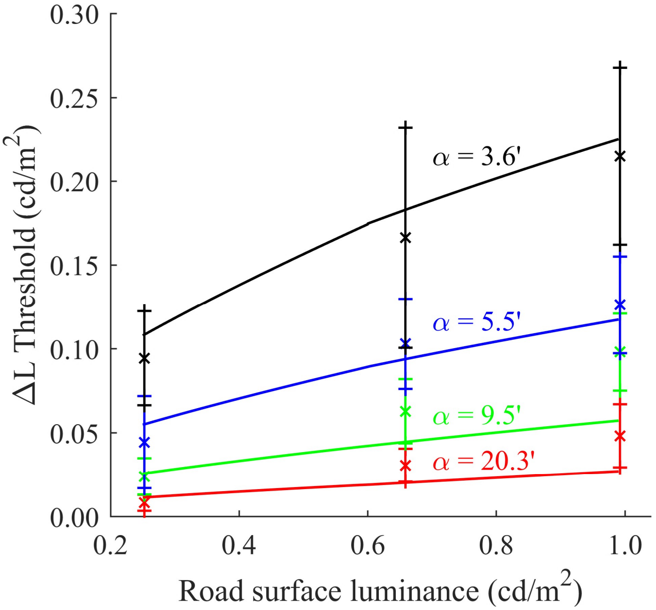

Figure 2.8: The measured luminance difference threshold plotted as a function of the road surface luminance for different values of the angular size of the arrow (separated by color). The means of the measured thresholds per condition are indicated by crosses, and at each cross, the corresponding 95% confidence interval is shown. Solid lines indicate the prediction by Adrian's model.

[23]), and one using a best fit after optimizing the model parameter k. They result in R^2 values of 0.75 and 0.75, respectively. In addition, Fig. 2.10 also shows that the "best fit" line is very close to Adrian's model, indicating that the thresholds needed for discriminating the direction of an arrow can be estimated with Adrian's detection threshold model without taking into account the anticipated higher thresholds because of the higher complexity of the visual task.

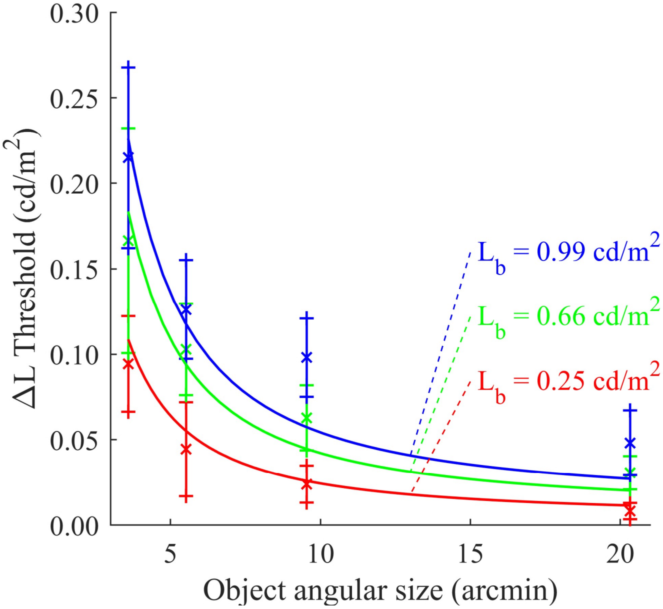

Figure 2.9: The measured luminance difference threshold plotted as a function of the arrow angular size for different values of the road surface luminance (separated by color). The means of the measured thresholds per condition are indicated by crosses, and at each cross, the corresponding 95% confidence interval is shown. Solid lines indicate the prediction by Adrian's model.

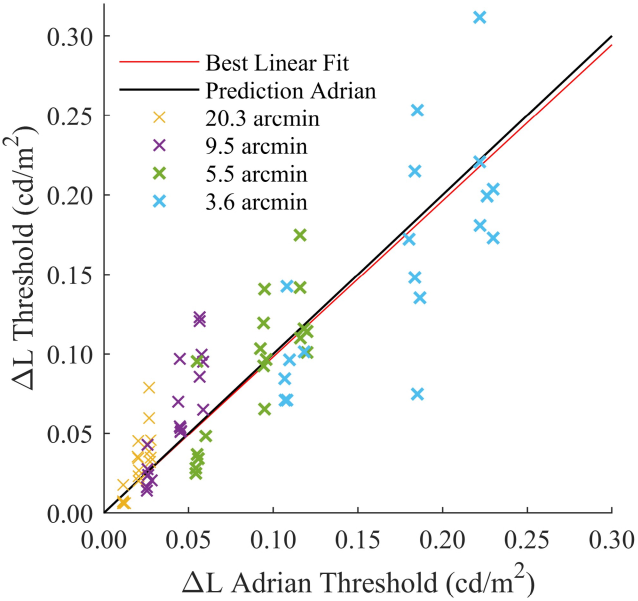

Figure 2.10: Our measured data plotted against the thresholds predicted by the visibility model of Adrian (black line). Crosses indicate the observed threshold for each participant and condition. The red line gives the best fit for an optimized model parameter k of 2.55.

2.5.3 Thresholds for the Tadmor & Tolhurst model

For each scene presented to the observers, we calculated the Difference of Gaussian (DoG) value (as proposed by Tadmor and Tolhurst [18]) per pixel in a frame of 150 x 150 pixels around the road marking arrow. We chose to use one fixed frame to encompass all road marking arrows, where the largest arrow (i.e., 20.3 arcmin) covered 2.3% of the frame, whereas the smallest arrow (i.e., 3.6 arcmin) covered 0.4% of the frame. To calculate the DoG value per pixel, we first converted the RGB-image within the frame to a luminance image using the look-up table (mentioned in section 2.4.4 Calibration and measurements). We then applied the DoG model (Eqs. 2.2, 2.3 and 2.4) with some modifications.

The first modification is that we wanted to use a global DoG value per scene C_{DoG}, and therefore, summed all local DoG-values over the N_p (i.e., 150x150) pixels of the image [73, 74]:

$$C_{\mathrm{DoG}} = \sum_{p=1}^{N_p} |\mathrm{DoG}(x, y)| \tag{2.17}$$

To do so, we replaced the DoG values by their absolute values in order to avoid compensation when adding positive and negative DoG pixel values [73, 74].

Second, instead of using the 0.85 weighting factor in the calculation of the surround receptive field (Eq. 2.3), we chose a center/surround weighting factor of 1, which ensured that a region of uniform luminance extending from the edge of the surround receptive field did not contribute to C_{DoG}. As a consequence, the amount of background pixels included in the final C_{DoG} value was much lower.

Finally, although theoretically the DoG value of a pixel for which the center and surround completely cover a uniform luminance region is meant to be zero, the discrete integral approximation as proposed by Tadmor and Tolhurst resulted in a small value of 0.00067. Although very small, when multiplied by the whole frame (of 150 x 150 pixels), this might become such a large value that it masked the contribution of the fewer pixels signaling real contrast. To obtain an absolute zero DoG value for a uniform center and surround, the discrete integral values of the two bivariate Gaussians were rounded to five decimals and slightly adjusted to the values shown in the supplemental material.

Finally, the center radius r_c was set at 1 pixel and the surround radius r_s at 2 pixels, resulting in a center/surround ratio of 1:2. As the images were projected on a screen with a field of view of 42° vertically and 68° horizontally, each pixel represented 0.89 arcmin horizontally and 1.17 min vertically. As such, the center radius r_c of 1 pixel was in line with the angular resolution of the eye of 0.7 to 0.8 arcmin [75, 76] at the fovea. The center to surround ratio of the receptive field radii corresponded to the ratio reported by Simone, Pedersen, and Hardeberg [21]. An example of a DoG-filtered image is given in Fig. 2.11.

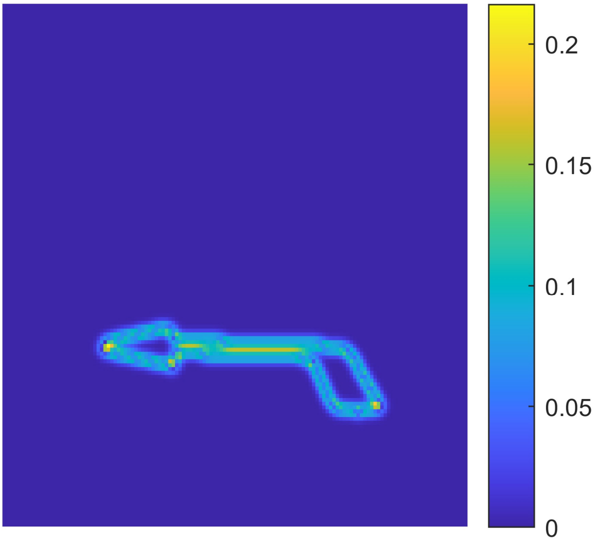

Figure 2.11: DoG-filtered image of the 150 x 150 pixels of a road marking image for a road surface luminance of 0.99 cd/m^2, road marking luminance of 1.19 cd/m^2, and an arrow's angular size of 20.3 arcmin. The color bar at the right indicates the DoG values that correspond to the colors.

We then plotted psychometric curves (in the same way as explained before), but now using the calculated C_{DoG} values instead of ΔL values on the ordinate. Fig. 2.12 illustrates these psychometric curves for participants 1, 2, and 3, indicating the proportion correct responses for the four different angular sizes of the arrow, measured for a road surface luminance of 0.25 cd/m^2. All psychometric curves result in an average R^2 of 0.91 and R^2-values ranging between 0.25 and 1.00 indicating a good fit to the data, except for participant 10 at a road surface luminance of 0.25 cd/m^2 and angular size of 3.6 min of the arrow. As explained before, the latter data were overly dispersed (R^2 of -0.88).

The mean C_{DoG} thresholds (corresponding to the C_{DoG}-value at 0.75 proportion correct, averaged over all 6 participants per road surface luminance) are plotted in Fig. 2.13(a) together with their 95% confidence interval (calculated using Bayesian statistics), similar to Fig. 2.9. Fig. 2.13(b) presents the overall linearity between our experimental

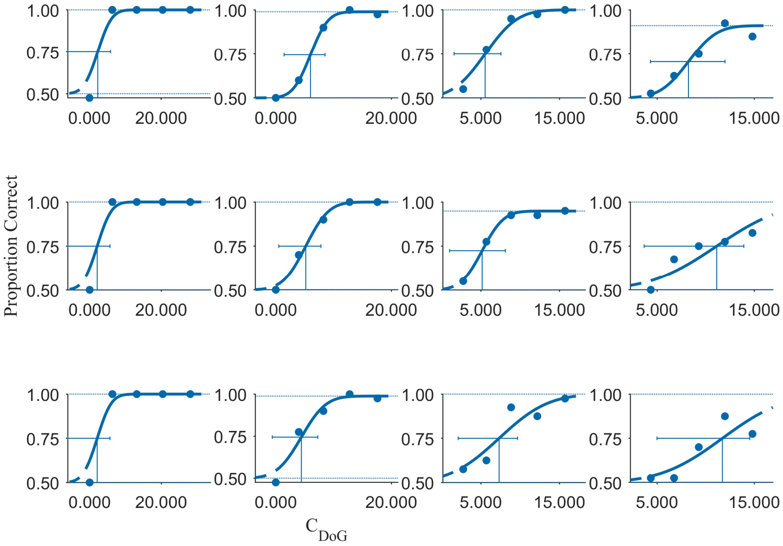

Figure 2.12: The psychometric curves fitting the proportion correct responses as a function of C_{DoG} values for participants 1, 2, and 3 (from top to bottom, respectively). The psychometric curves were plotted for each angular size of the arrow: i.e., 20.3, 9.5, 5.5, and 3.6 arcmin (from left to right, respectively). All plots refer to a road surface luminance of 0.25 cd/m^2.

data and the C_{DoG} thresholds in a scatter plot, similar to Fig. 2.10. Overall, threshold values decrease with increasing angular size and decreasing road luminance, in analogy with the luminance difference thresholds. If the C_{DoG} model would perfectly correlate with the discrimination of an arrow's direction, one unique C_{DoG} threshold value would emerge, irrespective of background luminance and angular size of the arrow.

Unfortunately, this is not the case. The average C_{DoG} threshold value at 0.66 cd/m^2 background luminance varies over 44% between the highest and lowest value across all angular sizes of the arrow. The average C_{DoG} threshold values at 0.66 cd/m^2 background luminance vary over about 44% between the highest and lowest value across all angular sizes of the arrow. The variation in threshold values at 10 arcmin angular size across the various levels of the road surface luminance numbers 76%. Note that the C_{DoG} model indeed does not include a global adaptation factor.

In addition to determining the C_{DoG} thresholds, also, similarly, the thresholds for the

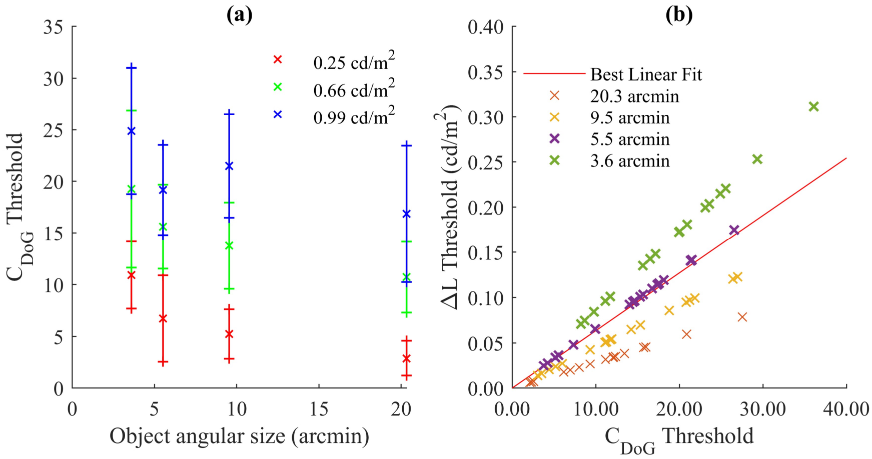

Figure 2.13: (a) The averaged C_{DoG} thresholds (indicated by the crosses) and their 95% confidence interval plotted against the angular size of the arrow for each road surface luminance (i.e., 0.25, 0.66, and 0.99 cd/m^2). (b) Our measured data plotted against the C_{DoG} thresholds. Crosses indicate the observed threshold for each participant and condition. The red line gives the best fit (R^2 = 0.72).

normalized contrast estimates (C_c, C_s, and C_{cs}) were determined based on Eqs. 2.5, 2.6, and 2.7. For the contrast estimates C_c, C_s, and C_{cs}, all psychometric curves resulted in an average R^2 of 0.91 and R^2-values ranging between 0.25 and 1.00 indicating a good fit to the data, except for participant 10 at a road surface luminance of 0.25 cd/m² and angular size of 3.6 min of the arrow. The mean C_c, C_s, and C_{cs} threshold values (again, corresponding to the 0.75 proportion correct, averaged over the six participants per road surface luminance) are plotted in Fig. 2.14 together with their 95% confidence interval. Overall, threshold values decrease with increasing angular size. The average C_c, C_s, and C_{cs} threshold values at 0.66 cd/m² background luminance vary over about 44% between the highest and lowest value across all angular sizes of the arrow. The variation in threshold values at 10 arcmin angular size across the various levels of the road surface luminance is about 0.051%. The overall linearity between our experimental data and the C_c, C_s, and C_{cs} thresholds is presented in separate scatter plots in Fig. 2.15.

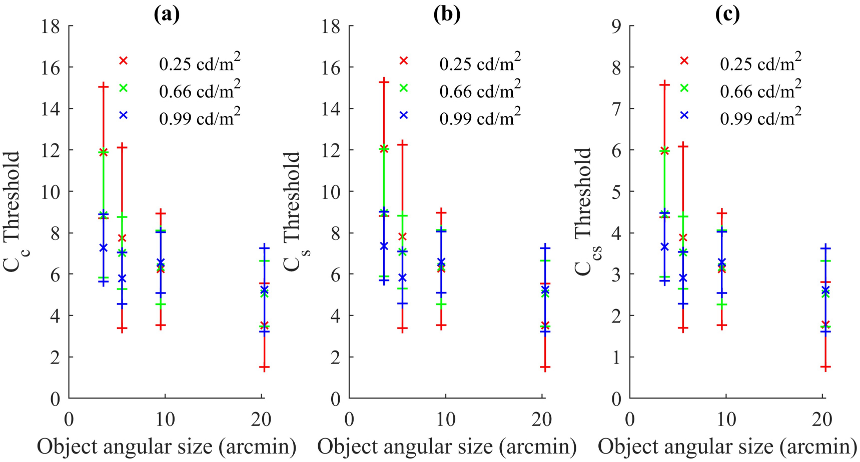

Figure 2.14: The averaged C_c (a), C_s (b), and C_{cs} (c) thresholds (indicated by the crosses) and their 95% confidence interval plotted against the angular size of the arrow for each road surface luminance (i.e., 0.25, 0.66, and 0.99 cd/m^2).

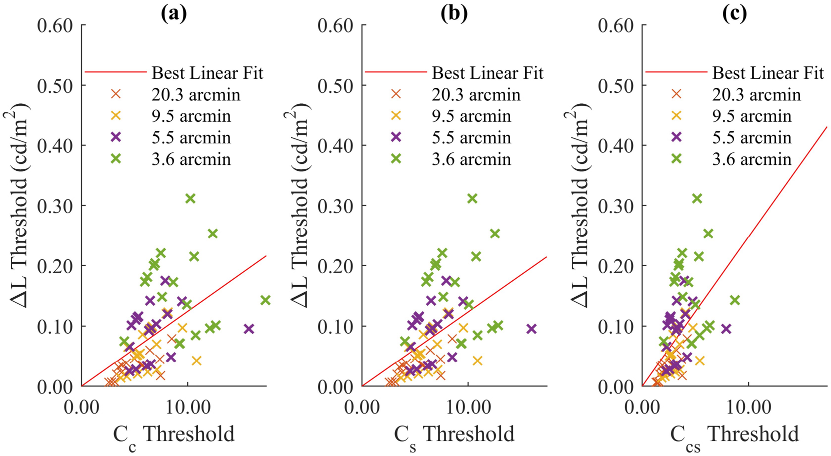

Figure 2.15: Our measured data plotted against the C_c (a), C_s (b), and C_{cs} (c) thresholds. Crosses indicate the observed threshold for each participant and condition. The red line gives the best fit ($R^2 = 0.28$ (a), 0.28 (b), 0.28 (c)).

2.5.4 Thresholds for the Rizzi et al. model

In addition to determining the thresholds with the C_{DoG} model, we determined the C^{RAMM} threshold contrast values for each angular size, road surface luminance, and road marking luminance. Again, the RGB image of 150 x 150 pixels around the road marking arrow was converted into a luminance image, and subsequently used to calculate the C^{RAMM} values according to Eq. 2.8. Also, these C^{RAMM} values were compared to the proportion correct, and these data were used to fit psychometric curves, as illustrated in Fig. 2.16. Similarly, as with the other contrast measures, the psychometric curves resulted in an average R^2 of 0.91 with R^2 values ranging between 0.25 and 1.00, except for participant 10 at a road surface luminance of 0.25 cd/m^2 and an angular size of 3.6 arcmin of the arrow.

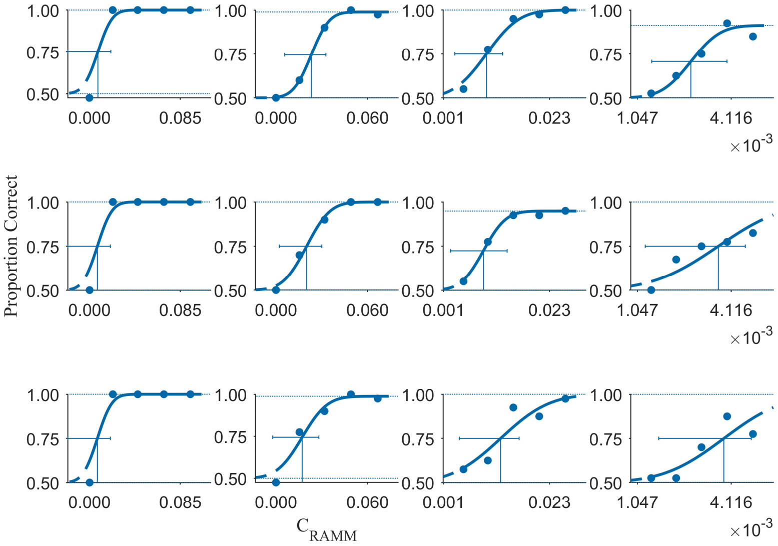

Figure 2.16: Psychometric curves fitted through the proportion correct responses as a function of the C^{RAMM} values. The plotting arrangement is similar to Fig. 2.12

.

The averaged C^{RAMM} threshold values (again, corresponding to 0.75 proportion correct, averaged over the six participants per road surface luminance) are plotted in Fig. 2.17(a) together with their 95% confidence interval, similar to Figs. 2.9, 2.13(a), and 2.14. Fig. 2.17(b) presents the overall linearity between our experimental data and the C^{RAMM} thresholds in a scatter plot, similar to Figs. 2.10, 2.13(b), and 2.15. The average C^{RAMM} threshold value at 0.66 cd/m^2 road surface luminance varies over 87% between the highest and lowest value across the various angular sizes. The variation in threshold values at 10 arcmin angular size across the various levels of the road surface luminance numbers 34%.

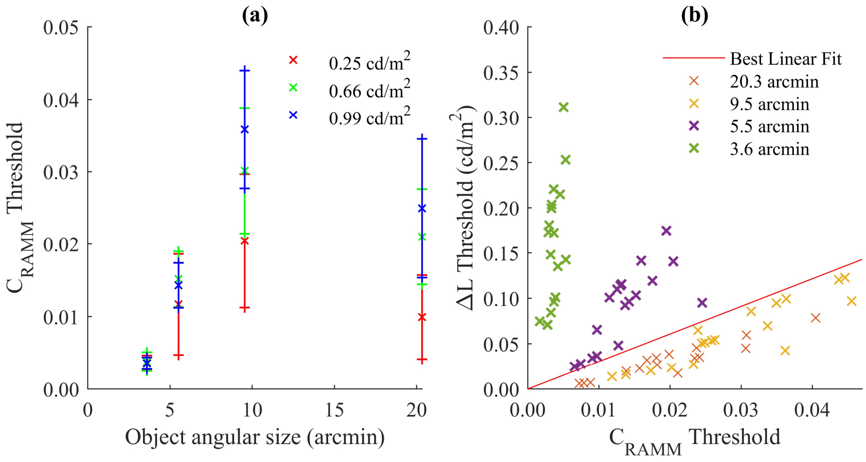

Figure 2.17: (a) The averaged C^{RAMM} threshold values (indicated by the crosses) and their 95% confidence interval plotted against the angular size of the arrow for each road surface luminance (i.e., 0.25, 0.66, and 0.99 cd/m^2). (b) Our measured data plotted against the C^{RAMM} thresholds. Crosses indicate the observed threshold for each participant and condition. The red line gives the best fit ($R^2 = -0.85$).

2.5.5 Joulan et al. model

To compare our experimentally measured arrow-direction detection thresholds to the Joulan et al. visibility model, we transferred all stimuli (i.e., for each angular size, road surface luminance, and road marking luminance) into C_{SDoG}-values using Eq. 2.10, but with a similar modification as what we used in the Tadmor and Tolhurst model, i.e., that we summed all C_{SDoG}-values over the N_p (i.e., 150x150) pixels of the image, resulting in:

$$C_{\mathrm{SDoG}} = \sum_{p=1}^{N_p} SDoG(x, y) \tag{2.18}$$

Subsequently, the proportion correct arrow-direction detections were plotted against the resulting C_{SDoG}-values, and fitted to a psychometric curve. Overall, also the C_{SDoG}-values yielded good fits of the psychometric function to the fraction correct answers with a goodness of fit very comparable to the other visibility measures we considered so far (i.e., an average R^2 of 0.91 and R^2-values ranging between 0.25 and 1.00). The mean C_{SDoG}-threshold values (again, corresponding to 0.75 proportion correct, averaged over the six participants per road surface luminance) are plotted in Fig. 2.18(a) together with their 95% confidence interval. When compared to the average contrast threshold values of other contrast models, the average C_{SDoG} threshold values show more consistency across different angular sizes of the arrow for a given road surface luminance. The average C_{SDoG} threshold value at 0.66 cd/m² road surface luminance varies over 16% between the highest and lowest value across the various angular sizes. The variation in threshold values at 10 arcmin angular size across the various levels of the road surface luminance numbers 30%. The overall linearity between our experimental data and the C_{SDoG} thresholds is illustrated in a scatter plot in Fig. 2.18(b).

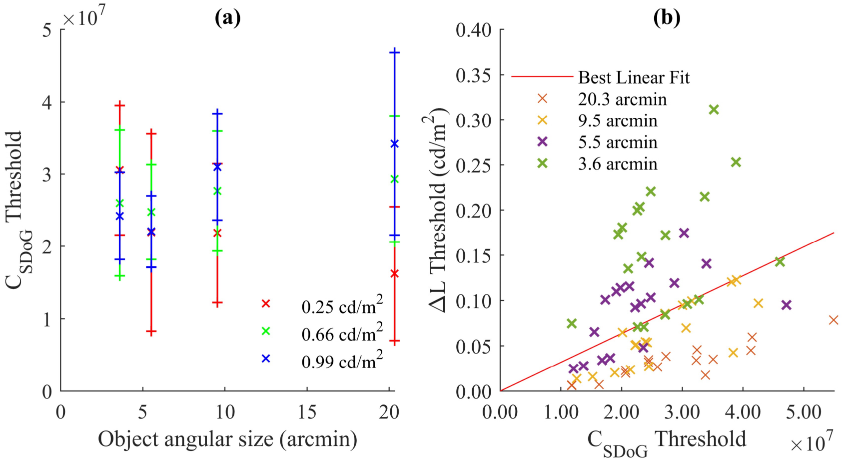

Figure 2.18: (a) The averaged C_{SDoG} threshold values (indicated by the crosses) and their 95% confidence interval plotted against the angular size of the arrow for each road surface luminance (i.e., 0.25, 0.66, and 0.99 cd/m^2). (b) Our measured data plotted against the C_{SDoG} thresholds. Crosses indicate the observed threshold for each participant and condition. The red line gives the best fit ($R^2 = 0.092$).

2.5.6 Simone et al. model

The Simone et al. model is the final one that we evaluated for predicting our experimental data. Also in this case, we calculated for each angular size, road surface luminance, and road marking luminance the corresponding C_{WLF}-value, using Eqs. 2.11, 2.12, 2.13, and 2.14 on the RGB images with a size of 150 x 150 pixels. The proportion correct responses measured in the experiment were then plotted as a function of the resulting C_{WLF}-values, and these data were used to fit psychometric curves. The resulting psychometric curves fitted the data somewhat less well than for the earlier visibility models we evaluated, since the average R^2 is reduced to 0.75 (from around 0.9). From the fits, we determined the mean C_{WLF}-threshold values (again, corresponding to 0.75 proportion correct, averaged over the six participants per road surface luminance), and plotted them in Fig. 2.19(a) as a function of the angular size of the arrow, together with their 95% confidence interval. When compared to the average contrast threshold values of other contrast models, the average C_{WLF} threshold values show less consistency across different angular size road surface luminance (99% variation over angular size at 0.66 cd/m^2 road surface luminance and 74% variation over road surface luminance at 10 arcmin angular size). The overall linearity between our experimental data and the C_{WLF} thresholds is shown in a scatter plot in Fig. 2.19(b).

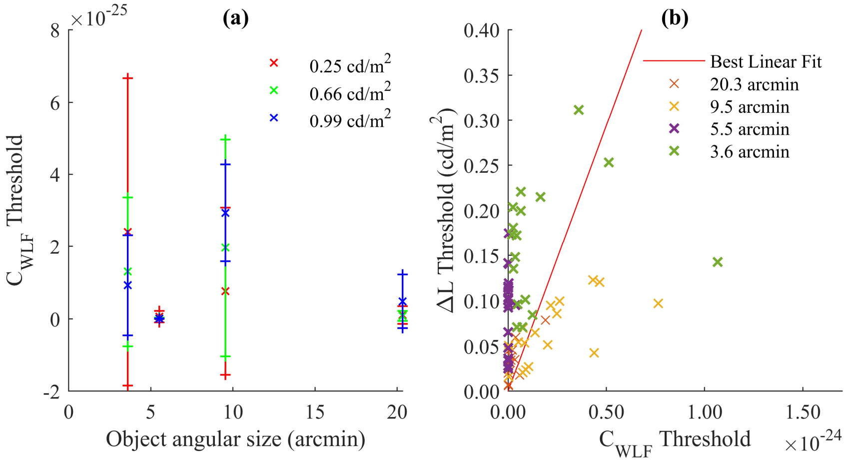

Figure 2.19: (a) The averaged C_{WLF} threshold values (indicated by the crosses) and their 95% confidence interval plotted against the angular size of the arrow for each road surface luminance (i.e., 0.25, 0.66, and 0.99 cd/m^2). (b) Our measured data plotted against the C_{WLF} thresholds. Crosses indicate the observed threshold for each participant and condition. The red line gives the best fit ($R^2 = -12.00$).

2.6 Discussion

Our experimentally measured thresholds between a road marking luminance and the road surface luminance corresponded well ($R^2 > 0.7$) with the luminance difference thresholds predicted by the visibility model of Adrian [23]. Our participants had to indicate the pointing direction of a road arrow, which is a considerably different paradigm from the one used before by Blackwell [22], where participants had to indicate the presence of a stimulus. In that sense, it is a surprising result that the visibility model of Adrian predicts our experimental results so well; it shows that the model is more broadly applicable than where it originally was intended for. Although the results, in general, are very good, Fig. 2.10 shows that the prediction of the threshold for discriminating the pointing direction of an arrow is worse at small angular sizes of the arrow than at larger ones. A possible explanation is that there was more variation in experimental threshold values at the smaller angular sizes. Participants had difficulties in really seeing the actual direction of the road marking arrow at larger distances. Not surprisingly, we found the same effects of road surface luminance and arrow size on the discrimination of the arrow direction, as could be expected from existing literature on the detectability of objects. Furthermore, in calculating the size of the road marking arrow, we chose for the plane angle subtended by the length of the road marking arrow in front of the eye. Another option would have been to use the equivalent target size as reported in COST331 for transverse road markings, which is expected to provide slightly larger angular sizes [51].

Having a contrast threshold value that varies with the road surface luminance and the size of the arrow is inconvenient when having to design road lighting concepts. Ideally, designers can make use of a single visibility threshold value, independent of the background and arrow luminance and the size of the latter. This single visibility threshold would allow road lighting designers to determine the minimal level and direction of illumination for detecting the direction of a road marking arrow. Not only the Probeam illumination concept would benefit from such a single visibility threshold; it would also be useful for the optimization of road lighting and car headlights in general. Hence, we evaluated multiple existing visibility measures to check whether they yielded a single contrast threshold value.

In addition to Adrian's model, we applied image-based contrast models to an image cut out around the road marking arrow. We replaced the ΔL values by these contrast values to determine the corresponding visibility threshold of the contrast metric under consideration. Some of these measures resulted in more spread over the different background luminance values, and some measures resulted in more spread over the different angular sizes of the arrow. Our results suggest that the Joulan et al. model allows for the largest reduction in the variation in contrast threshold across different angular sizes of the arrow; however, there is still a substantial variation in contrast threshold across different road surface luminance values. Besides the Joulan et al. model, also the C_c, C_s, and C_{cs} contrast measures of the Tadmor and Tolhurst model show a reduction in variation in contrast threshold across different angular sizes of the arrow and the road surface luminance values. Also, alternatively to the summation used in Eqs. 2.17 and 2.18, taking the maximum or average of all local (S)DoG was examined; however, we consider a summation more appropriate than a maximum or average to account for the effect of size (i.e., the larger the arrow, the larger the sum of DoG values; the smaller the arrow, the smaller the sum of DoG values).

The average C^{RAMM} threshold values seem to indicate a bell-shaped behavior as seen with the contrast sensitivity functions in Barten's research. Though, when considering the confidence intervals, the bell shape of the curves might be an artifact. The large variation in contrast threshold values and the relatively small C_{WLF} values found with the Simone et al. model are most likely due to the fact that we used substantially lower luminance values as they recommended in their paper.

The Tadmor and Tolhurst and Joulan et al. contrast models show promising results for achieving a unique threshold value, irrespective of background luminance, object luminance, and object angular size for the experimental paradigm used in this study. These promising results suggest that image-based contrast models allow predicting contrast thresholds in simulated road environments with a larger complexity, although more research is needed to improve consistency, optimize the parameters, and investigate the applicability of these models to the whole complex scene.

Future research should also include more recent contrast models [50], and extend the analysis towards additional (natural) objects encountered while driving, as suggested in the study by Brémond, Bodard, Dumont, and Nouailles-Mayeur [77]. Furthermore, future work may include the replication of this study with more participants.

2.7 Conclusions

We measured luminance difference thresholds for a rendered highway environment consisting of a road marking arrow in positive contrast to a road surface. Luminance of the arrow and the road surface, as well as the angular size of the arrow, were considered as important parameters. Experimental data of the proportions correct detection of the arrow direction were used to fit a psychometric curve as a function of the difference in luminance between the arrow and the road surface for various experiment conditions. These fits were then used to determine the luminance difference thresholds, and the resulting values corresponded very well (R^2 of 0.75) with thresholds predicted by the Adrian visibility model, with the highest deviations occurring at the smaller angular sizes.

The results suggest that some image-based contrast models allow for a reduction in the variation in contrast threshold across different angular sizes of the arrow and road surface luminance values. As such, these models show promising results, but didn't deliver yet the ultimate solution: a unique threshold value, irrespective of background luminance, luminance difference, and object angular size.

Image-based contrast models also allow predicting contrast thresholds in simulated road environments with a larger complexity, although more research is needed to improve the reliability and to optimize the parameters.

Chapter 3

Road marking contrast threshold for the elderly and the impact of glare

Abstract: As the global population continues to age, with projections indicating that individuals over 60 will comprise 17% of the world's population by 2030, it is crucial to address the disparity between current road lighting guidelines, based on data from healthy young adults, and the needs of elderly drivers. This study examines the impact of age and glare on contrast thresholds for individuals above 60 years old in the context of road lighting and its effect on detecting road marking arrows. Results indicate a large negative effect of age and glare, such that the required luminance difference between the road marking arrow and the background should be increased up to a factor of 2 for elderly compared to young drivers. We also found that measured luminance difference thresholds increased for elderly participants compared to the younger ones. In addition, the results show a poor agreement with Adrian's visibility model which can only be slightly improved by using a different measure for the veiling luminance. Still, given these findings, the current European standard EN13201 should adapt the calculation of the threshold increment to also accommodate the needs for the elderly drivers and warranting safe roadways for the aging population.

Spieringhs, R. M., Smet, K., Cuijpers, R. H., Heynderickx, I., & Hanselaer, P. (2024). Road marking contrast threshold for the elderly and the impact of glare. *Leukos.* https://doi.org/10.1080/15502724.2024.2337385

What follows is the complete and unedited content of this paper.

3.1 Introduction

Traffic and driver safety are obviously related to the luminance contrast between the road surface, on the one hand, and road markings and possible obstacles, on the other hand. To keep visibility of road markings and obstacles – important for lane keeping, anticipating one's trajectory, identification and discrimination - as constant as possible, the road illumination should be uniform as well. In addition, glare of road luminaires and car headlamps may deteriorate the visibility of road markings and obstacles, and hence, should be avoided. The required thresholds for the luminance contrast are lower for younger drivers with normal vision than for elder drivers and drivers suffering from visual impairments, as the visual performance of the latter group deteriorates and their susceptibility to glare increases [31]. Despite the worldwide trend of an aging population – with an ever-increasing number of people over 60 estimated to reach 17% of the world's population by 2030 [78] – the current road lighting guidelines are still designed for a standard 23-years old user [79]. To converge to guidelines and regulations formulated for the population as a whole, including the elderly, it is imperative to investigate road marking contrast thresholds for the latter group, also including the possible negative impact of glare.

The International Commission on Illumination (CIE) recognizes the importance of providing guidance on lighting for the elderly and highlights several visual changes that come with age: reduced accommodation, increased intraocular light scatter, reduced spatial contrast sensitivity, reduced retinal illuminance, and slower dark adaptation. The intraocular light scattering by the crystalline lens is known to increase with age. Proteins in the crystalline lens increase in size and prevalence over time which clouds the lens (known as cataract). Common early complaints of cataract are blurry vision, loss of contrast and color, and halos surrounding bright lights [80]. Various optical factors (i.e., an increase in the density of proteins in the crystalline lens, increased scattering and a decrease in pupil aperture) and neural factors (i.e., a decrease of the quantum efficiency, the photoreceptor density, and the ganglion cell density) contribute to an age-related decline in spatial contrast sensitivity [31, 81]. The two factors that mainly contribute to age-related diminution of retinal illuminance are pupillary (senile) miosis (i.e., reduced pupil size) and the increased spectral absorption of the crystalline lens at shorter wavelengths [31]. Finally, the slower dark adaptation for elderly people is mostly attributed to delayed rhodopsin regeneration [31, 82]. Therefore, elderly individuals require a prolonged photo-stress recovery from a bright light source.

Given the above effects of age on object visibility and the need for lighting guidelines including the elderly, we measured – as a kind of first stepping stone – the luminance contrast thresholds needed to detect the direction of a road marking on a road surface as a function of age, and in addition determined the impact of a glare source in the field of view. Due to Adrian's contrast threshold model being found to be effective in determining thresholds for young people in the context of discriminating road markings [83], we extend this research to elderly and glare conditions and examine the corresponding parameters in Adrian's model. Two experiments were conducted: in one experiment only the older age group was tested for their ability to discriminate the direction of a road marking arrow of different sizes presented on different road surfaces, creating as such various luminance contrasts between arrow and road surface. In the second experiment, a glare source (in this specific case a luminaire) was added to the set-up, and its effect on the visibility thresholds was measured. Both experiments were conducted on a monitor display showing rendered highway scenes, allowing us to have full control on all relevant parameters. Subsequently, we evaluated to what extent current road lighting guidelines and regulations with their fixed age-parameter of 23 years need to be expanded or modified to make them applicable to an aging population as well. Therefore, we first give an overview of how the impact of glare on visibility thresholds is modeled (section 3.2). Later in the paper, we explain the experimental methods used (section 3.3) and describe and discuss the results (section 3.4).

3.2 Modelling Glare

The CIE defines disability glare as "glare that impairs the vision of objects without necessarily causing discomfort" [43]. For road lighting, the effect of disability glare on the visibility of objects is often accounted for by the threshold increment (TI, expressed as a percentage increase in contrast required between an object and its background for the object to be seen equally well with a source of glare present). According to CIE and in the European standard EN 13201 [79, 84], the TI is approximated in terms of the "equivalent veiling luminance" L_v and "background luminance" L_b as:

$$TI(\%) = 65\frac{L_v}{L_b^{0.8}} \tag{3.1}$$

This formula is valid within a background luminance range from 0.05 to 5 cd/m^2. The equivalent veiling luminance is the luminance in object space which produces a retinal illuminance in an ideal eye that is equal to the illuminance generated by the scattering in the non-ideal eye. Its value can be calculated by summing up the contributions of each luminaire in the field of view, starting with the first luminaire that is at or under a viewing angle of 20 degrees and limiting it to glare sources within a distance of 500 m. This results in:

$$L_v = \sum_{i=1}^{n} L_{v,i} \tag{3.2}$$

where $L_{v,i}$ is the equivalent veiling luminance from glare source i. Depending on the glare source angle θ_i, i.e., the angle between the viewing direction towards source i and the horizontal (in degrees), the equivalent veiling luminance is calculated as:

$$L_{v,i,1} = 9.86 \left[1 + \left(\frac{A}{66.4} \right)^4 \right] \frac{E_{gl_i}}{\theta_i^2} \quad (1.5 < \theta_i < 60) \tag{3.3}$$

$$L_{v,i,2} = \left(\frac{10}{\theta_i^3} + \left(\frac{5}{\theta_i^2} \right) \left[1 + \left(\frac{A}{62.5} \right)^4 \right] \right) E_{gl_i} \quad (0.5 < \theta_i < 1.5) \tag{3.4}$$

where E_{gl_i} is the illuminance measured at the eye of source i, and A is the age in years (but used dimensionless). The indices 1 and 2 refer to two ways to calculate the equivalent veiling luminance. It should be noted that both Eqs. 3.3 and 3.4 are practical approximations, describing the effect of intraocular straylight on glare perception. In later years, a complete function [85] that accounts for the primary components of entopic scatter in the human eye has become available but is not used in road lighting standards yet.

The European standard EN 13201 prescribes that disability glare is avoided by limiting TI to between 10% and 30%, where the exact value depends on the geometry of the road, the quality of visual guidance and signaling, the ambient luminance, and the traffic characteristics [79]. In the standard Lv and TI calculation, the age parameter is fixed to 23 years, which makes the limiting values appropriate for this age group but probably insufficient for the older population. As an example, a TI of 15% for a 23-years old person for a lighting class M4 (using Eqs. 3.1 and 3.3 for $L_b = 0.75$ cd/m^2, $\theta_i = 20°$, and $A = 23$ years) leads to 28% for a 65-years old person (using Eqs. 3.1 and 3.3 for $L_b = 0.75$ cd/m^2, $\theta_i = 20°$, $A = 65$ years).

The calculation of the effect of age on glare perception, as given here, only accounts for the averaged increase in eye scattering with age. To really evaluate the size of the effect, it would be better to measure the actual light scattering in eyes of aged individuals. This is possible since Van den Berg introduced in 1986 the direct compensation method [86], which later resulted in the small portable device called the straylight meter (Oculus C-Quant). Currently, this straylight meter consists of an annulus flickering light source that is presented around a test field. This annulus then, as the consequence of intraocular scattering, produces some flicker in the test field; by compensating this flicker with a counterphase flickering light of a certain amount, the amount of straylight can be measured. Since, however, we are most interested in evaluating the road lighting standards, we do not pursue modeling of glare perception based on measured straylight for individuals.

An alternative way to determine the equivalent veiling luminance L_v is formulated in terms of the point spread function (PSF) [87] – here given for a single light source:

$$L_{v,3} = \mathrm{PSF} \cdot E_{gl} \tag{3.5}$$

with PSF = s/θ^2

where s refers to the straylight parameter, and the index 3 refers to a third way of calculating the equivalent veiling luminance. Scattering in the human eye results in a point source not being imaged on the retina as a single point but more spread out. In 1999, researchers Vos and van den Berg, in the CIE report on disability glare, proposed a more complete PSF as the CIE standard glare observer [85]:

$$\begin{aligned}
\mathrm{PSF} =& [1 - 0.08 \cdot (A/70)^4] \cdot \left[\frac{9.2 \cdot 10^6}{[1 + (\theta/0.0046)^2]^{1.5}}\right. \\
&\left.+\frac{1.5 \cdot 10^5}{[1 + (\theta/0.0045)^2]^{1.5}}\right] \\
&+ [1 - 1.6 \cdot (A/70)^4] \cdot \left\{\left[\frac{400}{[1 + (\theta/0.1)^2]^{1.5}} + 3 \cdot 10^{-8} \cdot \theta^2\right]\right. \\
&\left.+ p \cdot \left[\frac{1300}{[1 + (\theta/0.1)^2]^{1.5}} + \frac{0.8}{[1 + (\theta/0.1)^2]^{0.5}}\right]\right\} \\
&+ 2.5 \cdot 10^{-3} \cdot p
\end{aligned} \tag{3.6}$$

It takes age into account through the factor A (i.e., age in years, but used dimensionless) and it includes the pigmentation factor p, which is 0 for very dark eyes, 0.5 for brown eyes, and 1.0 for blue-green Caucasian eyes. The practical applicability of using the complete PSF for determining the TI in the context of road lighting has, to the best of our knowledge, not been explored.

Apart from the effect on glare, age also affects contrast perception through additional deteriorating mechanisms, which should be incorporated. Adrian did so by including an age factor AF in his model for the visibility threshold of targets [23]:

$$\Delta L_{\text{threshold}} = k\left(\frac{\sqrt{\Phi}}{\alpha} + \sqrt{LF}\right)^2 \cdot PF \cdot EF \cdot AF \tag{3.7}$$

where $\Delta L_{\text{threshold}}$ refers to the difference in luminance between the target and background at threshold visibility, Φ to the luminous flux function, α to the angular size of the object in arc minutes, LF to the luminance function (a function related to the background luminance L_b), and k to a constant that is dependent on the experimental conditions. Finally, PF and EF are factors accounting for contrast polarity and exposure time, respectively. Adrian established this model by combining the data from Blackwell (1946) with the contrast threshold data from other studies [24–28]. The resulting model is an attempt to describe deterioration in the human visual system using practical optical parameters and yields a roughly linear relationship. It is worth mentioning, however, that at suprathreshold perception generally behaves non-linear. We recently evaluated Adrian's contrast threshold model and found it valid in experimental conditions relevant for road lighting [83].

The age factor in Adrian's model is determined by the following equations:

$$\text{if } 23y < A < 64y \quad AF = \frac{(A-19)^2}{2160} + 0.99 \tag{3.8}$$

$$\text{if } 64y < A < 75y \quad AF = \frac{(A-56.6)^2}{116.3} + 1.43 \tag{3.9}$$

where A indicates age in years. Disability glare is included through the equivalent veiling luminance (L_v) which is considered as an additional adaptation luminance around the area of the target. This is accounted for by substituting L_b with $L_b + L_v$ when calculating the luminance function. L_v is calculated according to Adrian (1989) [23] as:

$$L_{v,4} = \left((0.0752A - 1.883)^2 + 9.2\right) \sum_{i=1}^{n} \frac{E_{gl_i}}{\theta_i^2} \tag{3.10}$$

Note that in the calculation of L_v, age itself is also a parameter, and the index 4 refers to yet another way of calculating the equivalent veiling luminance.

In this study, the resulting data of the two experiments are used to analyze the effect of multiple ways to calculate the equivalent veiling luminance, and of different ways to account for age-related effects in Adrian's model.

3.3 Method

3.3.1 Experimental Setup

In both experiments (i.e., with and without the presence of a glare source), the basic experimental setup consisted of a calibrated 65-inch Samsung QE65Q90 monitor with a resolution of 3840 x 2160 (4k) pixels. To enable high resolution in the low luminance range, the absolute full-brightness value of the display was reduced. The display's calibration and characterization are crucial since low luminance values and small luminance differences are used. A detailed description of the calibration and characterization of the display using a Bentham TEL301 fiber-connected telescope and an air-cooled Ocean Optics QE65 Pro spectrometer, as well as the stability of the display over time, can be found in a previous publication [83]. This careful calibration resulted in luminance values with a standard deviation of less than 0.15%.

For creating a field of view (FOV) of 42° in the vertical direction and 68° in the horizontal direction, to encompass a large part of the visual field, the participants were seated at a distance of 108 cm centered to the screen. This distance was kept constant by asking the participants to use a chin rest. The whole set-up was put in a fully dark room.

On the display, we rendered test scenes, using Mitsuba [56], of a (typical Dutch) highway, i.e., a road split into two lanes, with some light poles, railings, road surface, and road markings, as illustrated in Fig. 3.1. In both experiments, similar scenes were used. They consisted of a road surface luminance value (i.e., either 0.25, 0.66, or 0.99 cd/m^2, relevant for road lighting [79, 83]) with one arrow pointing either left or right and varying in luminance [83]. The angular size of the arrow was either 5.5, 9.5, or 20.3 arcmin, calculated from the plane angle subtended by the length of the arrow at different distances from the driver (i.e., 80, 60, and 40 m, respectively) as described in more detail by Spieringhs et al. [83].

For the experiment including a glare source, a white power LED was mounted on top of the display at a glare source angle of 20 degrees (between the glare source and the horizontal) and a distance of 1.26 m, mimicking the situation of having a glary luminaire (see Fig. 3.2).

We chose a representative and relevant value for the glare source illuminance at the eye, such that it is considered disturbing (i.e., above 10 lux [88]), and expected to impair vision of objects. The latter means a TI value larger than 15%, calculated according to the EN 13201 (i.e., Eqs. 3.1 and 3.3; for a 23-year old person). For the three road surface luminance values 0.25, 0.66, and 0.99 cd/m^2, this resulted in a TI of 21%, 29%, and 62%, respectively. The resulting E_{gl}, measured with the Gigahertz Optik Optometer P9710, at the eye level is 13 lux (around 10 times larger than the

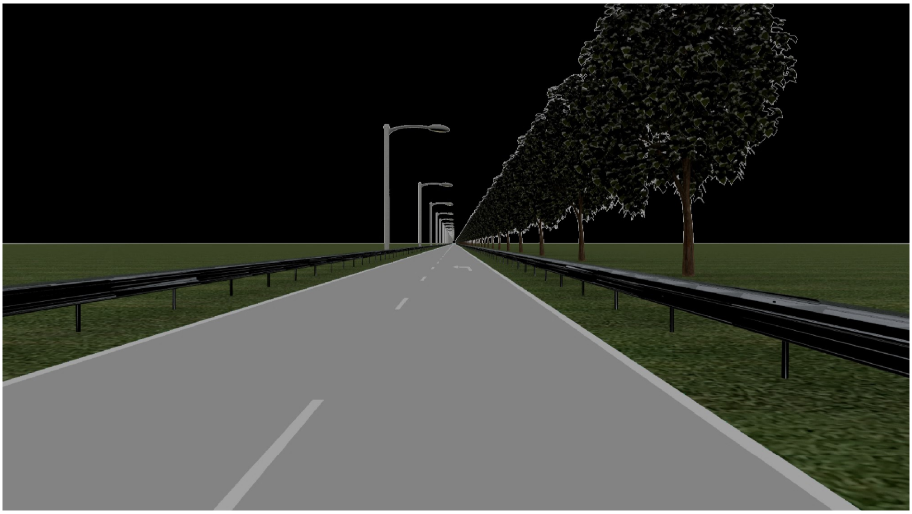

Figure 3.1: A representative highway scene rendered by Mitsuba for a constant environment where the sky, road surface, and road markings are unaltered.

illuminance coming from the display), and the resulting average luminance, measured with the LMK5-5 at the position of the observers' eyes directed to the center of the display and considering only pixel values larger than 500 cd/m^2 within the circle indicated in Fig. 3.3, is 57150 cd/m^2.

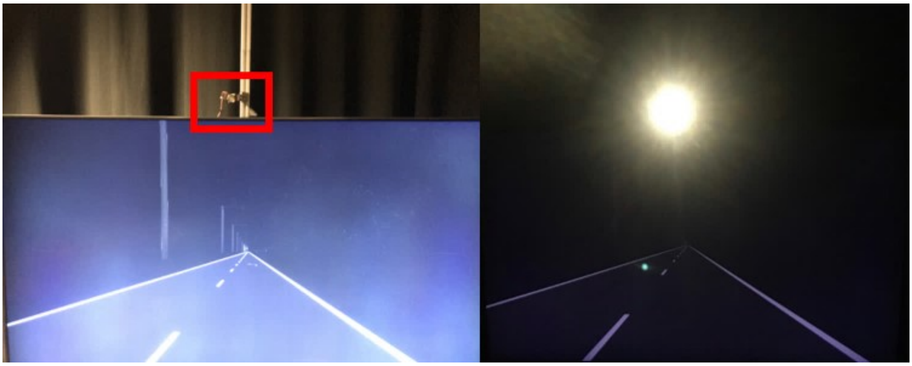

Figure 3.2: Picture of the display and light source with the glare light source switched off (left) and on (right).

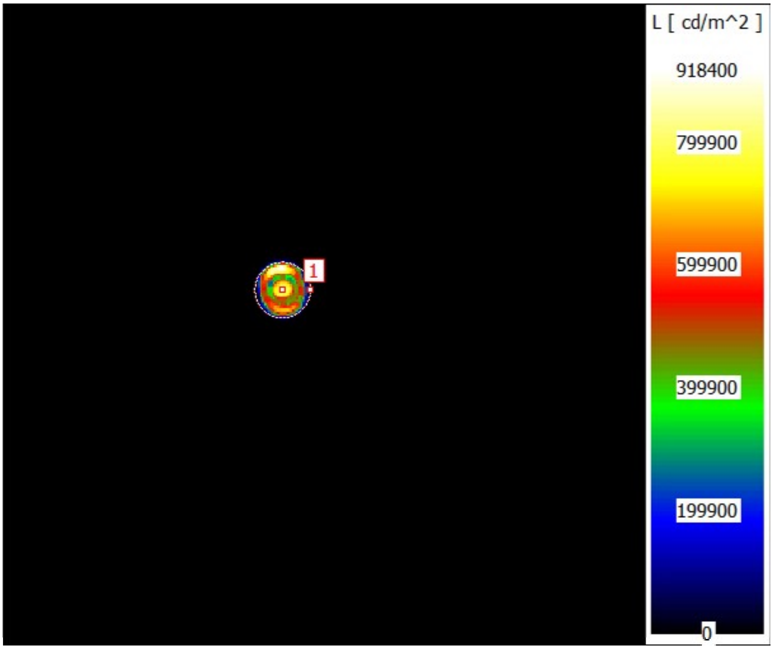

Figure 3.3: Luminance image of the glare light source.

3.3.2 Participants

Participants were recruited among the participant database of the department of Industrial Engineering and Innovation Sciences at the Eindhoven University of Technology. In line with a similar experiment, 18 participants conducted both experiments, yielding a power of over 0.9 when using the effect size of the interaction between arrow angular size and road surface luminance [83]. Of these 18 participants, 5 were female, and 13 were male. The participants were aged from 63 to 79 years old, with an average age of 70.2 years (SD = 4.3); 4 participants were 75 years or older. Three participants reported having visual impairments: one with cataract and two with exotropia (i.e., a misalignment of the eyes).

3.3.3 Visual decimal acuity and straylight test

To check the corrected visual capabilities of these older observers (so with their corrective glasses on where applicable), they participated in the Landolt-C visual decimal acuity test from TNO. They were asked to indicate the direction of the gap in the letter C for different sizes of the letter at a distance of 5 m. Visual acuity data were gathered as they might explain outliers in the data.

The Oculus C-quant [89] was used to accurately measure the amount of straylight in each eye for each individual. The measurement uses an image composed of an annular straylight source, a gray background, and two half circular test fields in the center (Fig. 3.4). One test field is always relatively black (i.e. 1.8 cd/m^2), but seems to flicker in phase with the flickering straylight source due to straylight in the eye. The other test field contains added compensation light that flickers in counterphase with the straylight source. Participants perform a two alternative forced choice task (i.e., which test field flickers more clearly/strongly), while the amount of compensation light in the second test field is changed. When no difference in flicker is observed in the second test field, the luminance ratio between the black test field and the test field with the added compensation light is reported. This test was performed for each eye separately [80].

3.3.4 Experimental task, design, and procedure

The aim of both experiments (i.e., with and without the presence of a glare source) is to measure the visibility threshold between arrow and road surface for nine different conditions, each being a combination of one out of three road luminance values with one out of three angular sizes of the arrow. To measure this visibility threshold, we changed the luminance of the arrow in subsequent trials, and participants were asked to indicate whether the arrow on the road pointed to the left or to the right. In principle

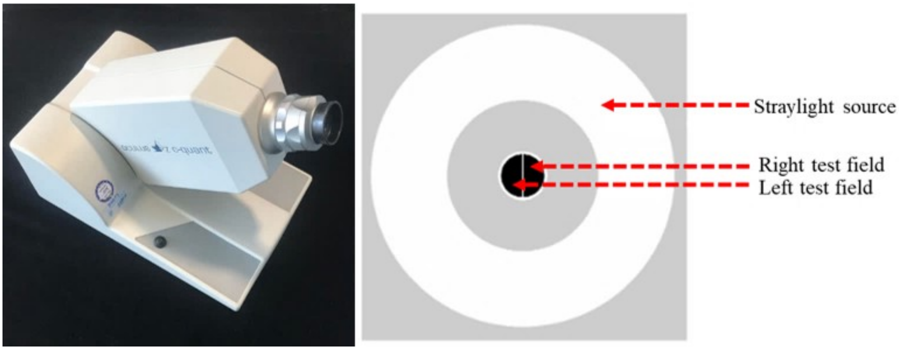

Figure 3.4: (Left) A photograph of the Oculus C-Quant and (right) a picture of the image shown within the Oculus C-Quant with the straylight source at the outer annulus and the right and left half-circle test fields located in the center.

this is a discrimination task but based on the previous research by Spieringhs et al. [83], where Adrian's model was found useful in predicting contrast thresholds for the task of discriminating road marking arrows, we repeated this specific experimental task. The change in arrow luminance for subsequent trials was determined using the QUEST+-method formulated by Watson [90]. It resembles a staircase method in the sense that the luminance of the next trial is affected by the response on the previous trials, but not in the simple way that a correct detection reduces the luminance, while an incorrect detection increases the luminance. The method actually is a Bayesian adaptive testing procedure for estimating simultaneously the threshold, slope (i.e., standard deviation), and lapse rate of the psychometric function (i.e., cumulative Gaussian) from a sequence of psychophysical trials that allows plotting the proportion correct against the luminance of the arrow. The original QUEST method is a variant of maximum likelihood procedures where the underlying theory is that after each response of the participant, the next presented scene is calculated based on maximizing the probability of the current set of responses for the scenes already presented [91].

The starting values for the QUEST+-method are based on prior data obtained with a very similar set-up [83]. Based on these earlier findings, we hypothesized 20 threshold values (or "hypotheses") that were evenly linearly distributed along the range of potential luminance difference threshold values. The range of potential luminance difference threshold values (μ) for each condition is given in Table 3.1. In addition, for the standard deviation of the cumulative Gaussian, we hypothesized 3 values based on our prior data and on the results of a small pilot study with two elderly participants. As expected, one standard deviation of the earlier findings with young participants was not large enough to encapsulate the results of the elderly participants. Therefore, the average standard deviation from the earlier findings was multiplied by 1.25 and 1.5 to get the two additional larger standard deviations for each condition. All three standard deviations per condition are also given in Table 3.1. The adaptive QUEST+ procedure for a given condition started with presenting a random stimulus value, i.e., one of the 20 threshold values within the range given in Table 3.1, with one of the 3 standard deviations. The responses to subsequent trials were used to update the probability of each of the given “hypotheses”, and continued until the entropy of a given threshold and the standard deviation was lower than 3 or if the maximum number of trials of 200 was exceeded.

Table 3.1: Three standard deviations and the range of hypothesized values, for each combination of road surface luminance (in cd/m^2) and angular size of the arrow (in arcmin), as used in experiment 1.

Arrow size (’)	Lroad (cd/m^2)	μ	σ_1	σ_2	σ_3
20.3	0.25	0.25-0.43	0.0142	0.0177	0.0212
9.5	0.25	0.25-0.43	0.0156	0.0195	0.0235
5.5	0.25	0.25-0.43	0.0321	0.0401	0.0481
20.3	0.66	0.66-0.99	0.0295	0.0369	0.0442
9.5	0.66	0.66-0.99	0.0326	0.0407	0.0489
5.5	0.66	0.66-0.99	0.0654	0.0817	0.0981
20.3	0.99	0.99-1.41	0.0485	0.0606	0.0727
9.5	0.99	0.99-1.41	0.0529	0.0662	0.0794
5.5	0.99	0.99-1.41	0.0566	0.0707	0.0849

The design of the experiment was a full-factorial within-subject design with the luminance of the road surface (i.e., 3 levels: 0.25, 0.66, and 0.99 cd/m^2), the arrow’s angular size (i.e., 3 levels: 20.3, 9.5, and 5.5 arcmin), and the equivalent veiling luminance (i.e., 2 levels, 0 and 0.29 cd/m^2, with and without glare source respectively) as independent variables, and the luminance difference thresholds between arrow and road surface as the dependent variable.

The experimental procedure started with the Landolt-C visual acuity test and the measurement of the straylight factor s for each eye with the Oculus C-Quant following the procedure described in Appendix F ’Practical guide for the C-Quant’ [80]. After completing the visual acuity and Oculus C-Quant test, the contrast threshold experiment (with and without glare source) started using the experimental setup as described in section 2.1 [83].

Before starting the contrast threshold measurement, an introduction was given to the participants, followed by a few practice trials and an opportunity to ask questions. Then, they were asked to adapt to a gray image (0.31 cd/m^2) for two minutes. After that, we displayed the first trial for 3 seconds, followed by the full gray adaptation image for 3 seconds. In each trial, the participants were asked to indicate the direction of the arrow using a keyboard arrow key. If no arrow was observed, the participants could abstain from responding. All trials – intermingled for the nine different conditions per experiment – were presented in random order. All participants first performed the experiment without glare source, and then the experiment with glare source. In the latter experiment, participants were instructed to avoid direct eye contact with the glare source and not to squint or frown. The total experimental procedure took about 60 minutes to finish. During the experiments, participants were allowed to have a break in case they felt fatigued.

3.4 Results and Discussion

3.4.1 General Analysis of the Experiments

3.4.1.1 Oculus C-Quant

The results of the Oculus C-Quant indicate an increasing relationship between the average logarithmic straylight value $\log(s)$ of both eyes and age in years, as shown in Fig. 3.5. There was only one outlier (indicated by the blue x in Fig. 3.5) which was, as expected, the participant who reported to have cataract. The participant with cataract is expected to be more susceptible to disability glare [80].

3.4.1.2 Exposure Time

During the pilot study, it became apparent that some participants needed a longer exposure time than the 2 seconds we used in our previous study [83]. As a result, the exposure time in this study was set at 3 s, but in addition to the response, we also recorded the response time. The average response time of the participants in this study was 1.87 s with a standard deviation of 0.50 s.

The factor for exposure time using Adrian's model (EF in Eq. 3.7) was, for the lowest arrow angular size and luminance background (worst case scenario), 1.08 for a 2 seconds exposure time and 1.05 for a 3 seconds exposure time, indicating only a minor

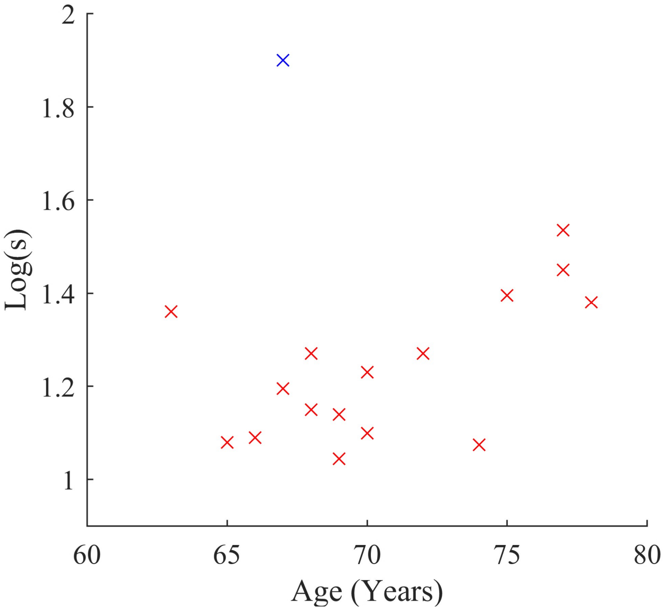

Figure 3.5: The logarithm of the straylight parameter of the Oculus C-Quant plotted against age in years. The blue cross indicates the straylight parameter of the participant diagnosed with cataract.

difference. In all other conditions, EF was even closer to 1, and compared to the age factor – in the range of 3 to 4 – close to negligible.

3.4.1.3 Contrast Thresholds

The QUEST+ procedure started for each of the 9 conditions separately and stopped when participants reached an entropy of 3 for which the luminance difference threshold value was recorded. On average, participants spent 21.4 trials on each condition. Participants provided on average a left-response in 45% of the trials and a right-response in 46% of the trials; in the remaining 9% of the trials, participants did not respond in time, and a value of 0.5 proportion correct (i.e., the guessing average) was recorded. Participants responded correctly to the direction of the arrow in 78% of the trials.

To determine and compare the inter-observer variability, the standard residual sum of squares (STRESS), as defined by Garcia et al. [69], was computed for each road surface luminance separately (i.e., 18 observers). The STRESS values for the road surface luminance of 0.25, 0.66, and 0.99 cd/m^2 were 18%, 19%, and 15% for the experiment without glare source, and 16%, 16%, and 13% for the experiment with glare source, respectively. According to the research on multidimensional scaling, these STRESS scores would be regarded as being in the range of poor (20%) to fair (10%) [69, 70]. In a similar experiment with young observers [83], lower inter-variability STRESS scores of 11%, 10%, and 5% for the road surface luminance of 0.25, 0.66, and 0.99 cd/m^2, respectively, were reported. The larger variability in the data for elder observers may be due to the larger impact of age on (corrected) vision above 60 years than around 27 years of age.

When excluding the participants with a visual impairment, the inter-observer STRESS values were only 2% lower at maximum, which motivates our decision to include their results in the analysis.

Comparison of Contrast Thresholds with and without Glare

The average luminance difference thresholds of each condition for the experiment without glare source (horizontal axis) are plotted against their counterpart with glare source (vertical axis) including their corresponding confidence intervals in Fig. 3.6. In addition, in Fig. 3.7, the average luminance difference thresholds are plotted against the object angular size for the experiment with and without glare source separately.

In Fig. 3.6, the thresholds for old observers in most conditions including a glare source are higher than the ones measured without; as a result, they are above the black line, especially for the conditions with a lower background luminance (i.e., 0.25 cd/m^2). This suggests that glare affects the luminance difference thresholds. To confirm the statistical significance of the increase in luminance difference threshold with glare for an elderly population, we performed a repeated-measures full factorial ANOVA with the road surface luminance, glare, and arrow angular size as independent factors (including also their interaction) and with the measured luminance difference threshold as a dependent factor. Prior to further analysis, the assumptions of homogeneity of variance and sphericity were checked. The sphericity hypothesis according to Mauchly's test across all conditions was rejected ($p < .001$); therefore, a Greenhouse-Geisser correction was used. Subsequently, the analysis revealed a statistically significant main effect for the angular size of the arrow ($F(17,1) = 129.50, p < .001, \eta^2 = .88$), for the road surface luminance ($F(17,1) = 158.59, p < .001, \eta^2 = .90$), and for glare ($F(17,1) = 75.33, p < .001, \eta^2 = .82$). Furthermore, it revealed a significant interaction between arrow angular size and road surface luminance ($F(17,1) = 160.54, p < .001, \eta^2 = .90$), between arrow angular size and glare ($F(17,1) = 77.94, p < .001, \eta^2 = .82$), between road surface luminance and glare ($F(17,1) = 99.50, p < .001, \eta^2 = .85$), and between arrow angular size, glare, and road surface luminance ($F(17,1) = 108.35, p < .001, \eta^2 = .86$). This indicates that there is an effect of glare, however, also that this effect of glare depends on both angular size of the arrow and on the road surface luminance.

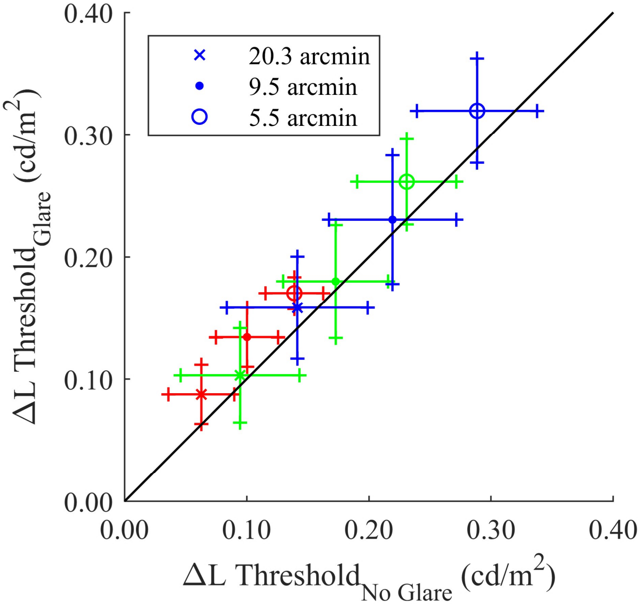

Figure 3.6: Experimental threshold data with glare source plotted against the measured data without glare source. The black line indicates a 1:1 ratio. The road surface luminance values are separated by color: red = 0.25 cd/m^2, green = 0.66 cd/m^2, and blue = 0.99 cd/m^2. The different symbols indicate the different object angular sizes (i.e., 5.5, 9.5, and 20.3 arcmin) as indicated in the legend.

Comparison of the Contrast Thresholds Between a Younger and Older Population

As mentioned earlier, the recorded exposure times show that the majority of elderly participants responded within 2 s, therefore we still can compare our current results with those of our previous study with young participants (Spieringhs et al. 2022) [83]. Besides the difference in exposure time, we also used a different method in our previous study (i.e., method of constant stimuli then vs. QUEST+ now), but both methods yield a luminance difference threshold value. The luminance difference thresholds of the previous study (i.e., young), are plotted against the luminance difference thresholds of the current study (i.e., old and without glare) in Fig. 3.8. It indicates, as expected, an effect of age with an almost perfect linear relationship (i.e., red line with a slope of 0.54 and intercept of -0.027, and a goodness of fit (R^2) of 0.99) over all conditions between the younger and older age group.

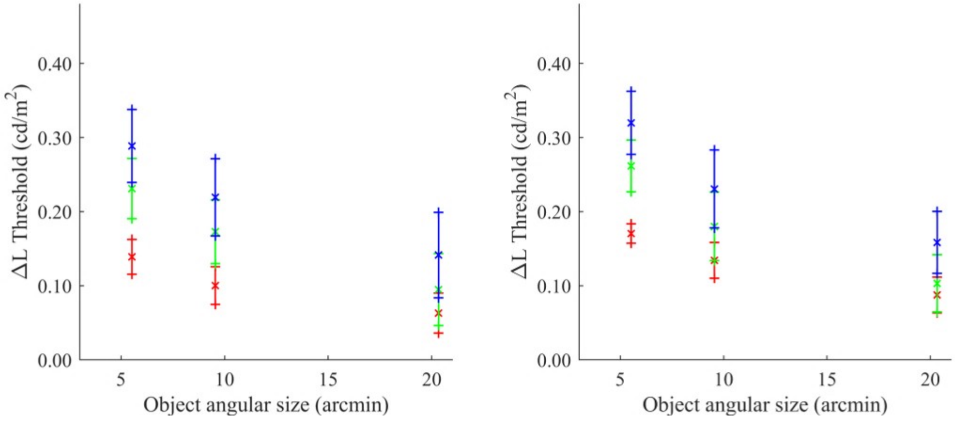

Figure 3.7: Experimental threshold data of the experiment without (left) and with (right) glare source plotted as a function of arrow angular size for different road surface luminance values (separated by color). The means of the measured thresholds per condition are indicated by crosses, and at each cross, the corresponding 95% confidence interval is shown.

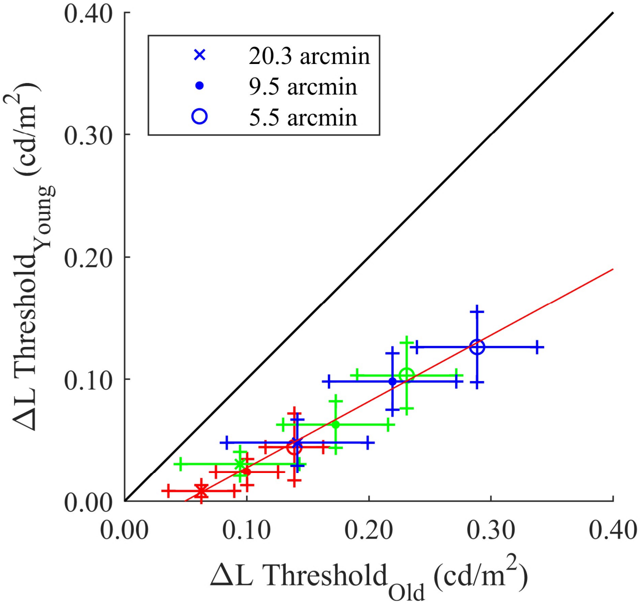

Figure 3.8: The luminance difference thresholds from the previous study (i.e., young; Spieringhs et al., 2022) [83] plotted against the thresholds from the current study (i.e., old). The black line indicates a 1:1 ratio. The road surface luminance values are separated by color: red = 0.25 cd/m^2, green = 0.66 cd/m^2, and blue = 0.99 cd/m^2. The different symbols indicate the different object angular sizes (i.e., 5.5, 9.5, and 20.3 arcmin) as indicated in the legend.

3.4.1.4 Visual Decimal Acuity

The visual decimal acuities reported from the Landolt-C test range between 1.5 and 0.5, with a median value of 0.8, and the 25% and 75% quartiles at 0.8 and 1.25, respectively. For reference, the smallest object angular size in the experiment of 5.5 arcmin results in an acuity of 1/5.5 and is lower than the lowest visual acuity measured with the Landolt-C test (i.e., 0.5). Therefore, it is expected that all participants were able to discriminate the arrow if presented in sufficiently high contrast. Fig. 3.9 shows, per condition, the individually measured luminance difference thresholds as a function of the participant's visual acuity. These graphs seem to show a general negative correlation between visual acuity and the luminance difference threshold, which is stronger in some conditions compared to others, as indicated in table 3.2.

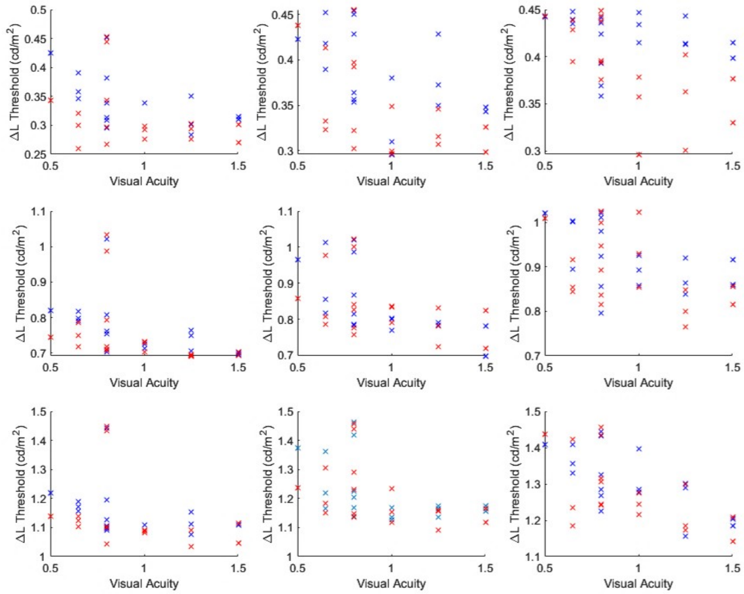

Figure 3.9: Experimental threshold data without glare source in blue and with glare source in red plotted against the visual acuity for each condition in a separate graph: road surface luminance is 0.25, 0.66, and 0.99 cd/m^2 from top to bottom, and object angular size is 20.3, 9.5, and 5.5 arcmin from left to right.

Table 3.2: The correlation coefficients between visual acuity and luminance difference thresholds for each condition of road surface luminance, glare, and object angular size.

Road surface luminance (cd/m^2)	Glare	Object angular size (arcmin)		
		20.3	9.5	5.5
0.25	Present	-0.30	-0.55	-0.64
0.66	Present	-0.36	-0.43	-0.47
0.99	Present	-0.30	-0.44	-0.59
0.25	Absent	-0.53	-0.47	-0.18
0.66	Absent	-0.48	-0.64	-0.50
0.99	Absent	-0.37	-0.50	-0.68

3.4.2 Applicability of the Adrian Model

3.4.2.1 Without Glare Source

Using the experimentally measured luminance difference threshold values, we calculated the mean value over all observers that meet Adrian's criteria (i.e., participants younger than 75 and not diagnosed with a visual impairment, N=11) per road surface luminance and arrow angular size, and compared them against the values predicted by the visibility model of Adrian (Eq. 3.7). The results are shown in the left part of Fig. 3.10, with the solid lines indicating the predicted luminance difference threshold values by Adrian's model as a function of road surface luminance for different angular sizes and using the average age, while the experimental data are shown by the crosses and their 95% confidence interval. Generally, the predictions of Adrian's model are not that far from the reported mean values; however, for some conditions, Adrian's prediction is outside the experimental confidence interval. There is a general trend of a slight underestimation of luminance difference thresholds for arrows with an angular size of 9.5 and 20.3 arcmin, as well as an overestimation of thresholds for arrows with an angular size of 5.5 arcmin.

A scatter plot in Fig. 3.10 (right) shows the overall correspondence of the experimental data per condition and participant with Adrian's model using the corresponding age of each participant, the road surface luminance and angular size per condition, and an exposure time of 3 s. The solid black line would indicate perfect correspondence between the experimental data and Adrian's model. The goodness of fit for the standard model parameter k of 2.6 (Adrian 1989; Spieringhs et al. 2022) [23, 83] is 0.30, while it is 0.39 for the best linear fit, indicating only a moderate fit to the data in both cases. Causes for the huge variance and for the deviation in best fit of Adrian's model are not clear at this point, but may need an expansion of the model to higher ranges of ages or by including other than optical visual effects. In addition, the cognitive task of choosing the direction of the arrow (i.e., discrimination task) needs the processing of spatial details which was not the case in the experiments used in Adrian's model (i.e., detection task).

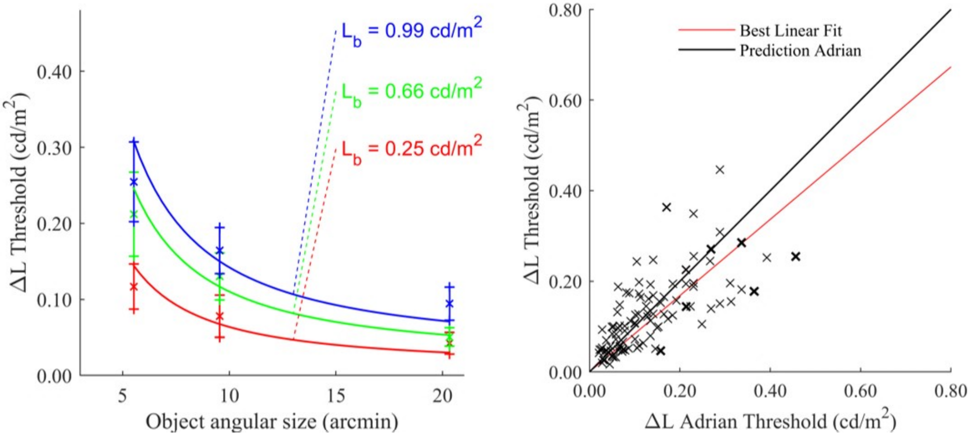

Figure 3.10: (left) Experimental threshold data of the experiment without glare source plotted as a function of arrow angular size for different road surface luminance values (separated by color). The means of the measured thresholds per condition are indicated by crosses, and at each cross, the corresponding 95% confidence interval is shown. Solid lines indicate the prediction by Adrian's model using the mean age. (right) Experimental threshold data of the experiment without glare source plotted against the thresholds predicted by the visibility model of Adrian (black line). Crosses indicate the observed threshold for each participant and condition. The red line gives the best fit for an optimized model parameter k of 2.6.

In addition, further investigation revealed that participants diagnosed with visual impairments (i.e., N=3) exhibited higher measured luminance difference thresholds than the general population that meets Adrian's criteria (i.e., participants younger than 75 with no visual impairments; Fig. 3.11). Indeed, a literature search indicates that patients with cataract or exotropia show reduced contrast sensitivity and, therefore, should be treated separately (Kwon and Lee 2020) [92].

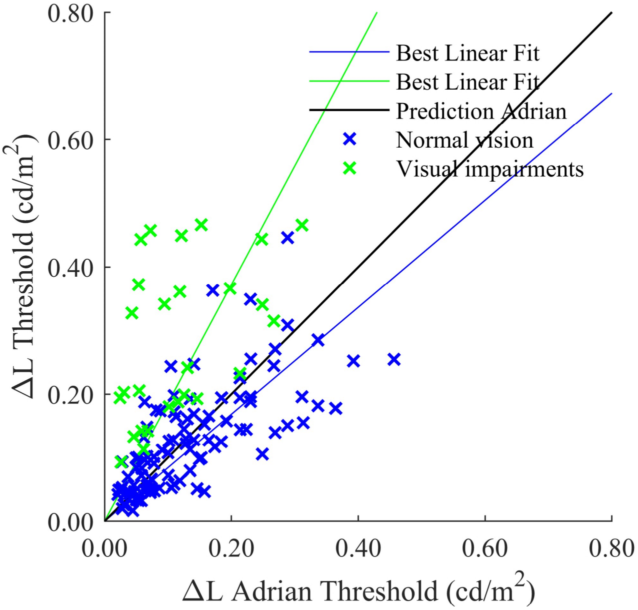

Figure 3.11: Experimental threshold data without glare source plotted against the thresholds predicted by the visibility model of Adrian (black line). The measured threshold for each person and condition is indicated by a cross. The blue crosses indicate all participants that meet Adrian's criteria, whereas the green crosses indicate the participants diagnosed with a visual impairment. The green (slope: 1.86) and blue (slope: 0.84) solid lines indicate the best linear fit to the corresponding measured data.

In addition, Fig. 3.12 looks more specifically at the effect of age by separating – in line with Adrian's age criterion – the group of observers under 75 (indicated by blue crosses, N=11) with the group of participants older than 75 (indicated by green crosses, N=4). The visually impaired persons are excluded from both groups. The younger group appears to follow Adrian's model (black line) reasonably closely; the best linear fit for this group has a coefficient of determination (R^2) of 0.51, whereas the standard prediction from Adrian (black line) for this group provides a poor fit with an R^2 of -2.77 (i.e., a negative value because the sum of squares around the black line is larger than the sum of squares around the best-fitted line). The observers older than 75 years seem to require a significantly lower threshold than predicted by Adrian, which suggests that the age parameter saturates at higher ages (i.e., beyond 75 years) and that the correction to the luminance difference threshold should be lower than what the extrapolation of Adrian's age parameter provides.

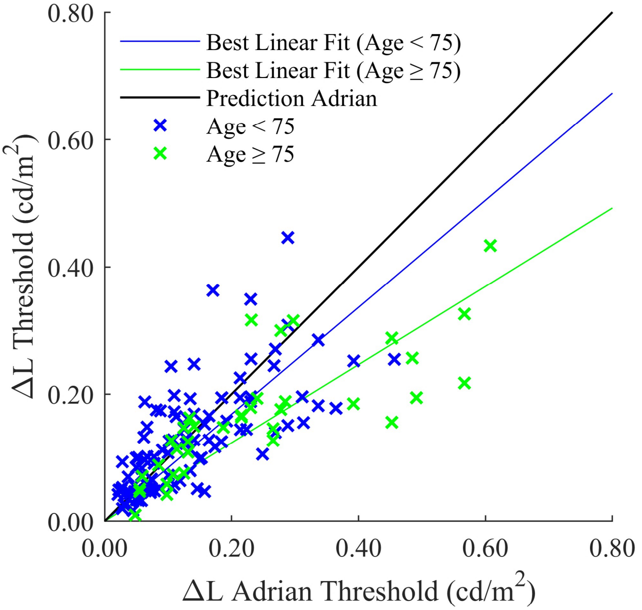

Figure 3.12: Experimental threshold data without glare source plotted against the thresholds predicted by the visibility model of Adrian (black line). The observed threshold for each person and condition is indicated by a cross. The blue crosses indicate all participants younger than 75 years old, and the green crosses indicate all participants older or equal to 75 years old. The visually impaired are excluded from both groups. The green (slope: 0.62) and blue (slope: 0.84) solid lines indicate the best linear fit to the corresponding measured data.

3.4.2.2 With Glare Source

The luminance difference threshold values were experimentally measured with a glare source present, and mean values over all participants (along with their respective confidence intervals) that meet Adrian's criteria (i.e., participants younger than 75 and not diagnosed with a visual impairment) were calculated per road surface luminance and arrow angular size, and compared to the predicted values from Adrian's model (using the standard calculation of $L_{v,4}$ for the veiling luminance given in Eq. 3.10). The solid lines in Fig. 3.13 (left) indicate the predicted luminance difference threshold by Adrian's model as a function of road surface luminance and angular size, while the mean of the experimental data is represented by the crosses. Adrian's model significantly underestimates the thresholds at an object angular size of 20.3 arcmin and overestimates luminance difference thresholds at an object angular size of 5.5

arcmin.

In Fig. 3.13 (right), a scatter plot illustrates the overall correspondence between our experimental data with glare source for participants that meet Adrian's criteria and Adrian's model (for Adrian's standard calculation of $L_{v,4}$ following Eq. 3.10). The solid black line indicates perfect correspondence assuming for the model a visibility level of 1 and the standard model parameter k of 2.6. The R^2 for the standard model parameter and the best linear fit were -0.14 and 0.11, indicating a relatively poor fit to the data.

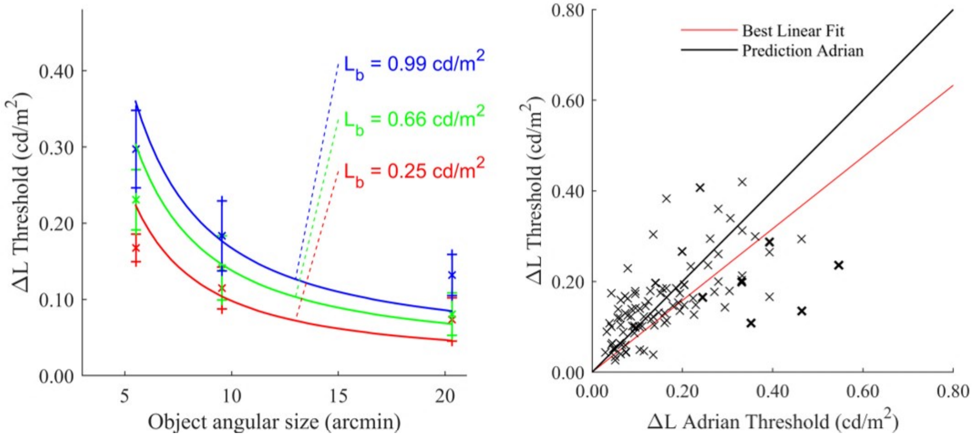

Figure 3.13: (left) Experimental threshold data of the experiment with glare source plotted as a function of arrow angular size for different road surface luminance values (separated by color). (right) Experimental threshold data, of the participants that meet Adrian's criteria, of the experiment with glare source plotted against the thresholds predicted by the visibility model of Adrian (black line).

In Fig. 3.14 (left) again we can observe a similar behavior as before in Fig. 3.11, where the participants diagnosed with a visual impairment (indicated in green, N=3) require a larger luminance difference, compared to the participants that meet Adrian's criteria (indicated in blue, N=11), for the arrow to be visible. In Fig. 3.14 (right) again Adrian's prediction underestimates the luminance difference threshold for participants 75 years or older (N=4) as indicated in green.

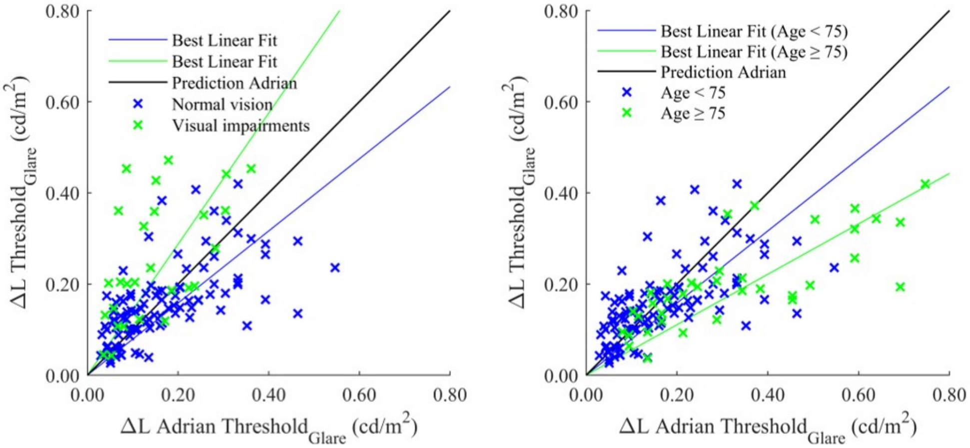

Figure 3.14: Experimental threshold data with glare source plotted against the thresholds predicted by the visibility model of Adrian (black line), similar to Figs. 3.11 and 3.12 for left and right respectively. The observed threshold for each person and condition is indicated by crosses. The green crosses indicate (left) the visually impaired participants and (right) the participants older than 75, and the blue crosses (left and right) indicate the participants that meet Adrian's criteria. The green (slopes: (left) 1.44 and (right) 0.55) and blue (slope: 0.79) solid lines indicate the best linear fit to the corresponding measured data.

3.4.2.3 Impact of Veiling Luminance Calculation (with Glare Source)

So far, Eq. 3.10 was used to calculate the equivalent veiling luminance that, together with the luminance background, results in the adaptive background luminance taken as input to Adrian's model in Eq. 3.7. However, as previously discussed, other formulae are available to estimate equivalent veiling luminance. In addition, the straylight parameter, measured with the Oculus C-Quant, can also be converted directly into the PSF and used to calculate equivalent veiling luminance.

To determine the best way to calculate the veiling luminance, we compared the overall correspondence between the experimental data measured with a glare source and Adrian's model using Eqs. 3.3, 3.5, and 3.10, or the measured straylight parameter for the veiling luminance. Table 3.3 gives, in each cell, the coefficient of determination R^2 when comparing the experimental data with Adrian's model (using parameter k of 2.6 and one of the methods to determine the veiling luminance), and within brackets, the R^2 of the best linear fit through the same data. Generally, Adrian's prediction of the measured luminance difference thresholds (for participants < 75 years and without visual impairment) is poor (with R^2-values < 0). The R^2-values are higher for the best linear fit through the data, ranging from 0.10 (Eq. 3.3) to 0.21 (measured straylight parameter).

Table 3.3: Coefficient of determination R^2 for comparing our experimental data (limited to the participants that meet Adrian's criteria, N=11) with Adrian's model (using parameter k of 2.6) for different calculations of the veiling luminance. The R^2 of the best linear fit through the data of the same group of participants is added between brackets.

	Adrian's Standard Model (Eq. 3.10)	EN 13201 (Eq. 3.3)	PSF (Eq. 3.5)	Measured Straylight Parameter
Age ≤ 75 and No Visual Impairment	-0.14 (0.11)	-0.71 (0.10)	-0.37 (0.11)	-0.20 (0.21)

A large amount of variance remains unexplained when using any of the four veiling luminance calculations for Adrian's model with parameter k of 2.6. More variance is explained when using the best linear fit. Thus, Adrian's standard model parameters should be adjusted and extended to improve the accuracy of Adrian's model for our dataset. Ideally, in predicting the luminance difference threshold for the group that meets Adrian's criteria, the straylight parameter should be directly measured, with, for example, the Oculus C-Quant, as this will explain some of the variance.

3.5 Conclusion

This study measured the luminance difference thresholds, needed to detect the direction of road marking arrows on a road surface, with an elderly participant group in the presence and absence of a glare light source. The road marking arrow had different angular sizes and was simulated on a road surface with various relatively low luminance values. Participants, repeatedly, had to indicate the direction of the arrow on the road, and the luminance difference threshold was determined by changing the luminance of the arrow using the QUEST+ method. The results indicate an interaction effect between arrow angular size, road surface luminance, and glare. On average, the luminance difference thresholds were always higher in the presence of a glare source than without a glare source, with a difference of up to 20%. As expected, this difference was largest at the lowest road surface luminance: an equivalent veiling luminance of the glare source of 0.29 cd/m^2 has indeed the largest effect when the road surface luminance is lowest. In addition, comparing our current results with our previous results (Spieringhs et al. 2022) [83] measured with young participants, we observed an effect of age, indicating that, not surprisingly, older participants have higher luminance difference thresholds than younger participants, with an increase of up to 100%. As mentioned in the introduction, the current road lighting standards assume a 23-year old observer; however, based on the significant differences found in this study, and the aging society we are facing, these standards should be revisited to include needs for elderly drivers as well.

The luminance difference thresholds of both experiments (i.e., glare and no glare source) were compared to the thresholds predicted by Adrian's model. In both cases, Adrian's standard model (i.e., k of 2.6) provided a moderate to poor fit to the measured thresholds (i.e., $R^2 < 0.40$). When using the best linear fit, instead of the standard model parameter k, some of the variances were reduced; however, it still resulted in at best a moderate fit to our dataset. In addition, we found that Adrian's model cannot simply be extrapolated to participants older than 75 years and needs adaptation of the age factor AF for this participant group. Our results seem to imply that the change of luminance difference threshold with age saturates at higher ages, since the simple extrapolation in Adrian's model provides luminance difference thresholds that are higher than our experimental data. Moreover, our study also seems to recommend an additional multiplicative factor in Adrian's model for visually impaired elderly.

Besides the standard Adrian's model, we also extended the analysis with different equations and with the measured straylight parameter to calculate the veiling luminance, caused by the glare source. Using the best linear fit, the R^2 can be improved when using Adrian's model with the complete point spread function of the CIE standard glare observer or the measured straylight parameter to calculate the veiling luminance (for the group of participants that meet Adrian's criteria) (i.e., R^2

of 0.11 and 0.21). Surprisingly, when using the formulae mentioned in EN 13201 to calculate the veiling luminance, using the best linear fit, the R^2 didn't improve (i.e., from 0.11 to 0.10).

All in all, a large negative effect of age and glare, and increased variances between participants are observed when comparing the measured luminance difference thresholds between younger and elderly participants. The results indicate an overestimation by Adrian's model for the age group above 75 years old. As such, this study suggests a possible saturation of the age factor in Adrian's model for these ages and the possible implementation of the complete point spread function in calculating the equivalent veiling luminance or using a measured straylight parameter. Given these results, the current European standard EN13201 may benefit from adjusting the recommended age in calculating the TI from 23 to 75 and exchanging Eqs. 3.3 and 3.4 with the complete point spread function in limiting disability glare of road lighting for the elderly.

Chapter 4

A road marking BRDF model applicable for a wide range of incident illumination conditions

Abstract: To drive safely and comfortably, an adequate contrast between the road surface and road markings is needed. This contrast can be improved by using optimized road illumination designs and luminaires with dedicated luminous intensity distributions, taking advantage of the (retro)reflective characteristics of the road surface and road markings. Since little is known about road markings' (retro)reflective characteristics for the incident and viewing angles relevant for street luminaires, BRDF-values of some retroreflective materials are measured for a wide range of illumination and viewing angles using a luminance camera in a commercial near-field goniophotometer setup. The experimental data are fitted to a new and optimized "RetroPhong" model, which shows good agreement with the data ($RMSE < 0.13$, $NRMSE < 0.04$, and $NCC > 0.8$). The RetroPhong model is benchmarked with other relevant (retro)reflective BRDF models, and the results suggest that the RetroPhong model is most suitable for the current set of samples and measurement conditions.

Spieringhs, R. M., Audenaert, J., Smet, K., Heynderickx, I., & Hanselaer, P. (2023). Road marking BRDF model applicable for a wide range of incident illumination conditions. *JOSA A*, 40(3), 590-601. https://doi.org/10.1364/JOSAA.470968

What follows is the complete and unedited content of this paper.

4.1 Introduction

Retroreflective materials have the property that they also reflect light in directions close to the incident light direction. For this reason, retroreflective materials are intensively used in road signaling to increase safety while driving at night time when car headlamps are the main illumination source. Both vertically oriented road signs and horizontal road markings make use of these retroreflective properties for improving road signalization, while retroreflective textiles and strips improve the visibility of pedestrians and cyclists. Retroreflective properties of materials are created by adding glass beads in the substrate, such as in road markings and textiles, or by using prismatic foils (as used in road signals) [93]. The retroreflective behavior is due to specular reflection, refraction, and total internal reflection.

Because good visibility of objects and signs is crucial to prevent accidents and to guide traffic, controlling and improving the retroreflective properties of materials in different weather conditions is an important objective for material manufacturers. Currently, the requirements for the optical characteristics of retroreflective materials are formulated in dedicated standards and documents, namely CIE 54.2 [39] and EN1436 [37] for road markings, CIE 74 [35] and EN12899 [36] for road signs, and EN20471 [94] for high visibility clothing. These standards specify the retroreflective properties for dedicated directions of illumination and viewing, in terms of the coefficient of retroreflection R_A and coefficient of retroreflected luminance R_l, which are defined as the quotient of the luminous intensity reflected by the material in the standardized angular direction and the surface illuminance multiplied by its area, and the quotient of the luminous intensity reflected by the material in the standardized angular direction and the surface illuminance multiplied by its projected area respectively.

Currently, these retroreflective materials are optimized under the assumption that only car headlights interact with these materials, limiting the range of the incident angles of the illumination. Traditional road lighting is not designed to contribute to the retroreflection of these materials. However, a road lighting concept called "Probeam" [44, 46] shows promising advantages over other, more common, road lighting concepts such as symmetrical road lighting. With Probeam, luminaires direct most of their luminous flux forwards parallel to the driving direction; as such, their light contribution might become relevant at distances beyond the reach of car headlights. Consequently, the range of incident and viewing angles with respect to the retroreflective materials becomes quite different from the range of angles involved when only car headlights are taken into consideration. Unfortunately, the retroreflective characteristics of road markings and signals are not available for this extended range of incident angles. This lack of data hampers a qualitative and quantitative analysis of alternative lighting concepts, and makes it impossible to make accurate renderings of the scene as observed by the driver.

In general, the reflection properties of a material for different viewing angles and different angles of incident of the light are described by the "Bidirectional Reflectance Distribution Function", or shortly BRDF [95]. Typically, a photometric BRDF is determined as the ratio between the elementary luminance in a particular viewing angle (dL) and the elementary illuminance measured on a surface of the material from a particular incident direction (dE). Mathematically the BRDF is defined as follows:

$$f_r(\theta_i, \phi_i, \theta_o, \phi_o) = \frac{dL(\theta_o, \phi_o)}{dE(\theta_i, \phi_i)} \tag{4.1}$$

where f_r represents the BRDF in sr^{-1}, θ_i is the polar angle of incidence, ϕ_i is the azimuth angle of incidence, θ_o is the polar angle of viewing, ϕ_o is the azimuth angle of viewing (with all angles expressed in degrees), L is the luminance, and E is the illuminance. The polar coordinate is defined towards the external normal of the sample, while the azimuthal coordinate is defined towards a two-dimensional coordinate system within the sample surface. BRDF is a function used to provide a complete indication of the reflection characteristics of a material. For special applications, such as the description of the retroreflectivity of a material at standardized angles, secondary quantities such as R_A and R_l are used.

To determine a complete BRDF dataset experimentally is quite time-consuming due to its four-dimensional nature. One way of handling this huge amount of data is to fit the data to a suitable analytical model, of which its parameters are optimized to the data. These models are also necessary to import material characteristics in physically based renderers (PBRs) [96]. Several analytical BRDF models can be found in literature [97], but there is a lack of BRDF models including retroreflection. Belcour et al. [96] suggested a set of updated and improved parametric BRDF models (i.e., updated Blinn, updated Beckmann, updated ABC distribution, and the Lafortune model) that include retroreflection. They measured gray, yellow, and orange retroreflective tape, typically used in safety jackets, for a few incident angles (i.e., $\theta_i = 15°, 30°, 60°$) and many viewing angles. However, these updated and improved parametric BRDF models have not yet been applied to glass bead-based retroreflective road markings.

In this study, first, BRDF-values of retroreflective road markings are derived from measurements at multiple incident and viewing angles more relevant to road lighting (i.e., luminaires), and different from the traditional incident and viewing angles mentioned in CIE 54.2 [39] for road lighting by car headlights (i.e., $\theta_i, \phi_i, \theta_o$, and ϕ_o are $88.8°, 0°, 87.7°$, and $0°$ respectively). These measurements, thereafter, are used to develop a new retroreflective BRDF model. The developed model is then benchmarked against existing parametric retroreflective BRDF models. The new BRDF model can lead to new insights into the visibility of retroreflective road markings at a broader range of incident angles and can lead to a more qualitative and quantitative analysis of new road lighting designs such as Probeam, which make optimal use of these retroreflective characteristics.

4.2 BRDF models

This section gives a short overview of various existing BRDF models that are used later in this paper to fit our experimental data.

4.2.1 Classic Phong model

The classic Phong model is one of the most well-known and popular BRDF models used in computer graphics because of its simplicity and relatively low computational cost. The classic Phong model is categorized as an empirical BRDF model that does not account for energy conservation and reciprocity. The model contains an exponential parameter n for the 'shininess' of the material (i.e., a large n generally indicates a large specular highlight), a parameter for the diffuse reflection k_d, and a parameter for the specular reflection k_s:

$$f_r(\theta_i, \varphi_i, \theta_o, \varphi_o) = \frac{k_d}{\pi} + k_s\,(\mathbf{i_s} \cdot \mathbf{o})^n \tag{4.2}$$

where $\mathbf{i_s}$ is the specular reflection unit vector in the direction of $\varphi_i + \pi$, and $\mathbf{o}$ is the unit vector in the direction of the viewer.

The model is often modified for energy conservation using the approach introduced by Lafortune [97], with k_d and k_s fulfilling the constraint $k_d + k_s < 1$, as shown in Eq. 4.3:

$$f_r(\theta_i, \varphi_i, \theta_o, \varphi_o) = \frac{k_d}{\pi} + \frac{k_s(n+2)}{2\pi}\,(\mathbf{i_s} \cdot \mathbf{o})^n \tag{4.3}$$

4.2.2 BRDF models including retroreflection

The Beckmann distribution model refers to the assumption that the distribution of the microfacet normals follows a normal distribution, asserting that real material surfaces can be represented using microfacets with different orientations. The Beckmann model is determined by a Fresnel term F (fraction of light that is reflected from an entire surface), a Geometric attenuation factor G (factor describing the effect of masking), and the distribution of microfacets D:

$$f_r(i, o, n) = \frac{F(\mathbf{o} \cdot \mathbf{h_r})G(\mathbf{i}, \mathbf{o}, \mathbf{h_r})D(\mathbf{h_r})}{4 \cdot |\mathbf{i} \cdot \mathbf{n}| \cdot |\mathbf{o} \cdot \mathbf{n}|} \tag{4.4}$$

where $\mathbf{h_r}$ is the halfway vector (between $\mathbf{i}$ and $\mathbf{o}$), and $\mathbf{n}$ is the normal vector. A more detailed description of the factors F, G, and D is given by Smith [98], Beckmann and Spizzichino [99], Schlick [100], and Belcour et al. [96].

The updated Beckmann model, here called Beckmann-Retro model and formulated by Belcour et al. [96], is different from the original model with respect to the inputs of the factors F and G; furthermore, an alternative microfacet distribution D_b is introduced:

$$f_b(i, o, n) = \frac{F(\mathbf{o}' \cdot \mathbf{b})G(\mathbf{i}, \mathbf{o}, \mathbf{h_r})D_b(\mathbf{b})}{4 \cdot |\mathbf{i} \cdot \mathbf{n}| \cdot |\mathbf{o} \cdot \mathbf{n}|} \tag{4.5}$$

where $\mathbf{o}'$ is the vector in the opposite direction of the viewer and $\mathbf{b}$ is the so-called back vector, which is the halfway vector between $\mathbf{i}$ and $\mathbf{o}'$. The altered microfacet distribution including retroreflection is given by:

$$D_b(\mathbf{b}) = \frac{1}{\pi\alpha^2 \cos(\mathbf{b} \cdot \mathbf{n})^4} e^{\frac{\cos^2(\mathbf{b} \cdot \mathbf{n}) - 1}{\alpha^2 \cos^2(\mathbf{b} \cdot \mathbf{n})}} \tag{4.6}$$

where $\mathbf{b}$ is the back vector and $\mathbf{n}$ the normal, and α is a parameter for the apparent roughness for retroreflection.

Furthermore, Schlick's approximation of the Fresnel term is adopted:

$$F(\mathbf{o} \cdot \mathbf{h_r}) = \left(\frac{\eta_1 - \eta_2}{\eta_1 + \eta_2}\right)^2 + \left(1 - \left(\frac{\eta_1 - \eta_2}{\eta_1 + \eta_2}\right)^2\right)(1 - \cos(\mathbf{o} \cdot \mathbf{h_r}))^5 \tag{4.7}$$

where η_1 is the refractive index of medium 1 and η_2 is the refractive index of medium 2.

The Blinn model [101] is a quite simple cosine model. It consists of the dot product between the halfway vector $\mathbf{h_r}$ and the surface normal vector $\mathbf{n}$:

$$f_r = (\mathbf{h_r} \cdot \mathbf{n})^\alpha \tag{4.8}$$

with α being a power factor that is related to the 'shininess' of the material. The Blinn model was extended to include retroreflection (Blinn-Retro model) by simply replacing the halfway vector with the back vector [96]:

$$f_b = (\mathbf{b} \cdot \mathbf{n})^{\alpha} \tag{4.9}$$

The third model, the (original) ABC model, was first introduced in 1989 by Church et al. [102] based on the Raleigh-Rice theory. It was later adapted by Löw et al. in 2012 [103] to derive a new microfacet BRDF model:

$$f_r = \frac{A}{(1 + B(1 - (\mathbf{o} \cdot \mathbf{h_r})))^C} F(\mathbf{o} \cdot \mathbf{h_r}) \tag{4.10}$$

where A, B, and C are parameters (referring to the ABC model), and F is the Fresnel term. A is a general scaling parameter, whereas B and C determine the width of the specular peak and fall-off rate of the wide-angle scattering, respectively. This model was further modified to include retroreflection (ABC-Retro model) by Belcour et al. in 2014 [96]:

$$f_b = \frac{A}{(1 + B(1 - \cos B))^C} F(\mathbf{o}' \cdot \mathbf{b}) \tag{4.11}$$

4.3 Measurement setup

The BRDF measurements have been performed with a "Large Near-Field Goniometer" (LNFG) manufactured by TechnoTeam, shown in Fig. 4.1. Typically, the LNFG is used for measuring luminaires based on near-field luminance camera recordings for which the luminaire is placed at the center of the goniometer. For the BRDF measurements, the setup was altered as shown in Fig. 4.1, where a sample was placed in the center and an external light source was added at a fixed position.

The measurement setup consists of three elements: the (additional) light source, the holder for the test object, and the luminance camera. The light source, shown in the red frame of Fig. 4.1, consists of a QTH10(/M) Quartz Tungsten-Halogen 50W 12V lamp with a broadband emission between 400 and 2200 nm and connected to a programmable Delta Elektronika SM1500 DC power system. An optical system consisting of a lens and two Newport M-ID-1.5 iris diaphragms projects a circular light spot with a diameter of 7.5 cm at the test sample when the illumination is perpendicular to the sample. In the measurement setup, a halogen light source is used as an illuminant (as also used in EN1436), although in road lighting typically

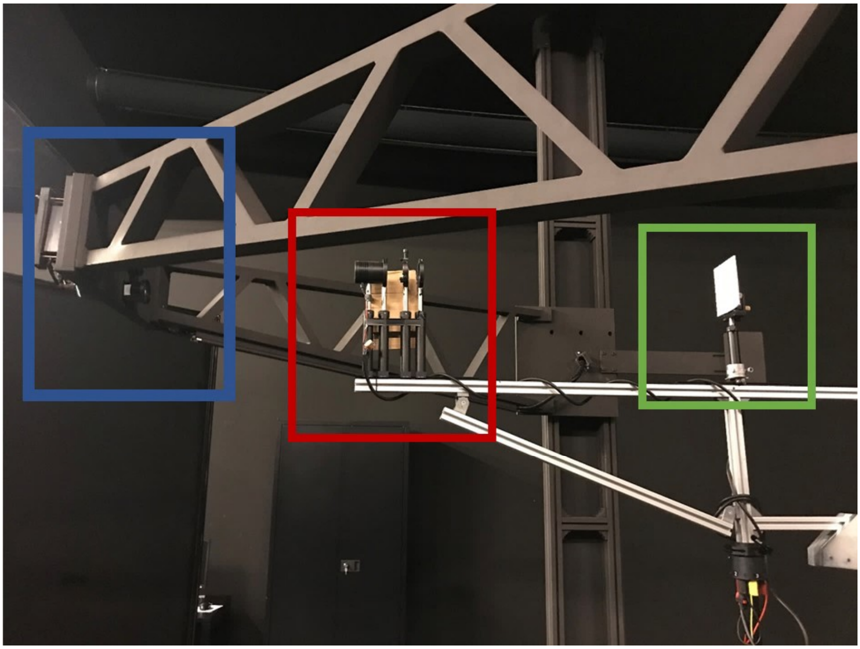

Figure 4.1: The measurement setup where the blue box indicates the luminance camera, the red box the fixed light source, and the green box the sample and sample holder.

LED light sources are used. In principle, the photometric BRDF is dependent on the spectral distribution of the illuminant. However, the spectral reflectance of road markings shows almost no dependency on wavelength (neutral samples); as such, the impact of the spectral distribution of the illuminant on the photometric BRDF values is negligible. The light spot can be seen more clearly in Fig. 4.2. The whole optical system is mounted on a dedicated lever and is fixed in that position.

The sample holder, shown in the green frame of Fig. 4.2, is adjustable and can be rotated around both a vertical and horizontal axis in such a way that any incident angle (θ, φ) can be selected.

The camera, shown in the blue box of Fig. 4.1, consists of a TechnoTeam LMK 98-4 high-tech calibrated luminance camera with a resolution of 1390 x 1040 pixels and is mounted in the RIGO801 LNFG. The RIGO801 LNFG can move freely so that all desired viewing angles can be measured.

The camera and the RIGO801 LNFG are linked to a computer so that the position of the arm of the LNFG can be set via the TechnoTeam software, and luminance images are recorded. After each series of measurements, the illuminance on the test sample

Figure 4.2: A photograph of the sample and sample holder, showing the circular light spot with a diameter of 7.5 cm on the test sample at perpendicular incidence.

was measured at perpendicular incidence with a Gigahertz Optik Optometer P9710 and stored in a text file. The illuminance at non-normal incident angles was calculated by multiplying the measured illuminance with the cosine of the incident polar angle.

4.4 Measurement geometry

Three road marking cutout test samples containing glass beads are considered and shown in Fig. 4.3:

1. SWARCO Limboplast D480 with Megalux 0.6-1.5 KT14
2. SWARCO Limboplast D480 with P21 3:1
3. 3M Stamark A650

In Fig. 4.4, the geometry of the measurement system is shown. A fixed global XYZ coordinate system (GCS) is defined with the Z-axis vertically and with the origin at

Figure 4.3: Photographs taken from the 3 test samples, (1) SWARCO Limboplast D480 with Megalux 0.6-1.5 KT14, (2) SWARCO Limboplast D480 with P21 3:1, and (3) 3M Stamark A650.

the center of the LNFG. A sample coordinate system (SCS) is defined with the local z-axis aligned with the normal to the retroreflector, and the local x- and y-axis are marked on the sample to form a right-handed coordinate system. If the sample is positioned appropriately, the origin of the SCS coincides with the origin of the GCS. The illumination system aperture is positioned at $(X, Y, Z) = (0, -0.92, 0)$, and the direction of the fixed incident beam (L_i) is parallel to the Y-direction.

In the home position, the sample is oriented with the z-axis parallel to the minus Y-axis and the x-axis parallel to the X-axis; this situation corresponds to an incident angle $\theta_i = 0°$. The home position of the camera is at $(X, Y, Z) = (0, 0, 1.54)$, corresponding to a viewing angle of $\theta_o = 90°$ and $\varphi_o = 90°$. The incident angles can be changed by rotating the sample normal (z-axis) around the vertical Z-axis in the positive direction over an angle θ_i. Rotating the sample around the new z-axis allows changing φ_i. The viewing angles can be changed by rotating the camera around the horizontal Y-axis and the vertical Z-axis of the goniometer.

The new positions of the SCS axes and the camera position vector (L_o) after the rotations can be found by applying the general formula for a rotation of a vector **B** around a vector **A** over an angle α given by:

$$\mathbf{B}' = \mathrm{rm}(\mathbf{A}, \alpha) \cdot \mathbf{B} \tag{4.12}$$

with $\mathbf{B}'$ the rotated position of $\mathbf{B}$ and the rotation matrix $\mathrm{rm}(\mathbf{A}, \alpha)$ given by:

$$\mathrm{rm}(\mathrm{A}, \alpha) = \frac{1}{|\mathrm{A}|} \begin{pmatrix} A_x^2 + \cos\alpha(A_y^2 + A_z^2) & A_x A_y(1-\cos\alpha) - A_z|\mathrm{A}|^{1/2}\sin\alpha & A_x A_z(1-\cos\alpha) + A_y|\mathrm{A}|^{1/2}\sin\alpha \\ A_x A_y(1-\cos\alpha) + A_z|\mathrm{A}|^{1/2}\sin\alpha & A_y^2 + \cos\alpha(A_x^2 + A_z^2) & A_y A_z(1-\cos\alpha) - A_x|\mathrm{A}|^{1/2}\sin\alpha \\ A_x A_z(1-\cos\alpha) - A_y|\mathrm{A}|^{1/2}\sin\alpha & A_y A_z(1-\cos\alpha) + A_x|\mathrm{A}|^{1/2}\sin\alpha & A_z^2 + \cos\alpha(A_x^2 + A_y^2) \end{pmatrix} \tag{4.13}$$

This equation can be used for each rotation involved. Once a new position vector is known in GCS, the spherical coordinates towards the SCS can be calculated.

Fig. 4.4 shows an overview of the local (black x, y, z) and global (red X, Y, Z) coordinate system within the LNFG; the direction of the incident light is shown as L_i (orange).

As discussed previously, HDR luminance images of the sample were taken at different viewing angles for different angles of incident. An example of such a luminance image can be seen in Fig. 4.5. After applying a dark correction, the average luminance of a group of central pixels (70 pixels x 70 pixels), belonging to the area of the road marking that is illuminated, was calculated. This luminance was then divided by the illuminance at the chosen angle of incidence to determine the BRDF-value for that specific angle of incidence and viewing.

A wide variety of incident angles was chosen to get a good idea of the reflection properties of the road markings. The selected incident angles can be found in Table 4.1.

Table 4.1: The selected θ angles of incident for each selected φ angle of incidence in degrees.

Incident Angles	
φ_i	θ_i
0	0, 10, 20, 30, 40, 50, 60, 70, 80, 85
23	70, 80, 85
45	70, 80, 85

To check the angular dependence of the reflectivity on φ_i, φ_i of 23° and 45° were included where only the more relevant θ_i angles of 70°, 80°, and 85° were used. For each incident angle, a wide variety of viewing angles was chosen with a higher concentration around the incident angle, to measure the retroreflectivity in more detail. The viewing angles are shown in Table 4.2 for the angle of incidence $\varphi_i = 0°$ and $\theta_i = 0°$.

Note that the illumination and viewing angles mentioned in Table 4.1 and Table 4.2 have been selected according to the situation we are targeting, i.e. the illumination of

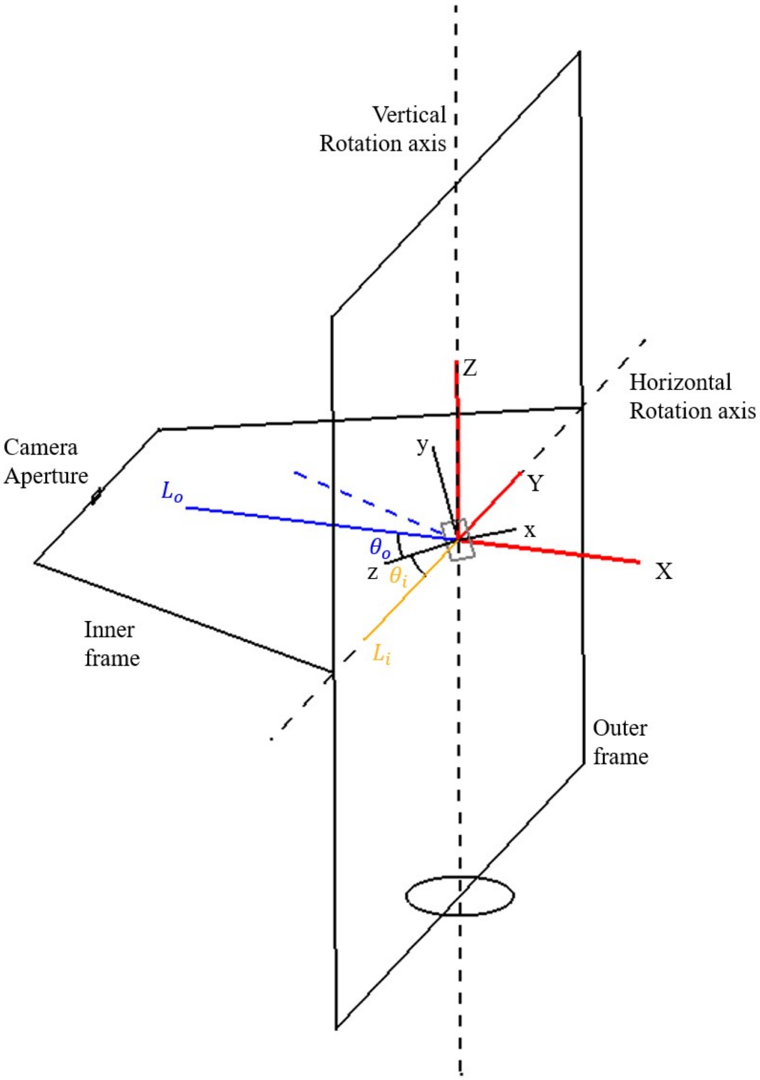

Figure 4.4: Overview of the local (black x, y, z) and global (red X, Y, Z) coordinate system within the LNFG; the direction of the incident light is shown as L_i (orange).

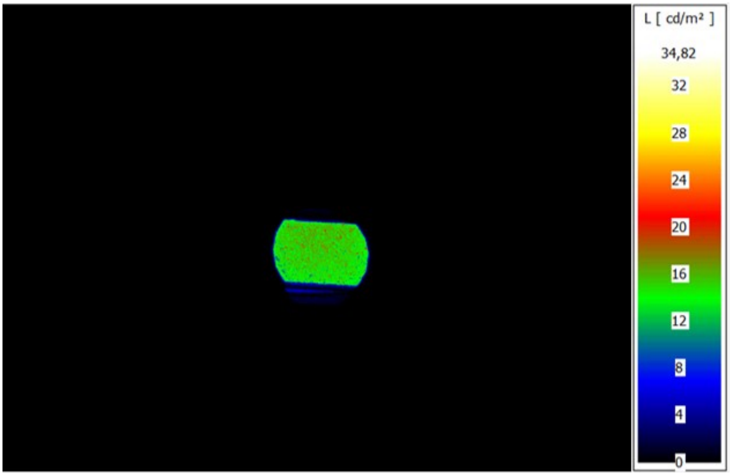

Figure 4.5: Luminance image of road marking 1 for an angle of incidence (θ_i, φ_i) of $(0°, 0°)$ and a viewing angle (θ_o, φ_o) of $(21°, 51°)$.

Table 4.2: The selected θ viewing angles chosen for each selected φ viewing angle in degrees, for an angle of incidence of $\varphi_i = 0°$ and $\theta_i = 0°$.

Viewing Angles	
φ_o	θ_o
25.7	3.3, 10.7, 21.3, 34.8, 50.8, 69.3
51.4	3.3, 10.7, 21.3, 34.8, 50.8, 69.3
77.1	3.3, 10.7, 21.3, 34.8, 50.8, 69.3
102.9	3.3, 10.7, 21.3, 34.8, 50.8, 69.3
128.6	3.3, 10.7, 21.3, 34.8, 50.8, 69.3
154.3	3.3, 10.7, 21.3, 34.8, 50.8, 69.3
180	3.3, 10.7, 21.3, 34.8, 50.8, 69.3
205.7	3.3, 10.7, 21.3, 34.8, 50.8, 69.3
231.4	3.3, 10.7, 21.3, 34.8, 50.8, 69.3
257.1	3.3, 10.7, 21.3, 34.8, 50.8, 69.3
282.9	3.3, 10.7, 21.3, 34.8, 50.8, 69.3
308.6	3.3, 10.7, 21.3, 34.8, 50.8, 69.3
334.3	3.3, 10.7, 21.3, 34.8, 50.8, 69.3
360	3.3, 10.7, 21.3, 34.8, 50.8, 69.3

the road and road signs by the road luminaires and observation of the reflected light by the car driver.

4.5 Measurement data

For each incident angle, the BRDF-value was determined for all viewing angles, a visualization of which is shown in Fig. 4.6 for one particular angle of incidence. The BRDF-value at each measured viewing angle (represented by a dot) is relative to the length of the incident vector (represented by the red dashed line with length 1). The large BRDF-values in the direction of incidence indicate the retroreflective character of the road marking material.

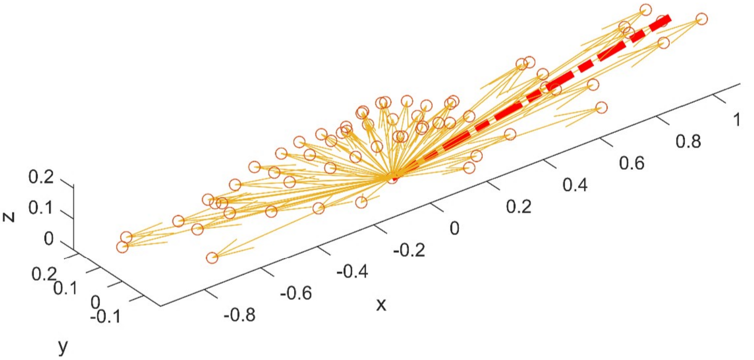

Figure 4.6: Example of the resulting BRDF for an angle of incidence (θ_i, φ_i) of $(80°, 0°)$ for road marking sample 1. The incident vector is shown with the red dashed line and has a length of $1\ \mathrm{sr}^{-1}$. The absolute BRDF-values are represented by dots, and the corresponding viewing direction is indicated by arrows.

To make the elementary retro- and specular reflections more visible, the BRDF values are also plotted in polar diagrams with the perimeter representing the various viewing directions. Fig. 4.7 shows an example at a fixed φ_o of 0° and 180°, and for the incident angles $\theta_i = 10°, 60°$, and $80°$ for a fixed φ_i of $0°$. The polar diagram is in the plane of $\varphi_o = 0°$ (on the left) and $\varphi_o = 180°$ (on the right). In addition, the dotted blue lines indicate the (ideal) specular reflection vectors. These (ideal) specular reflection vectors are also 1 sr^{-1} in length. The BRDF-values in sr^{-1} are indicated with crosses. The red crosses indicate the BRDF-values for a φ_o of $0°$ (retroreflective hemisphere), and the blue crosses indicate the BRDF-values for a φ_o of $180°$ (specular hemisphere).

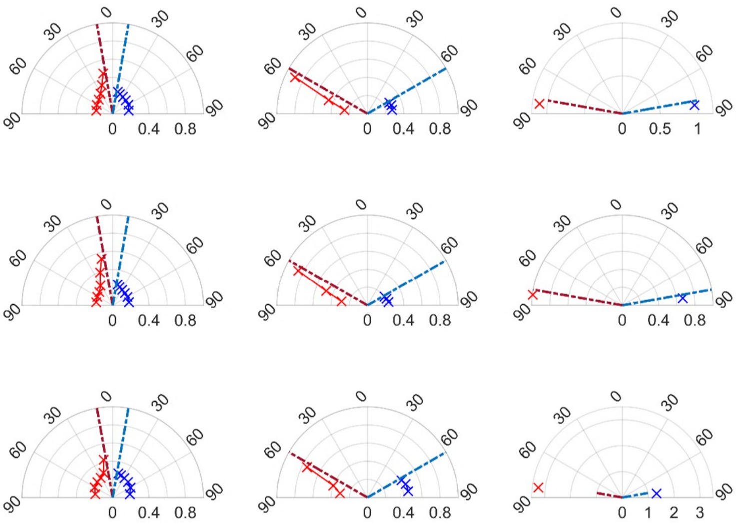

Figure 4.7: Polar plots of the BRDF-values where the red crosses and dashed lines indicate the retroreflective hemisphere, and the blue crosses and dashed lines represent the specular hemisphere. The dotted red lines indicate the incident vectors that are given a length of 1 sr^{-1}. Plotted on the top row for sample 1, middle row for sample 2, and on the bottom row for sample 3; the three plots in a row represent incident angles of $\theta_i = 10°, 60°$, and $80°$ for a fixed $\varphi_i = 0°$, from left to right, respectively. The radius of the polar diagrams is in sr^{-1}, and the angles in the polar diagrams represent the θ angles in degrees.

The general observation of all measured BRDF-values is that the retroreflection increases as the incident angle θ_i increases (see Fig. 4.7). Furthermore, it is noteworthy that with the larger angles of incident θ_i, in addition to an increasing retroreflection, the specular reflection also increases (see Figs. 4.6 and 4.7). In general, for incident angles of $\theta_i > 80°$ and $\varphi_i = 0°$, the BRDF-value in the direction of retroreflection is close to or greater than 1.

4.6 Optimization of a BRDF model

To describe the measured data of the retroreflective glass bead road markings for further use, we need a BRDF model that summarizes the data accurately. Therefore, in this section, we first explore to what extent an existing generic BRDF model fits the data and then adapt the model where needed.

Since the data exhibit a peaked (retro)reflective cosine-lob like behavior, we investigated the Phong model modified for energy conservation. We also considered a classic Fresnel reflection, but that turned out to provide a worse fit to our data than the modified cosine-lob Phong model. The modified Phong model only exhibits a peaked specular reflective cosine-lob, but not any retroreflective behavior. Therefore, this model is extended such that a second peaked cosine-lob is added in the direction of the incident light vector for retroreflection:

$$f_r(\theta_i, \varphi_i, \theta_o, \varphi_o) = \frac{k_d}{\pi} + \frac{k_s(n+2)}{2\pi}(i_s \cdot o)^n + \frac{k_r(n+2)}{2\pi}(i \cdot o)^n \tag{4.14}$$

where k_r is the parameter for retroreflection with energy conservation fulfilling the constraint $k_d + k_s + k_r < 1$, and i the incident unit vector. This BRDF model applies a specular and retroreflective cosine-lob, where the maximum value is irrespective of the incident angle. However, as mentioned before, the measured BRDF-values increase with an increase in the incident angle, which can be integrated into the model by making the parameters k_r and k_s dependent on the incident angle θ_i. Our measured data also indicate a difference in only the length of the cosine-lob and not so much in its width. Since the diffuse component does not change much with changes in the incident angle, the parameters k_d and n can remain constant. This results in:

$$f_r(\theta_i, \varphi_i, \theta_o, \varphi_o) = \frac{k_d}{\pi} + \frac{k_s(\theta_i)(n+2)}{2\pi}(i_s \cdot o)^n + \frac{k_r(\theta_i)(n+2)}{2\pi}(i \cdot o)^n \tag{4.15}$$

To determine the best function for $k_r(\theta_i)$ and $k_s(\theta_i)$, the measurement results of road marking sample 1 were taken, and the k_r, k_s, k_d, and n parameters were determined for a randomly chosen incident angle (i.e., θ_i of 80° and a φ_i of 0°) by minimizing the root mean squared error (RMSE) between the calculated $f_r(\theta_o, \varphi_o)$-values using Eq. 4.15 and the measured $f_m(\theta_o, \varphi_o)$-values. The RMSE is given by:

$$RMSE = \sqrt{\frac{1}{N}\sum_{\theta_o, \varphi_o}(f_m(\theta_o, \varphi_o) - f_r(\theta_o, \varphi_o))^2} \tag{4.16}$$

where N is the total number of viewing angles. The optimization was done in Matlab with the Global Optimization Toolbox using the Genetic Algorithm with no constraints. This resulted in a k_r of 0.168, k_s of 0.132, a k_d of 0.620, and n of 24.0 with an RMSE of 0.106. In a next step, the optimization was repeated for all other incident angles, but then with the parameters k_d and n fixed at 0.620 and 24.0. The resulting k_r- and k_s-values are plotted against $1-\cos(\theta_i)$ in Fig. 4.8 (a) and (b), respectively. The RMSE of the fit was lower than 0.185 for all incident angles. The k_r-values were higher than the k_s-values except at θ_i of 85°, meaning that the retroreflection was larger than the specular reflection except at θ_i of 85°.

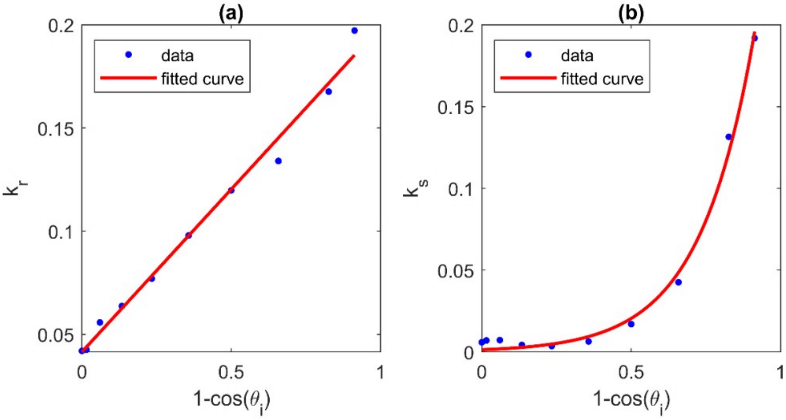

Figure 4.8: The resulting k_r and k_s values plotted against $1-\cos(\theta_i)$.

Fig. 4.8. The k_r- (a) and k_s- (b) values resulting from the optimization plotted against $1-\cos(\theta_i)$ indicated by the blue dots. The solid red line indicates the fit to the data points.

The k_r-values in Fig. 4.8(a) could be fitted with a simple linear function:

$$k_r(\theta_i) = k_1(1-\cos(\theta_i)) + k_2 \tag{4.17}$$

resulting in an R^2 of 0.99 with the parameters k_1 and k_2 being equal to 0.158 and 0.0415, respectively. The k_s-values in Fig. 4.8(b) were fitted with a simple exponential function:

$$k_s(\theta_i) = k_3 e^{k_4(1-\cos(\theta_i))} \tag{4.18}$$

resulting in an R^2 of 0.99 with the parameters k_3 and k_4 being equal to 0.00133 and 5.467, respectively. The full BRDF model according to Eq. 4.15, using Eqs. 4.17 and 4.18 and the optimized parameters, is plotted for the data at an angle of incidence (θ_i, φ_i) of $(80°, 0°)$ for road marking 1 (so, the measurement data shown in Fig. 4.6) in Fig. 4.9.

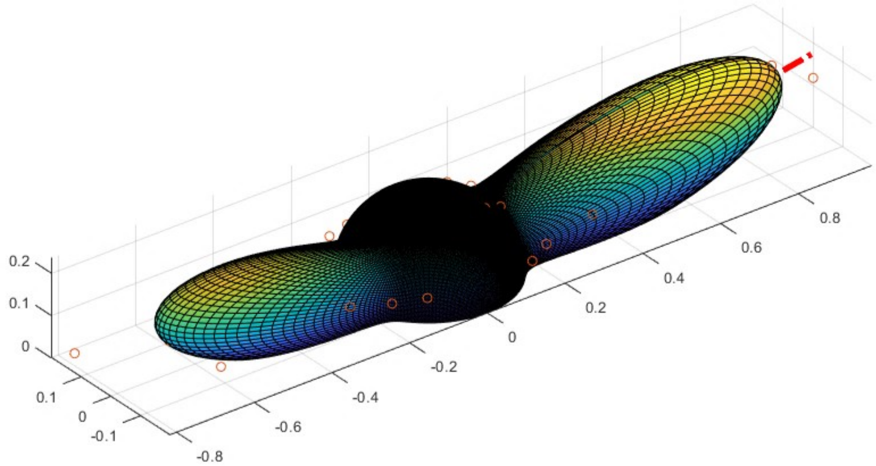

Figure 4.9: Example of the fitted BRDF (colored grid) for an angle of incidence (θ_i, φ_i) of $(80°, 0°)$ for road marking 1. The incident vector is shown with the red dashed line and is 1 sr^{-1} in length. The measured BRDF-values for each viewing angle are relative to the length of the incident vector and shown by the dots.

To quantify the goodness of fit of the BRDF model, we also calculated the normalized root mean squared error (NRMSE) and the normalized cross-correlation ratio (NCC) [104]. The NCC and NRMSE are defined as:

$$NCC = \frac{\sum_{\theta_i,\varphi_i,\theta_o,\varphi_o}\left[(f_m(\theta_i,\varphi_i,\theta_o,\varphi_o)-\overline{f_m})(f_r(\theta_i,\varphi_i,\theta_o,\varphi_o)-\overline{f_r})\right]}{\sqrt{\sum_{\theta_i,\varphi_i,\theta_o,\varphi_o}\left(f_m(\theta_i,\varphi_i,\theta_o,\varphi_o)-\overline{f_m}\right)^2\sum_{\theta_i,\varphi_i,\theta_o,\varphi_o}\left(f_r(\theta_i,\varphi_i,\theta_o,\varphi_o)-\overline{f_r}\right)^2}}, \tag{4.19}$$

$$NRMSE = \frac{\sum_{\theta_i,\varphi_i,\theta_o,\varphi_o}\sqrt{[f_m(\theta_i,\varphi_i,\theta_o,\varphi_o)-f_r(\theta_i,\varphi_i,\theta_o,\varphi_o)]^2}}{\max(f_m,f_r)N}, \tag{4.20}$$

with $\overline{f_m}$ and $\overline{f_r}$ being the modeled and measured BRDF-values, respectively, averaged over all incident and viewing angles. The max function is defined as the maximum over all f_m and f_r-values. The NCC is a measure of similarity and varies between 0 and 1, with 0 indicating no correlation (0%) and 1 indicating a perfect match (100%) between the relative shape of the BRDF model and measured values [105]. The RMSE, NRMSE, NCC, and the optimization parameters are summarized in Table 4.3 for the BRDF model, defined through Eqs. 4.15, 4.17, and 4.18 (hereafter referred to as 'RetroPhong' model) optimized to the data of road marking sample 1, 2, and 3.

Table 4.3: The selected θ viewing angles chosen for each selected φ viewing angle in degrees, for an angle of incidence of $\varphi_i = 0°$ and $\theta_i = 0°$.

RM	RMSE	NRMSE	NCC	k_d	n	k_1	k_2	k_3	k_4
1	0.102	0.0370	0.879	0.620	24.0	0.158	0.0415	0.00133	5.47
2	0.106	0.0201	0.861	0.594	24.0	0.0696	0.0733	6.58e-05	8.74
3	0.280	0.0216	0.814	0.701	68.0	0.184	1.53e-12	0.00570	3.40

Additionally, to check the validity of the model, a cross-validation is performed where the RMSE, NRMSE, and NCC are calculated for the RetroPhong model optimized to the data of road marking 1, and applied to the data of road marking 2 and 3 (as shown in Table 4.4).

In this cross-validation, the increase in RMSE and NRMSE, and the decrease in NCC is quite small between using optimized parameters of road marking sample 1 for road marking sample 2 on the one hand or using the optimized parameters for road marking sample 2 on the other hand (i.e., 0.121, 0.0251, and 0.837 compared to 0.106, 0.0201, and 0.861, respectively). This means that the RetroPhong model parameters

Table 4.4: The RMSE, NRMSE, and NCC for the RetroPhong model for road markings (RM) 2 and 3 using the optimized parameters of road marking 1.

RM	RMSE	NRMSE	NCC	k_d	n	k_1	k_2	k_3	k_4
2	0.121	0.0251	0.837	0.620	24.0	0.158	0.0415	0.00133	5.47
3	0.361	0.0247	0.757	0.620	24.0	0.158	0.0415	0.00133	5.47

that have been optimized to the data of road marking sample 1 can also be effective in predicting the BRDF-values of road marking sample 2. For road marking sample 3, the RMSE, NRMSE, and NCC differences are larger, meaning that the set of parameters determined by the optimization of road marking sample 1 are less suitable in predicting the BRDF-values of road marking sample 3. It is worth noting that road marking samples 1 and 2 are both Limboplast D480 samples and are, therefore, different from road marking sample 3. Road marking 1 and 2 are cold plastics, whereas road marking sample 3 is a preformed tape with a special polyurethane top coating.

Furthermore, the effect on the RMSE, NRMSE, and NCC when excluding the specular component in Eq. 4.15 was investigated and is given in Table 4.5. Excluding the specular component allows us to compare the retroreflective component of the RetroPhong model with other retroreflective models that exclude specular reflection, see below. When excluding the specular component from the RetroPhong model, the RMSE increases by 0.070, and the NRMSE and NCC decrease by 0.0062 and 0.265, respectively. Thus, the specular component does seem to have some added value to the RetroPhong model.

Table 4.5: The RMSE, NRMSE, and NCC for the RetroPhong model for road marking (RM) 2 and 3 using the optimized parameters of road marking 1.

<table>
<tr><th colspan="10">RetroPhong without specular component</th></tr>
<tr><th>RM</th><th>RMSE</th><th>NRMSE</th><th>NCC</th><th>k_d</th><th>n</th><th>k_1</th><th>k_2</th><th>k_3</th><th>k_4</th></tr>
<tr><td>1</td><td>0.102</td><td>0.0370</td><td>0.879</td><td>0.620</td><td>24.0</td><td>0.158</td><td>0.0415</td><td>0.00133</td><td>5.47</td></tr>
<tr><th colspan="10">RetroPhong without specular component</th></tr>
<tr><th>RM</th><th>RMSE</th><th>NRMSE</th><th>NCC</th><th>k_d</th><th>n</th><th>k_1</th><th>k_2</th><th>k_3</th><th>k_4</th></tr>
<tr><td>1</td><td>0.172</td><td>0.0308</td><td>0.614</td><td>0.620</td><td>24.0</td><td>0.158</td><td>0.0415</td><td>-</td><td>-</td></tr>
</table>

4.7 Benchmarking of the RetroPhong model

The RetroPhong model actually is similar to the Lafortune model, one of the models described in the paper by Belcour et al. [96] , but here specifically defined for the condition of one retroreflective and one specular lobe. In addition, we added the modeling of k_s and k_r as a function of the incident angle (i.e., Eqs. 17 and 18) to this specific Lafortune model, resulting in the so-called RetroPhong model. This is benchmarked against four other parametric BRDF models: an improved classical Lambertian model introduced by Oren and Nayar [106], an updated Blinn lobe, an updated Beckmann distribution, and an updated ABC distribution, all introduced by Belcour et al. [96] and updated by including retroreflection ($k_d/\pi + f_r + f_b$). The Oren-Nayer parametric BRDF model was included in the benchmark because of its retroreflective property with increasing surface roughness and its ability to explain the view-dependent reflective properties of matte surfaces with geometric optics. The updated Blinn, updated Beckmann, and updated ABC distribution were included based on the similarities in reflective properties of the road markings with the retroreflective gray, yellow, and orange tape used in the study by Belcour et al. [96]. Likewise, in the optimization of the RetroPhong model, the parameters in the BRDF models were optimized to minimize the RMSE with the measured data. For the optimization, we again used the Genetic Algorithm of the Global Optimization Toolbox of Matlab. An overview of the RMSE, NRMSE, and NCC for each BRDF model is given in Table 4.6.

From these benchmarked models, the ABC-Retro model comes closest to the RetroPhong model with a RMSE around 0.19 and a NRMSE less than 0.09; the NCC is higher than 0.4 for road marking sample 1, but lower than 0.3 for road marking samples 2 and 3. Worth mentioning is that the Beckmann-Retro model outperforms the RetroPhong model in terms of higher NCC for road marking sample 1, but nonetheless has a higher RMSE and NRMSE. So, all models result in higher RMSE and NRMSE values for all three road marking samples when compared to the RetroPhong model. Even when only considering the retroreflective component of RetroPhong model, as suggested in Table 4.5, the RMSE and NRMSE are lowest for the RetroPhong model, though the differences with the other BRDF models become smaller. Regarding NCC, the highest values are found for the RetroPhong model, with the exception of the Beckmann-Retro model for road marking 1.

Finally, all optimization coefficients are documented in Table 4.8 for all three road markings and all BRDF models.

Table 4.6: The RMSE, NRMSE, and NCC parameters for each road marking and BRDF model.

Road Marking 1	RMSE	NRMSE	NCC	Number of Coefficients
RetroPhong	0.102	0.0370	0.879	6
Oren-Nayar	0.203	0.0515	0.310	2
Beckmann-Retro	0.160	0.0676	0.615	3
Blinn-Retro	0.194	0.0871	0.285	3
ABC-Retro	0.116	0.0477	0.819	8
Road Marking 2	RMSE	NRMSE	NCC	Number of Coefficients
RetroPhong	0.106	0.0201	0.861	6
Oren-Nayar	0.203	0.0820	0.399	2
Beckmann-Retro	0.171	0.0475	0.582	3
Blinn-Retro	0.197	0.0547	0.316	3
ABC-Retro	0.125	0.0305	0.804	8
Road Marking 1	RMSE	NRMSE	NCC	Number of Coefficients
RetroPhong	0.280	0.0216	0.814	6
Oren-Nayar	0.415	0.0428	0.508	2
Beckmann-Retro	0.490	0.0396	0.581	3
Blinn-Retro	0.487	0.0393	0.219	3
ABC-Retro	0.224	0.0181	0.886	8

Table 4.7: The RMSE, NRMSE, and NCC parameters for each road marking and BRDF model.

4.8 Discussion

The new RetroPhong model shows good agreement with the measured reflectivity of the three road markings containing glass beads and for the wide set of incident and viewing angles used in this study. As we focus on road markings illuminated by road lighting, for which different angles of incident and viewing angles are relevant than for illumination by car headlights, we did not measure the incident angles and viewing angles as specified in the CIE 54.2 [39] report. In this paper, the maximum polar incident angle was for practical reasons limited to 85°, implying that it is still unclear how well the RetroPhong model predicts reflectivity beyond this angle. We set the limitation to 85° because the measurements beyond this incident angle would become too noisy to accurately determine a BRDF-value in our measurement setup. Nonetheless, when comparing the BRDF value given by the RetroPhong model for the particular incidence (88.8°) and viewing (87.7°) angle with the BRDF value as required

Table 4.8: The optimization coefficients for each road marking and BRDF model.

Oren-Nayar	α_m	ρ						
Road marking 1	0.865	0.268						
Road marking 2	0.705	0.275						
Road marking 3	1.26	0.470						
Beckmann-Retro	k_d	α	R_0					
Road marking 1	0.796	8.20	0.995					
Road marking 2	0.822	9.36	0.993					
Road marking 3	0.996	1.61e3	1.00					
Blinn-Retro	k_d	α_b	α_r					
Road marking 1	0.919	2.77e3	7.91e3					
Road marking 2	0.881	2.50e3	7.10e3					
Road marking 3	0.993	6.72e3	1.65e4					
ABC-Retro	k_d	R_0	A_b	B_b	C_b	A_r	B_r	C_r
Road marking 1	0.534	0.0472	1.82	13.5	1.51	1.02	0.0775	6.97
Road marking 2	0.0303	0.140	1.59	32.6	1.08	1.19	0.00779	0.0179
Road marking 3	0.747	0.00466	6.66	37.8	0.710	3.58	22.9	0.729
RetroPhong	k_d	n	k_1	k_2	k_3	k_4		
Road marking 1	0.620	24.0	0.158	0.0415	0.00133	5.47		
Road marking 2	0.594	24.0	0.0696	0.0733	6.58e-05	8.74		
Road marking 3	0.701	68.0	0.184	1.53e-12	0.00570	3.40		

in EN1436 [37], retrieved by converting the R_l value of the technical data sheet, it is found that for road marking 2 the difference in BRDF values is relatively small (< 0.13), whereas the difference is larger for road markings 1 and 3 (0.63 and 0.91, respectively).

Furthermore, the RetroPhong model was checked regarding energy conservation, meaning that the sum of the diffuse, specular, and retroreflective parameters ($k_d + k_s + k_r$) should be less than 1. This does seem to be the case within the measurement range of this study; however, this is violated when extrapolating towards $\theta_i > 85$. This implies that the functions that are shown in Fig. 4.8 based on Eqs. 4.17 and 4.18 most likely show a fall-off in specular and retroreflective parameters towards reaching 90°. Since we did not measure beyond a polar incident angle of 85°, it is still uncertain what the exact behavior of these parameters would be beyond this angle. However, this is not a severe limitation for this study since we focus on a suitable BRDF model for road markings illuminated by road lighting (i.e., luminaires).

From all (retro)reflective BRDF models evaluated in this study, in general, the RetroPhong model fits our data best. Also, when excluding the specular component from the RetroPhong model, it still shows a better agreement with the data than the existing (retro)reflective BRDF models of the benchmark. It is worth mentioning that in this particular case, the RetroPhong model includes six optimization parameters, whereas the other BRDF models use between one and eight optimization parameters.

4.9 Conclusion

By measuring three glass beads embedded road marking samples for a larger set of incident and viewing angles, BRDF-values relevant for road lighting (i.e., illumination by luminaires) are reported. The BRDF-values are determined using a commercial LNFG adapted to our needs and equipped with an imaging luminance measurement device.

Based on the general observation that the BRDF-values in the specular and retroreflection region increase as the angle of incidence increases and follow a cosine-lobe like behavior, a new RetroPhong BRDF model was created. In this model, the retroreflection is modeled by a cosine-lob in the direction of the incident vector, with the peak of the lobe increasing with the theta incident angle. The increase in specular reflection is modeled by a cosine-lob in the direction of the specular direction, with the peak of the lobe also increasing with the polar incident angle.

To determine the relevance and relative ’goodness’ of fit to the data, the RetroPhong BRDF model was benchmarked to four other (retro)reflective BRDF models: Oren-Nayar, Beckmann-Retro, Blinn-Retro, and ABC-Retro. The RMSE and NRMSE were found to be the lowest for the RetroPhong model for each road marking when compared to these other models. The NCC was found highest for the RetroPhong model with the exception of the Beckmann-Retro model for road marking 1. In general, it can be concluded that the RetroPhong model fits the measurements better than the other models.

In order to allow the new model to be used in rendering software, some practical implementation steps need to be taken. An example of how to implement the RetroPhong model in a physical based renderer such as Mitsuba [56] can be found in the appendix.

Future work will be to examine and parametrize the RetroPhong model for more and different sets of retroreflective materials and to extend the angles of incidence beyond 85° in order to reach a fully generic model. Such a generic model would be of great use for improving the accuracy of modeling the visibility of road markings illuminated by both road lighting luminaires and car headlights in PBRs such as Mitsuba.

Chapter 5

An asymmetric road lighting concept: Probeam

Abstract: An asymmetric road lighting concept known as Probeam is investigated in this study for energy efficiency, contrast, and visibility of vertical objects and road markings in highway lighting. Calculations based on road lighting standards, road surface and markings reflection characteristics, and typical Dutch highway geometry, reveal that probeam lighting improves the average visibility of objects and road markings over symmetrical lighting, however, with a 14% increase in luminous flux as per current road lighting standards. This increase in luminous flux is attributed to the symmetrical lighting's advantage in specular road surface reflection, leading to a reduction in the counterbeam lobe size in the light intensity distribution when designed to meet the current road luminance requirement. Notably, by designing the probeam luminaire to match symmetrical lighting's average visibility of vertical objects, for removing the road luminance requirement and dimming the luminaire, energy consumption is reduced by 52%. Halving the probeam luminaire's mounting height leads to an impressive 82% energy savings. The study highlights the possibility of a balance in energy use and road safety using the Probeam concept, considering advancements in road luminaires and retroreflective materials.

Spieringhs, R. M., Smet, K., Heynderickx, I., & Hanselaer, P. (2024). An asymmetric road lighting concept: Probeam. *Lighting Research & Technology.*

What follows is the complete and unedited content of this paper.

5.1 Introduction

The aim of road lighting is to improve the driving conditions for motorized traffic when driving during the night. Road lighting improves visual performance, visual guidance, driver's alertness, and visual comfort. In this way, it is an important factor to improve the safety for drivers, pedestrians, and cyclists. The relationship between the application of road lighting and the decrease in accidents at night time has been extensively reported in the literature [3, 7, 8].

When illuminating a road for motorized traffic, generally two sources of illumination are considered, being car headlights and road luminaires. It is generally agreed that dipped or low-beam (halogen) car headlights only contribute up to 60 meters in front of the observer to the illumination of the road surface, although recently it has been reported that low-beam high-intensity discharge or LED car headlights can influence visibility even up to 80 m [2, 107–113]. Beyond this distance, road luminaires provide illumination of the road and the road markings.

Today, a wide-scale conversion from traditional light sources in road luminaires, such as HID and low-pressure sodium lamps, towards LED light sources is going on. LED lighting is more energy-efficient and cost-effective than other types of lighting. This is not only due to an inherent higher luminous efficacy of the conversion process (reaching 120 lumen/watt and more) but also to better control of the Luminous Intensity Distribution (LID) as one can take advantage of the small dimensions of an individual LED to develop dedicated secondary optics. Additionally, LED lights are more durable, making them ideal for harsh outdoor environments, and can be dimmed easily.

Since the 1930s, many standards for road lighting have been developed [4, 114, 115]. They first covered several practical aspects, such as the minimum luminaire mounting height and maximum luminaire spacing, later on including some basic photometric units such as minimum illuminance [115]. Most of these standards from the 1900s prescribe the basic lighting system characteristics (such as average road surface luminance or horizontal illuminance) rather than specifying performance metrics (such as Adrian's visibility or the relative visual performance model). It was not only till the late 1900s and early 2000s that one became aware that new standards should be inspired and underpinned by studies about visibility and contrast of obstacles [42, 116, 117].

The current standard road illumination concept for highways consists of luminaires with a symmetrical LID, a pole height of 18 m, a pole distance of 90 m, and a uniform maintained road luminance of 0.75 cd/m^2 [83, 118]. As such, it follows lighting class M4, one of the lighting classes defined by standard EN 13201-2 for various road uses, requiring different average road surface luminance and luminance uniformity

[118]. Although the concept of visibility and visual performance gained popularity in scientific research about road lighting, standardization committees were not able to agree on how to include these metrics in the standards [50]. In some standardizations, visual performance was briefly included, but later removed based on limitations of such metrics and the lack of consensus on target size and model [50]. Not surprisingly, several limitations in current road lighting standards have recently been identified by Fotios and Gibbons [4], prompting a request for new standards with more evidence-based visibility models and contrast thresholds of road markings.

These insights have triggered the reconsideration of the standard illumination concept as adopted in the early 2000s. For tunnels and pedestrian lighting, the use of asymmetric LIDs is currently being investigated, and the results seem very promising [44–47]. Therefore, also for road lighting different LIDs, categorized as symmetrical, counterbeam, and probeam lighting (as shown in Fig. 5.1) are being considered. Symmetrical lighting is currently most commonly used. The Counterbeam concept aims most light intensity towards the driver, whereas the Probeam concept aims most light intensity in the direction of traffic.

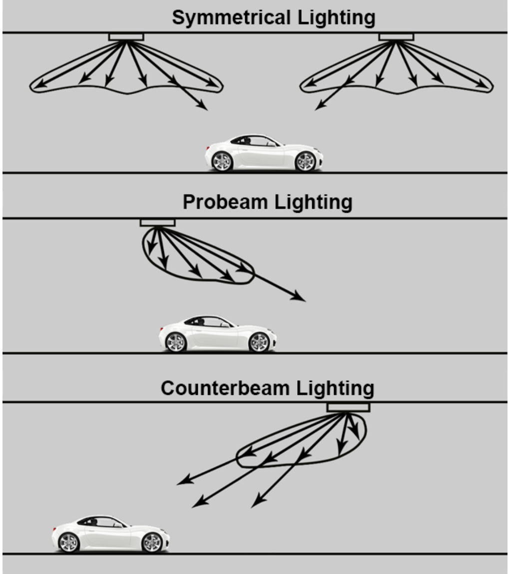

Figure 5.1: Three types of lighting distributions for tunnel lighting. Top: symmetrical lighting, middle: probeam Lighting, and bottom: counterbeam lighting.

It would be interesting to investigate if the use of such asymmetric road lighting concepts could improve visibility and contrast without increasing energy consumption.

Energy use is such an important aspect nowadays that road lighting is often just turned off on highways in many countries. The road surface is then lit almost exclusively by car headlights. This reduces energy consumption, but at the expense of an increase in accidents, a reduced visibility of objects beyond 60 meters, and reduced visual guidance, which makes this approach not recommendable. As LEDs are easily dimmable, one can, therefore, wonder which illumination levels and which lighting concept can reach the right balance between energy consumption and user safety.

In this context, technological advancements in road marking retroreflective materials should be mentioned as they contribute to visual contrast and road guidance. Over the past few decades, the use of retroreflective materials has progressed from use in cinema for increasing the brightness of image material to widespread use in road signs, road markings, and clothing to improve nighttime visibility. They usually include encapsulated lenses, glass beads, or microprisms, which have been further optimized to enhance the retroreflection of incident light from vehicle headlights [34, 37]. This development may also add to some advantages of the probeam lighting concept, which is mainly relying on retroreflection of the light on the road (with its signs and markings) to guide the driver.

Next to human visibility, the impact of road lighting on image-based systems as occurring in the advanced driver-assistance systems (ADAS) of new vehicles should also be considered. These systems are increasingly helpful in preventing accidents, but it is known that the imaging systems do struggle to detect road markings due to a lack of contrast [119, 120]. In addition, automotive imaging systems are known to be susceptible to light bloom and light flare caused by symmetrical and counterbeam road lighting [120].

Triggered by the promising results reported on the use of the Probeam concept for tunnels and lighting for pedestrian crossings, one-directional traffic on highways, and the fact that there are over 4000 km of highway in just Belgium and the Netherlands (i.e., at least 4% of the total road transportation network), this paper reports on the investigation of the potential of the Probeam concept for highway illumination. Recent new insights regarding visual contrast and visibility are taken into account [50, 83]. Effects on contrast and visibility, glare, road guiding, and energy consumption are discussed, and the results are underpinned by models and calculations.

5.2 General Principles in Classical Road Lighting Design

The current most important road lighting quality parameters for motorized traffic are defined in the relevant CIE publication 115 [41] and mentioned in the European standard EN13201 [42]. An overview of all the aspects involved is given below, and is used later in the paper to evaluate the Probeam lighting concept.

5.2.1 Contrast

Visibility in conventional road lighting is based on the Silhouette Principle [2, 41, 50, 121]. According to this principle, the silhouette of any object or person beyond the reach of car headlights should be clearly visible and distinct from the background [42]. This allows drivers to distinguish objects and people on the side of the road and reduces the risk of accidents. The aim is to illuminate the road such that objects appear in negative contrast (i.e., objects appear darker than the road surface) to the driver. Important aspects for creating this negative contrast are the average luminance and the luminance uniformity of the road surface. The Luminous Intensity Distribution (LID) of the luminaires is typically symmetrical, and the height to distance ratio is such that some overlap in horizontal illumination on the road exists. Depending on the position of the object on the road surface with respect to the position of the luminaires, the object will, however, appear in positive or negative contrast.

5.2.2 Reflection Characteristics

To determine the luminance of the road surface, the road markings, and obstacles under particular illumination conditions, the reflection characteristics of these materials are required. The reflection of a road surface is sometimes approximated as a (perfect) Lambertian distribution, which means that the luminance of the road surface is identical for any viewing angle, irrespective of the direction of the incident light. In practice, however, this is a rough approximation, since road surfaces, in specific asphalt concrete (i.e., gap, open, and dense graded asphalt), illuminated at grazing angles exhibit an important specular reflection caused by small surface facets (microfacets), the contribution of which is neglected when describing the reflection of light on the road with a Lambertian distribution [32, 33].

To improve a road lighting design, one needs to implement the complete reflection characteristics of the road surface at different incident and viewing angles.

In determining the reflectance characteristics of the road surface, the CIE 144 [32] describes the use of R-tables. The Luminance Reduction Coefficient R is expressed in cd/m^2/lux and is related to the more fundamental luminance coefficient q, defined by the ratio of the luminance (L) of point p (in cd/m^2) in a particular viewing direction (i.e., fixed viewing angle) due to reflection over the horizontal illuminance (E) at that point p (in lux):

$$q = \frac{L}{E} \tag{5.1}$$

The illuminance of the road can be expressed in terms of the relevant intensity (I) of the luminaire, the height of the luminaire H, and the incident light angle relative to the downward vertical of the light source γ. Taking this into account, the luminance can be written as

$$L = q \cdot E = q \cdot \cos^3(\gamma) \cdot \frac{I}{H^2} = R \cdot \frac{I}{H^2} \tag{5.2}$$

The luminance reduction coefficient R, therefore, is

$$R = q \cdot \cos^3(\gamma) \tag{5.3}$$

Note that q and yet R are dependent on the viewing conditions. For road surface reflection, in the European standard, the polar viewing angle α_1 with respect to the road normal is fixed to 89 degrees while the azimuthal viewing angle β is expressed by the angle between the observation plane and the light incidence plane.

For describing the road surface reflection with singular numbers, the CIE, in 1976, adopted two parameters. The lightness parameter Q_0 is the average of the luminance coefficient q weighted by the solid angle Ω:

$$Q_0 = \frac{1}{\Omega} \int q \, d\Omega \tag{5.4}$$

The specularity parameter S1 is defined as the ratio between two particular R-values from the R-table:

$$S_1 = \frac{R(\gamma = 63, \beta = 0)}{R(\gamma = 0, \beta = 0)} \tag{5.5}$$

Finally, the reflection characteristics of road markings (positioned horizontally) and road signs (positioned vertically) are known to be very different from those of road surfaces as they exhibit mainly retroreflection [34–37, 39]. In describing the reflectance characteristics of road markings, the CIE 54.2 [39] describes the use of the Coefficient of Retroreflected Luminance R_L expressed in mcd/m^2/lux, for a particular illumination and viewing angle.

5.2.3 Lighting Level (Lav)

The lighting level (Lav) is the average luminance of the road surface in the region located beyond the surface illuminated by the headlights of the car. The measurement area is defined in the EN 13201 starting from 60 m away from the car located between the first and second light pole, until 160 m from the car [42]. This region acts as the background to which objects must be seen for most driving speeds.

5.2.4 Uniformity (U_o and U_l)

U_o refers to the overall uniformity of the road surface luminance, determined by dividing the minimum luminance by the average luminance of the road surface [42]. U_l refers to the lengthwise uniformity, calculated by dividing the minimum road surface luminance along the lengthwise line parallel to the road axis by the average road surface luminance along the same line [42].

5.2.5 Edge-illuminance ratio (EIR)

The edge-illuminance ratio (EIR) is calculated by dividing the average of the horizontal illuminance at two strips (each typically 3.5 m width, i.e., the width of one lane) bordering the road at the left and right side (outwards) by the average illuminance of the road surface itself for 3.5 m strips at the left and right side (inwards) [42].

5.2.6 Glare Restriction (TI)

Glare is caused by local refraction and diffusion in the human eye around a bright light source in an otherwise dark field of view. It may create discomfort and/or hamper the visibility of objects near the bright light source. Disability glare is the impairment of the visibility of objects without necessarily causing discomfort glare [43].

In road lighting recommendations and standards for motorized traffic, the measure for disability glare is given by the threshold increment TI defined as:

$$TI = 65\frac{L_v}{L_{av}^{0.8}} \tag{5.6}$$

where L_v represents the equivalent veiling luminance due to light scattering in the human eye [42]. It is the luminance in object space which produces a retinal illuminance in a perfect eye equal to the illuminance generated by the scattering in the non-perfect eye. Depending on the glare source angle θ_i, i.e., the angle between the viewing direction towards source i and the horizontal (in degrees), the equivalent veiling luminance is defined as:

$$L_v = \left(10/\theta_i^3 + 5/\theta_i^2\right)\left[1 + \left(\frac{A}{62.5}\right)^4\right] E_{gl} \quad 0.5 < \theta_i < 1.5 \tag{5.7}$$

$$L_v = 9.86\left[1 + \left(\frac{A}{66.4}\right)^4\right] \frac{E_{gl}}{\theta_i^2} \quad 1.5 < \theta_i < 60 \tag{5.8}$$

where E_gl is the illuminance measured at the eye of source i, and A the age factor.

5.3 The Probeam Concept

In 2019, Kimura and co-authors expressed that most crashes in tunnels are vehicle rear-end and tunnel wall collisions [46]. Therefore, they and other tunnel lighting researchers considered probeam lighting as an alternative to symmetrical lighting, since it mainly illuminates and increases the visibility of the rear end of the car, tunnel walls, and lane markings on the road surface [44, 46, 47]. Increasing the amount of light in the direction of view of the driver increases the average vertical illuminance by 40% [46]. This concept, therefore, provides a higher subjective appraisal of the visibility of the rear of a preceding vehicle when compared to symmetrical low-pressure sodium lamp installations [44]. Moreover, Canazi and co-authors report higher attentional and visual performance for the elderly when exposed to probeam as compared to symmetrical lighting [122]. This may be due to more stress-free viewing conditions and the absence of glare when applying Probeam.

At pedestrian crossings, probeam is often used instead of symmetrical lighting because the road surface that serves as the pedestrian's background is not always fully illuminated with symmetrical lighting, or in some cases, the road surface does not cover the entire pedestrian's background, which makes the silhouette principle ineffective [123].

As the use of Probeam in tunnels and at pedestrian crossings indicates promising results, it becomes interesting to investigate to what extent it can be applied to highway illumination as well. There, it could contribute to improved visibility of objects and road markings, combined with reduced energy consumption. Generalization of the promising results, however, is not straightforward, since the illumination of highways largely adopts different conditions such as larger pole heights, larger distances between light poles, larger road widths, and other road lighting standards. Therefore, in this paper, the Probeam lighting concept will be investigated for illuminating highways, and the pros and cons will be discussed. This goal, however, might not be as simple as it looks. Due to the different illumination conditions of the road surface and road markings compared to the conditions induced by symmetrical lighting, the standard reflection characteristics will not apply anymore. In addition, recent information regarding the visibility and corresponding contrast thresholds will be applied.

5.4 Modelling Probeam: Proof of Concept

5.4.1 Geometry

For evaluating the Probeam lighting concept, we chose a typical Dutch highway, in particular a two-lane roadway, each lane 3.5 m wide, with 18 m high light poles located on the left side of the roadway [118]. The light poles are 90 m apart, and the driver is positioned 60 m in front of the measurement field, which extends between luminaire 2 and luminaire 3. The location of the driver is at 1.5 m in height and 4.8 m in width. Each luminaire illuminates the same area of 90 m long (the distance between two poles) and 7 m wide. This specific configuration is shown in Fig. 5.2 for a symmetrical concept and in Fig. 5.3 for a Probeam concept.

The retroreflective characteristics of the road markings require most of the light coming from large incident angles (with respect to the normal). Therefore, to illustrate the Probeam concept, the choice has been made to illuminate the measurement field only with luminaire 1. For the symmetrical concept, the same measurement field is illuminated by both luminaires 2 and 3, where luminaire 2 illuminates the first half and luminaire 3 the second. In practice, some overlap between the illuminated regions will occur within the measurement grid, but for investigating the proof of concept, sharp cutoffs are assumed in both concepts. As such, stray light contributions are neglected.

A measurement grid is established over the measurement field, and photometric calculations are performed for each point (p) of this measurement grid. The size of the measurement grid is determined according to EN 13201, with distances between the measurement points of 0.5 m in width and 1 m in length, resulting in 2639 points [42].

As a highway is (in general) a road with a moderate to high driving speed and traffic intensity, road lighting classification M4 is used. This implies that the road surface is illuminated in a perfectly uniform way (U_o and U_l are 1), with an absolute luminance of 0.75 cd/m^2 (Lav = 0.75), and an edge-illuminance ratio (EIR) of 0.3. For the road surface, the reported reflection characteristics of a CIE class 2 Dutch porous asphalt (ZOAB) are used, again representing a typical Dutch highway [32].

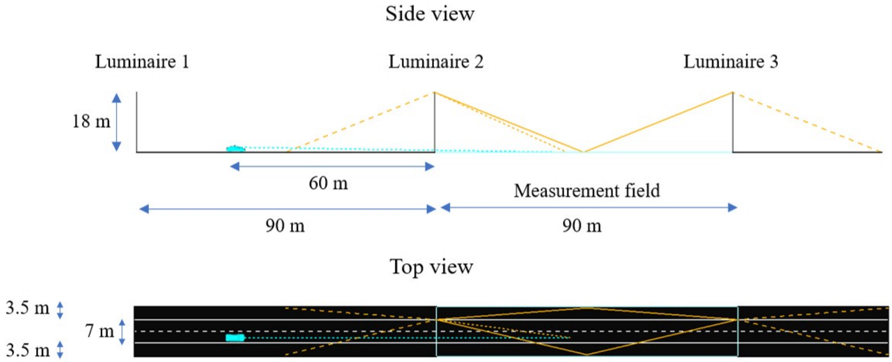

Figure 5.2: Side and top view of the Symmetrical lighting concept. The measurement field is indicated between luminaires 2 and 3 in light blue. The driver is represented by the light blue car situated at 60 m before the second light pole (i.e., luminaire 2), and the solid orange lines in both views indicate the relevant illumination pattern from a symmetrical LID (i.e., the first half of the measurement field illuminated by luminaire 2 and the second half by luminaire 3).

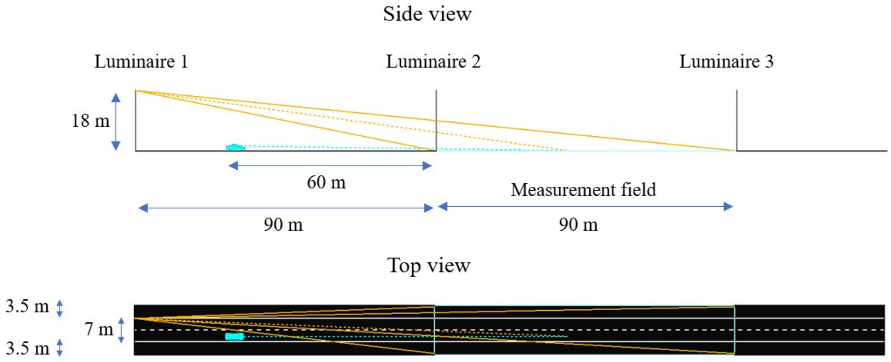

Figure 5.3: Side and top view of the Probeam lighting concept, similar to Fig. 5.2. Again, the solid orange lines indicate the illumination pattern from a probeam LID (i.e., the measurement field is fully illuminated by luminaire 1).

5.4.2 Calculation of the Luminaire LID

Starting from a uniform absolute luminance of 0.75 cd/m^2 in each point of the grid for both lighting concepts, the horizontal illuminance $E_{h,p}$ needed to produce this luminance value can be calculated in each point p, on condition that the reflection characteristics, in particular the luminance coefficient of the road for each condition of illumination and viewing, is known. These values are taken from the CIE R-table for ZOAB, and by applying Eq. 5.3, one can write:

$$E_{h,p}(\theta_i, \phi_i, \theta_o, \phi_o) = \frac{L_{Road}}{q(\theta_i, \phi_i, \theta_o, \phi_o)} = \frac{0.75}{q(\theta_i, \phi_i, \theta_o, \phi_o)} \tag{5.9}$$

where θ_i is the polar angle of incidence, ϕ_i the azimuth angle of incidence, θ_o the polar angle of viewing, and ϕ_o the azimuth angle of viewing. The reflection characteristics of this ZOAB road surface for a particular illumination geometry are illustrated in Fig. 5.4. A distinct specular reflection, superimposed on a diffuse contribution, is clearly visible. Consequently, in the Symmetrical concept, a uniform luminance can be obtained with a lower intensity of luminaire 3 in the back half of the measurement field, because of the advantageous specular reflection.

Using the reflection characteristics of the road of Fig. 5.4, the illumination distribution needed to generate a uniform road surface luminance of 0.75 cd/m^2 can be calculated with Eq. 5.9, and results in a distribution shown in Fig. 5.5 for a Symmetrical lighting concept and in Fig. 5.6 for the Probeam lighting concept. Note that in both figures, the measurement grid (i.e., main road) of 7 m is extended by 3.5 m at each side of the road (left and right, an extra lane width) to accommodate standard EN13201; this area is illuminated assuming an EIR of 0.3.

Fig. 5.5 clearly shows the effect of the strong specular reflection of the road (as shown in Fig. 5.4) on the required illumination in the Symmetrical lighting concept. The sharp transition between both halves of the measurement field will, in practice, be smoother, but it is a direct result of the simplification to sharp-edged LIDs of the luminaires, as explained before. This transition is absent when using the probeam lighting (in Fig. 5.6), where the uniform illumination pattern results from the diffuse reflection of the road surface in the retroreflective direction (see again Fig. 5.4).

Once the horizontal illuminance at each point p is known, the required intensity to each point can be determined using the basic photometric relationship:

$$I_p(\theta_i, \phi_i, \theta_o, \phi_o) = \frac{E_{h,p}(\theta_i, \phi_i, \theta_o, \phi_o) \cdot D^2}{\cos(\theta_i)} \tag{5.10}$$

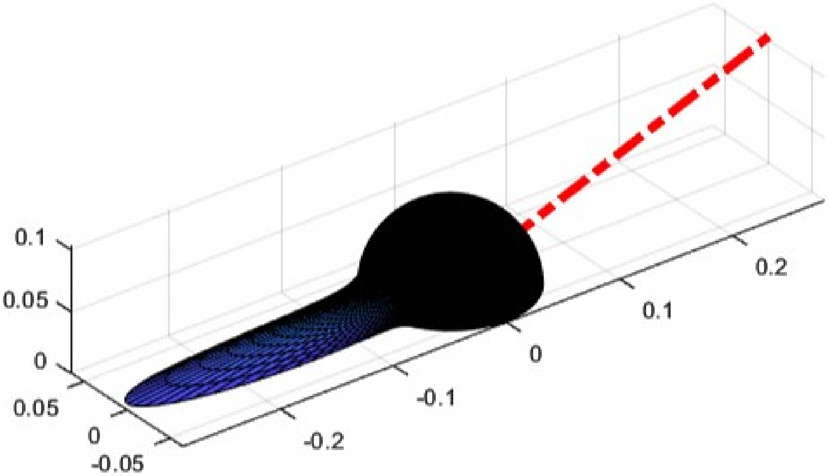

Figure 5.4: Example of the modeled reflective characteristics of a ZOAB road surface for an angle of incidence $(\theta_i, \phi_i) = (70°, 0°)$. The incident vector is shown by the red dashed line and is 0.3 sr^{-1} in length.

where D is the Euclidean distance from the luminaire to point p. Note that the contribution of headlights is neglected as the measurement field is outside their reach. After interpolating the intensities between each calculation point, the resulting LID for both the symmetric and probeam lighting are given in Fig. 5.7.

As expected, the probeam luminaire should have a very sharp and distinct asymmetric LID. Surprisingly, but understandable from the distribution of the illumination as a consequence of the specular reflection of the road surface, the “symmetrical” luminaire is also quite asymmetric.

Knowing the intensity distribution of the luminaire, the luminous flux can be calculated as:

$$\Phi = \int_0^{2\pi} \int_0^{\pi} I(\theta_i, \phi_i) \sin(\theta_i) d\theta_i d\phi_i \tag{5.11}$$

Doing so, we find that in our simplified proof-of-concept, the probeam luminaires require 14% more luminous flux (i.e., 15246 lm) than the symmetrical luminaires (i.e.,

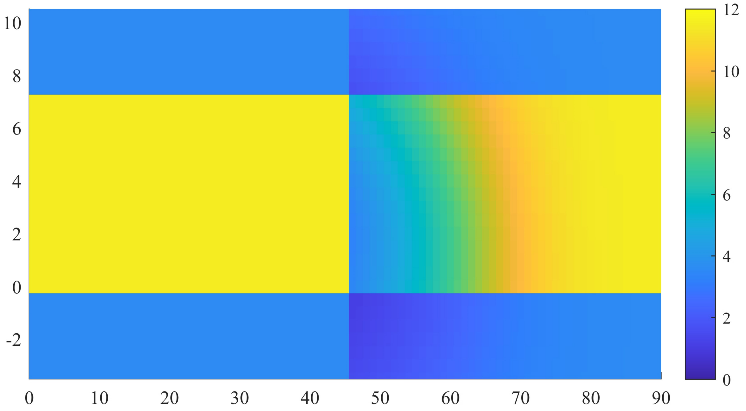

Figure 5.5: The horizontal illuminance calculated for each measurement point on the measurement grid in case of symmetrical lighting. The x-axis indicates the meters in length of the measurement grid and the y-axis the meters in width. The corresponding horizontal illuminance values are color-coded using the color bar in units of lux.

13357 lm) because the probeam luminaires do not take advantage of the specular reflection of the road.

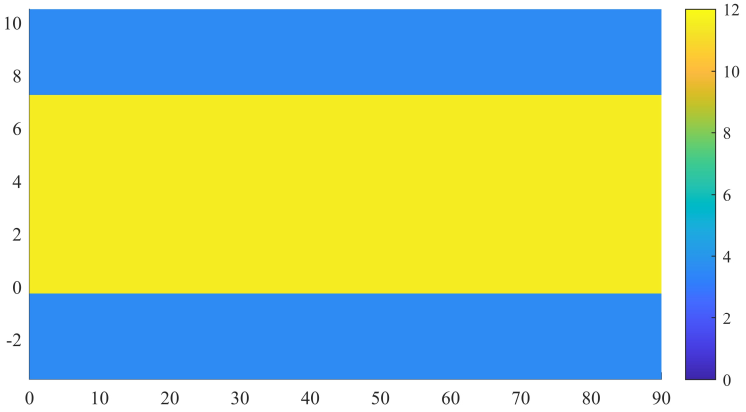

Figure 5.6: The horizontal illuminance calculated for each measurement point on the measurement grid in case of probeam lighting. The x-axis indicates the meters in length of the measurement grid and the y-axis the meters in width. The corresponding horizontal illuminance values are color-coded using the color bar in units of lux.

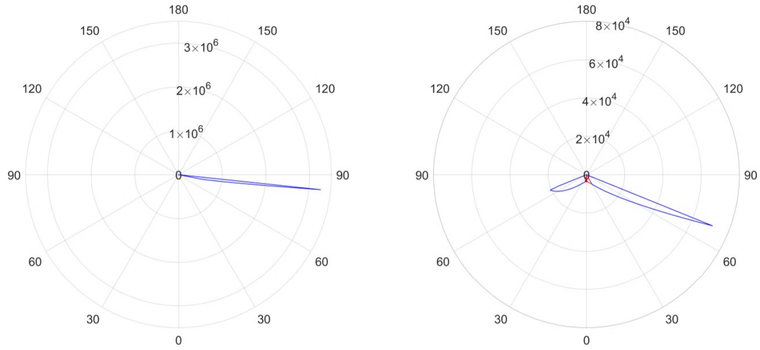

Figure 5.7: The light intensity distribution of the probeam luminaire (left) and the symmetrical luminaire (right) in the C180-C0 plane (C0 being in the direction of the driver). The radius indicates the intensity in cd. Note that for the symmetrical lighting concept, the LID of the luminaire is asymmetrical as lower intensity in the counterbeam direction is required due to the advantageous specular reflection as mentioned before.

5.4.3 Luminance Contrast for a Vertical (Non-Retroreflective) Obstacle

Once the LID of the luminaires is known, the vertical illuminance $E_{v,p}$ on any point p within the measurement field can be calculated. Assuming a vertical obstacle (for simplicity reasons assuming a height of 0 m), diffusely reflecting with a reflectance of 10%, the difference in luminance ΔL_p between the object and the road surface (0.75 cd/m^2) can be determined:

$$\Delta L_p = \frac{0.1}{\pi} E_{v,p} - 0.75 \tag{5.12}$$

Figs. 5.8 and 5.9 show the calculated luminance differences between an object and the road surface at each point of the measurement field for symmetrical lighting and probeam lighting, respectively. In both figures, the two extra lanes at each side of the road, illuminated assuming an EIR of 0.3, are included in case the object would be located aside the main road. As expected, because of an EIR of 0.3, the luminance differences are lower in these strips, independent of the type of lighting concept.

For symmetrical lighting and with the object appearing in the back half of the measurement field (see Fig. 5.8), the luminance differences are negative (equal to -0.75), and the object will only be visible in negative contrast (i.e., with the silhouette principle). When appearing in the front half of the measurement field, a small positive contrast (ΔL_p around 0.15) emerges due to the illumination from luminaire 2. In practice, the change from positive to negative contrast will not be that sharp but it definitely will create a periodic visual experience when driving. The probeam illumination (see Fig. 5.9) creates a consistent positive contrast between the object and road surface at any point of the measurement grid; this contrast gradually increases with distance due to the increasing luminous intensity. The difference in luminance is typically between 1 and 3 cd/m^2 and much higher than for the symmetrical illumination.

Although the difference in luminance between an obstacle and the road allows comparing contrast between both lighting concepts, it may be more appropriate to apply visibility models which provide contrast thresholds to allow for easy discrimination. In a recent article, Spieringhs et al. [83] have shown that visibility thresholds for road markings can be very well predicted by Adrian's visibility model [23]. In this model, the minimal difference in luminance between the target and background at threshold visibility, $\Delta L_{\text{threshold}}$, is given by:

$$\Delta L_{\text{threshold}} = k \left(\frac{\sqrt{\Phi}}{\alpha_2} + \sqrt{L} \right)^2 \cdot PF \cdot EF \cdot AF \tag{5.13}$$

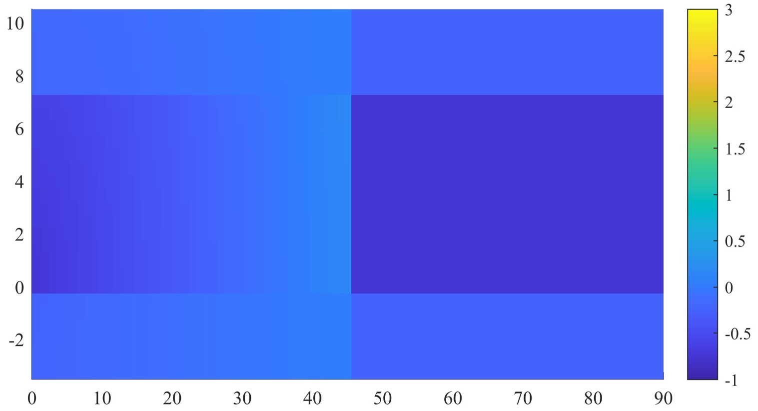

Figure 5.8: The luminance differences between a vertical diffusely reflecting object and the road surface calculated for each measurement point on the measurement grid in case of symmetrical lighting. The x-axis indicates the meters in length of the measurement grid and the y-axis the meters in width. The corresponding ΔL values are color-coded using the color bar in units of cd/m^2.

where Φ refers to the luminous flux function, α_2 to the size of the object in arc minutes, L to the luminance function, and k is a constant dependent on the experimental conditions. Finally, EF, AF, and PF are factors accounting for exposure time, age, and contrast polarity, respectively. The visibility level (VL) can be determined as the ratio of the actual luminance difference between the obstacle and road surface and the corresponding threshold luminance difference from Adrian's model:

$$VL = \frac{\Delta L}{\Delta L_{\text{threshold}}} \tag{5.14}$$

Using Eqs. 5.13 and 5.14, the average visibility level for a uniform road surface luminance of 0.75 cd/m^2, an object of 10 arcmin (i.e., 25x25 cm), a 23-year-old observer, and a 2-second exposure time results in a value of 12.6 (with VLs ranging from 0.0049 to 27.1) for the symmetrical lighting and a value of 29.7 (with VLs ranging from 7.5 to 65.1) for the probeam lighting. These numbers illustrate the higher visibility of

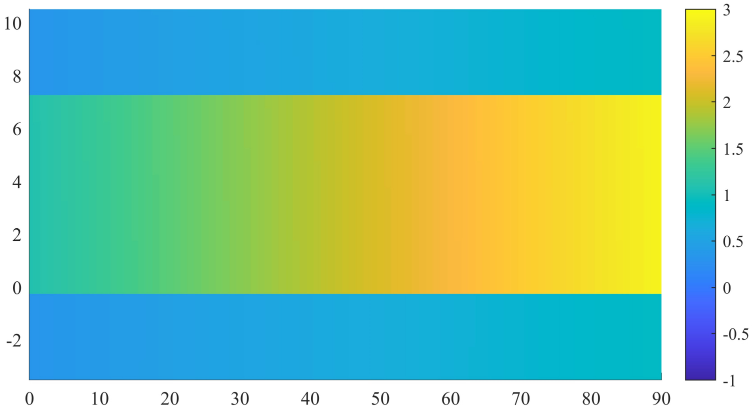

Figure 5.9: The luminance differences between a vertical diffusely reflecting object and the road surface calculated for each measurement point on the measurement grid in case of probeam lighting. The x-axis indicates the meters in length of the measurement grid and the y-axis the meters in width. The corresponding ΔL values are color-coded using the color bar in units of cd/m^2.

objects along the road when applying the probeam lighting concept. As a consequence, there may be some room to lower the luminous flux emitted by the luminaires while maintaining sufficient visibility when using probeam luminaires (see below).

5.4.4 Visibility of Horizontal Retroreflective Road Markings

Driving safely and comfortably also requires adequate contrast between the road surface and the horizontal road markings. These road markings are typically retroreflective, optimized to efficiently reflect light from car headlights up to a distance of approximately 60 m in front of the car. However, in the Probeam concept, not only car headlights but also the luminaires can contribute to the visibility of road markings, even at distances outside the reach of the headlights. As such, probeam lighting can create a guiding effect at longer distances.

In order to calculate the luminance of road markings in the driver's direction, one needs to know their retroreflective characteristics when illuminated by the road luminaires. However, retroreflection coefficients for the incident and viewing angles relevant to probeam lighting are not widely available. Therefore, we recently conducted a study specifically designed to measure and model the retroreflective behavior of road markings across a wide range of incident and viewing angles. [37] The experimental data of this study could be fitted very well to the analytical RetroPhong model for the luminance coefficient q (also called Bidirectional Reflectance Distribution Function or BRDF). One of the retroreflective materials studied in that paper is the commonly used SWARCO Limboplast D480 (Megalux 0.6-1.5 KT14) road marking with a reported R_L of 202 mcd/m^2/lx. The modelled reflective characteristics are given in Fig. 5.10 showing a clear retroreflective, specular and diffuse contribution for a typical incident angle of $(\theta_i, \phi_i) = (70°, 0°)$.

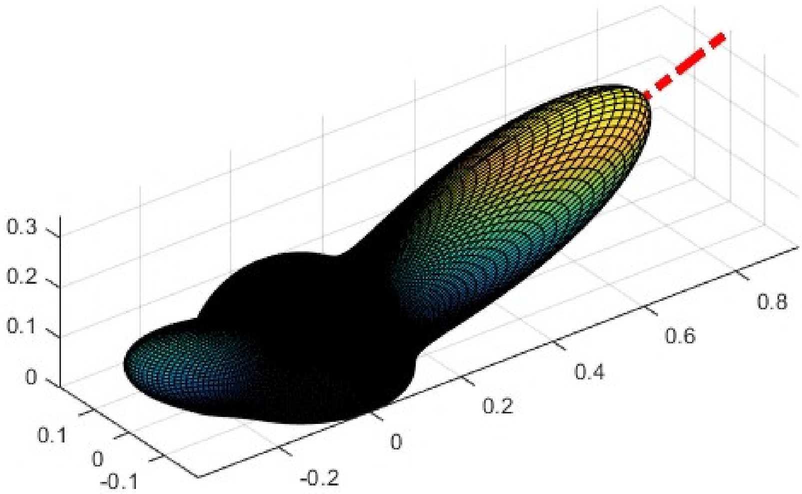

Figure 5.10: Example of the modelled luminance coefficient (or BRDF) of a SWARCO D480 road marking for an angle of incidence $(\theta_i, \phi_i) = (70°, 0°)$. The incident vector is shown by the red dashed line and is 1 sr^{-1} in length.

Using the RetroPhong model to determine the road marking luminous coefficient $q_{RM,p}$ for any incident and viewing direction, and knowing the horizontal illuminance, the difference in luminance between a horizontal retroreflective road marking and the road surface can be determined by:

$$\Delta L_p = L_{\text{Road Marking},p} - L_{\text{Road}} = q_{RM,p}(\theta_i, \phi_i, \theta_o, \phi_o) \cdot E_{h,p} - 0.75 \qquad (5.15)$$

These results are shown in Fig. 5.11 for symmetrical lighting and in Fig. 5.12 for probeam lighting. When using symmetrical lighting, the luminance contrast between horizontal road marking and road is always very low, because light at the incident angles of the luminaires is only reflected diffusively by both the road marking and the road in the first half of the measurement field; in the second half of the measuring field, the small retroreflective contribution cannot compensate for the lower illuminance (see Fig. 5.11). When using probeam lighting, the incident angles of the light are much closer to the viewing angles allowing more of the (retro)reflected light of the horizontal road marking to be visible to the driver, and as such increasing the difference in reflection between the road marking and the road.

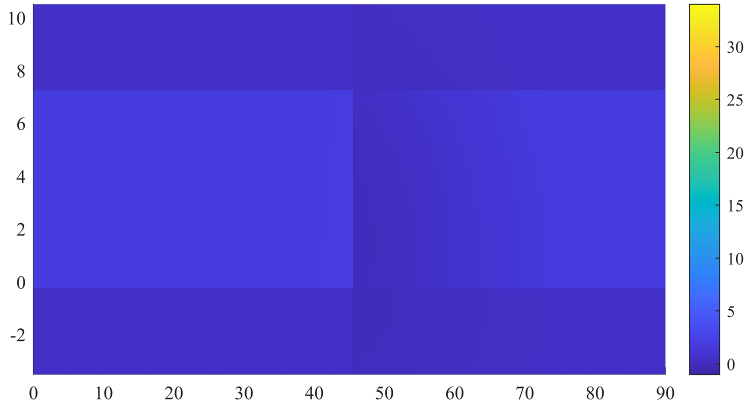

Figure 5.11: The luminance differences between road marking and road surface calculated for each measurement point on the measurement grid in case of symmetrical lighting. The x-axis indicates the meters in length of the measurement grid, and the y-axis the meters in width. The corresponding ΔL values are color-coded using the color bar in units of cd/m^2.

Using Eqs. 5.13 and 5.14 for a road surface luminance of 0.75 cd/m^2, a road marking of 5.5 arcmin, a 23-year-old observer, and a 2-second exposure time results in an average

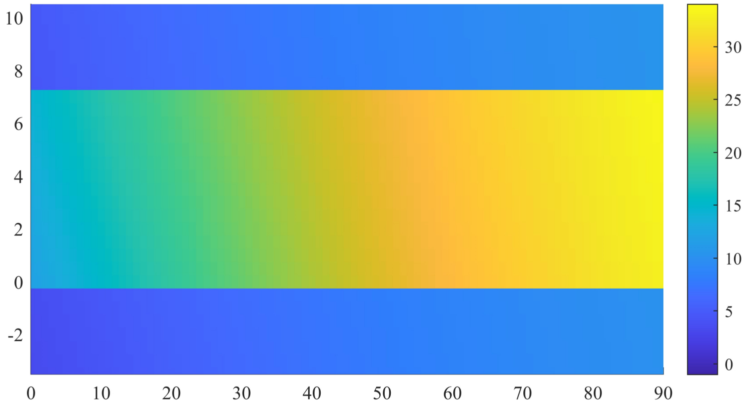

Figure 5.12: The luminance differences between road marking and road surface calculated for each measurement point on the measurement grid in case of probeam lighting. The x-axis indicates the meters in length of the measurement grid, and the y-axis the meters in width. The corresponding ΔL values are color-coded using the color bar in units of cd/m^2.

visibility level of the road marking of 10.3 (with VLs ranging from 8.0e-5 to 19.9) for symmetrical lighting, and an astonishing value of 166 (with VLs ranging from 32.8 to 337) for probeam lighting.

5.4.5 Visibility of Vertical Retroreflective Road Markings

When considering vertical retroreflective surfaces, the illumination is drastically different from horizontal surfaces, but we can follow the same approach. Using the RetroPhong model for the viewing and incident angles to a vertical surface, we can calculate the difference in luminance between a vertical retroreflective road marking and the road surface by:

$$\Delta L_p = L_{\text{Road Marking},p} - L_{\text{Road}} = q_{RM,p}(\theta_{i,v}, \phi_{i,v}, \theta_{o,v}, \phi_{o,v}) \cdot E_{v,p} - 0.75 \qquad (5.16)$$

where $\theta_{i,v}$ is the polar angle of incidence, $\phi_{i,v}$ the azimuth angle of incidence, $\theta_{o,v}$ the polar angle of viewing, and $\phi_{o,v}$ the azimuth angle of viewing, all relative to the vertical surface normal.

Again, when comparing the resulting luminance differences for the symmetrical and Probeam lighting concepts (Figs. 5.13 and 5.14, respectively), we observe a consistently positive contrast for the probeam lighting, whereas in the symmetrical lighting, the luminance differences in the second half of the measurement field are negative (i.e., -0.75 cd/m^2, since no light is falling on the vertical road marking from the light pole behind). Using Eqs. 5.13 and 5.14 for a road surface luminance of 0.75 cd/m^2, a vertical retroreflective marking of 5.5 arcmin, for a 23-year-old observer and a 2-second exposure time, we found an average visibility level of 12.3 for the symmetrical lighting (with VLs ranging from 0.022 to 62.7) and an impressive 1349 for the probeam lighting (with VLs ranging from 196.8 to 3529). The better performance for the probeam lighting is a direct consequence of the higher vertical illuminance combined with the higher retroreflectance for the smaller difference between incident and viewing angles.

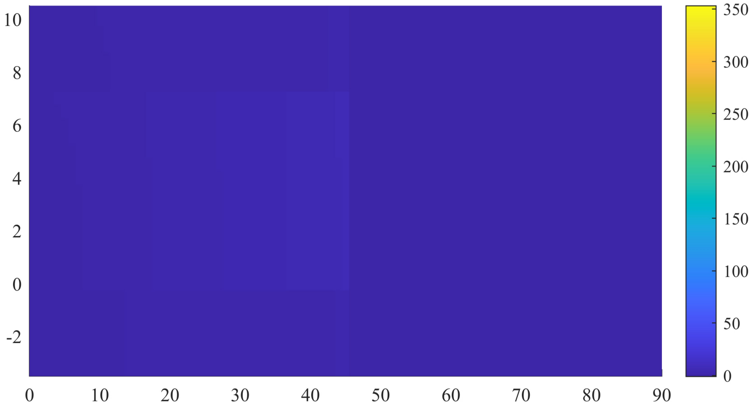

Figure 5.13: The luminance differences between a vertical road marking and the road surface calculated for each measurement point on the measurement grid in case of symmetrical lighting. The x-axis indicates the meters in length of the measurement grid, and the y-axis the meters in width. The corresponding ΔL values are color-coded using the color bar in units of cd/m^2.

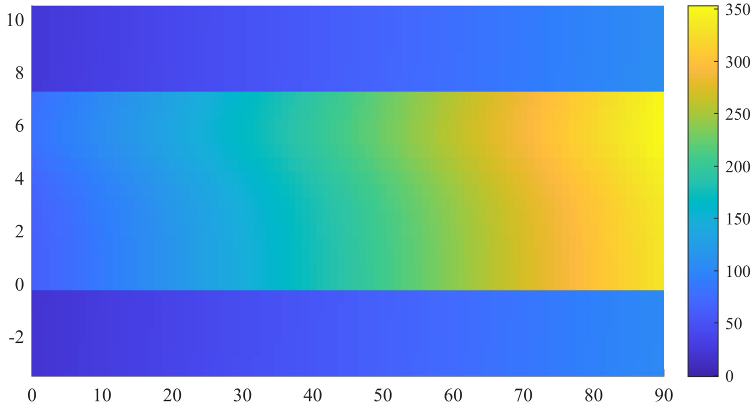

Figure 5.14: The luminance differences between a vertical road marking and the road surface calculated for each measurement point on the measurement grid in case of probeam lighting. The x-axis indicates the meters in length of the measurement grid, and the y-axis the meters in width. The corresponding ΔL values are color-coded using the color bar in units of cd/m^2.

5.4.6 Glare

Using Eqs. 5.6 and 5.7, we calculated the TI-values as specified in section 5.2.6. The resulting values are 7% and 0% for the symmetrical and probeam luminaires, respectively. The TI value of 0% for the probeam luminaires results from an E_{gl} of 0 lux (i.e., no light from the probeam luminaire reaches the eye directly), and thus the probeam lighting is very advantageous from the point of view of direct glare into the driver's eyes. This advantage becomes even stronger if we consider elderly drivers. If we replace in Eqs. 5.7 and 5.8 the age factor A from the current standard 23 years old to a 70 years old driver, the resulting TI values become 16% and 0% for the symmetrical and probeam luminaires, respectively.

5.4.7 Discussion

To outline the differences between symmetrical and probeam lighting, the luminous flux, TI, and average visibilities of a vertical object, road marking, and vertical reflector are reported for both types of luminaires in Table 5.1.

Table 5.1: Comparison of luminous flux, average visibility, and threshold increment for symmetrical and probeam luminaires.

	Flux (lm)	VL vertical object	VL road marking	VL vertical retroreflector	TI (%)
Symmetrical	13357	12.6	10.3	12.3	7
Probeam	15246	29.7	166	1349	0

Table 5.1 clearly shows that the three types of visibility levels we evaluated are much higher for probeam than for symmetrical lighting, albeit with a somewhat higher luminous flux to accommodate the road lighting standard of an average road surface luminance of 0.75 cd/m^2. Furthermore, the threshold increment only applies to symmetrical lighting (i.e., 7%), and not to probeam lighting assuming one-way traffic. The higher luminous flux of probeam lighting is a direct consequence of the starting requirement in the proof-of-concept framework of maintaining an average road surface luminance of 0.75 cd/m^2. This requirement favors the Symmetrical lighting concept as it makes better use of the specular reflectance of common road materials, allowing for the reduction of the counterbeam lobe in the LID (as shown in Fig. 5.7).

As mentioned before, the luminance requirement is inspired by the silhouette principle, where a dark object is observed in negative contrast with the road. According to our calculations in Section 5.4.3, this corresponds with symmetrical lighting to an average visibility level of 12.6. If we drop the road luminance requirement but replace it with the requirement that the same visibility level of 12.6 should be reached with probeam lighting in the whole measurement area, we would end up with a different LID for the probeam lighting, resulting in a luminous flux of 6463 lm, and thus saving 52% energy compared to the luminous flux required for symmetrical lighting.

Also additional variations of the standard common practice may reduce the luminous flux, and hence energy consumption of the probeam lighting concept. Typically, the minimum mounting height of (symmetrical) luminaires is limited in order to reduce direct glare (e.g., TI of maximum 15%). As with probeam lighting the TI value remains 0%, a lower mounting height can be considered. We explored this possibility by reducing the height of the probeam luminaires with 50%, so from 18 m to 9 m, keeping the original illumination requirement, and related LID. The visibility level of the 10 arcmin object would then increase from 29.7 (see Section 5.4.3) to 70.6 and the visibility level of the road marking would increase from 166 (see Section 5.4.4) to 574. These are significant improvements compared to using a mounting height of 18 m. If we now - in addition - drop the road luminance requirement, and use the requirement of a visibility level of 12.6 everywhere, we could dim the probeam luminaire to a luminous flux of 2722 lm and save more than 80% of energy.

A number of other variations, such as the selection of the illuminated zone with respect to the position of the probeam luminaire and allowing for an overlap between luminaires, could be explored for further increasing the performance of the probeam lighting concept or further reducing its energy consumption. However, before doing so, we consider it more important to first perform field measurements with the probeam lighting concept to check the basics of the proof-of-concept framework. Furthermore, to realize probeam lighting it is necessary to design lenses in front of the (small sized) LED sources to generate the appropriate light distribution. [124, 125]

Although the Probeam concept seems to have some important advantages with respect to visibility and contrast, there are also some practical limitations. In probeam luminaires, the light intensity is distributed over a very narrow solid angle, as can be observed in Fig. 5.7 (left). Currently, no optimized lenses exist to realize such specific light intensity distributions, and creating such lenses or luminaire designs may prove to be very complex and challenging. Additionally, the optical design is more sensitive to small deviations in the mounting of the luminaire or to weather implications such as gusts of wind. For example, for a light pole with a height of 18 m, a variation of 1 degree in the mounting position of the luminaire will result in a misalignment of 12 m on the road surface. In practice, typically there will be some overlap in the covered area of the luminaires and this variation will be less of an issue. Finally, the Probeam concept is merely limited to one-directional traffic as traffic going in the opposite direction may be heavily blinded by probeam luminaires.

5.5 Conclusions

This study aims to investigate an asymmetric road lighting concept “Probeam” for the use in outdoor lighting of highways. Based on current road lighting standards, reflection characteristics of the road surface and the geometry of a typical (Dutch) highway, LIDs were calculated for both a Probeam and Symmetrical road lighting concept. Both concepts were investigated for their performance in terms of glare, the visibility of a vertical (non-retroreflective) object, and the visibility of horizontal and vertical retroreflective road markings.

Compared to symmetrical lighting, the Probeam concept results in higher visibility levels, but at a 14% increase in luminous flux, at least when designed to meet current road lighting standards. This increase in luminous flux is explained by the specular reflection of the road surface which favors the symmetrical lighting, reducing as such the size of the counterbeam lobe. When designed to meet the same average visibility level of a vertical object in symmetrical lighting and dropping the road luminance requirement, the probeam luminaire can be dimmed, resulting in an energy saving of 52%. If, in addition, the mounting height of the probeam luminaire is halved, it can be further dimmed, resulting in an energy saving of 82%.

Chapter 6

Probeam field tests and concept update

To validate the former simulations and calculations of the Probeam concept, two field studies were conducted: a small-scale one at the KU Leuven-Gent, campus Rabot and one at the RDW testcentrum Lelystad. The lessons learned from these experiments have led to an update of the primary Probeam concept.

During the field study at the KU Leuven-Gent campus Rabot, both the Probeam and Counterbeam concepts (when observing Probeam from the opposite direction) were investigated. Symmetrical lighting was not explored due to the constraint of having only one light mast, whereas achieving accurate representations necessitates a minimum of two light masts. Conversely, in the field study at the RDW test center Lelystad, both Probeam and symmetrical lighting were compared.

6.1 KU Leuven-Gent, campus Rabot

6.1.1 Experimental setup

A parking lot at the KU Leuven-Gent, campus Rabot was used as a test field for measurements performed during some evenings in March and April 2021. The measurement setup consisted of a light mast of the brand AIC, holding a small luminaire as shown in Fig. 6.1 (right). The luminaire was an Innolumis ('Probeam') mini-Victoria 740 40W Narrow 48-60 fixture, containing 4 LEDIL $C15962_{S}TRADA -$

$2X2 - FS3$ lenses. The luminaire was mounted at a height of 4.66 m relative to the road surface and was rotated 20 degrees counterclockwise such that the peak of the intensity distribution (see Fig. 6.2 for the resulting LID) is aimed to the zone between luminaire 2 (supposed to be at a distance of 23,3 m) and 3 (supposed to be at a distance of 46,6 m) as described in the Probeam concept section of the previous chapter. The road was 3.8 m wide and approximately 80 m long (Fig. 6.1 left).

Figure 6.1: top view of the parking lot showing the position of the light pole in orange (left) and a photo of the light pole and luminaire (right).

To check object visibility, several representative objects such as a bicycle, a road marking sample, and three test plates each having a different reflectance (i.e., white, gray, and black) were used. These plates were 60 cm high and 30 cm wide, as shown in Fig. 6.3. Additionally, some pedestrians were invited to wear dark, light, or retroreflective clothing, and to position themselves at a number of distances from the luminaire. For the road markings, SWARCO 2-K LIMBOPLAST D480 SolidPlus 50 300-850 T15 M30 samples were used

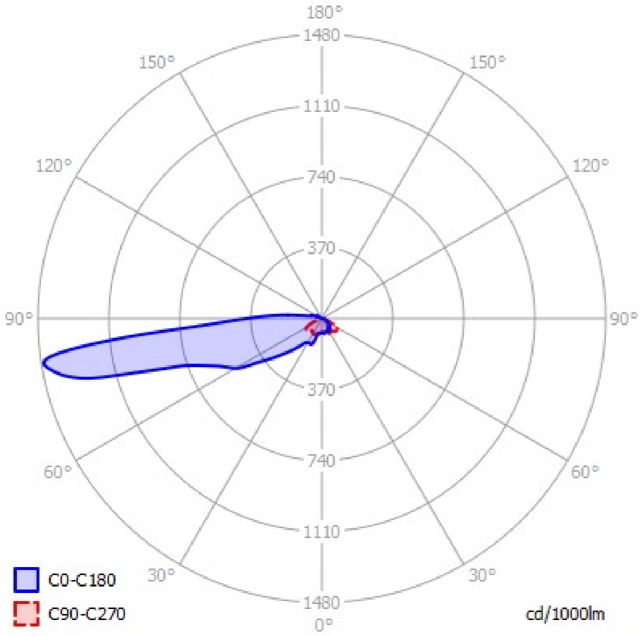

Figure 6.2: LID of the probeam luminaire as mounted (KU Leuven-Gent, campus Rabot). The C0-C180 plane is indicated in blue and the C90-C270 plane in red.

6.1.2 Photometric measurements

The measurements were performed in the evening from the moment the illumination from the ambient light, measured horizontally on the road surface, was lower than 1 lux. The measurements consisted of (a) illuminance measurements at different locations on the road surface and (b) luminance images of the road surface, road markings, and a set of test objects.

6.1.2.1 Illuminance

The illuminance meter was a Gigahertz Optik Optometer P9710 and the horizontal illuminance measurements were performed at distances (in length) of 5 m, 10 m, 15 m, 20 m, 25 m, 30 m, and 40 m away from the light mast, and at 3 positions in width, namely at 0.2 m, 1.9 m, and 3.6 m from the road edge. Measuring at distances beyond 40 m from the light mast was not meaningful, since the horizontal illuminance was reduced to less than 0.5 lux. The operator of the illuminance meter was wearing black clothing and care was taken to prevent any unwanted shadows or reflections.

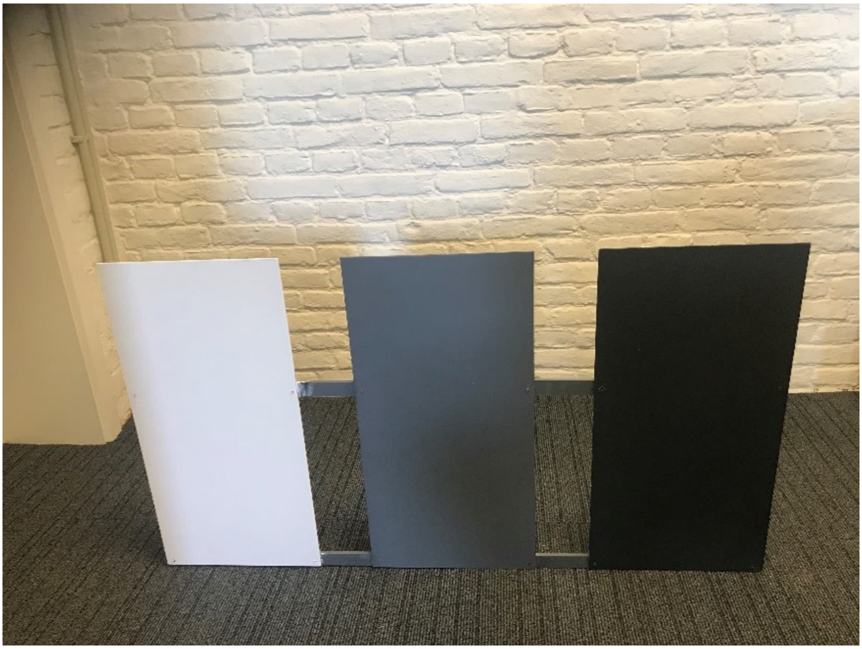

Figure 6.3: photograph of the test plates painted white, gray, and black.

The horizontal illuminance measurements are given in table 6.1. They were obtained by subtracting the recordings when the luminaire was switched off (typically a value of 0.5 lux) from the recordings with the luminaire switched on, in order to account for the ambient lighting. These results can then be compared with the calculated illuminance values using the DIALUX software for the Innolumis probeam luminaire and based on the LID measured in the lab (table 6.1).

Table 6.1: Background corrected horizontal illuminance values and, between brackets, the calculated values from the LID (in lux) for each measurement point; columns indicate the distance to the light mast in length and the rows indicate the distance from the road edge in width.

m	5	10	15	20	25	30	40
0.2	20.33 (17.53)	12.13 (9.74)	7.53 (5.09)	3.96 (2.98)	1.95 (1.60)	1.08 (0.93)	0.30 (0.33)
1.9	14.49 (12.95)	10.50 (8.53)	7.65 (4.75)	3.66 (2.96)	1.90 (1.59)	0.91 (0.92)	0.28 (0.33)
3.6	10.15 (7.80)	9.70 (6.52)	7.99 (4.55)	3.57 (3.03)	2.11 (1.63)	0.92 (0.94)	0.28 (0.33)

From table 6.1, some differences between the measured and calculated illuminance can be observed, especially near the edges of the road and at a distance of 15 m.

The measured illuminance values are on average 22% larger than the values calculated from the LID. The variation can be largely explained by the difference in temperature between the field measurements (outdoors) and the lab measurements (indoors). The LID data obtained with the large near field goniometer (LNFG) in the Light&Lighting Laboratory are taken at an ambient temperature of 25.4 degrees. The outdoor measurements, however, were conducted at much lower temperatures, close to 10 °C. The total emitted luminous flux of the LEDs is known to increase 1% per degree decrease in temperature [126], which can account for more than 50% of the observation.

Another source of deviation is the inaccuracy of mounting the luminaire on the pole. The very particular and narrow intensity distribution makes the illumination distribution very sensitive to its positioning.

6.1.2.2 Luminance

A TechnoTeam LMK5-5 Color luminance camera was used for taking luminance images. The luminance camera was set up at the position of the pole, centrally on the road in width (i.e., 1.9 m from the road edge), as shown in Fig. 6.4.

In order to illustrate the differences between Probeam and Counterbeam, the luminance camera was also positioned at 23.3 m (i.e., 5 times the mast height) away from the mast and pointing towards its direction.

Road surface and road markings

The luminance of the road marking sample and the road surface were measured at different locations, resulting in different viewing and incident angles with respect to the surface under test. Again, the luminance data has been taken with the luminaire switched on as well as off, the latter in order to get an estimate of the background contribution. Note that in table 6.2 the Probeam situation is indicative for retroreflection conditions ($\phi_o = 270$,$\phi_i = 270$) while the Counterbeam situation is indicative for specular reflection conditions ($\phi_o = 90$, $\phi_i = 270$). Note that Probeam and Counterbeam has not been measured on the same evening, yet at different circumstances.

One can conclude that

- The luminance of the road surface is slightly higher in Counterbeam than in Probeam because of the specular reflection component of the road surface.

Figure 6.4: photograph of the experimental setup including the LMK5-5 Color luminance camera.

Table 6.2: background corrected luminance values in cd/m^2 for different viewing and incident angles, for both the road marking and road surface. Distance is always in meter from the pole.

Viewing angles ϕ_o	θ_o	Incident angles ϕ_i	θ_i	Distance (m)	$L_{\text{Road marking}}$	$L_{\text{Road surface}}$
Probeam (retroreflection)						
270	73.3	270	47.0	5	1.64	0.34
270	81.5	270	65.0	10	0.86	0.16
270	84.3	270	72.7	15	0.45	0.050
270	85.7	270	76.9	20	0.21	0.018
270	86.6	270	79.4	25	0.20	0.011
Counterbeam (specular reflection, corrected for difference in illuminance)						
90	83.6	270	65.0	10	0.46	0.17
90	79.8	270	72.7	15	0.13	0.06

- The luminance of the road surface in Probeam decreases with distance from the pole mainly because the illuminance decreases. The BRDF actually slightly increases with distance from the pole.

- The luminance of the road marking is -although the illuminance is the same- always higher than the luminance of the road surface. When the incident and viewing polar angle come closer, one would expect an increasing luminance due to an increased retroreflection. However, this effect is masked by the decreasing illuminance.
- The luminance of the road markings are larger in Probeam than in Counterbeam because of the retroreflective component of the road markings.

As an illustration, a luminance measurement of a road marking sample where the viewing angle is approximately equal to the angle of incidence (condition of optimal retroreflection) is shown in Fig. 6.5. The luminance value at this position reaches 7.0 cd/m^2.

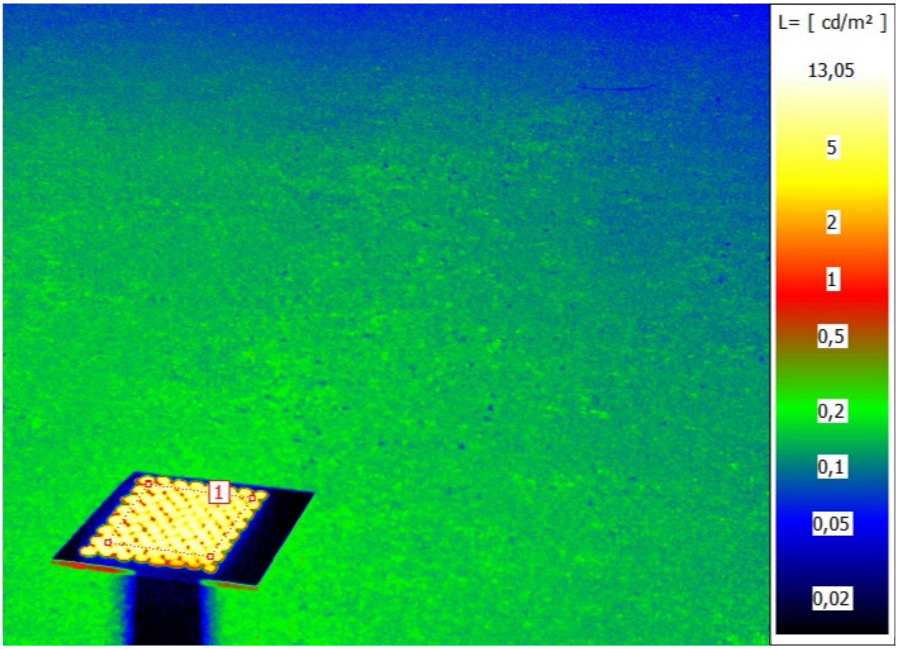

Figure 6.5: luminance image of the road marking sample where the incidence and viewing angle are approximately equal, as becoming evident from the shadow of the luminance camera (bottom left corner below the sample).

Objects

The three plates (Fig. 6.3) having a different reflectance were placed at a distance to the light mast of 10 m for probeam as well as for counterbeam illumination. A luminance image was created as shown in Figs. 6.6 and 6.7, respectively. These figures clearly demonstrate that for the white plate the contrast of the plate with respect to the road is larger under probeam illumination than under counterbeam illumination. This has 2 main reasons: (1) the much higher frontal illumination of the plate and the higher reflectance results in a high plate luminance in Probeam, while (2) the low road reflectance (no specular reflection in Probeam) results in a low road surface luminance. For the dark plate, the situation is different, illustrating the silhouette principle where the object appears in negative contrast against a brighter road surface background.

The low contrast for the dark plate in Probeam can be explained by the very low BRDF value of the dark plate (i.e, 0.02 $sr^{-}1$) compared to the larger BRDF value of the road surface (i.e., 0.07 $sr^{-}1$) at one hand and the larger vertical illuminance at the dark plate and the lower horizontal illuminance on the road at the other hand. This results in a luminance difference of 0.01 cd/m^2. This observation is in correspondence with simulations of the previous chapter. Ideally the road surface should be made darker to increase the contrast under probeam illumination. Furthermore, although the negative contrast under counterbeam lighting is relatively large (luminance difference of -0.53 cd/m^2), for symmetrical lighting it will be significantly lower due to the presence of a second luminaire that still provides light to the front surface of the object, thereby reducing the negative contrast significantly. It is therefore crucial that the next field measurements do include a comparison between probeam and symmetrical lighting

In addition to the test plates, a bike was also used as a test object. Similar as before, the bike was positioned at 10 m, and the image was taken in both probeam and counterbeam illumination, as shown in Figs. 6.8 and 6.9, respectively. Since the bike is a more complex object and non-uniform in reflectance, one can observe a similar behavior: the low reflective regions exhibit a stronger contrast for the counterbeam illumination and the high reflective regions exhibit a stronger contrast for the probeam illumination.

To further supplement and investigate the effect of Probeam, participants were positioned at a distance of 25 m wearing a retroreflective, light, and dark vest. A luminance image for the (vertical) retroreflective vest is shown in Fig. 6.10. As expected, the contrasts of the participants wearing retroreflective and light clothing were very large, indicating that a probeam luminaire at these relatively large distances can yield high visibility. The contrast of the participant wearing dark clothing was, however, relatively low, and mostly the face and pants were visible.

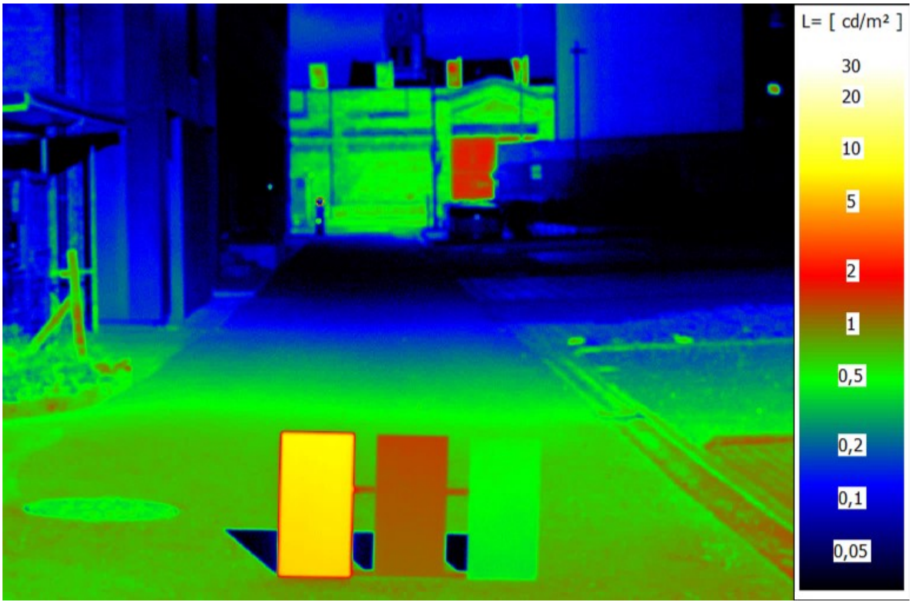

Figure 6.6: luminance image of the (from left to right) white, gray, and black test plate under probeam illumination. The test plates are positioned at 10 m from the light mast centered on the road surface. The luminance is color coded by the color bar on a logarithmic scale.

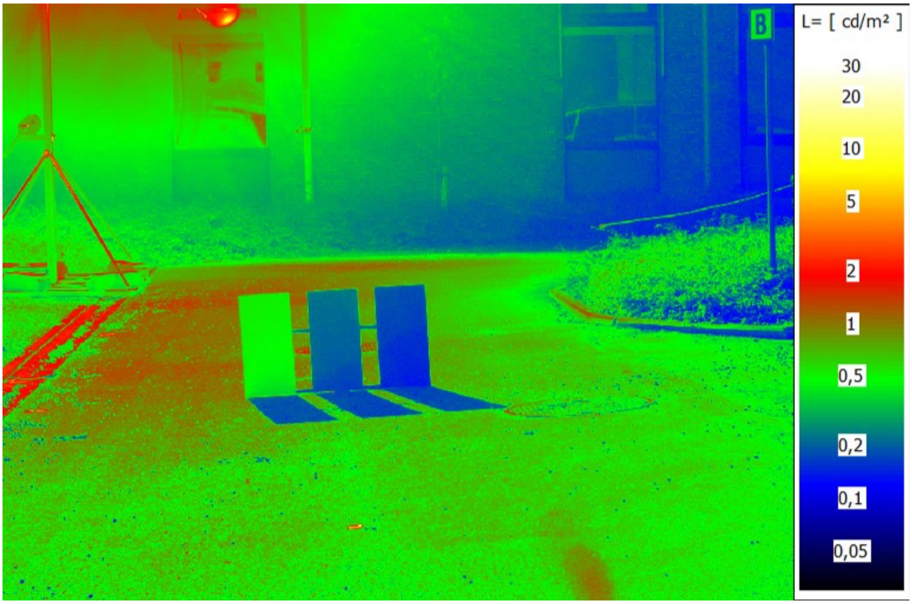

Figure 6.7: luminance image of the (from left to right) white, gray, and black test plate under counterbeam illumination. These test plates are positioned at 10 m from the light mast centered on the road surface. The luminance is color coded by the color bar on a logarithmic scale.

Figure 6.8: luminance image of the bike positioned at 10 m from the light mast using probeam illumination. The luminance is color coded by the color bar on a logarithmic scale.

Figure 6.9: luminance image of the KU Leuven bike positioned at 10 m from the light mast using counterbeam illumination. The luminance is color coded by the color bar on a logarithmic scale.

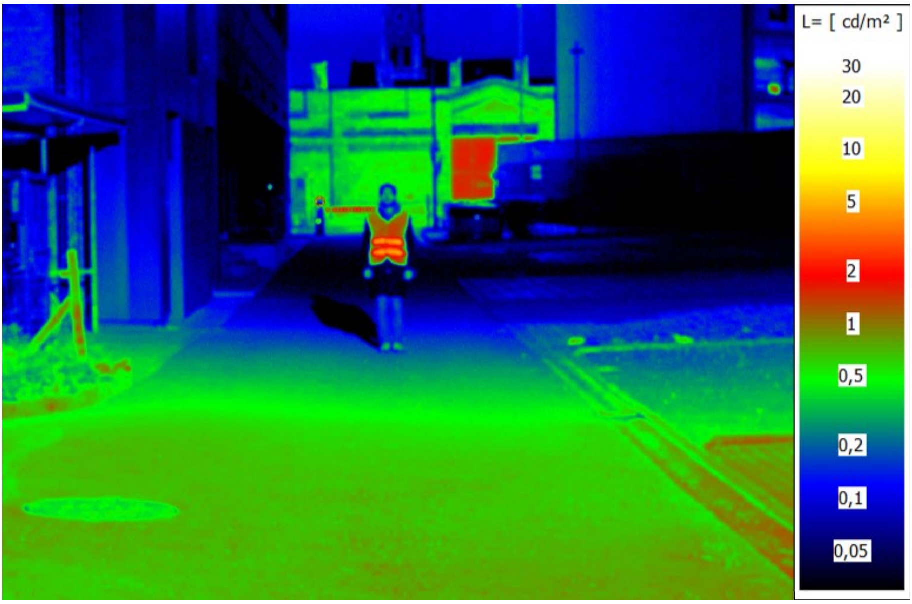

Figure 6.10: luminance image of a pedestrian wearing a retroreflective vest positioned at 25 m from the light mast using probeam illumination. The luminance is color coded by the color bar on a logarithmic scale.

6.1.2.3 BRDF

The measurement of the horizontal illuminance and the luminance at different positions allows to calculate the BRDF value from the field measurements. A comparison to the BRDF values obtained in the laboratory is however only possible in a qualitative way because the road surface and road marking materials used in the field are not the same as the small sample used for the laboratory measurements.

In Table 6.3, the BRDF values calculated from the luminance and the illuminance measurements are gathered, together with the laboratory measurement values which are reported in brackets. Although there are differences between the laboratory measurements and the values from the field study, the general patterns of retroreflection of the markings and specular reflection of the road surface are quite similar.

As expected, the BRDF values of the road marking generally are larger for retroreflection than for specular reflection, especially when the difference between the viewing angle and incident angle gets smaller. In addition, the BRDF values of the road marking are clearly larger than the BRDF values of the road surface.

Interestingly, the BRDF of the road surface appears to increase with decreasing difference between the viewing angle and the incident angle in the retroreflection direction, pointing to a retroreflective component while a more diffuse reflection was expected. The specular reflection of the road marking was also lower than expected.

Table 6.3: BRDF values for different viewing and incident angles for both the road marking and road surface in $sr^{-}1$. Distance is always in meter from the pole. The BRDF values from the laboratory measurements are reported between brackets.

Viewing angles		Incident angles		Distance (m)	$\text{BRDF}_{\text{Road marking}}$	$\text{BRDF}_{\text{Road surface}}$
ϕ_o	θ_o	ϕ_i	θ_i			
Probeam (retroreflection)						
270	73.3	270	47.0	5	0.21 (0.21)	0.043 (0.065)
270	81.5	270	65.0	10	0.41 (0.35)	0.074 (0.065)
270	84.3	270	72.7	15	0.70 (0.54)	0.079 (0.065)
270	85.7	270	76.9	20	1.01 (0.67)	0.086 (0.065)
270	86.6	270	79.4	25	1.79 (0.76)	0.10 (0.065)
Counterbeam (specular reflection)						
90	83.6	270	65.0	10	0.22 (0.22)	0.083 (0.093)
90	79.8	270	72.7	15	0.20 (0.38)	0.10 (0.12)

6.1.3 Preliminary conclusions

This very basic field study of the Probeam (and Counterbeam) concept has revealed some important insights:

1. The simulations and laboratory test results show a good qualitative correspondence to the data measured in the field. Quantitatively, some variance was observed. Temperature differences, limitations of the illuminance measurement device and the sensitivity to the exact positioning of the luminaire make a quantitative comparison between the simulated and measured values challenging. Not surprisingly, the strong dependency of the luminous flux of LED luminaires with temperature is of major influence. The performance of lighting installations can, therefore, greatly vary depending on the time of day and year.
2. Luminance values indicate a greater contrast for retroreflective or high reflectance targets under probeam illumination than under counterbeam illumination. However, for targets with a low reflectance, the counterbeam illumination could have an advantage confirming the adoption of the silhouette principle. While the difference between horizontal and vertical illumination at the road surface can be considerable under probeam illumination, this effect can be compensated when the reflectance of the vertical object is lower than the reflectance of the horizontal road surface, resulting in a quite small luminance difference. Therefore, for probeam illumination, very dark road surfaces are favorable. This is in contradiction to the requirement of the actual standards which impose a minimum road surface luminance.

Although the field measurements as described above have increased the insights about both the illumination concepts, the test site has also its limitations:

- Only a single light source was investigated. In practice, typically a number of luminaires are used and some overlap in illumination generated by these luminaires exists.
- The illuminated area was too short, ranging between 0 m and 40 m, to experience a representative highway driving experience where the illuminated area typically varies between 60 m and 90 m.
- The luminaire height was relative low, i.e., 4.66 m, compared to the typical mounting height of luminaires on the highway, i.e., varying between 9 m and 18 m.
- The luminous flux of the luminaire was rather small; the electrical power was only 40 W, whereas typical highway luminaires are consuming 200 W.

- The restricted placement and conditions only allowed to test probeam and counterbeam lighting. Optimally, also symmetrical lighting should be included.

Based on the lessons learned from this experiment, a new and upgraded field experiment in a more realistic environment has been set up.

6.2 RDW Testcentrum Lelystad

The second field study was performed at the testcentrum RDW Lelystad in an evening of December 2021. Unfortunately, in the available time slot, the weather was rainy, windy, and cold with temperatures close to freezing. Because of the rain and ice on the road surface and road markings, the absolute luminance values couldn't be obtained very accurately. In addition, the wind made the light mast vibrating, leading to some variance in the measured illuminance values as well. For this reason, BRDF-values were not calculated.

6.2.1 Experimental Setup

The RDW testcentrum is a closed oval shaped car track with three to five lanes, of which a small section, i.e., 1 lane of about 100-150 m, was made available for this study (see Fig. 6.11).

The experimental setup consisted of five light masts with a height of 9 m and placed 45 m apart. Three light masts were selected to mount a probeam luminaire, whereas the remaining two were used for symmetrical lighting. Both the probeam and symmetrical luminaires could be dimmed or switched off separately. The probeam luminaires were Innolumis ('Probeam') maxi-Victoria 740 200W Narrow 48-60 fixtures with LEDIL C15962_STRADA-2X2-FS3 lenses, whereas the symmetrical luminaires were Innolumis ('symmetrical') maxi-Victoria 740 200W Narrow 48-60 fixtures with LEDIL C17446_STRADA-2X2-LN1 lenses; the LIDs of luminaires are shown in Figs. 6.12 and 6.13.

The measurement field for the probeam luminaires was between the second and third mast (assuming that the probeam luminaire was mounted on the first mast), and the measurement field for the symmetrical luminaires was between the first and second light mast (as both were provided with a symmetrical luminaire). The measurement field was, therefore, in both cases 45 m in length and 3.5 m in width. The luminance camera was positioned 1.5 m above the road surface at a distance of 60 m from the measurement field as indicated in Fig. 6.14. The measurement points within

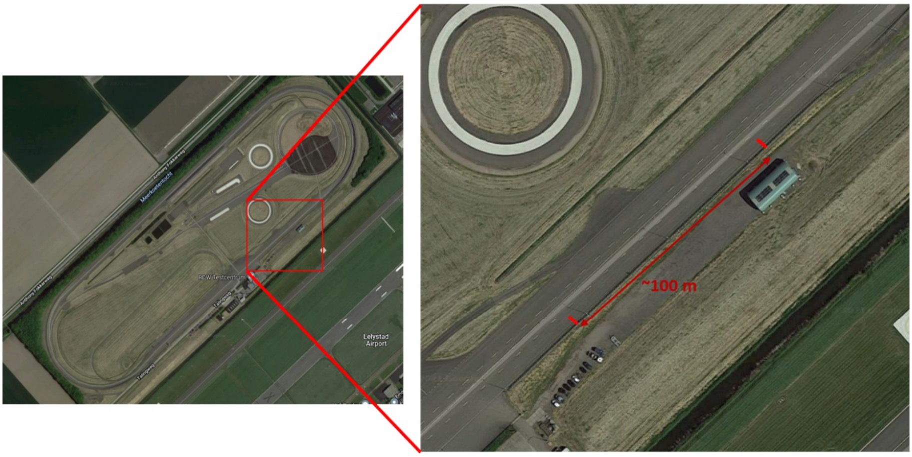

Figure 6.11: satellite view of the RDW testcentrum where the area that was used for the experimental setup is highlighted.

the measurement field were selected according to EN13201-3. The road markings consisted of type 1 3M Stamark A650 tape.

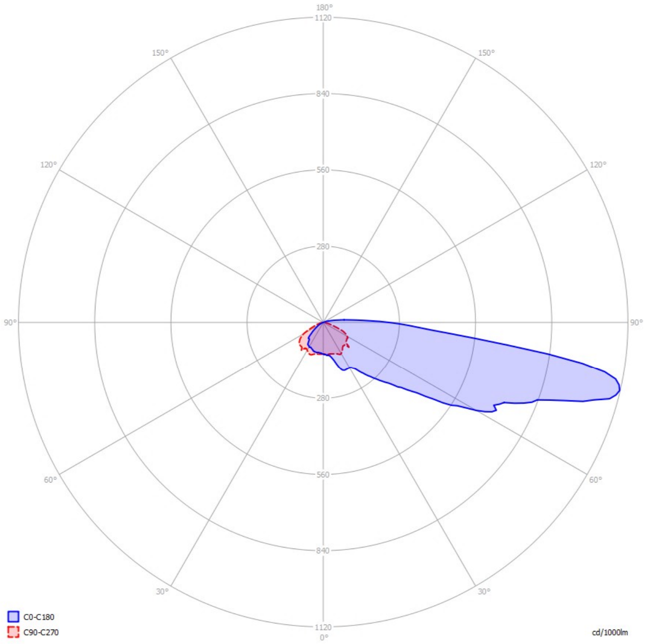

Figure 6.12: light intensity distribution of the probeam luminaire that was investigated. The C0-C180 plane is indicated in blue and the C90-C270 plane in red.

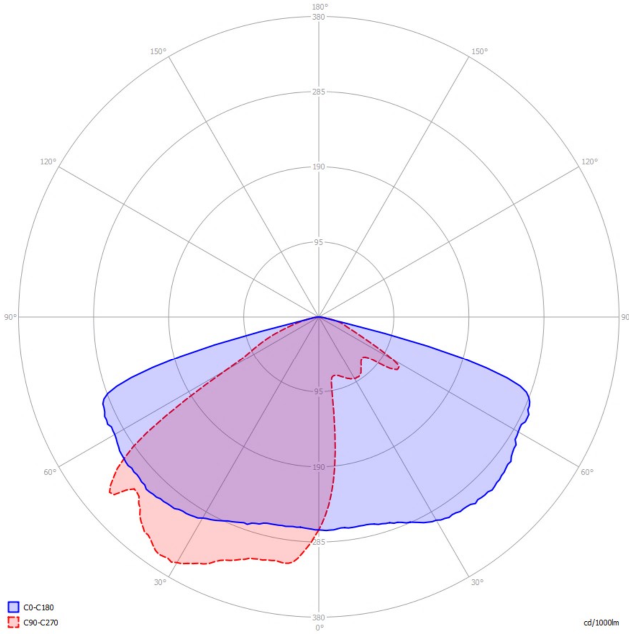

Figure 6.13: light intensity distribution of the symmetrical luminaire that was investigated. The C0-C180 plane is indicated in blue and the C90-C270 plane in red.

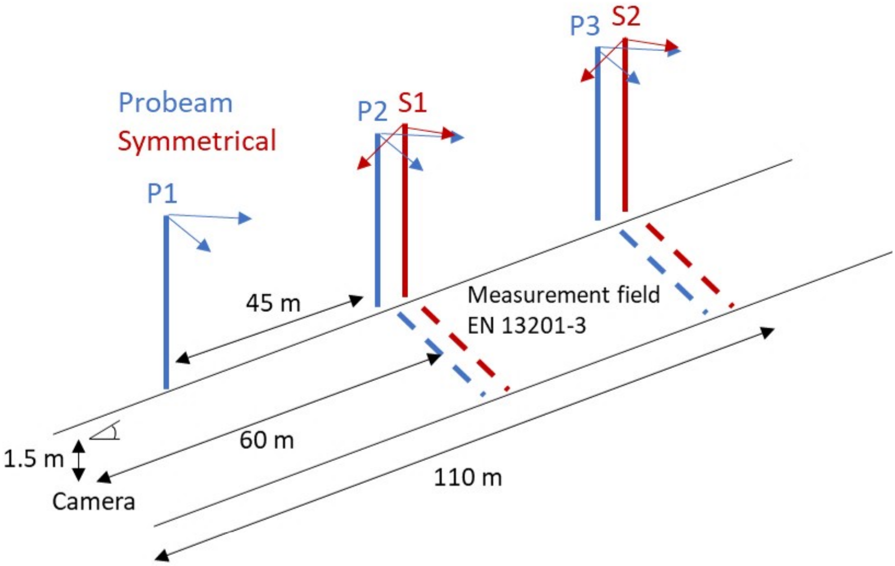

Figure 6.14: Schematic representation of the experimental setup containing three probeam and two symmetrical luminaires. The measurement field is indicated between the first and second symmetrical luminaire, and between the second and third probeam luminaire. The position of the observer (and of the camera) is indicated at the center of the road in width at 60 m distance from the start of the measurement field.

6.2.2 Measurements

The measurements consisted of luminance images of different objects and illuminance measurements at different locations on the road. A TechnoTeam LMK5-5 Color luminance camera was used for the luminance images. The illuminance meter was a Gigahertz Optik Optometer P9710. The measurements were performed in the evening after the ambient illumination, measured horizontally on the road surface, was lower than 0.1 lux.

6.2.2.1 Illuminance

The horizontal illuminance values (in lux) for each measurement point as generated by the probeam illumination are shown in table 6.4. These values are compared to the calculated values using DIALUX software and based on the LID measured in the lab. Similarly, the horizontal illuminance values for symmetrical illumination within the measurement field was measured and calculated (see table 6.5).

Table 6.4: the measured horizontal illuminance values and, between brackets, the calculated values from the LID (in lux) for each measurement point when using probeam illumination; the columns indicate the distance to the start of the measurement field in length and the rows indicate the distance in width from the road edge.

m	1.5	4.5	7.5	10.5	13.5	16.5	19.5	22.5	25.5	28.5	31.5	34.5	37.5	40.5	43.5
0.7	35.7	33.9	27.8	16	12.9	10.9	9.5	8.3	7.2	6.2	6.1	9.5	16.9	31.8	33.9
	(33.3)	(39.2)	(25.7)	(21.6)	(18.5)	(16.3)	(13.5)	(10.4)	(7.9)	(6.7)	(6.1)	(7.1)	(12.9)	(31.9)	(30.9)
2	33.1	31.1	25.4	15.2	12	9.9	8.9	7.8	6.8	5.9	6.1	10.2	17.3	34.5	30.1
	(31.3)	(33.6)	(23.4)	(18.9)	(16.8)	(15.1)	(12.8)	(9.9)	(7.7)	(6.5)	(6.0)	(7.1)	(12.8)	(34.8)	(29.5)
3.3	27.3	25.5	22.8	13.9	10.6	8.9	8.4	7.4	6.4	5.6	5.8	9.7	17.7	33.1	25.8
	(24.8)	(24.9)	(19.5)	(16.3)	(15)	(13.7)	(12)	(9.3)	(7.4)	(6.3)	(5.8)	(6.8)	(12.4)	(31.6)	(27.8)

Table 6.5: the measured horizontal illuminance values and, between brackets, the calculated values from the LID (in lux) for each measurement point when using symmetrical illumination; the columns indicate the distance to the start of the measurement field in length and the rows indicate the distance in width from the road edge.

m	1.5	4.5	7.5	10.5	13.5	16.5	19.5	22.5	25.5	28.5	31.5	34.5	37.5	40.5	43.5
0.7	103.9	87.4	59.2	36.4	22.2	15.6	13	12.8	14.2	17.3	24.1	37.9	60.4	84.8	95.5
	(88.1)	(75.2)	(51.8)	(32.3)	(20.6)	(14.4)	(11.9)	(11.2)	(12.1)	(14.7)	(21.0)	(32.7)	(51.8)	(74.2)	(86.9)
2.0	95.7	82.3	60.1	37.8	23.2	16.4	13.6	13.7	15.0	18.2	24.8	38.3	58.4	79.2	87.0
	(81.0)	(70.3)	(52.0)	(33.6)	(21.7)	(15.2)	(12.6)	(12.1)	(12.8)	(15.4)	(22.1)	(34.2)	(52.4)	(69.7)	(80.9)
3.3	86.4	74.5	58.0	39.8	24.1	16.6	14.3	14.3	15.7	18.6	25.4	39.6	57.3	68.4	73.0
	(72.0)	(64.2)	(51.2)	(34.8)	(22.3)	(15.6)	(13.2)	(12.5)	(13.3)	(15.8)	(22.8)	(35.1)	(51.1)	(63.5)	(72.3)

Generally, the relative difference between calculated and measured horizontal illuminance values for symmetrical illumination varies between 6% and 20%, the measured values being consistently higher than the calculated values. This is probably a consequence of the difference in temperature between the lab measurements (at about 25 degrees) and outdoor measurements (at about 5 degrees) and the well-known increasing luminous efficacy of LEDs at lower temperatures. The relative difference between the calculated and measured horizontal illuminance for probeam illumination shows a more complex behaviour, varying between -35% and 45%. This is probably due to the very narrow luminous intensity distribution, the large sensitivity of the data to the exact positioning of the luminaire and the impact of the wind. Furthermore, in both probeam and symmetrical illumination the horizontal illuminance first seems to decrease with distance until a certain point and then starts increasing again; this can be explained by the influence of the second light mast (i.e., P2 and S2 in Fig. 6.14).

6.2.3 Luminance

In Fig. 6.15, a scene showing horizontal road markings and vertical traffic cones is shown when illuminated with probeam and symmetric luminaires respectively.

This pictures illustrate the consistency in contrast with probeam illumination, making most vertical surfaces and horizontal road markings seen in positive contrast.

With symmetrical illumination, however, the vertical surfaces are seen in positive or negative contrast, depending on their position in the measurement field. This can create an unwanted dynamic effect while driving. The horizontal road markings are mostly seen in positive contrast although the contrast is much lower than compared to probeam illumination.

The difference in visibility of vertical surfaces is also illustrated in the luminance images of Figs. 6.16 and 6.17, showing a street scene with retroreflective warning triangles and a pedestrian wearing a retroreflective vest, illuminated with symmetrical and probeam luminaires, respectively. These figures indicate that, despite the lower horizontal illuminance and road luminance, retroreflective materials show much higher luminance values under probeam illumination than under symmetrical illumination, which is explained by the higher vertical illuminance and the more convenient incidence angles for retroreflection. In addition, Probeam illumination may cast larger shadows in front of any driving vehicle. This is, however, considered a negligible concern, since this shadow will not exceed a distance illuminated by car headlights. For example, in the case of a truck with a standard height of 4.5 m, the shadow of the Probeam illuminaire will not exceed 25 m far, which is well within the range of its headlights.

One of the main advantages of Probeam is that it causes no direct glare to the driver because the light is oriented in the direction of travel. This effect is illustrated in the full scene luminance images (luminaires included) as shown in Fig. 6.18 for

Figure 6.15: photographs of traffic cones that were placed diagonally in the measurement field illustrative of typical (vertical) objects found on the road; probeam lighting (left) and symmetrical lighting (right).

symmetrical lighting and in Fig. 6.19 for probeam lighting. Fig. 6.18 clearly shows a very high luminance in the direction of the camera (or driver) coming from the symmetrical luminaire, while in Fig. 6.19 the luminance of the probeam luminaire is hardly visible.

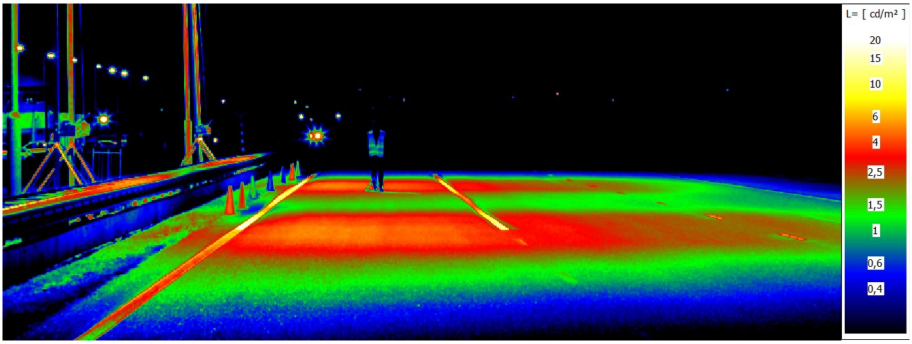

Figure 6.16: luminance image of a pedestrian wearing a retroreflective vest positioned at 30 m from the start of the measurement field for symmetrical lighting. The luminance is color coded by the color bar on a logarithmic scale.

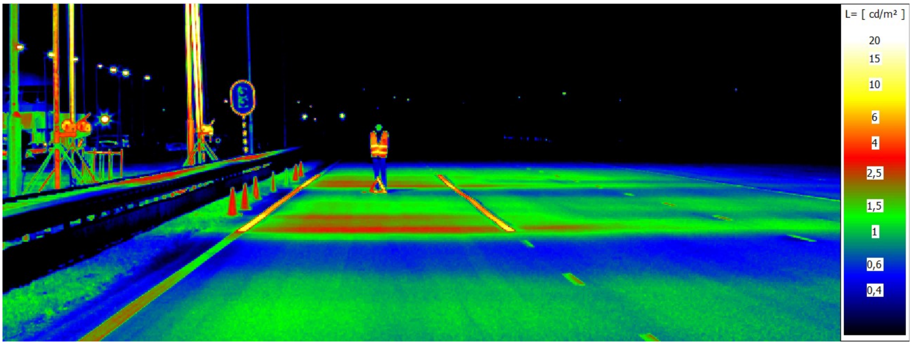

Figure 6.17: luminance image of a pedestrian wearing a retroreflective vest positioned at 30 m from the start of the measurement field for probeam lighting. The luminance is color coded by the color bar on a logarithmic scale.

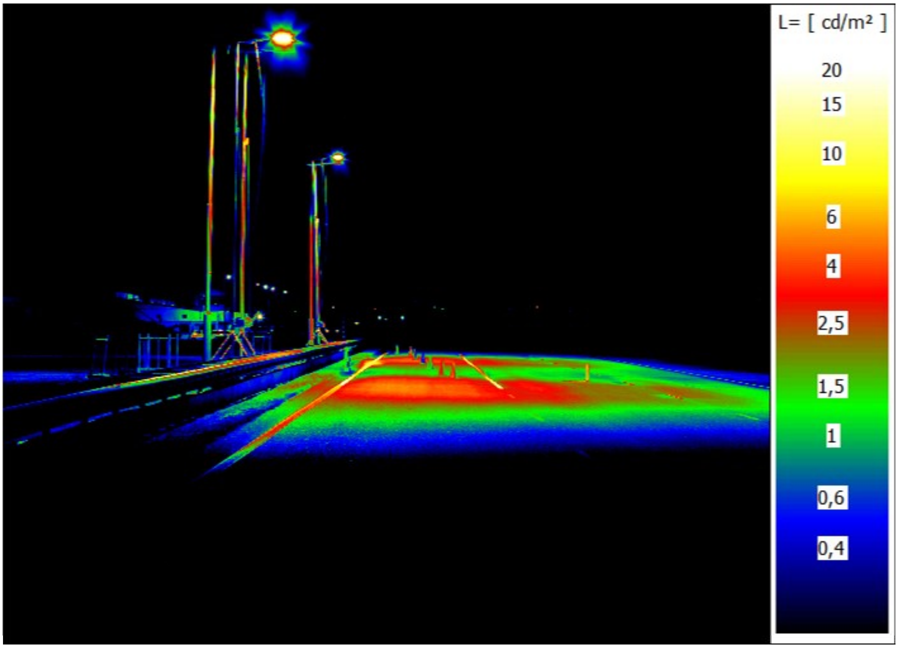

Figure 6.18: luminance image of the measurement scene including the luminaires with symmetrical lighting. The luminance is color coded by the color bar on a logarithmic scale. The maximum luminance is cutoff at 20 cd/m² to have more distinctive colors at the measurement field. The maximum luminance supplied by the luminaires was 14040 cd/m².

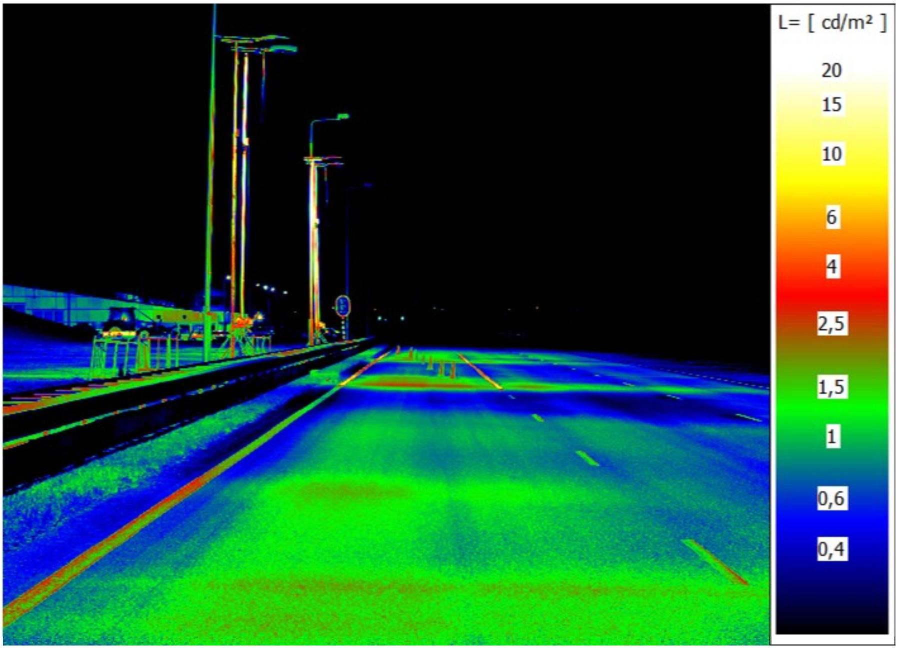

Figure 6.19: luminance image of the measurement scene including the luminaires with probeam lighting. The luminance is color coded by the color bar on a logarithmic scale.

6.2.4 Glare in Mirrors

One of the main striking observations at the RDW test lane was the glare observed in the left-side mirror of the car, an effect which is obviously much more prominent in the Probeam setup. This is illustrated in Fig. 6.20, showing a picture of the left-side mirror of the car, in which the image of the probeam luminaire can cause disability and discomfort glare.

In this field study, the cutoff angle for the reflection in the left-side mirror becomes visible is at a γ-angle of 80-85 degrees, the exact values depending on the driver's height and position and the orientation of the mirror.

In Fig. 6.12, the LID of the probeam luminaire is depicted; from those data, a similar luminance distribution can be drafted. For the conditions applicable to the car driver, the apparent surface of the luminaire becomes very small, resulting in a very high luminance, even though the intensity is quite moderate.

Figure 6.20: photograph of the glare experienced in the left side mirror from the driver's position in the car with the Probeam prototype installation.

6.3 Probeam concept update

6.3.1 Simulation

In a first step, a simulation of the luminance visible in the left-side outdoor mirror is performed in order to enhance the understanding of the parameters invoking the glare. In a next step, an updated light distribution of the probeam luminaire will be proposed to avoid glare from the mirror.

For determining the luminance of the image of the luminaire in the side mirror of the car, backward raytracing in the MATLAB software is used. A standard mirror with the size of 0.20x0.10 m (WxH) was used and centered at the XYZ coordinates (0.73, -0.58, 1.28), see Fig. 6.21, where the X-axis indicates the width along the road surface, the Y-axis the length along the road surface for the driving direction, the Z-axis the height, with the origin at the bottom of the first light mast. The eye of the viewer was positioned at the XYZ coordinates (1.30, -1.54, 1.50), assuming a driver of 1.75 m in length seated in a Citroën C3. To calculate the field zone reflected in the mirror, the coordinates of the four outer points of the mirror were determined being (0.83, -0.56, 1.23), (0.64, -0.61, 1.23), (0.83, -0.55, 1.33), and (0.63, -0.60, 1.33). These four points depict a mirror that is not rotated and is aligned with the Y-plane. In reality, however, a mirror is rotated to optimally reflect the environment to the driver. To find these optimal rotation angles with the two degrees of freedom, we used the Blender software to build a virtual 3d scene of the car in its environment, with its mirror at the location described above, and with the virtual camera at the position of the driver. The situation is shown in Fig. 6.21. In this virtual scene, the mirror was rotated, by trial and error, around both the Z- and X-axes (i.e., two degrees of freedom) to recreate the best reflected image of the environment for the position of the driver. The final reflected image by the mirror, rendered with Mitsuba, was obtained for a rotation around the Z-axis of 14.50 degrees and around the X-axis of -5.84 degrees (Fig. 6.22).

Now that the position of the mirror is fixed, ray tracing can be used to determine what the driver sees from the environment through this mirror. Starting from the observer, rays are projected to each outer point of the mirror and the reflected rays are determined. Fig. 6.23 shows the basic configuration resulting from ray tracing with the four relevant reflected rays depicted as dashed red lines.

From the four reflected rays, one can determine those luminaires which are visible to the driver in the side-mirror. To do so, the intersection of the four edge rays with the XZ plane through each luminaire is calculated. The intersection points for each of the four rays I_1, I_2, I_3, and I_4 is calculated from the normal vector of the plane of the mirror (n), any point on the plane of the mirror (p_o), the start points of the mirror edges (p_{m1}, p_{m2}, $_pm3$, and p_{m4}) and the endpoints along the reflected vector (p_{r1}, p_{r2},

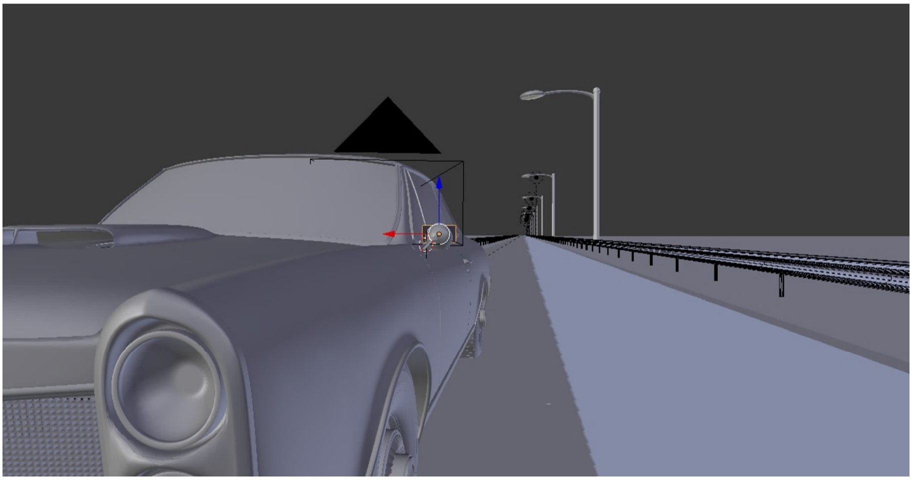

Figure 6.21: car model and the virtual scene in Blender.

p_{r3}, and p_{r4}). For one of the rays, given as an example, this results in:

$$I_1 = p_{m1} + \left(-\frac{n \cdot (p_{m1} - p_0)}{n \cdot (p_{r1} - p_{m1})} \right) (p_{r1} - p_{m1}) \tag{6.1}$$

The field of view resulting from the formulas, as depicted in Figs. 6.22 and 6.23, was practically validated in a small field study where the distance to the point where the luminaire was not visible in the car was experimentally validated.

When a luminaire contributes to the field of view of the driver through the mirror, its luminance in the drivers direction can be determined by calculating the (C,γ) angles to the mirror's normal at its centre. The intensity I of the luminaire in this direction can be found in the light intensity distribution file, and can be converted to the luminance using the surface of the luminaire A:

$$L_{\text{Luminaire}} = \frac{I(C,\gamma)}{A \cdot \cos(\gamma)} \tag{6.2}$$

Figure 6.22: the Mitsuba rendered image of the car model, virtual scene, and the rotated mirror.

Fig. 6.24 sketches the actual situation, where 12 probeam luminaires (18 m in height and 90 m apart) behind the driver are considered for their contribution to glare in the side-mirror. If a luminaire is within the field of view, it is highlighted in green and the corresponding luminance is reported. Note that the specular reflectance of the mirror has been considered to be 100%. The same situation is sketched in Fig. 6.25 for 12 symmetrical luminaires (using the characteristics of the prototypes of the real field test). Currently this field of view is determined for a standard car height, with the first four luminaires being out of sight. For trucks the field of view would only slightly change with an increase of observer height of only about 2 m, implying that only the first three luminaires are out of sight, while actually having two luminaires out of sight would be sufficient.

Comparing Figs. 6.24 and 6.25 clearly shows that the symmetrical luminaires provide a much smaller luminance in the field of view of the driver than the probeam luminaires. This is a direct consequence of the difference in light distribution for the two types of luminaires. In the Probeam concept, luminaire 1 illuminates the zone between luminaire 2 and 3. As such, the luminous intensity is mostly focused around 80 degrees (see Fig 6.2 for the LID), aiming most of the intensity towards the mirror. For the symmetrical luminaires, on the contrary, the intensity around 80 degrees is almost

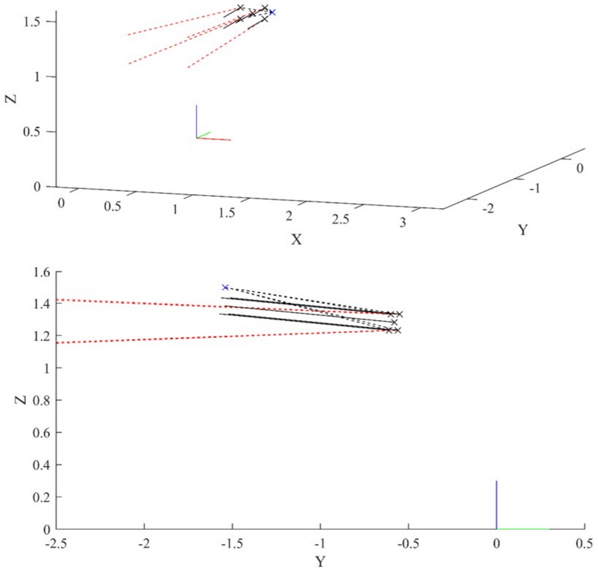

Figure 6.23: view of the backward raytracing situation in 3d (top) and 2d side view (bottom); in both figures the observer position is given by a blue cross, the four outer points and center point of the mirror are indicated with black crosses, the incident rays from the observer to the mirror are given as dashed black lines, the mirror's normal is given by the solid black line, and the backward reflected rays are indicated with dashed red lines.

zero. Note that while the luminance in the side mirror using the Probeam concept is rather high, it is still about half of what typical car headlights contribute to glare in the side mirror. Nevertheless, the glare generated by the side-mirror forces us to update the Probeam concept as proposed in the previous chapter.

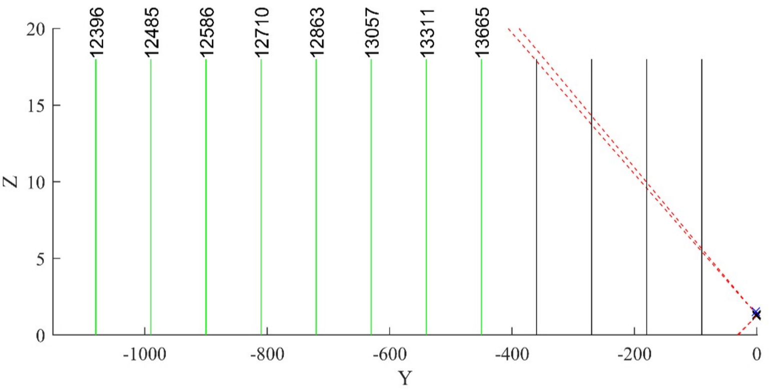

Figure 6.24: view of 12 probeam luminaires that according to backward raytracing are in the field of view of the driver through the mirror. Luminaires that contribute to the field of view are indicated in green and their luminance contribution (in cd/m²) is reported. The non-contributing luminaires are shown as black vertical lines.

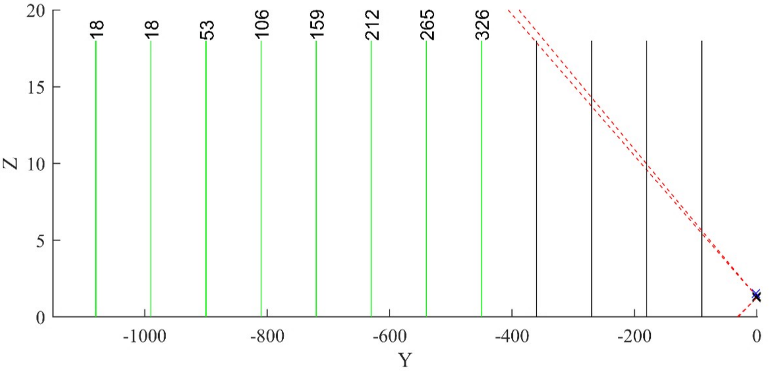

Figure 6.25: view of the 12 symmetrical luminaires that according to backward raytracing are in the field of view of the driver through the mirror. Luminaires that contribute to the field of view are indicated in green and their luminance contribution (in cd/m^2) is reported. The non-contributing luminaires are shown as black vertical lines.

6.3.2 Updated Probeam concept

In the initial proof of concept (see section 5), luminaire 1 targeted the illumination of the road surface area between luminaire 2 and 3. The corresponding large angles of incidence favor the retroreflection of the road markings from the luminaires, which indeed leads to a very good guiding effect for the driver at distances beyond the reach of the car headlights. Under this condition, the optimization of the probeam luminaire was confined to the current road lighting standards (i.e., L_{av}, U_o, U_l, EIR, and TI). However, being aware of the amount of glare observed in the car side mirror, two changes to the original concept has been made.

1. The illumination zone provided by luminaire 1 is brought closer to luminaire 1, keeping the observation angle the same but changing the incident angle. This will certainly lead to less glare induced by the side mirror reflection as the incident angles become less horizontal. However, the retroreflective contribution of the luminaires to the luminance of the road markings could become less important.
2. The optimization of the probeam luminaire is not driven by the standard anymore, but by the requirement that the visibility level as given by Adrian, and yet the safety, are maximum and by the requirement that electricity consumption is minimal.

In Chapter 2, Adrian's contrast threshold model was found to be more or less valid, so it seems to offer a good criterium for the optimization. The veiling luminance resulting from light reflected in the side mirror is also included in the optimization.

Ideally, the optimized LID of the Probeam concept would result in a visibility level VL larger than 1 at each point of the measurement field. Literature suggests, however, to use a minimum visibility level of 7 to bridge the gap between visual performance in controlled laboratory settings and actual visual performance on the road [50, 127–131]. Therefore, the requirement that VL should be equal or larger than 7 was included in the optimization.

A genetic algorithm (GA) was implemented in MATLAB , often used for solving constrained or unconstrained optimization problems. The algorithm repeatedly modifies a group of individual solutions and during each iteration, the GA randomly selects individuals from the current "population" and employs them as "parents" to generate the offspring for the subsequent generation. Across several "generations", the population gradually moves towards an optimal solution. Using this approach we optimize the LID for a minimal luminous flux with the constraint VL>= 7, the optimization results in a probeam luminaire with an LID as shown in Fig. 6.26. The illumination zone starts at 5.3 m from luminaire 1 with a much lower luminous flux of 5744 lm and higher average VL of 16.6 compared to the 15246 lm and 10.3 for the symmetrical lighting of the previous chapter, while the glare in the mirror and the direct glare by the luminaire is reduced to zero. Also, it is expected that the optical design of the luminaire will be slightly easier, compared to the previous concept, because of the peak intensity being projected at a lower γ-angle and the LID being less narrow. The updated concept meets the road lighting standard regarding U_o, U_l, EIR, and TI, except for the average road luminance which is currently 0.15 cd/m² instead of the 0.75 cd/m² as recommended in lighting standards. However, this may be considered as a minor issue, because dimming the light level on the road surface is currently already frequently used on highways to safe energy.

As an illustration, the luminance difference between a road marking and the road surface within the illumination field provided by the updated probeam luminaire is shown in Fig. 6.27.

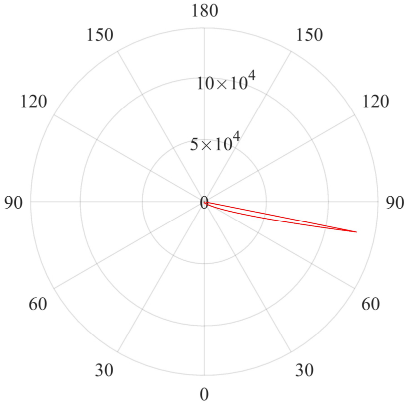

Figure 6.26: the light intensity distribution of the optimized probeam luminaire in the C180-C0 plane (C0 being in the direction of the driver which in this figure is the right half at which also most intensities are distributed). The radius indicates the intensity in cd. The angles indicate the γ-angle.

It shows an increase in luminance difference along the length of the measurement field, which can be explained by the increase in retroreflection of the road marking

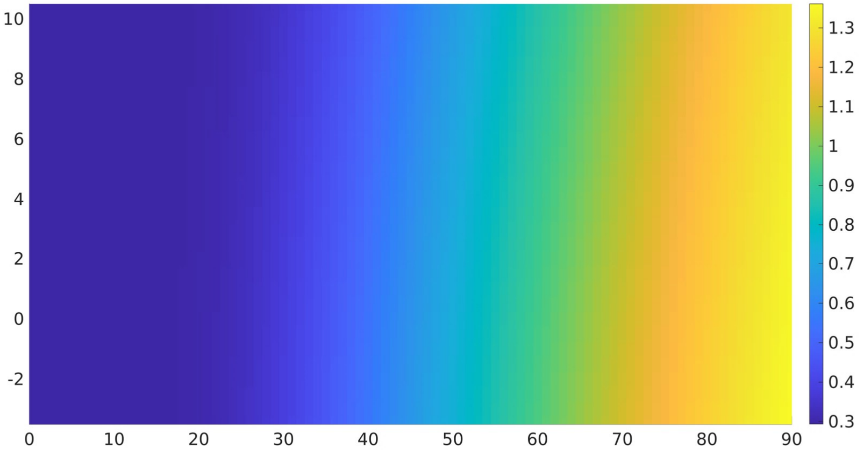

Figure 6.27: the luminance differences (in cd/m²) between road marking and road surface calculated for each measurement point of the measurement field for illumination by the optimized probeam luminaire. The X-axis indicates the meters in length of the measurement field and the Y-axis the meters in width. The corresponding ΔL values are color coded using the color bar.

while the reflection of the road surface almost remains the same. As mentioned before, the luminance differences result in a VL of the road marking of at least 7.

6.4 Conclusion

Two field studies with the aim to validate the first simulations and calculations of the Probeam concept have been performed. The first field study existed of a small-scale experimental setup on the KU Leuven-Gent, campus Rabot investigating both the Probeam and Counterbeam concepts. The results of this field study generally indicate a good correspondence between the laboratory tests, simulations, and the data measured in the field, although some variance was observed due to limitations of the illuminance measurement device, temperature differences, and the sensitivity to the exact positioning of the luminaire. Furthermore, the luminance values indicate greater contrast for retroreflective or high reflectance targets under probeam illumination compared to counterbeam. Though, for low reflectance objects, the contrast was larger under counterbeam illumination compared to probeam. This was explained by considering that the difference in illuminance is counteracted by the difference in BRDF values of the object and the road surface resulting in a relative lower contrast.

Based on some limitations of this first field study, i.e., only using one light source, a limited illuminated area, the restricted setup leading to only probeam and counterbeam illumination and a lower luminaire height, a second field study was conducted at the RDW testcentrum Lelystad. In this second field study, using 3 probeam luminaires and 2 symmetrical luminaires, similar observations were made. In addition, with symmetrical illumination, the vertical surfaces are seen in positive or negative contrast, depending on their position in the measurement field. This can create an unwanted dynamic effect while driving [132]. With probeam illumination, the contrast is always positive. However, one of the most striking observations was the glare observed in the left-side mirror, an effect that was evidently much stronger with Probeam. When aiming light intensities sufficiently far away, they will be reflected via the side mirror towards the driver generating quite large luminance values.

The field experiments resulted in an updated Probeam concept where some of the issues found were addressed. Additionally, two changes were made to the original concept, namely the variation of the start of the illumination zone and the optimization of the probeam luminaire based on the visibility level (dropping the road luminance target as imposed by the standard). This resulted in an updated probeam luminaire, creating good visibility (VL>7) and driver safety at minimal electricity consumption and absence of glare.

Chapter 7

Valorization plan: developing a new asymmetric luminaire

7.1 Introduction

As mentioned in the introduction of this doctoral thesis, the Netherlands set a goal to reduce energy consumption of road lighting by 50% in 2030 [10]. One way of achieving this is by replacing all old sodium lamps with LED lighting, which is relatively easy to do, but yields an insufficiently large reduction of energy consumption [10]. An alternative way for reducing the energy consumption of road lighting is to use dimming, which results in a reduction of the energy consumption by 30%, which is still insufficient and heavily conflicts with the government policy to reduce road accidents to zero by 2050 [133].

Therefore, the road lighting industry needs to find innovative ways to reduce the energy consumption of road lighting while maintaining traffic safety. In light of this need, this chapter describes a plan for converting the knowledge and research outcomes of this doctoral dissertation into practical applications with significant economic, social, and environmental value. This plan is worked out in collaboration with a specific industrial partner from the lighting industry, namely Innolumis. We describe the motivation for this valorization plan in detail in the next section, followed by a study of the business model, including aspects as freedom to operate and potential legal obstacles. Finally, we elaborate on the exploitation trajectory.

7.1.1 Background

To address the issue of reducing energy consumption while maintaining traffic safety, currently, most high and low pressure sodium road lighting is replaced by LED lighting. Aside from reducing energy consumption, LED lighting allows for better control of the light intensity distribution (LID), which may help to illuminate the most important part(s) of the road with minimal energy. A nice example is described in the recent literature about tunnel and pedestrian lighting research. Since a typical road surface only reflects about 8% of the light, it is most of the time inefficient to create the traditional silhouette view of objects, where mainly the road surface is illuminated and objects become visible as dark shadows. For tunnels and pedestrian crossings, therefore, new luminaires are currently being used that have their LID optimized to increase vertical illuminance and to illuminate objects rather than the road surface.

Another advancement that might help to maintain traffic safety at a lower energy consumption is related to a better contrast between the road marking and the road surface. The retroflectivity of road markings is optimized towards a high reflection of light coming from the headlights of the car in the direction of the driver: for optimal reflection of road markings, the angle of the incident light should align closely with the viewing angle. Thus, the contrast between road marking and road surface can be optimized by using incident light at acute angles, which is exactly the idea of the Probeam road lighting concept that has been described in more detail in the previous chapters.

The Probeam concept addresses a number of advantages: it increases the vertical illuminance and enhances the contrast between road markings and road surface and, in addition, Probeam also reduces disability glare, as light is mostly directed away from the (eyes of the) driver. Since disability glare reduces the visibility of objects and can cause eye strain and fatigue, it definitely negatively affects traffic safety. Finally, not only drivers, but also image based advanced driver-assistance systems (ADAS) profit from Probeam because of the enlarged contrasts, and as such this increases traffic safety for ADAS as well.

The Probeam concept is not new, as it has been investigated for pedestrian and tunnel lighting. However, there is a gap in scientific research activities investigating the use of Probeam on highways. This thesis has covered that gap, and wants to provide the necessary insights for industrial partners to develop a dedicated Probeam luminaire.

7.2 Business model canvas

The business model canvas is a comprehensive approach to understand and develop a valorization plan in a broader context. It includes all elements relevant to constructing a business, and was initially proposed by the PhD work of Alexander Osterwalder in 2005 [134]. The business model canvas exists of nine indispensable building blocks, including the key partners, key activities, key resources, value proposition, customer relationships, channels, customer segments, cost structure, and revenue streams. Although the knowledge in this doctoral dissertation is relevant for multiple societal and industrial partners in highway road lighting, we here focus on describing a business model canvas for a specific company (i.e., Innolumis) that has the aim to develop and sell Probeam luminaires with optimized lenses. Innolumis is a small to medium sized lighting company that specializes in providing light exactly where it is needed, without waste and unnecessary light pollution.

7.2.1 Key partners

The key partners in this business model include local and state government agencies, public utility companies, road marking manufactures, and commercial companies tasked with installing or maintaining road lighting. From a production perspective, the key partners are lens manufacturers, as well as custom lens designers, such as Physionary, Lumixprint, and LEDIL. In addition, also material suppliers for the LEDs, their drivers and printed circuit boards (PCBs) are relevant partners and may include companies such as Signify, Samsung and MCL.

7.2.2 Key activities

The key activities in this valorization plan for Innolumis are mostly related to the design and manufacturing of the luminaires, that include the specific lenses for the Probeam concept. For being able to do so, they depend on a full chain of activities, ranging from providing the materials and the lens design to activities related to the communication and collaboration with standardization bodies and governmental agencies. The full chain of activities consists of research and development new materials for road surface and road markings, and of new lighting concepts. This knowledge is needed for the design and manufacturing of the lenses, that subsequently will be assembed to produce the luminaires. Essential is to perform product testing at all levels from LEDs to lenses and luminaires. Once the Probeam luminaires are produced and tested, activities start including delivering and installing the luminaires, providing customer service and support, and communicating to future potential costumers and to local and state government agencies.

7.2.3 Key resources

The key resources in this business model are (production) materials, (manufacturing, characterizing and testing) equipment and skilled staff. These resources are needed to design and produce the lenses, as well as to assemble luminaires and install and maintain them on highways. For the (production) materials and equipment, there will be a need for a workshop and storage. To determine the qualifications of the luminaire (e.g., amount of LEDs and types of lenses) and the amount of luminaires for a specific scenario of a customer, there will be a need for lighting designers with expertise of the Probeam concept.

7.2.4 Value proposition

The basic value proposition of the Probeam concept is reducing energy consumption while maintaining traffic safety, and as such addressing the current needs of mainly governmental agencies. The Probeam concept differs from competitive concepts in that it removes (disability) glare, increases the vertical illuminance, increases visibility levels of road markings and objects, and results in an increase in driving comfort. Cost savings can be realized by dimming the probeam luminaires to acceptable visibility levels. The value proposition for Innolumis specifically is that it may provide road lighting luminaires for this Probeam concept.

7.2.5 Customer relationships

Customer relationships are key for realizing a business. The final customers of the Probeam concept are governments providing specifications to luminaire manufacturers for an optimal light installation at minimal costs. Luminaire manufacturers have to assemble and provide maintenance; they depend themselves on component manufacturers. There are hardly any changes to LEDs or driver components needed for the Probeam concept, but lens components must be modified significantly. The luminaire manufacturers for the Probeam road lighting concept, therefore, are mainly dependent on the lens manufacturers. In turn, they depend on lens designers who provide the specifications for the lens production.

Typically in the road lighting industry, customer relationships between governmental institutions and luminaire manufacturers are highly important. These relationships involve providing pre- and post-sales support, and providing high-quality products and services, and therefore, strongly build upon trust in each other. The latter can be realized by sharing knowledge and results of studies performed by well-established research institutions such as KU Leuven (i.e., Light&Lighting Laboratory) and TU/e. Setting up field tests that visualize the potential of the product and striving for co-creation can be effective tools in constructing a fundamental base of trust with current and future clients. Sharing free samples and sharing knowledge via fairs and conferences can help to reach new customers and to build new customer relationships.

7.2.6 Channels

The channels to sell possible probeam luminaires are the governmental institutions for road lighting. These channels are reached through direct sales, and via intensive contacts, since buying luminaires for illuminating a highway is a long-term substantial investment. Additional channels can be established through existing contacts as well as through knowledge institutions within the lighting industry (such as Groen Licht Vlaanderen (GLV), Belgisch Instituut voor Verlichtingskunde (BIV), Intelligent Lighting Institute (ILI), Openbare Verlichting Nederland (OVLNL), and Nederlandse Stichting voor Verlichtingskunde (NSVV)), through important fairs (such as the 'lichtdag', 'dag van openbare ruimte', 'vakbeurs ruimte en licht', and 'Future Lighting'), and through (online) marketing or business channels such as LinkedIN, [inst] Allicht, and LED professionals. The most cost efficient channels are the direct relationships with the clients.

7.2.7 Customer segments

The main customer segment are the state governmental agencies responsible for the maintenance and practical execution of public works, for example Rijkswaterstaat (NL) and Agentschap Wegen & Verkeer (BE). These state governmental agencies provide the largest potential for a market of the Probeam concept, being – at the moment – mainly applicable to highways for mostly one directional traffic. Other customers related to this customer segment are, as already mentioned in the key partners, public utility companies (i.e., subcontractors for government agencies, such as: SPIE, van Gelder, Citytec, Swarco, etc.) and other commercial companies tasked with installing or maintaining road lighting installation.

7.2.8 Cost structure

The cost structure mainly consists of costs for assembling and delivering the luminaires, including costs for buying the components as well as the assembling and testing equipment, and costs for the required personnel. Based on the study by Lee (2022) [135], luminaire manufacturers of outdoor luminaires are facing six main business costs, namely, LEDs, lenses, drivers, assembly, overhead (i.e., personnel, rent, development, and testing), and housing (i.e., housing of the light source, heat sink elements, electrical connectors, and mechanical fasteners). In addition, Lee mentions that the retail price includes a mark-up of typically about 20% to 30%. For an average standard outdoor luminaire in the 200 W power range, the total costs are estimated at around 420 euros with a retail price of 546 euros excluding shipping costs [135]. The distribution of these costs is 9% to the LEDs, 5% to the lenses, 16% to the driver(s), 8% assembly costs, 4% to overhead, and 58% to the housing and related components. Considering a minimum of 4000 km of highway (excluding state roads/highways) in the Netherlands and Belgium, assuming a light mast distance of 90 m (i.e. worst-case scenario) and two luminaires per light mast (one for each direction), the minimum market size for retrofitting in the Netherlands and Belgium would be almost 90 000 luminaires. Assuming that on average 15000 luminaires are sold per year (i.e., 1250 luminaires per month) would imply that a small to medium sized lighting company, such as Innolumis, has on average 47250€ monthly costs on LEDs, 26250€ on lenses, 84000€ on drivers, 42000€ on assembly, 21000€ on overhead, and 304500€ on housing, summing up to a total monthly cost of 525k€. By reducing the luminous flux, the Probeam concept could save on equipment costs, requiring fewer LEDs, lenses and drivers, and thus also reducing the housing costs. Probeam, however, would likely require larger overhead and lens costs for including a dedicated lighting designer with expertise of the Probeam concept and manufacturing the customized lenses.

Not included yet in this cost structure are the transportation costs. They are though less important for the business model of Innolumis, since transportation costs are typically transferred directly to the customer. These costs typically depend on the size of the order, and transportation in general is done by dedicated logistics companies.

A specific type of costs that needs to be taken into account are patent rights in case the knowledge for designing the Probeam concept is not generated by Innolumis itself. In the particular case of this project, where the knowledge is generated in the collaboration with KU Leuven and TU Eindhoven, Innolumis needs to incorporate costs for paying patent rights, where these costs will depend on the scope, the phase, and the number of patents they need to take into account. The procedure for a patent application is summarized by KU Leuven Research & Development (LRD) in 4 phases. The first phase is the reporting phase, followed by the second phase, in which the priority of the patent application is determined. For these two phases, LRD carries the costs. If considered relevant, a patent then enters the third phase, consisting of an international Patent Cooperation Treaty (PCT). In this third PCT phase, there are two types of costs namely those for filing an application for the search report, and those for supplementary search, each estimated to about 10000-15000 and 4000 euros, respectively. In the last phase, a patent is submitted to different countries and regions to be granted. This phase is accompanied by four types of costs: the submission costs (about 2000-6000€), the costs to get the patent granted (about 2000-10000€), costs when the patent has been granted (about 500-4000€), and cumulative annual fees (about 3000-17000€), all per country or region. So, in case KU Leuven wants to protect its knowledge on the Probeam concept in patents, they have to decide in which countries they submit the patents, as costs rise steeply with each country or region in which the patent is granted. Innolumis needs to take into account that they will have to pay patent rights if they want to operate in countries in which KU Leuven has protected the Probeam concept.

7.2.9 Revenue streams

The revenue streams for Innolumis include the sales of the outdoor luminaires, as well as associated services (i.e., installation, replacement, and maintenance). In case Innolumis has part of the patent rights, it can also expect revenues from patent royalties. In addition, governmental subsidies may be expected in case of a new highway lighting system with clear governmental advantages.

The revenue stream consists of the 30% markup on top of the costs of 420€, resulting in a sales price of 546€ per luminaire. The amount of markup often depends on the price set by the client. Assume Innolumis could sell 1250 luminaires per month with a 30% markup price, then the revenue stream per month would result in 682.5k€. Following the industry standard L70 for the lifetime of a LED (i.e., a minimum of 50000 hours), and including other practical factors influencing the lifetime, a LED luminaire lifetime can range anywhere from 10000 to 50000 hours. Considering an outdoor luminaire that produces light about 8 hours a day would imply that the probeam luminaires would be functional from 4 up to 19 years. Initially, the replacement contracts will generate large revenues, however, over time will decline because of the long lifetime of LED luminaires. After around 5 to 10 years, maintenance revenues will start to come in.

The revenue from subsidies largely depends on the approved applications. The costs associated with development and patent application may be covered by a subsidy proposal filed by Innolumis to for example Interreg Vlaanderen-Nederland. Interreg supports regional development of cross-border projects. Since Innolumis operates in both the Netherlands and Belgium, there is a large probability for an interreg European fund. The revenue of this subsidy can range from 7000 to 13000 euros per month up to 4 years.

Based on the expected monthly costs (i.e., 525k€ excluding any development or patent costs) and expected monthly revenues (i.e., 682.5k€) for 1250 luminaires per month, the business could be positive, provided there is freedom of operation, and any development costs or patent costs can be covered by governmental subsidies.

7.3 Freedom to operate (FTO)

To supplement the business model canvas and determine any legal barriers that could prevent the commercialization and development of the business model, a freedom to operate (FTO) analysis is conducted. We review relevant patents, patent applications, trademarks, and other intellectual property rights related to the technology, as well as any potential problems with regulations and compliance, and describe strategies to address them.

7.3.1 Scientific literature

A scientific literature overview regarding Probeam has already been given in the preceding chapters. For reason of completeness, they are summarized in this paragraph.

Road lighting makes essentially use of luminaires having three types of LID: Symmetrical, Counterbeam, or Probeam. Until now, only the symmetrical lighting is used in practice on highways. In tunnels, however, more often a combination of probeam and counterbeam lighting is used. Counterbeam is often used at the entrance of tunnels to improve the transition from the outside of the tunnel to the inside of the tunnel. Probeam is sometimes used within tunnels to create higher vertical illuminance, and as such a higher positive contrast of objects with the road surface.

In 2007 Lee and Lee published their research on a simulation analysis for the implementation of Probeam in tunnels in the journal of Korean Tunneling and Underground Space Association [48]. In their study, they simulated four different lighting conditions at the end of the tunnel, two conditions with a probeam luminaire with a triangular shaped LID and two condtions with a symmetrical LID. This is one of the first studies mentioning the LID of a probeam luminaire, albeit with an LID that is significantly different from the very narrow probeam LID described in the previous chapters of this manuscript.

Another published study on the use of Probeam in tunnels is by Sato and Hagio in 2014 [44], where they describe the replacement of symmetrical (sodium) lighting with probeam (LED) lighting at several places in Japan. Despite mentioning Probeam, the corresponding LID is not published.

Also in 2014, Hirakawa, Karasawa, and Yoshida [47] describe a comparison between symmetrical lighting and probeam lighting. The probeam luminaires used in this study follow a slightly more peaked LID directed at an incident light angle of 45 degrees, which is still substantially different from the much narrower probeam LID used in highway lighting that is directed at an incident light angle closer to 80 degrees.

Later in 2018, Renzler et al. [45] created a road tunnel model in which they varied driving speed, brightness, luminaire distance, and luminance distribution. In this study they analyzed three different LIDs, namely Symmetrical, Probeam, and Counterbeam, where the probeam LID exists of two intensity lobes, with one directed at an incident angle of about 20 degrees and the other at 70 degrees.

Besides tunnel lighting, another application where the Probeam technology has been investigated and implemented, is at pedestrian crossings. Tomczuk, in 2012 [49], started investigating the use of Probeam for this kind of application. In 2019 Tomczuk et al. [123] published a new study about the lighting requirements (i.e., luminance of the pedestrian and vertical illuminance at the pedestrian) for pedestrian crossings when using positive contrast. In this study, Tomczuk et al. introduced lighting requirements for asymmetric lighting, including Probeam. He used a simulation to show the effectiveness of the light source for different LIDs. The resulting probeam LID was directed primarily at an incident angle of 40 degrees to increase the vertical illuminance of pedestrians, again different from the probeam LID used to illuminate highways.

In conclusion, some studies investigated Probeam for their use in tunnels and at pedestrian crossings, however, none focused on the application of highway lighting. The probeam LID for the use of highway lighting is found sufficiently different to the probeam LIDs used in tunnel lighting and at pedestrian crossings in either shape or directed incident angle, indicating a large degree of freedom to operate based on scientific literature.

7.3.2 Patents

Besides the scientific literature it is also important to determine the patent landscape of the Probeam lighting concept. A patent search was performed to determine relevant patents and applications of the Probeam concept. The Espacenet database, a database with access to over 140 million patents in Europe and worldwide, was used. In total, four different queries were applied to the Espacenet search engine: ‘Probeam’, ‘Probeam + road lighting’, ‘Probeam + lenses’, and ‘Probeam + luminaire’. The results in terms of number of potential competing patents are shown in Table 7.1.

The initial inquiry ‘Probeam’ provided 36 search results, of which only 8 were relevant to the Probeam concept. The other 28 patents dealt with energy modulator systems and radiation analysis apparatus and much more. The second inquiry ‘Probeam + road lighting’ provided 9 results, of which only 8 were relevant. These were the same patents as found with the first inquiry search. These relevant patents provide

Table 7.1: Results of the patent search in the Espacenet database for four different (combinations of) keywords.

	Keywords	Database	Raw number of patents
1	Probeam	Espacenet	36
2	Probeam + road lighting	Espacenet	9
3	Probeam + lenses	Espacenet	4
4	Probeam + luminaire	Espacenet	4

solutions for lighting in tunnels and mention only mechanical implications to the luminaire as a solution; none mentioned the use of customized lenses or the use of Probeam in outdoor lighting. The inquiry of ‘Probeam + lenses’ provided 4 results of which none were relevant. The last inquiry ‘Probeam + luminaire’ provided 4 results, all of which were relevant to Probeam road lighting. However, again, these patents focus heavily on tunnel lighting and mechanical changes in a tunnel luminaire using very different LIDs compared to the Probeam concept for the lighting of highways. All relevant patents with international patent classification (IPC) were issued from Japan with the applicants being, Toshiba Lighting&Technology group, Panasonic corp., Matsushita electronics works, and Koito Kogyo.

Although probeam lighting is well known, based on this patent search we can conclude that no no patented works are available on probeam road lighting outside tunnels. The LID of the Probeam concept for lighting of highways is sufficiently unique and currently not yet patented, which means there is a great deal of freedom to operate.

7.4 Exploitation trajectory

In this section, the timeline for market entry and the impact on society for the general exploitation trajectory is discussed. This includes a subsidy proposal and the first prototype test.

7.4.1 Timeline for market entry

Innolumis could start a market validation study, in which they collaborate with standardization bodies and governmental agencies to understand the practical requirements for using probeam lighting on highways. They then need to team up with a lens designer and manufacturer to produce the components needed to construct luminaires for the study. Meanwhile they can apply for an interreg European subsidy fund to cover future development and patent costs of the customized probeam lenses. Using the new customized probeam lenses, an early prototype can be created. This prototype can then be tested at the innovation project in the Netherlands called innovA58 and possibly adapted to different dutch highways. When successfully tested, Innolumis can work towards a finalized probeam luminaire. Market entry will be first in close collaboration with Rijkswaterstaat to increase the adoption rate of Probeam, and can then later be extended to different government institutions towards a more global market.

7.4.2 Impact on society

The development of customized probeam lenses will result in luminaires that increase driver safety and comfort; Probeam can solve disability glare for older drivers, increase vertical illuminance, provide consistency in contrast (i.e., positive contrast), and (optimally) use the retroreflective properties of road markings with glass beads. Depending on the adoption rate of Probeam and a corresponding shift in current lighting standards, using customized probeam lenses allows for a reduction in energy consumption by dimming probeam luminaires to acceptable visibility levels. Customized probeam lenses, therefore, could prove to be usefull in the difficult quest of government institutions trying to reduce energy consumption while maintaining traffic safety. Instead of turning off the lights to drastically reduce energy consumption, government institutions are provided with a different solution that does not necessarily compromise driver safety and comfort. As such, this solution could possibly lead to fewer accidents on the road and lower energy consumption, resulting in a positive effect on society.

Chapter 8

Conclusions and Future works

8.1 Conclusions

Currently, the conceptual way of thinking about road lighting is hampered by current road lighting standards that are very restrictive. Yet, society needs new innovative ways to reduce energy consumption of road lighting while maintaining traffic safety. One such innovative option takes advantage of a new generation of road lighting sources (LEDs) and road marking materials, and uses the improved control of light to direct most of the light flux in the forward viewing direction of the driver, i.e. the Probeam concept. Recently, Probeam has shown promising results in tunnel and pedestrian lighting in terms of object visibility, but its use in illuminating highways has not been explored so far. Car headlights contribute to the guiding effect of the car driver due to the retroreflective properties of road markings, however only for roughly the first 60 meters. At larger distances the road lighting should take over. To determine the added value of Probeam in this context, a number of investigations were undertaken, funded by Rijkswaterstaat in The Netherlands. First of all, we needed to know the contrast threshold between a road marking and the surrounding road surface for this type of illumination (with its specific incident and viewing angles), for both younger and older drivers. Secondly, we need to understand the reflection characteristics of road markings and the road surface under the very particular geometry of illumination inherent to this concept. With this knowledge, we define guidelines for an effective probeam illumination concept, leading to a reduction of energy consumption while maintaining traffic safety.

According to the scope of this doctoral research, the following research questions were addressed:

1. How well do current contrast models predict the contrast threshold for the discrimination of a road marking surrounded by the road surface? Is the impact of the age of the observer and of the presence of glare sources sufficiently covered in existing models?
2. What are the reflective characteristics of road marking materials under non-conventional incident angles inherent to Probeam and how to model these characteristics? Based on this knowledge, simulations of the luminance of these retroreflective materials, and yet the contrast, become possible.
3. Can we reduce energy consumption while maintaining traffic safety using the probeam road lighting concept? What is the best location of the illumination zone covered by a probeam luminaire?

A combination of controlled perception research, simulations and field studies to answer the above research questions has led to the following main conclusions.

8.1.1 Road marking contrast threshold revisited

The first step to evaluate the Probeam concept is to determine a single, comprehensive and well established contrast threshold model that is applicable for any combination of object angular size, road and object luminance and age of the observer. This contrast (threshold) model is crucial to determine the minimum required contrast between road surface and road marking for safe and comfortable driving. Today, the contrast threshold model introduced by Adrian in 1989 is still commonly used in road lighting. To evaluate this model, a highway was rendered and an experiment was conducted to determine the contrast threshold for the discrimination of the direction of a road marking arrow for different sizes of the arrow as well as for different luminance values of the road surface. In this rendering, a road marking arrow pointed either to the left or right, and participants had to indicate the direction of the arrow. Depending on whether their answer was right or wrong, the luminance of the arrow was changed, such that we could determine the direction detectability threshold from a psychometric curve. In addition, we evaluated more recent contrast models, such as a difference of gaussian receptive field model and a pyramidal multilevel model. The latter two models are image-based, and thus only require a luminance image as input without specific information about object angular size, background luminance, or luminance of the target, which makes these models more easily applicable in realistic complex scenes. With these image-based models, only contrast values are provided rather than contrast threshold values. Therefore, contrast thresholds for each condition were determined. Ideally, these contrast models allow one to define one contrast threshold value regardless of the luminance of the road and arrow or the size of the arrow to detect arrow direction.

The results suggest that some image based contrast models allow for a reduction in the variation in contrast threshold across different angular sizes of the arrow and road surface luminance values. As such, these models show promising results, but they don't deliver yet the ultimate solution: a unique threshold value, irrespective of background luminance, luminance difference and object angular size.

In addition, Adrian's contrast threshold model, that requires a set of input parameters such as object size and background luminance, shows to be useful and more robust than expected, in handling these complex scenes. The experimental luminance difference thresholds correspond very well (R^2 of 0.75) with thresholds predicted by Adrian's visibility model, with the highest deviations occurring at the smaller angular sizes of the arrow.

8.1.2 Road marking contrast threshold for the elderly and the impact of glare

Although Adrian's model showed to be useful for the set of parameters investigated in the previous experiment, two important factors of the model remained untouched, namely the age factor and the impact of glare. Therefore, we repeated the experiment described above, but now with elderly participants (i.e., 60 years or older) and with a glare source (i.e., 13 lux measured at eye level) added to the experimental setup.

The results indicate an interaction effect between arrow angular size, road surface luminance and glare. On average, the luminance difference thresholds are higher in the presence of a glare source than without a glare source. As expected, this difference is largest at the lowest road surface luminance due to the larger impact of the veiling luminance and scattering in the eye. In addition, comparing the results with results obtained with young participants, we observe an effect of age, indicating that, not surprisingly, older participants have higher luminance difference thresholds than younger participants.

For the observer group that meets Adrian's criteria, Adrian's standard model provides a moderate to poor fit to the measured thresholds (i.e., $R^2 < 0.40$). For the group that does not meet Adrian's criteria (i.e., participants older than 75) the fit becomes even worse. As such, we conclude that the age factor in Adrian's model cannot simply be extrapolated to higher ages. Moreover, our study also seems to recommend an additional multiplicative factor in Adrian's model for visually impaired elderly. Using the formulae mentioned in EN 13201 to calculate the veiling luminance, does not improve the fit. We, therefore, limited the evaluation of the Probeam concept for the visibility of road marking arrows to drivers younger than 75.

8.1.3 Road marking BRDF model applicable for a wide range of incident illumination conditions

To answer the second research question, we measured the reflective characteristics of road marking materials using a commercial LNFG and a wide range of incident illumination angles. BRDF-values were determined based on luminance and illuminance measurements.

All road marking materials, as expected, exhibit retroreflective behavior, where the retroreflection increases as the incident angle increases. Furthermore, it is noteworthy that also the specular reflection increases at larger angles of incidence. The BRDF-values also indicate that both the retroreflection and specular reflection follow a cosine-lobe like behavior. Based on these observations, a new RetroPhong BRDF model is designed. In this model, the retroreflection is modeled by a cosine-lobe in the direction of the incident vector, with the peak of the lobe increasing with the incident angle. The increase in specular reflection is modeled by a cosine-lobe in the specular direction, with the peak of the lobe also increasing with the incident angle. The RetroPhong BRDF model was benchmarked to other BRDF models adapted for retroreflection. From this benchmark, the ABC-Retro model performs closest to the RetroPhong model, however, still results in a slightly worse fit. Therefore, we can conclude that the RetroPhong model fits the measurements better than the other models, and thus should be used to simulate the luminance towards the viewer from a road marking illuminated by a probeam luminaire.

8.1.4 An asymmetric road lighting concept: Probeam

With a well-established contrast (threshold) model and the availability of a model for the retroreflective characteristics of road markings, we can answer the third research question and simulate and develop a Probeam road illumination concept which provides overall sufficient visibility without causing discomfort and disability glare.

In a first step, we calculated the LID of the luminaire required to meet the current road lighting standards for both a Probeam and Symmetrical road lighting concept, using typical reflection characteristics of the road surface and the geometry of a typical (Dutch) highway. In this Probeam concept, the illumination zone of luminaire 1 was located between the poles carrying luminaires 2 and 3. This concept was compared to the Symmetrical lighting concept for their performance in terms of glare, the visibility of a vertical (non-retroreflective) object, and the visibility of horizontal and vertical retroreflective road markings. When designed to meet the current road lighting standards, Probeam produces higher visibility levels, but at a 14% increase in luminous flux compared to symmetrical lighting. This increase in luminous flux is attributed to the minimum road luminance required by the standard. Indeed, the specular reflection of the road surface does not contribute to its luminance with probeam illumination and favors symmetrical lighting. However, when designing the concept based on meeting the same average visibility level of a vertical object, the probeam luminaire can be dimmed to save 52% of energy compared to symmetrical lighting. Moreover, for meeting the same visibility level when halving the mounting height of the probeam luminaire, in addition to dropping the road luminance requirement, an energy saving of 82% compared to symmetrical lighting is realized.

8.1.5 Probeam field tests and concept update

The proof of concept calculations were practically validated with field measurements at the KU Leuven-Gent, campus Rabot and at the test centrum of Dienst Wegverkeer (RDW) in Lelystad. The field measurements at the KU Leuven-Gent, campus Rabot indicated good qualitative correspondence between the data measured and simulated. Some variance was observed due to limitations of the illuminance measurement device, temperature differences, and the sensitivity to the exact positioning of the luminaire. The luminance values indicated higher contrast under probeam illumination than under counterbeam illumination for retroreflective and high-reflective targets, but larger contrast under counterbeam illumination for targets with a lower reflectance than the road surface.

The field measurements at the RDW also pointed to a similar good qualitative correspondence. The visibility of vertical surfaces under probeam or counterbeam illumination depended on their position in the measurement field, but their contrast with the background remained constant. As the contrast of a vertical surface under symmetrical illumination changed from positive to negative and back, this created an unwanted dynamic effect. With probeam lighting, vertical surfaces were always seen in positive contrast but, unfortunately, the measurements at the RDW revealed the occurrence of an annoying reflection/glare in the side mirror of the car.

This issue was further investigated with simulations and led to a different illumination zone targeted by the probeam luminaire, which was shifted to the luminaire pole. This updated concept maintained all the previous advantages and could avoid glare in the side mirror of the car. A corresponding optimized LID of the probeam luminaire has been proposed.

All in all, a reduction in energy consumption while maintaining traffic safety seems possible with the updated probeam road lighting concept, though at the cost of the road luminance requirement which is mentioned in the actual standard. This road luminance requirement in the standard, however, is not relevant in the case of dimming.

A more detailed overview of all the advantages and disadvantages that were revealed in the field tests and simulations, of both probeam and symmetrical lighting, are provided in Table 8.1.

8.1.6 Valorization of the Probeam road lighting concept

The research on the Probeam lighting concept is performed in close collaboration with the Dutch governmental institution Rijkswaterstaat, as well as with the luminaire manufacturer Innolumis. This collaboration resulted in a valorization plan for the development and design of customized lenses following the Probeam road lighting concept. This included a business model canvas, a patent survey, and a freedom to operate analysis.

The Probeam road lighting concept is a long-term substantial investment for Rijkswaterstaat and is useful in reducing the energy consumption of road lighting while maintaining traffic safety. This aligns well with the long term goal of Rijkswaterstaat and other government institutions to reach net zero greenhouse gas emissions by 2050. Furthermore, by reducing the luminous flux, the Probeam concept could eventually save on equipment costs, requiring fewer LEDs, lenses and drivers, and thus also reducing the luminaire housing costs.

The Probeam road lighting concept would also require a substantial investment for Innolumis for the possible future patent rights and to develop a dedicated lighting design, however, Innolumis can benefit from being first to the market and significantly increase sales to Rijkswaterstaat by providing probeam luminaires.

The freedom to operate analysis indicated a limited amount of patents for the Probeam concept. The patents for the Probeam concept that do exist are designed for lighting in tunnels and have very particular LIDs different to the LIDs needed for probeam illumination on highways. Patented works on the probeam road lighting concept outside of tunnels do not exist, therefore, there is a large freedom to operate.

8.2 Future work

The research described in this thesis provides a detailed analysis of the asymmetric road lighting concept Probeam in its application to highways. To develop the concept further, additional work is still required both on a research and a development level, especially regarding improved image based models for contrast perception, further optimization of the lens design and of retroreflective materials, and how to generalize the findings to different road lighting scenarios. In this section, some of these possible future steps are discussed.

Table 8.1: Summary of the advantages and disadvantages of probeam and symmetrical lighting.

Type of Lighting	Advantages	Disadvantages
Probeam lighting	• No disability and discomfort glare • No straylight by luminaires in the windshield • Higher reflection of retroreflective materials • Dimming will reduce energy consumption while keeping good visibility of road markings • Higher vertical illuminance • Lower light masts are possible with an improvement in the visibility of road markings	• Higher energy consumption when maintaining to an average road surface luminance of 0.75 cd/m^2 • Currently, no industrially available lenses on market as optics are more complex for its use on highways • Can only be used for one directional traffic • Sensitivity to the exact mounting position of the luminaire due to the narrow beam • Lower contrast for darker objects • Mirror reflection
Symmetrical lighting	• Lower energy consumption when confirming an average road surface luminance of 0.75 cd/m^2 • Currently optimized lenses available for its use on highways • Can be used for two directional traffic • Dark objects (partially) appear in silhouette view	• Disability and discomfort glare is a problem • Dimming will lower energy consumption without maintaining good visibility of road markings • The switch between counterbeam and probeam lighting can create a dynamic effect of objects seen in positive and negative contrast

1. In the first contrast threshold experiment, image based contrast models were evaluated and the contrast thresholds were determined for each condition. Although these image based contrast models allow to predict contrast thresholds in simulated road environments with larger complexity, further research is necessary to improve the reliability and optimize the parameters to reach a robust image based contrast model that provides a unique threshold value, irrespective of background luminance, luminance difference and object angular size.

2. In our contrast models we used the photopic light sensitivity curve, which is consistent with existing literature and European standardization for road lighting. This is not fully accurate, since our data – as well as data on which existing models in literature are based – are measured in rather mesopic light conditions. To the best of our knowledge the effect of using the photopic sensitive curve for predicting contrast under mesopic light conditions has not been evaluated yet. Possibly adding a correction factor to Adrian's visibility model could bridge this gap between photopic and mesopic conditions. Investigating this to the full extent is critical for improving Adrian's visibility model as a performance metric in road lighting.

3. In the contrast threshold experiment using a glare source, one should include more (elderly) participants in order to model the interaction between age and disability glare. Currently, even with the individually measured straylight parameters, there is still a large amount of unexplained variance in the comparison between the modeled and measured contrast visibility thresholds. Possibly, extending the experiment and conditions can help in reducing this variation by adding individual characteristics of the visual system (e.g., neural factors such as photoreceptor density and quantum efficiency, pupillary miosis, and spectral absorption of crystalline lens) to the model, similar as what is being investigated regarding the implementation of individual cone sensitivity variation in color research.

4. It would be useful to optimize the BRDF experimental setup. Currently, the minimum possible difference in viewing and incidence angle is too limited to allow measuring retroreflectivity for all relevant angles, because the view on the road marking material is obstructed by the light source. Using a smaller light source or a different optical setup could decrease this minimum difference, and extend the range of measured angles to better model the BRDF.

5. It should be noted that the proof of concept investigated in this PhD research has a focus on a single direction highway, existing of two lanes. Possible extensions of the research could be to evaluate how sensitive the particular design is to

changes in the context, for example for different road widths, for curved roads, or for people driving in the opposite direction on the highway.

6. In both contrast threshold experiments reported, the participants were shown multiple static scenes of a rendering of a highway. As such, this study already provided a more realistic environment than earlier studies, however, a real driving experience is not static but mostly dynamic, and contains distractions around the road marking arrow (such as additional road signs, and other cars and objects) and temporal effects (such as impact of driving speeds). In future research, therefore, researchers should create a dynamic environment (i.e., a clip of a road simulation in VR instead of a static image), in which all parameters can be individually controlled, including the size and luminance of multiple objects. Although computationally expensive, ideally, we would show participants a dynamic physical based rendering of a real road environment on a calibrated virtual reality headset and include temporal aspects of the human visual system. Another improvement in such a rendering would be that objects would not be assumed to have a uniform luminance – as we did in our experiments for the road marking arrow – but that we could include the non-uniformity in luminance of objects and the road surface. In addition and ideally, these contrast threshold experiments are also repeated in the field. This would require a semi-permanent location where participants are invited on different evenings. Having contrast threshold data measured in a more realistic setting could improve the image-based contrast threshold models as well. Specifically, the presence of multiple light poles in the scene, as such extending the occurrence of glare from multiple equivalent veiling luminance sources, would increase the performance of the model.

7. In this study, we focused on existing road marking materials, determined their BRDF for a wide range of incident illumination conditions, and designed a Probeam road lighting concept based on these data. The development of a new generation of retroreflective materials optimized for Probeam (a high retroreflection when illuminated by luminaires) could further enhance the contrast levels.

8. Furthermore, currently the spectral power distribution of the luminaire was not included in the optimization and achromatic contrast was assumed. For the development of a luminaire with minimal energy consumption while maintaining traffic safety, Adrian's model should be extended including contrast per cone-type (i.e., long, medium and short wavelength sensitive cones). This also requires the measurement of the spectral reflectance of the road surface and road markings.

9. The optimized probeam LID suggests a minimum decrease of 60% in energy consumption compared to the current symmetrical LID. This potential reduction in energy consumption should be compared, or maybe complemented with other emerging innovations in road lighting, including dynamic/smart lighting to only use lighting where actually needed, optimized reflectivity of road surfaces and road markings to make arrows more visible, dimming solutions to save energy (though at the expense of visibility), and higher energy efficient LEDs [10]. In future research, it is crucial to explore the potential of these options, and if relevant their integration with the Probeam concept to further reduce energy consumption while ensuring traffic safety. Additionally, dynamic/smart lighting has the potential to enhance the Probeam concept by dynamically adjusting the luminous flux based on traffic density.

10. Finally, as research of autonomous vehicles progresses and possibly in the future will start to appear more on the public roads, the effects of the road lighting concepts on advanced driver assistance systems (ADAS) should be further investigated. The optimization of the LID and spectral power distribution to camera based ADAS could prove useful in reducing system errors.

Bibliography

[1] B. M. Matesanz, L. Issolio, I. Arranz, C. de la Rosa, J. A. Menéndez, S. Mar and J. A. Aparicio, "Temporal retinal sensitivity in mesopic adaptation", *Ophthalmic and Physiological Optics*, vol. 31, no. 6, pp. 615–624, 2011.

[2] W. Van Bommel, *Road lighting: Fundamentals, technology, and application.* Springer, 2014.

[3] C. Fors and S. O. Lundkvist, *Night-time traffic in urban areas: A literature review on road user aspects.* Statens väg-och transportforskningsinstitut, 2009.

[4] S. Fotios and R. Gibbons, "Road lighting research for drivers and pedestrians: The basis of luminance and illuminance recommendations", *Lighting Research & Technology*, vol. 50, no. 1, pp. 154–186, 2018.

[5] J. W. Alferdinck, "Target detection and driving behaviour measurements in a driving simulator at mesopic light levels", *Ophthalmic and Physiological Optics*, vol. 26, no. 3, pp. 264–280, 2006.

[6] W. Jory, "Testing night vision for driving", *BMJ*, vol. 322, no. 7287, p. 672, 2001.

[7] P. O. Wanvik, "Effects of road lighting: An analysis based on dutch accident statistics 1987–2006", *Accident Analysis & Prevention*, vol. 41, no. 1, pp. 123–128, 2009.

[8] R. Elvik, "Meta-analysis of evaluations of public lighting as an accident countermeasure", *Transportation Research Record*, vol. 1485, pp. 112–123, 1995.

[9] "Verkeersongevallen - bestand geregistreerde ongevallen nederland". Accessed on 2023-07-20. ().

[10] Ministry of Infrastructure and Water Management. "Energiegebruik en emissies eigen organisatie, duurzaamheidsverslag ienw 2021". Accessed in 2023. (2021), [Online]. Available: https://magazines.rijksoverheid.nl/ienw/duurzaamheidsverslag/2022/01/energiegebruik-en-emissies-eigen-organisatie (visited on 2023).

[11] Rijkswaterstaat Duurzaamheid en Leefomgeving (RWS DuLo), *Rapport naar meer efficiënte en duurzame openbare verlichting voor rijkswegen*, In opdracht van Rijkswaterstaat Duurzaamheid en Leefomgeving (RWS DuLo) en in het kader van Verduurzaming Openbare Verlichting (VOV) Contactpersoon: Bart Wolfs (WVL) Uitgevoerd namens de NSVV door: Ellen de Vries en Rienk Visser m.m.v.: Toine Adams Elkin Petrici Martin Vergeer Rob Trieling Nico de Kruijter Aad de Winter Roel Haamberg Willem Zandvliet Dirk Hetebrij Piet Zijlstra Gé Hulsmans, 2021.

[12] R. W. Rodieck and J. Stone, "Analysis of receptive fields of cat retinal ganglion cells", *Journal of Neurophysiology*, vol. 28, no. 5, pp. 833–849, 1965.

[13] R. W. Rodieck, "Quantitative analysis of cat retinal ganglion cell response to visual stimuli", *Vision Research*, vol. 5, no. 12, pp. 583–601, 1965.

[14] F. M. De Monasterio, "Properties of ganglion cells with atypical receptive-field organization in retina of macaques", *Journal of Neurophysiology*, vol. 41, no. 6, pp. 1435–1449, 1978.

[15] R. Shapley and V. H. Perry, "Cat and monkey retinal ganglion cells and their visual functional roles", *Trends in Neurosciences*, vol. 9, pp. 229–235, 1986.

[16] C. Enroth-Cugell and J. G. Robson, "The contrast sensitivity of retinal ganglion cells of the cat", *The Journal of Physiology*, vol. 187, no. 3, pp. 517–552, 1966.

[17] D. H. Hubel and T. N. Wiesel, "Receptive fields, binocular interaction and functional architecture in the cat's visual cortex", *The Journal of Physiology*, vol. 160, no. 1, p. 106, 1962.

[18] Y. Tadmor and D. J. Tolhurst, "Calculating the contrasts that retinal ganglion cells and LGN neurones encounter in natural scenes", *Vision Research*, vol. 40, no. 22, pp. 3145–3157, 2000, ISSN: 00426989. DOI: 10.1016/S0042-6989(00)00166-8. [Online]. Available: http://www.sciencedirect.com/science/article/pii/S0042698900001668.

[19] R. Shapley and C. Enroth-Cugell, "Visual adaptation and retinal gain controls", *Progress in Retinal Research*, vol. 3, pp. 263–346, 1984.

[20] K. Joulan, N. Hautiere and R. Brémond, "Contrast sensitivity functions for road visibility estimation in digital images", in *Proceedings of 27th CIE Session*, Sun City, South Africa: International Commission on Illumination, 2011, pp. 1144–1149.

[21] G. Simone, M. Pedersen and J. Y. Hardeberg, "Measuring perceptual contrast in digital images", *Journal of Visual Communication and Image Representation*, vol. 23, no. 3, pp. 491–506, Apr. 2012, ISSN: 10473203. DOI: 10.1016/j.jvcir.2012.01.008. [Online]. Available: http://www.sciencedirect.com/science/article/pii/S1047320312000211.

[22] H. R. Blackwell, "Contrast thresholds of the human eye", *JOSA*, vol. 36, no. 11, pp. 624–643, 1946.

[23] W. Adrian, “Visibility of targets: Model for calculation”, *Lighting Research and Technology*, vol. 21, no. 4, pp. 181–188, 1989, ISSN: 1477-1535. DOI: 10.1177/096032718902100404. [Online]. Available: http://journals.sagepub.com/doi/abs/10.1177/096032718902100404.

[24] W. Adrian, “Die Unterschiedsempfindlichkeit des Auges und die Möglichkeit ihrer Berechnung”, *Lichttechnik*, vol. 21, no. 1, 2A–7A, 1969.

[25] E. Aulhorn, “Uber die Beziehung zwischen Lichtsinn und Sehscharfe”, *Albrecht Von Graefes Arch Ophthalmol*, vol. 167, no. 1, pp. 4–74, 1964.

[26] H. J. Schmidt-Claussen, “Lichttechnik”, vol. 21, 126A, 1969.

[27] H. R. Blackwell, *Lighting handbook*. New York (NY): Illuminating Engineering Society, 1966, vol. 4, pp. 2–8.

[28] O. M. Blackwell and H. R. Blackwell, “Individual responses to lighting parameters for a population of 235 observers of varying ages”, *J Illum Eng Soc*, vol. 9, no. 4, pp. 205–232, 1980.

[29] O. M. Blackwell and H. R. Blackwell, “Ieri: Visual performance data for 156 normal observers of various ages”, *Journal of the Illuminating Engineering Society*, vol. 1, no. 1, pp. 3–13, 1971.

[30] R. A. Weale, *The Aging Eye*. London: Lewis, 1963.

[31] C. I. de l’Eclairage, *CIE 227:2017. Lighting for older people and people with visual impairment in buildings*. Vienna: CIE, 2017.

[32] Commission Internationale de l’Eclairage, *Road surface and road marking reflection characteristics*. 2001.

[33] M. Roser and P. Lenz, “Camera-based bidirectional reflectance measurement for road surface reflectivity classification”, *IEEE Intelligent Vehicles Symposium*, pp. 340–347, 2010.

[34] R. M. Spieringhs, J. Audenaert, K. Smet, I. Heynderickx and P. Hanselaer, “Road marking brdf model applicable for a wide range of incident illumination conditions”, *JOSA A*, vol. 40, no. 3, pp. 590–601, 2023.

[35] I. C. on Illumination, “Roadsigns (CIE 74-1988)”, Vienna, Austria: International Commission on Illumination, Tech. Rep., 1988.

[36] E. C. for Standardization, “European Standard Fixed, vertical road traffic signs”, Brussels (BE): CEN, Tech. Rep. CEN-EN 12899: 2007, 2007.

[37] E. C. for Standardization, “Road marking materials - Road marking performance for road users”, Brussels (BE): CEN, Tech. Rep. CEN-EN 1436: 1999, 1999.

[38] C. M. Collier, X. Jin, J. F. Holzman and J. Cheng, “Omni-directional characteristics of composite retroreflectors”, *Journal of Optics A: Pure And Applied Optics*, vol. 11, no. 8, p. 085 404, 2009.

[39] I. C. on Illumination, “Retroreflection: Definition and Measurement (CIE 54.2-2001)”, Vienna, Austria: International Commission on Illumination, Tech. Rep., 2001.

[40] J. B. Deboer, V. Onate and A. Oostrijck, “Practical methods for measuring and calculating the luminance of road surfaces”, *Philips Research Reports*, vol. 7, no. 1, p. 54, 1952.

[41] Commission Internationale de l’Eclairage, *Lighting of roads for motor and pedestrian traffic*. 2010.

[42] E. C. for Standardization, “Road lighting part 3: Calculation of performance”, Brussels (BE): CEN, Report CEN-EN 13201-3:2015, 2015.

[43] C. I. de l’Eclairage, *CIE International Lighting Vocabulary*. Vienna: CIE, 1987.

[44] M. Sato and T. Hagio, “Visibility enhancement and power saving by pro-beam LED tunnel lighting method”, *J Light Visual Environ*, vol. 38, pp. 89–93, 2014.

[45] M. Renzler, N. Reithmaier, R. Reinhardt, W. Pohl and T. Ubmuller, “A road tunnel model for the systematic study of lighting situations”, *Tunnelling and underground space technology*, vol. 72, pp. 114–119, 2018.

[46] M. Kimura, Y. Hamada, Y. Ikeda, H. Motomura and M. Jinno, “Importance of a vector component and the vertical illuminance in road lighting for the obstacle visibility of the road”, *J Sci Technol Light*, vol. 42, pp. 17–21, 2019.

[47] S. Hirakawa, Y. Karasawa and Y. Yoshida, “Visibility evaluation of obstacles on road surface in consideration of vehicle headlamps and tunnel lighting based on total revealing power”, *Journal of the Illuminating Engineering Institute of Japan*, vol. 98, no. 8A, pp. 352–361, 2014.

[48] Y. Q. Lee and S. H. Lee, “A simulation analysis on the probeam lighting for the visibility at a tunnel with whitehole phenomenon”, *Journal of Korean Tunnelling and Underground Space Association*, vol. 9, no. 1, pp. 29–36, 2007.

[49] P. Tomczuk, “Assessment model of luminance contrast of pedestrian figure against background on pedestrian crossing”, *Przegląd Elektrotechniczny*, vol. 88, no. 3a, pp. 104–107, 2012.

[50] R. Brémond, “Visual performance models in road lighting: a historical perspective”, *LEUKOS*, vol. 17, no. 3, pp. 212–241, 2020.

[51] European Commission, DG Transport, “Requirements for horizontal road marking: final report of the action”, COST, Luxembourg, Technical report COST 331, 1999.

[52] M. S. Rea and M. J. Ouellette, “Relative visual performance: A basis for application”, *Lighting Research and Technology*, vol. 23, no. 3, pp. 135–144, 1991. DOI: 10.1177/096032719102300301. [Online]. Available: http://lrt.sagepub.com/content/23/3/135.abstract.

[53] A. Rizzi, T. Algeri, G. Medeghini and D. Marini, "A proposal for contrast measure in digital images", in *Conference on Colour in Graphics, Imaging, and Vision,* Society for Imaging Science and Technology, 2004, pp. 187–192.

[54] M. Berek, "Zeitschrift f. Instrumentenkunde", vol. 63, p. 297, 1943.

[55] P. G. Barten, *Contrast sensitivity of the human eye and its effects on image quality.* SPIE Press, 1999.

[56] W. Jakob, *Mitsuba physically based renderer,* https://www.mitsuba-renderer.org/, 2010.

[57] Blender Foundation, *Version Blender 2.79,* software, Amsterdam (NL), 2017.

[58] European Committee for Standardization, "Road lighting part 2: performance requirements", CEN, Brussels (BE), Report CEN-EN 13201-2:2015, 2015.

[59] J. Wu, C. Zheng, X. Hu and F. Xu, "Realistic simulation of peripheral vision using an aspherical eye model", *Retina,* vol. 5, p. 24, 2011.

[60] S. Mostafawy, O. Kermani and H. Lubatschowski, "Virtual eye: retinal image visualization of the human eye", *IEEE Comput Graph Appl,* vol. 17, no. 1, pp. 8–12, 1997.

[61] Ministerie van Infrastructuur en Waterstaat, *Richtlijn ontwerp autosnelwegen,* 2019.

[62] R. Ministerie van Verkeer en Waterstaat, *Richtlijnen voor de bebakening en markering van wegen,* 1991.

[63] G. Gescheider, "The classical psychophysical methods", in *Psychophysics: the fundamentals,* 3rd, Mahwah (NJ): Lawrence Erlbaum Associates, 1997, pp. 45–73.

[64] F. A. Wichmann and N. J. Hill, "The psychometric function: II. Bootstrap-based confidence intervals and sampling", *Perception & Psychophysics,* vol. 63, no. 8, pp. 1314–1329, Nov. 2001, ISSN: 0031-5117. DOI: 10.3758/BF03194545. [Online]. Available: http://www.springerlink.com/index/10.3758/BF03194545.

[65] J. Hill, "Testing hypotheses about psychometric functions", Ph.D. dissertation, University of Oxford, 2002.

[66] M. Kuss, F. Jäkel and F. A. Wichmann, "Bayesian inference for psychometric functions", *J Vis,* vol. 5, no. 5, p. 8, 2005.

[67] I. Fründ, N. V. Haenel and F. A. Wichmann, "Inference for psychometric functions in the presence of nonstationary behavior", *J Vis,* vol. 11, no. 6, p. 16, 2011.

[68] H. H. Schütt, S. Harmeling, J. H. Macke and F. A. Wichmann, "Painfree and accurate Bayesian estimation of psychometric functions for (potentially) overdispersed data", *Vision Res,* vol. 122, pp. 105–123, 2016.

[69] P. A. Garcia, R. Huertas, M. Melgosa and G. Cui, "Measurement of the relationship between perceived and computed color differences", *JOSA A*, vol. 24, no. 7, pp. 1823–1829, 2007.

[70] J. B. Kruskal, "Multidimensional scaling by optimizing goodness of fit to a nonmetric hypothesis", *Psychometrika*, vol. 29, pp. 1–27, 1964.

[71] Y. Cao, "A Driving simulation based study on the effects of road marking luminance contrast on driving", *Transp Res Rec*, vol. 1093, pp. 43–47, 2004.

[72] A. Mayeur, R. Brémond and J. C. Bastien, "The effect of the driving activity on target detection as a function of the visibility level: implications for road lighting", *Transp Res Part F Traffic Psychol Behav*, vol. 13, no. 2, pp. 115–128, 2010.

[73] M. A. H. Donners, M. Vissenberg, L. M. Geerdinck, J. H. F. Van Den Broek-Cools and A. Buddemeijer-Lock, "A psychophysical model of discomfort glare in both outdoor and indoor applications", in *Proceedings of 28th CIE Session*, vol. 216, 2015.

[74] G. H. Scheir, M. Donners, L. M. Geerdinck, M. C. J. M. Vissenberg, P. Hanselaer and W. R. Ryckaert, "A psychophysical model for visual discomfort based on receptive fields", *Lighting Research and Technology*, vol. 50, no. 2, pp. 205–217, Apr. 2018, ISSN: 14771535. DOI: 10.1177/1477153516660606. [Online]. Available: http://journals.sagepub.com/doi/10.1177/1477153516660606.

[75] R. N. Clark, *Visual astronomy of the deep sky*. Cambridge University Press, 1990.

[76] C. A. Curcio, K. R. Sloan, R. E. Kalina and A. E. Hendrickson, "Human photoreceptor topography", *J Comp Neurol*, vol. 292, no. 4, pp. 497–523, 1990.

[77] R. Brémond, V. Bodard, E. Dumont and A. Nouailles-Mayeur, "Target visibility level and detection distance on a driving simulator", *Light Res Technol*, vol. 45, no. 1, pp. 76–89, 2013.

[78] W. H. Organization. "Ageing and health". (2022), [Online]. Available: https://www.who.int/news-room/fact-sheets/detail/ageing-and-health#:~:text=Every%20country%20in%20the%20world,in%202020%20to%201.4%20billion.

[79] E. C. for Standardization, *Road Lighting Part 2: Performance requirements*. Brussels (BE): CEN, 2015, Report No: CEN-EN 13201-2:2015.

[80] L. Franssen and J. E. Coppens, "Straylight at the retina: Scattered papers", Ph.D. dissertation, Universiteit van Amsterdam, 2007.

[81] K. Joulan, R. Brémond and N. Hautière, "Towards an analytical age-dependent model of contrast sensitivity functions for an ageing society", *The Scientific World Journal*, vol. 2015, 2015.

[82] G. R. Jackson, C. Owsley and G. McGwin Jr, "Aging and dark adaptation", *Vision Research*, vol. 39, no. 23, pp. 3975–3982, 1999.

[83] R. M. Spieringhs, K. Smet, I. Heynderickx and P. Hanselaer, "Road marking contrast threshold revisited", *Leukos*, vol. 18, no. 4, pp. 493–512, 2022.

[84] C. I. de l'Eclairage, *CIE 31:1976. Glare and uniformity in road lighting installations.* Vienna: CIE, 1976.

[85] J. J. Vos and T. J. T. P. Van den Berg, "Report on disability glare", *CIE collection*, vol. 135, no. 1, pp. 1–9, 1999.

[86] T. J. T. P. Van den Berg, "Importance of pathological intraocular light scatter for visual disability", *Documenta Ophthalmologica*, vol. 61, pp. 327–333, 1986.

[87] T. J. Van Den Berg, "Analysis of intraocular straylight, especially in relation to age", *Optometry and vision science: official publication of the American Academy of Optometry*, vol. 72, no. 2, pp. 52–59, 1995.

[88] J. Theeuwes, J. W. Alferdinck and M. Perel, "Relation between glare and driving performance", *Human factors*, vol. 44, no. 1, pp. 95–107, 2002.

[89] T. J. T. P. Van den Berg and J. K. IJspeert, "Straylight meter", in *Noninvasive Assessment of the Visual System*, Optica Publishing Group, Feb. 1991, WE1.

[90] A. B. Watson, "Quest+: A general multidimensional bayesian adaptive psychometric method", *Journal of Vision*, vol. 17, no. 3, pp. 10–10, 2017.

[91] A. B. Watson and D. G. Pelli, "Quest: A bayesian adaptive psychometric method", *Perception & psychophysics*, vol. 33, no. 2, pp. 113–120, 1983.

[92] J. M. Kwon and S. J. Lee, "Factors affecting contrast sensitivity in intermittent exotropia", *Korean Journal of Ophthalmology: KJO*, vol. 34, no. 5, p. 392, 2020.

[93] R. C. Bible and N. Johnson, "Retroreflective material specifications and on-road sign performance", *Transportation research record*, vol. 1801, no. 1, pp. 61–72, 2002.

[94] E. C. for Standardization, "High visibility clothing - Test methods and requirements", Brussels (BE): CEN, Tech. Rep. CEN-EN-ISO 20471: 2013, 2013.

[95] F. E. Nicodemus, J. C. Richmond, J. J. Hsia, I. W. Ginsberg and T. Limperis, "Geometrical considerations and nomenclature for reflectance", NBS monograph, 160, Tech. Rep., 1992.

[96] L. Belcour, R. Pacanowski, M. Delahaie, A. Laville-Geay and L. Eupherte, "Bidirectional reflectance distribution function measurements and analysis of retroreflective materials", *JOSA A*, vol. 31, no. 12, pp. 2561–2572, 2014.

[97] E. P. Lafortune and Y. D. Willems, "Using the modified Phong reflectance model for physically based rendering", Ph.D. dissertation, Katholieke Universiteit Leuven. Departement Computerwetenschappen, 1994, p. 19.

[98] B. Smith, "Geometrical shadowing of a random rough surface", *IEEE transactions on antennas and propagation*, vol. 15, no. 5, pp. 668–671, 1967.

[99] P. Beckmann and A. Spizzichino, *The scattering of electromagnetic waves from rough surfaces*. Norwood, 1987.

[100] C. Schlick, “An inexpensive BRDF model for physically-based rendering”, *Computer graphics forum*, vol. 13, no. 3, pp. 233–246, 1994.

[101] J. F. Blinn, “Models of light reflection for computer synthesized pictures”, in *Proceedings of the 4th annual conference on Computer graphics and interactive techniques*, 1977, pp. 192–198.

[102] E. L. Church, P. Z. Takacs and T. A. Leonard, “The prediction of BRDFs from surface profile measurements”, in *Scatter from Optical Components*, SPIE, vol. 1165, 1990, pp. 136–150.

[103] J. Löw, J. Kronander, A. Ynnerman and J. Unger, “BRDF models for accurate and efficient rendering of glossy surfaces”, *ACM Transactions on Graphics (TOG)*, vol. 31, no. 1, pp. 1–14, 2012.

[104] J. Audenaert, F. B. Leloup, B. GielVan, G. Durinck, G. Deconinck and P. Hanselaer, “Impact of the accurateness of bidirectional reflectance distribution function data on the intensity and luminance distributions of a light-emitting diode mixing chamber as obtained by simulations”, *Optical Engineering*, vol. 52, p. 095 101, 2013.

[105] V. Di Gesu and V. Starovoitov, “Distance-based functions for image comparison”, *Pattern Recognition Letters*, vol. 20, no. 2, pp. 207–214, 1999.

[106] M. Oren and S. K. Nayar, “Generalization of Lambert’s reflectance model”, *Proceedings of the 21st annual conference on Computer graphics and interactive techniques*, pp. 239–246, 1994.

[107] W. J. Van Bommel and J. Tekelenburg, “Visibility research for road lighting based on a dynamic situation”, *Lighting Research & Technology*, vol. 18, no. 1, pp. 37–39, 1986.

[108] K. Rumar, *Visual environment in road traffic*. 1981.

[109] G. Johansson and K. Rumar, “Visible distances and safe approach speeds for night driving”, *Ergonomics*, vol. 11, no. 3, pp. 275–282, 1968.

[110] M. J. Flannagan, M. Sivak, S. Kojima and E. C. Traube, “Effects of overall low-beam intensity on seeing distance in the presence of glare”, University of Michigan, Ann Arbor, Transportation Research Institute, Tech. Rep., 1996.

[111] A. Ekrias, M. Eloholma and L. Halonen, “Effects of vehicle headlights on target contrast in road lighting environments”, *Journal of Light & Visual Environment*, vol. 32, no. 3, pp. 302–314, 2008.

[112] A. Ekrias, M. Eloholma and L. Halonen, “The contribution of vehicle headlights to the visibility of targets in road lighting environments”, *Int Rev Elect Eng (IREE)*, vol. 3, pp. 208–217, 2008.

[113] A. Erkan, D. Hoffmann, T. Singer, J. M. Schikowski, K. Kunst, M. A. Peier and T. Q. Khanh, “Influence of headlight level on object detection in urban traffic at night”, *Applied Sciences*, vol. 13, no. 4, p. 2668, 2023.

[114] J. M. Waldram, “The development of street lighting in great britain”, *Transactions of the Illuminating Engineering Society*, vol. 15, no. 8, pp. 285–313, 1950.

[115] J. Waldram, “The revealing power of street lighting installations”, *Trans Illum Eng Soc*, vol. 3, p. 173, 1938.

[116] B. S. Institution, *BS5489-2:1985 Draft Code of Practice for Road Lighting: Part 2.* London: BSI, 1985.

[117] Commission International de l’E’clairage, *Recommendations for the Lighting of Roads for Motorized Traffic.* Vienna: CIE, 1977.

[118] M. van Infrastructuur en Waterstaat, “Richtlijn ontwerp autosnelwegen”, Report, 2019.

[119] IEEE. “Ieee p2020 - standard for automotive system image quality”. (), [Online]. Available: https://standards.ieee.org/develop/project/2020.html.

[120] N. L. Koren, “Correcting misleading image quality measurements”, *Electronic Imaging*, vol. 2020, no. 9, pp. 242–1, 2020.

[121] J. Waldram, “The revealing power of street lighting installations”, Tech. Rep., 1938, p. 173.

[122] M. Canazei, W. Pohl and S. Staggl, “Influence of tunnel lighting on cognitive and visual performance parameters – a field study”, in *20th EVU Annual Congress*, 2011.

[123] P. Tomczuk, K. Jamroz, T. Mackun and M. Chrzanowicz, “Lighting requirements for pedestrian crossings–positive contrast”, *MATEC Web of Conferences*, vol. 262, p. 05 015, 2019.

[124] H.-Y. Liao, S.-Y. Chen, H.-T. Le, W.-L. Gao, F.-C. Chang, C.-C. Wen, Y.-C. Fang, C.-H. Chen, S.-H. Chang and H.-Y. Lee, “Design and prototyping of efficient led counter beam light with free-formed surface for meeting international tunnel lighting standards”, *Energies*, vol. 14, no. 2, p. 488, 2021.

[125] K. Desnijder, W. Ryckaert, P. Hanselaer and Y. Meuret, “Luminance spreading freeform lens arrays with accurate intensity control”, *Optics Express*, vol. 27, no. 23, pp. 32 994–33 004, 2019.

[126] M. E. Raypah, B. K. Sodipo, M. Devarajan and F. Sulaiman, “Estimation of luminous flux and luminous efficacy of low-power smd led as a function of injection current and ambient temperature”, *IEEE Transactions on Electron Devices*, vol. 63, no. 7, pp. 2790–2795, 2016.

[127] W. Adrian and R. Gibbons, “Fields of visibility of the nighttime driver”, *Light & Engineering*, vol. 3, pp. 1–12, 1995.

[128] J. B. De Boer, F. Burghout and J. van Heemskerck Veekens, *Fundamental Experiments of Visibility and Admissible Glare in Road Lighting*. Stockholm, CIE, 1951.

[129] M. S. Janoff, "The relationship between visibility level and subjective ratings of visibility", *Journal of the Illuminating Engineering Society*, vol. 21, no. 2, pp. 98–107, 1992.

[130] J. Lecocq, "Visibility in road lighting: Correlation of subjective assessments with calculated values", in *Lux Europe 97*, 1997.

[131] Z. Chen, Y. Tu, Z. Wang, L. Liu, L. Wang, D. Lou, K. Zhu and K. Teunissen, "Target visibility under mesopic vision using a driving simulator", *Lighting Research & Technology*, vol. 51, no. 6, pp. 883–899, 2019.

[132] C. Kang, G. Lin, L. Ye, C. Zhang, Z. Huang and K. Wu, "Influence of luminance and luminance longitudinal uniformity of tunnel lighting on drivers' comprehensive visual performance", *Tunnelling and Underground Space Technology*, vol. 140, p. 105 282, 2023.

[133] "Wat is de doelstelling voor het aantal verkeersslachtoffers?" Accessed in 2023. (2023), [Online]. Available: https://swov.nl/nl/fact/verkeersdoden-11-wat-de-doelstelling-voor-het-aantal-verkeersslachtoffers (visited on 2023).

[134] A. Osterwalder, *What is a business model?*, business-model-design.blogspot.com, Archived from the original on 2006-12-13. Retrieved 2019-06-19., Nov. 2005.

[135] K. Lee, "2022 solid-state lighting r&d opportunities", Guidehouse, Tech. Rep. DOE/EE-2542, 2022.

List of publications

Journal articles

Spieringhs, R. M., Smet, K., Heynderickx, I., & Hanselaer, P. (2024). An asymmetric road lighting concept: Probeam. “Lighting Research & Technology”.

Spieringhs, R.M., Smet, K., Cuijpers, R. H., Heynderickx, I., Hanselaer, P. (2024). Road marking contrast threshold for the elderly and the impact of glare. “LEUKOS”. doi: 10.1080/15502724.2024.2337385

Spieringhs, R.M., Audenaert, J., Smet, K., Heynderickx, I., Hanselaer, P. (2023). Road marking BRDF model applicable for a wide range of incident illumination conditions. “Journal Of The Optical Society Of America A-Optics Image Science And Vision”, 40 (3), 590-601. doi: 10.1364/JOSAA.470968

Spieringhs, R.M., Phung, T.H., Audenaert, J., Hanselaer, P. (2022). Exploring the Applicability of the Unified Glare Rating for an Outdoor Non-Uniform Residential Luminaire. “Sustainability”, 14 (20), Art.No. 13199. doi: 10.3390/su142013199

Phung, T.H., Spieringhs, R.M., Smet, K., Leloup, F., Hanselaer, P. (2022). Towards an image-based brightness model for self-luminous stimuli. “Optics Express”, 9035-9052. doi: 10.1364/OE.451265

Spieringhs, R.M., Smet, K., Heynderickx, I., Hanselaer, P. (2021). Road Marking Contrast Threshold Revisited. “LEUKOS”, 18 (4), 493-512. doi: 10.1080/15502724.2021.1993893

Conference proceedings

Bhaumik, U., Spieringhs, R.M., Smet, K. (2022). Color Characterization of Displays using Neural Networks. In: “CVCS2022 Proceedings: vol. 3271”, (Paper No. 5).

Presented at the Colour and Visual Computing Symposium 2022, Norway, 08 Sep 2022-09 Aug 2022.

Spieringhs, R.M., Phung, T.H., Hanselaer, P. (2022). Applying the Unified Glare Rating for a non-uniform residential luminaire. In: “Proceedings of 17th International Symposium on the Science and Technology of Lighting (LS:17)”. Presented at the EEDAL-LS-2022: International Conference on Energy Efficiency in Domestic & Light Sources, Toulouse, France. ISBN: 978-2-492754-00-5.

Spieringhs, R.M., Murdoch, M., Vogels, I. (2019). Time course of chromatic adaptation under dynamic lighting. In: “27th Color and Imaging Conference Final Program and Proceedings: vol. 2019”, (13-18). Presented at the Color and Imaging Conference, Paris, 21-25 Oct 2019.

Abstracts, presentations, posters

Spieringhs, R.M. (2022). Het waarnemen van contrasten, met en zonder verblinding. Presented at the “Future Lighting”, Gorinchem.

Spieringhs, R.M., Smet, K., Zandvliet, W., Heynderickx, I., Hanselaer, P. (2022). The development of a new road lighting concept. Poster presented at the “ILIAD 2022”, Eindhoven.

Spieringhs, R.M. (2022), "Development of a new road lighting concept", “WaveCoRE PhD seminar”, Ghent.

Spieringhs, R.M. (2020). Streetlighting and Road Marking performance. Presented at the European Working Group on Road Markings, Online.

Spieringhs, R.M., Murdoch, M. (contr.), Vogels, I. (contr.) (2020). Time course of chromatic adaptation under dynamic lighting. Presented at the “COLOUR GROUP (GB) JANUARY MEETING”, London.

Spieringhs, R.M. (2020). Contrasten bij Probeam snelwegverlichting. Presented at the “Rijkswaterstaat Symposium "Waarnemen bij kunstlicht"”, Amsterdam.

Spieringhs, R.M. (2019). Perception of color differences. Presented at the “Signify Mini-Symposium on Colour Rendition”, Eindhoven.

FACULTY OF ENGINEERING TECHNOLOGY
DEPARTMENT OF ELECTRICAL ENGINEERING
LIGHT & LIGHTING LABORATORY
Gebroeders De Smetstraat 1
B-9000 Ghent
rik.spieringhs@kuleuven.be
www.iiw.kuleuven.be/onderzoek/lichttechnologie

Eindhoven University of Technology
Department of Industrial Engineering & Innovation Sciences